

DISSERTATION ZUR ERLANGUNG DES DOKTORGRADES DER FAKULTÄT CHEMIE UND  
PHARMAZIE DER LUDWIG-MAXIMILIANS-UNIVERSITÄT MÜNCHEN

PHOTOSWITCHABLE PEPTIDES FOR  
PHOTOPHARMACOLOGICAL AND STRUCTURAL BIOLOGY  
APPLICATIONS

**TOM PODEWIN**

AUS BERLIN, DEUTSCHLAND

2016

## **ERKLÄRUNG**

Diese Dissertation wurde im Sinne von § 7 der Promotionsordnung vom 28. November 2011 von Frau Prof. Dr. Anja Hoffmann-Röder betreut.

## **EIDESSTATTLICHE VERSICHERUNG**

Diese Promotion wurde eigenständig und ohne unerlaubte Hilfe erarbeitet.

München,

Tom Podewin

Dissertation eingereicht am: 19. November 2016

Erstgutachter: Prof. Dr. Anja Hoffmann-Röder

Zweitgutachter: Prof. Dr. Wolfgang Zinth

Tag der mündlichen Prüfung: 23. Januar 2017

*"A good scientific idea should be explicable to a barmaid."*

Ernest Rutherford

## DANKSAGUNG

Nach etwas mehr als vier Jahren Promotionszeit und insgesamt zehn Jahren an der LMU ist es endlich soweit: Mit Abgabe dieser Dissertation und nach erfolgreichem Rigorosum erhalte ich die Doktorwürde. In dieser Zeit wurde ich von so vielen Leuten freundschaftlich, fachlich und moralisch unterstützt, dass es schlicht unmöglich ist, sie alle aufzulisten. Darum beschränke ich mich hier auf die wesentlichen Akteure und bitte um Verständnis all derer, die hier nicht aufgeführt sind, aber trotzdem meinen Dank verdient haben.

Zuallererst möchte ich meiner Familie für die stete Geborgenheit, Liebe, Rückhalt und Motivation danken. Ich bin froh Euch zu haben! Zu dieser Familie gehört auch Cosima, die mich als treue Weggefährtin durch schöne wie auch schwierige Zeiten begleitet hat. Dafür bin ich dir sehr dankbar. Du bedeutest mir unendlich viel.

Besonderen Dank möchte ich meiner Doktormutter Frau Prof. Dr. Anja Hoffmann-Röder aussprechen. Sie hat mir die Erarbeitung meiner Dissertation erst ermöglicht und mich während der gesamten Promotionszeit hervorragend betreut. Dabei war Sie stets offen für meine Ideen und Konzepte und ermöglichte es mir so, mich wissenschaftlich frei zu entwickeln.

Ich möchte mich auch bei den an den Projekten beteiligten Personen und Kooperationspartnern bedanken, ohne sie wäre meine Forschung und die Erstellung dieser Arbeit nicht möglich gewesen.

Danke an meinen Zweitgutachter Herrn Prof. Dr. Zinth für die Begutachtung meiner Arbeit und für die tolle Kooperation, die wir zwischen unseren Gruppen aufgebaut haben.

Danke an Herrn Prof. Dr. Dirk Trauner für die Mitentwicklung und Leitung der photopharmakologischen Forschungsprojekte und die Bereitstellung von Wissen, Geräten und Material.

Danke an Herrn Prof. Dr. David J. Hodson für die Aufnahme in seine Gruppe in Birmingham, und auch für die tolle Zeit abseits des Forschungsalltags. In diesem Zusammenhang danke ich auch der Europäischen Stiftung für Diabetesforschung, die mir durch ein Reisestipendium den Aufenthalt in Birmingham ermöglicht hat.

Danke auch an meine anderen Kooperationspartner Herrn Prof. Dr. Konstantin L. Karaghiosoff für die schöne Zeit am NMR, und Herrn Prof. Dr. Andreas Friebe für den tollen und produktiven Aufenthalt in Würzburg.

In diesem Sinne möchte ich mich auch bei meiner gesamten Prüfungskommission bedanken.

Danken möchte auch all den Forschungsgruppen denen ich angehört habe, allem voran der ganzen Hoffmann-Röder Gruppe. Ein Labor kann manchmal wie eine WG sein, mit all den Vor- und Nachteilen die damit einhergehen. Trotz gelegentlicher Reiberein hatte ich eine schöne Zeit mit Euch und ich hoffe, dass wir auch in Zukunft miteinander arbeiten werden.

Ganz besonders möchte ich mich bei Maxi bedanken, mit dem ich seit der Schulzeit durch dick und dünn gegangen bin. Du bist wie ein Bruder für mich und ich bin gespannt was die Zukunft für uns bereithält!

Ich möchte mich auch sehr bei Johannes bedanken, du hast mich an die ganze Thematik herangeführt und zusammen haben wir schöne Projekte und Ideen entwickelt. Danke Dir für Deine Unterstützung und Ratschläge in jeder Lebenslage, und für die schönen Pipettierabende!

Vielen Dank auch an die Familie Mauchart, die es mit geselligen Abenden immer wieder geschafft hat, das Konzept von Raum, Zeit, Stress, Termindruck und elaborierter Forschung auszuhebeln. Danke euch!

## READING MANUAL

Dear Reader,

Thank you for taking the time to read this thesis. Here you can find some brief explanations on the structure of this work. It represents a synopsis of past, current and future projects and shall give a good overview of what was achieved over the thesis period of four years. Some of these projects were already published in peer-reviewed journals or have been recently submitted. In either case, the publications and manuscripts are depicted in the different chapters. They are framed by an INTRODUCTION and an ADDITIONAL COMPOUNDS section, and completed by a SUMMARY AND OUTLOOK. At the end of every chapter one can find selected parts of the supporting information, *i.e.* supporting figures and tables, which are referred to in the publications and manuscripts. What is not shown are details on compound synthesis, experiments, methods and equipment, as this information can either be retrieved online from the publisher's homepage or from the enclosed CD. However, details on chemical synthesis and characterization of any additional compounds are listed in the EXPERIMENTAL section at the end of every chapter. In the APPENDIX, the reader can find general information which applies to all projects, *i.e.* details on peptide synthesis, general methods and equipment.

Enjoy!

## FORSCHUNGSZUSAMMENFASSUNG

Die Verwendung von optisch schaltbaren Molekülen in denen strukturelle Änderungen durch Beleuchtung hervorgerufen werden können, sogenannte Photoschalter, wurde in den letzten Jahren erfolgreich auf eine Vielzahl von Anwendungsgebieten ausgeweitet. Dazu gehören unter anderem die Photopharmakologie und Optogenetik, so wie die strukturelle Untersuchung von Proteinfaltungsprozessen. Während die ersten beiden Gebiete die strukturelle Änderung des Rezeptors nutzen um die Funktionen von biologischen Molekülen und Systemen zu steuern, wird diese bei der Untersuchung von Faltungsprozessen zur Bildung und Auflösung von Strukturelementen, wie zum Beispiel  $\alpha$ -helikalen oder  $\beta$ -Faltblatt Sekundärstrukturen, verwendet. Zudem zeigt die Verleihung des Nobelpreises in Chemie 2016 an die drei Forscher *Bernard Feringa*, *Jean-Pierre Sauvage* und *James Fraser Stoddart*, dass die Entwicklung von molekularen Maschinen und steuerbaren Molekülen in den letzten 30 Jahren weit vorangeschritten ist und auch in den nächsten Jahren spannende Neuerungen zu erwarten sind.

In dieser Arbeit wurden neue Systeme für die optisch-chemische Kontrolle von Rezeptoren und für die Peptidfaltung entwickelt. Voranstehend ist eine Zusammenfassung in Englisch und Deutsch zu finden, gefolgt von einer detaillierten Beschreibung der an den Projekten beteiligten Personen. Der allgemeinen Einleitung folgt TEIL I, welcher nach einer Einführung in die Welt der photoschaltbaren Moleküle die Entwicklung und Synthese von Azobenzol-basierten Photoschaltern beschreibt. Darunter befinden sich zum einen Photoschalter, welche als Festphasenbausteine in der Peptidsynthese zur Herstellung von optisch-responsiven Peptiden verwendet wurden, zum anderen photoschaltbare Crosslinker, welche über reaktive Gruppen in Peptide eingeführt werden.

In TEIL II werden zunächst allgemeine Aspekte der Pharmakologie, Photopharmakologie und Optogenetik besprochen, gefolgt von drei in dieser Arbeit aufgeführten (photo)pharmakologischen Projekten, welche die in TEIL I besprochenen Photoschalter zur Anwendung bringen. Dabei beschreibt KAPITEL 2 die Herstellung und Evaluation des Hormones TOP271, welches eine photoschaltbare Variante des Atrial Natriuretischen Peptides (ANP) ist. ANP ist ein potenter Vasodilator und hat eine Vielzahl von Funktionen, wie zum Beispiel die Blutdrucksenkung und die Regulation des Blut- und Wasserhaushaltes. Neue Erkenntnisse lassen zudem eine wesentlich vernetztere Rolle von ANP im Körper vermuten, allerdings wird hier der Effekt von ANP teils kontrovers diskutiert, da gegenläufige Ergebnisse zu unterschiedlichen Aussagen führen. Mit TOP271 konnte erfolgreich die Aktivität des Atrial Natriuretischen Peptid Rezeptors (NPR-A) mit Licht reguliert und somit direkt die Synthese von cyclischem Guanosinmonophosphat (cGMP) gesteuert werden. In weiterführenden Experimenten konnte in explantierten Aorten der Tonus der glatten Muskulatur mittels Licht reversibel beeinflusst werden, was eine Anwendung für kardiovaskuläre Untersuchungen ermöglicht. Zudem wurde in Langerhans-Inseln aus der Bauchspeicheldrüse, welche den NPR-A Rezeptor endogen exprimieren, eine reversible, licht-regulierte Unterdrückung der zellulären  $\text{Ca}^{2+}$ -Ströme mit TOP271 gezeigt. Um genaueren Einblick in die differenzielle NPR-A Rezeptor Aktivierung zu bekommen wurden Molekulardynamik-Simulationen durchgeführt, welche die unterschiedlichen Strukturen der beiden Isomere von TOP271 im Vergleich zu ANP zeigen. Die Simulationen des Apo- und

hormongebundenen Rezeptors lieferten dabei neue Erkenntnisse für den Mechanismus der Aktivierung von rezeptorgebundenen Enzymen.

KAPITEL 3 widmet sich der Herstellung und Evaluation des photoschaltbaren Hormones LirAzo, welches auf dem Medikament Liraglutide (Victoza<sup>®</sup>) zur Behandlung von Typ 2 Diabetes (T2D) basiert. T2D ist die häufigste Form von Diabetes, in der eine wachsende zelluläre Insulinresistenz durch eine erhöhte Insulinsekretion der  $\beta$ -Zellen der Bauchspeicheldrüse ausgeglichen werden muss. In fortgeschrittenem Stadium kann der Insulinbedarf nicht mehr gedeckt werden, was zu einer kontinuierlichen Abnahme der  $\beta$ -Zellmasse und ultimativ zum Verlust der endogenen Insulinproduktion führt. Liraglutide selbst ist ein langwirkendes Inkretin-Mimetikum, das dem endogenen Hormon Glucagon-like peptide 1 (GLP-1) nachempfunden ist. GLP-1 wird nach der Nahrungsaufnahme im Darm ausgeschüttet und erhöht in erster Linie die Insulinsekretion in  $\beta$ -Zellen der Bauchspeicheldrüse. Weitere Funktionen sind die Unterdrückung der Glukagonsekretion (dem Gegenspieler von Insulin), die Verzögerung der Magenentleerung und die Unterdrückung von Appetit. Die Halbwertszeit von GLP-1 im Blut beträgt nur 1-2 Minuten, wodurch eine beständige Sekretion stattfinden muss. Langwirkende Inkretin-Mimetika wie Liraglutide nutzen die Eigenschaften von GLP-1, um die verminderte Insulinsekretion in T2D Patienten, bei gleichzeitiger Bekämpfung von Ursachen wie Übergewicht, zu behandeln. Allerdings sind erst wenige Studien über die Langzeitwirkung dieser Medikamente bekannt, wobei jedoch erste Hinweise auf erhöhte Risiken für Bauchspeicheldrüsen- und Schilddrüsenkrebs vorliegen. Das photoschaltbare Inkretin-Mimetikum LirAzo ermöglicht es die Rezeptoraktivierung des GLP-1 Rezeptors und die folgenden intrazellulären Signaltransduktionskaskaden optisch zu steuern und zu untersuchen. Für G-Protein-gekoppelte Rezeptoren (GPCRs), zu denen auch der GLP-1 Rezeptor gehört, wurde bereits gezeigt, dass die unterschiedliche Rezeptoraktivierung zu verschiedenen intrazellulären Signalen führt. Die beiden Isomere von LirAzo bewirken dabei eine unterschiedliche Signalwirkung des GLP-1 Rezeptors über cyclisches Adenosinmonophosphat (cAMP) oder  $\text{Ca}^{2+}$ , was zum einem zu einer erhöhten Insulinausschüttung und zum anderen zu stimulierter Zellproliferation führt. Mit LirAzo konnte somit die Bedeutung des cAMP-Signalweges für die Insulinsekretion verstärkt und ein weiteres Puzzleteil für die komplexe Aktivierung von GPCRs geliefert werden.

In KAPITEL 4 wird ein weiteres modifiziertes Inkretin-Mimetikum, ExONatide, besprochen, welches auf dem T2D Medikament Exenatide (Byetta<sup>®</sup>) basiert. ExONatide besitzt eine Benzylguaningruppe, die durch einen flexiblen Linker und eine Disulfidbrücke an den Liganden gebunden ist. Die Benzylguaningruppe ermöglicht die kovalente Anbindung von ExONatide an ein reaktives Cystein eines SNAP-Tags. Um tieferen Einblick in die Rezeptor-Desensibilisierung nach Aktivierung und anschließender endosomaler Sortierung und Degradation zu bekommen, wurde ExONatide an den GLP-1 Rezeptor mit SNAP-Tag (SNAP-GLP-1R) gebunden. Durch das kovalent gebundene ExONatide wird der Rezeptor konstitutiv aktiviert und die Internalisierung sowie das Recycling des Rezeptor-Liganden-Komplexes konnte beobachtet werden. Dabei wurde gezeigt, dass kein Recycling des SNAP-GLP-1 Rezeptors mit gebundenen ExONatide stattfindet. Erst nach der reduktiven Abspaltung des Liganden findet eine Rückkehr des Rezeptors an die Zellmembran statt. Vor allem in Anbetracht der Frage, ob die beobachteten erhöhten

cAMP-Level nach GLP-1 Rezeptoraktivierung auf sehr schnelle Recycling-Prozesse oder auf endosomale cAMP-Produktion zurückzuführen sind, beweist ExONatide eindeutig, dass eine fortwährende Bindung des Liganden an den Rezeptor zu einem verzögerten Recycling führt.

Der dritte und letzte Teil dieser Arbeit widmet sich der Verwendung von photoschaltbaren Peptiden für die Untersuchung von Proteinfaltungsprozessen. Aufgrund der Komplexität dieser Vorgänge existieren bis heute nur wenige einheitliche Modelle, und diese ändern sich zudem stetig. Dank zunehmender Rechenleistung können heute die Strukturen und Faltungsvorgänge komplizierter Biomoleküle simuliert und detaillierte theoretische Modelle erstellt werden, welche jedoch der experimentellen Bestätigung bedürfen. In Anbetracht von neurodegenerativen Krankheiten wie Alzheimer oder Creutz-Feldt-Jakob, die mit einer erhöhten Fehlfaltung und Aggregation von Proteinen verbunden werden, ist das Verständnis der Proteinlebenszyklen – von der Proteinbiosynthese, über die Faltung und Qualitätskontrolle bis hin zur Degradation – von eminenter Wichtigkeit. Wie in der allgemeinen Einleitung zu TEIL III beschrieben, gibt es verschiedene Ansätze zur Untersuchung von Faltungsprozessen, wobei sich diese Arbeit auf kleine Modellsysteme von  $\beta$ -Hairpinpeptiden konzentriert. Bedingt durch die Vermutung, dass dieses Strukturmotiv in Proteinen als Kristallisationskeime für die Proteinfaltung dient, wurden in den letzten Jahrzehnten viele solcher Modellsysteme entwickelt. Dabei wurden Azobenzolphotoschalter, welche mit hoher zeitlicher und räumlicher Genauigkeit strukturelle Änderungen hervorrufen, verwendet, um die Faltungs- und Entfaltungsprozesse der  $\beta$ -Hairpinpeptide zu steuern. In KAPITEL 5 wird ein neues photoschaltbares  $\beta$ -Hairpinpeptid aufgezeigt, das auf dem Miniprotein Chignolin basiert. Anhand dieses AzoChignolin-Peptids und verwandter Mutanten können hydrophile und hydrophobe, stabilisierende Wechselwirkungen im  $\beta$ -Hairpin bei der Faltung und Entfaltung untersucht, und Rückschlüsse auf den jeweiligen Anteil bei Faltungsprozessen gezogen werden.

Zusammenfassend demonstriert diese Arbeit die Verwendung molekularer Schalter in verschiedenen Forschungsbereichen, von der praktischen Anwendung als „Biologische Forschungswerkzeuge“ in der Diabetesforschung, bis hin zu Modellsystemen für Proteinfaltungsstudien. Die photopharmakologischen Verbindungen wurden dabei in *in vitro*- und *ex vivo*-Studien biologisch evaluiert, wobei *in vivo*-Studien bereits in Planung sind. Die Peptidfaltung wurde mittels verschiedener spektroskopischer Methoden untersucht, allen voran der Ultrakurzzeit-Spektroskopie. In naher Zukunft sind weitere Untersuchungen und Modifikationen der neuentwickelten Systeme geplant.

## PUBLICATIONS AND COMMUNICATIONS

### Parts of this work have been published in peer-reviewed journals:

- 4 Podewin, T., Broichhagen, J., Fine, N. H. F., Leippe, P., Gailer, M., Buenaventura, T., Kanda, N., Janik, S., Tomas, A., Trauner, D., Hoffmann-Röder, A., Hodson, D. J. Constitutive activation and trafficking of a class B G-protein coupled receptor using tethered pharmacology, *submitted*.
- 3 Podewin, T.,\* Broichhagen, J.,\* Frost, C., Groneberg, D., Meyer-Berg, H., Fine, N. H. F., Friebe, A., Zacharias, M., Hodson, D. J., Trauner, D., Hoffmann-Röder, A. Optical control of a receptor-linked guanylyl cyclase using a photoswitchable peptidic hormone, *submitted*.
- 2 Broichhagen, J.,\* Podewin, T.,\* Meyer-Berg, H., von Ohlen, Y., Johnston, N. R., Jones, B. J., Bloom, S. R., Rutter, G. A., Hoffmann-Röder, A., Hodson, D. J., Trauner, D. Optical control of insulin secretion using an incretin switch. *Angew. Chem. Int. Ed.* **54**, 15565-15569 (2015), *Angew. Chem.* **127**, 15786-15790 (2015).
- 1 Podewin, T., Rampp, M., Turkanovic, I., Karaghiosoff, K. L., Zinth, W., Hoffmann-Röder, A. Photocontrolled chignolin-derived  $\beta$ -hairpin peptidomimetics. *Chem. Commun.* **41**, 4001-4004 (2015).

\* These authors contributed equally to the work.

### Parts of this work have been presented as oral or as poster communications at scientific conferences:

- 8 "Sweet hairpins: optical manipulation of hairpin structures in novel AzoGlycoChignolin compounds" and "LirAzo and AzoANP: Photopharmacological tools for the unraveling of signaling pathways" (poster presentations), Sonderforschungsbereich 749 (SFB749) annual meeting, March 2016, Kloster Irsee, Germany
- 7 "Photoswitchable peptides: Design, synthesis and photopharmacology" (talk), Oberseminar Ultrakurzzeitspektroskopie, Faculty of Physics, LMU, December 2015, Munich, Germany
- 6 "Optical control of insulin secretion using an incretin switch" (oral communication and poster presentation), 5<sup>th</sup> Austrian Peptide Symposium, December 2015, Vienna, Austria
- 5 "Optical control of insulin secretion using an incretin switch" (poster presentation), Tokio LMU Symposium, October 2015, Martinsried, Germany
- 4 "Photocontrolled azochignolin  $\beta$ -hairpin peptidomimetics" (poster presentation), 16<sup>th</sup> Tetrahedron Symposium, June 2015, Berlin, Germany
- 3 "Photocontrolled chignolin-derived  $\beta$ -hairpin model peptides" (poster presentation), 4<sup>th</sup> Austrian Peptide Symposium, December 2014, Salzburg, Austria
- 2 "Novel photoisomerizable  $\beta$ -hairpin peptides" (poster presentation), Gesellschaft Deutscher Chemiker (GDCh) Wissenschaftsforum, July 2013, Darmstadt, Germany
- 1 "Novel photoisomerizable  $\beta$ -hairpin peptides" (poster presentation), 14<sup>th</sup> Tetrahedron Symposium, June 2013, Vienna, Austria

## TABLE OF CONTENTS

DANKSAGUNG .....	I
READING MANUAL .....	III
FORSCHUNGSZUSAMMENFASSUNG .....	IV
PUBLICATIONS AND COMMUNICATIONS .....	VII
TABLE OF CONTENTS .....	VIII
ABSTRACT .....	1
ABSTRACT (DEUTSCH) .....	2
PROJECT AFFILIATION DISCLOSURE .....	3
GENERAL INTRODUCTION .....	4

## PART I - PHOTOSWITCHES: DESIGN AND SYNTHESIS

1	AZO BENZENES AS MOLECULAR SWITCHES .....	8
1.1	PRINCIPLES OF OPTICAL CONTROL .....	8
1.1.1	AZO BENZENE .....	9
1.1.2	TUNING THE SPECTRAL PROPERTIES OF AZO BENZENE .....	10
1.1.3	MODIFYING AZO BENZENE WITH SUBSTITUENTS .....	11
1.1.4	MODIFYING THE AZO BENZENE CORE .....	13
1.1.5	METHODS OF AZO BENZENE IMPLEMENTATION AND PHOTOCONTROL .....	14
1.2	RESULTS .....	16
1.2.1	SYNTHESIS OF FMOC-AMPP <b>1.26</b> .....	17
1.2.2	SYNTHESIS OF FMOC-AZOPHE <b>1.27</b> .....	18
1.2.3	SYNTHETIC ROUTE TOWARDS FMOC-AMBD <b>1.28</b> .....	18
1.2.4	SYNTHESIS OF <i>p</i> -BDCA <b>1.25</b> .....	20
1.2.5	SYNTHESIS OF <i>m</i> -BDCA <b>1.29</b> .....	21
1.2.6	SYNTHESIS OF DABT <b>1.30</b> .....	22
1.3	EXPERIMENTAL .....	25
1.3.1	SYNTHESIS .....	25
1.3.2	SPECTRAL DATA .....	40

## PART II - PHOTOPHARMACOLOGY AND TETHERED PHARMACOLOGY

2	OPTICAL CONTROL OF THE NATRIURETIC PEPTIDE RECEPTOR A USING A PHOTOSWITCHABLE HORMONE (AZOANP).....	56
2.1	MANUSCRIPT: OPTICAL CONTROL OF A RECEPTOR-LINKED GUANYLYL CYCLASE USING A PHOTOSWITCHABLE PEPTIDIC HORMONE.....	57
2.2	SUPPLEMENTARY FIGURES AND TABLES .....	65
2.3	ADDITIONAL COMPOUNDS AND DATA .....	81
2.4	SUMMARY AND OUTLOOK.....	83
2.5	EXPERIMENTAL.....	85
2.5.1	SPECTROSCOPIC AND SPECTROMETRIC DATA OF TOP263-271 .....	85
2.5.2	EXPERIMENTAL DATA OF ADDITIONAL COMPOUNDS N24AzOPHE-ANP <b>2.2</b> AND S25AzOPHE-ANP <b>2.3</b> .....	93
3	OPTICAL CONTROL OF INSULIN SECRETION USING AN INCRETIN SWITCH (LIRAZO) .....	96
3.1	ARTICLE: OPTICAL CONTROL OF INSULIN SECRETION USING AN INCRETIN SWITCH.....	99
3.2	SUPPLEMENTARY FIGURES AND TABLES .....	104
3.2.1	SUPPLEMENTARY FIGURES.....	104
3.2.2	SUPPLEMENTARY TABLES .....	114
3.3	ADDITIONAL COMPOUNDS AND DATA .....	116
3.4	SUMMARY AND OUTLOOK.....	118
3.5	EXPERIMENTAL.....	120
3.5.1	SPECTROSCOPIC AND SPECTROMETRIC DATA OF LIRAZO <b>3.6</b> .....	120
3.5.2	EXPERIMENTAL DATA OF ADDITIONAL COMPOUNDS LIRAZO2 <b>3.8</b> AND LIRAZO3 <b>3.6</b> .....	131
4	CONSTITUTIVE ACTIVATION OF A CLASS B G-PROTEIN COUPLED RECEPTOR USING TETHERED PHARMACOLOGY (EXONATIDE).....	134
4.1	MANUSCRIPT: CONSTITUTIVE ACTIVATION OF A CLASS B G-PROTEIN COUPLED RECEPTOR USING TETHERED PHARMACOLOGY.....	135
4.2	SUPPLEMENTARY FIGURES .....	139
4.3	ADDITIONAL COMPOUNDS.....	141
4.4	SUMMARY AND OUTLOOK.....	142
4.5	EXPERIMENTAL.....	143
4.5.1	SPECTROSCOPIC AND SPECTROMETRIC DATA OF EXONATIDE <b>4.2</b> .....	143
4.5.2	EXPERIMENTAL DATA OF ADDITIONAL COMPOUNDS S39C-Ex4(9-39) <b>4.7</b> , EXOFFATIDE <b>4.3</b> , G36C-LIRA <b>4.8</b> AND G36C-LIRAZO <b>4.9</b> .....	147

## PART II - PHOTOPHARMACOLOGY AND TETHERED PHARMACOLOGY

5	PHOTOCONTROLLED CHIGNOLIN-DERIVED $\beta$ -HAIRPIN PEPTIDOMIMETICS.....	159
5.1	COMMUNICATION: PHOTOCONTROLLED CHIGNOLIN-DERIVED $\beta$ -HAIRPIN PEPTIDOMIMETICS.....	161

5.2	SUPPLEMENTARY FIGURES .....	165
5.3	ADDITIONAL COMPOUNDS.....	170
5.3.1	AZOCHIGNOLIN-RELATED MUTANTS .....	170
5.3.2	THE Y2AZOPHE-CHIG PEPTIDE.....	173
5.4	SUMMARY AND OUTLOOK.....	179
5.5	EXPERIMENTAL.....	181
5.5.1	SPECTROSCOPIC AND SPECTROMETRIC DATA OF AZOCHIG1 <b>5.1</b> , AZOCHIG2 <b>5.2</b> AND AZOCHIG3 <b>5.3</b> .....	181
5.5.2	EXPERIMENTAL DATA OF ADDITIONAL COMPOUNDS CHIGNOLIN <b>5.1</b> , Y2W-AZOCHIG <b>5.5</b> , Y2V-AZOCHIG <b>5.6</b> , P4T-AZOCHIG <b>5.7</b> AND Y2AZOPHE-CHIG <b>5.8</b> .....	195

## APPENDIX

INDEX OF ABBREVIATIONS.....	202
INDEX OF COMPOUNDS.....	204
INDEX OF FIGURES .....	207
INDEX OF SCHEMES .....	209
INDEX OF TABLES .....	210
GENERAL REMARKS .....	211
GENERAL PEPTIDE SYNTHESIS.....	213
REFERENCES.....	214





## ABSTRACT

The development of photochromic peptides and ligands for ever more targets has delivered a growing library of various photopharmaceuticals and research tools, and has helped to promote the viability of these molecular machines not only in health and disease, but in many aspects of life. The optical control of proteins, the ubiquitous actors and regulators of cellular processes, life and death, is a key step in understanding and regulating biological processes. For this reason, the growing exploitation of optical research tools should enable it researchers to address almost any biological question in the future.

This work presents different photochromic compounds and tethered ligands, which were implied in the (optical) control of different biological targets, or as model systems for structural studies. Except for the different photoswitches discussed in PART I, the projects either have been already published or have been submitted to peer-reviewed journals, wherefore they appear as embedded articles or manuscripts. The conceptual idea and rational design, as well as the synthesis and testing of the different compounds are described in these files. To the addressed targets for optical control belong the Atrial Natriuretic Peptide Receptor (NPR-A) and the Glucagon-like Peptide 1 Receptor (GLP-1R). Furthermore, a novel photoswitchable  $\beta$ -hairpin peptide was developed that represents a model system for studying the folding processes in this protein structural element.

In each case, the photocontrol of the targeted processes was demonstrated in the corresponding system. For instance, optical regulation over NPR-A activity was demonstrated in Islets of Langerhans and *ex vivo* in explanted mouse aorta. The photocontrol of GLP-1R activity with a photochromic incretin-mimetic was also shown in Islets of Langerhans. Furthermore, compound-biased receptor signaling could be demonstrated, which leads to a differential stimulation of insulin secretion and cell proliferation. Utilizing a tethered ligand, the GLP-1R could be constitutively activated, facilitating the study of receptor internalization and trafficking. In case of the  $\beta$ -hairpin model system, the switching of the chromophore directs the folding and unfolding of the hairpin structure, allowing the monitoring of folding processes with spectroscopic methods. These optical research tools deliver a blueprint for the next generation of such systems, and will hopefully contribute to the progression of knowledge and understanding in these and related fields of research.

## ABSTRACT (DEUTSCH)

Der stetige Fortschritt auf dem Gebiet optisch-schaltbarer Moleküle hat zu der Entwicklung einer Vielzahl von Photopharmazeutika und Forschungswerkzeuge geführt, welche dabei helfen den Nutzen dieser Systeme in der Forschung, zur Bekämpfung von Krankheiten und in vielen weiteren Aspekten des Lebens, zu zeigen. Dabei ist die optische Kontrolle von Proteinen, den allgegenwärtigen Akteuren und Regulierern zellulärer Prozesse, der Schlüssel zu einem besseren Verständnis und Kontrolle biologischer Funktionen. Aus diesem Grund sollten Forscher in Zukunft in der Lage sein, jedwede biologische Fragestellung mittels optischer Forschungswerkzeuge zu adressieren.

Diese Arbeit stellt verschiedene photoschaltbare Verbindungen und angebundene Liganden vor, die entweder für die (optische) Kontrolle von verschiedenen biologischen Targets, oder aber als Modellsystem für Proteinfaltungsstudien verwendet wurden. Bis auf die Photoschalter, welche in TEIL I dieser Arbeit aufgeführt sind, wurden die Projekte bereits in angesehenen wissenschaftlichen Zeitungen publiziert oder zur Veröffentlichung eingereicht. Die Artikel und Manuskripte sind dementsprechend als Ganzes in diese Arbeit eingefügt, und geben Einblick in die Entwicklung der konzeptionellen Idee, über die Planung und Synthese der Verbindung bis hin zu der Untersuchung an den biologischen Targets. Zu diesen gehören unter anderem der Atrial Natriuretische Peptidrezeptor (NPR-A) und der Glucagon-like Peptid 1 Rezeptor (GLP-1R). Desweiteren wurde auch ein neues photoschaltbares  $\beta$ -Hairpinpeptid Modellsystem entwickelt, welches die Untersuchung von Faltungsprozessen in diesem Strukturelement ermöglicht.

Die optische Kontrolle der anvisierten Prozesse wurde in den entsprechenden Projekten in physiologisch relevanten System demonstriert. So wurde die lichtgesteuerte Regulierung des NPR-A Rezeptors in Langerhans'schen Inseln der Bauchspeicheldrüse und in explantierten Mauseaorten gezeigt. Die optische Kontrolle des GLP-1 Rezeptors konnte ebenfalls in den Inselzellen demonstriert werden, wobei die Verzerrung des Rezeptor-Signals zu einer unterschiedlichen Stimulierung von Insulinsekretion und Zellproliferation führte. Durch Verwendung eines angebundene Liganden konnte zudem der GLP-1 Rezeptor konstitutiv aktiviert werden, wodurch die Internalisierung und das Rezeptorrecycling unter diesen Bedingungen beobachtet werden konnte. Im Falle des  $\beta$ -Hairpinpeptid Modellsystems steuerte der Photoschalter die Faltung und Entfaltung der Hairpin-Struktur, was durch spektroskopische Methoden wie der Ultrakurzzeitspektroskopie beobachtet werden konnte. Diese optischen Forschungswerkzeuge stellen Blaupausen für die nächste Generation solcher Systeme dar, und sollen bei dem Verständnis und der Weiterentwicklung dieses Forschungsgebietes helfen.

## PROJECT AFFILIATION DISCLOSURE

Reading this work, the reader will notice that it avoids using the term “I”, but instead uses “we” at some points. This simply appreciates the involvement and contribution of many people to the projects and reflects how complex and networked modern day research is. Like in biological systems, where a small input signal can be amplified to a vast output, small ideas combined from many minds can spark great results. At this point, I again want to thank all my friends, interns, supervisors and collaborators involved in every single project, and will provide a detailed listing of their contribution to this work. Special thanks go to my PhD supervisor Prof. Dr. Anja Hoffmann-Röder, which devised and planned all the studies and thus is not listed for all the single chapters.

**Chapter 1:** Frederik Broszeit (Synthesis), Finn Burg (Synthesis), Dr. Johannes Broichhagen (Compounds and Support).

**Chapter 2:** Dr. Johannes Broichhagen (Analysis, assays and supervision), Christina Frost (MD simulations), Dr. Dieter Groneberg (Aortic tensometry), Helena Meyer-Berg (Analysis and assays), Nicholas H. F. Fine (Ca<sup>2+</sup> secretion assays), Prof. Dr. Andreas Friebe (Supervision), Prof. Dr. Martin Zacharias (Supervision), Prof. Dr. David J. Hodson (Supervision) and Prof. Dr. Dirk Trauner (Conceptual design and supervision).

**Chapter 3:** Dr. Johannes Broichhagen (Analysis and assays), Helena Meyer-Berg (Analysis and assays), Yorrick von Ohlen (Assays), Natalie R. Johnston (Assays), Ben J. Jones (Assays), Prof. Dr. Stephen R. Bloom (Cell lines), Prof. Dr. Guy Rutter (Facility), Prof. Dr. David J. Hodson (Conceptual design and supervision) and Prof. Dr. Dirk Trauner (Conceptual design and supervision)

**Chapter 4:** Dr. Johannes Broichhagen (Supervision), Nicholas H. F. Fine (Ca<sup>2+</sup> and insulin secretion assays), Dr. Daniela Nasteska (Ca<sup>2+</sup> and insulin secretion assays), Philipp Leippe (Synthesis and assays), Manuel Gailer (Synthesis), Teresa Buenaventura (Trafficking studies), Nisha Kanda (Trafficking studies), Sarah Janik (Synthesis), Dr. Alejandra Tomas (Trafficking studies), Prof. Dr. Dirk Trauner (Conceptual design and supervision) and Prof. Dr. David J. Hodson (Conceptual design and supervision).

**Chapter 5:** Stefan M. Hoffman (IR spectroscopy), Christina Frost (MD simulations), Finn Burg (Synthesis), Manuel Gailer (Synthesis), Dr. Michael Rampp (IR spectroscopy), Prof. Dr. Martin Zacharias (Supervision) and Prof. Dr. Wolfgang Zinth (Supervision)

## GENERAL INTRODUCTION

The fundamental challenge in solving a problem is to understand the underlying coherences and form a solution based upon this knowledge. This not only translates to many aspects in life but also to science and particularly to the interdisciplinary fields of biochemistry and chemical biology. Scientists working in this area of research combine biological approaches with chemical design and synthesis of small molecules, to tackle pressing global challenges such as future nutrition, environmental sustainability and pathologies. In the case of the latter these are represented by different diseases, such as metabolic (*i.e.* type 2 diabetes (T2D)), cardiovascular (*i.e.* atrial fibrillation and heart failure) and neurodegenerative (*i.e.* Alzheimer's and Creutz-Feldt-Jakob's) disorders, which affect a growing share of the global population and have far-reaching social and economic effects.

The first step towards every successful investigation of biological behavior, function and response is the dissection of complex biological signaling processes. A major approach is to gain control over biological systems through manipulation of biomolecules and their responses. Through introduction of responsive units, the action and function of the target molecules can be remotely altered and the role it plays in a biological ensemble can be detected. Light, with its high spatial and temporal precision, is used by a variety of organisms as regulatory signal in photoresponsive proteins, *i.e.* flavoproteins<sup>1</sup> and rhodopsins<sup>2</sup>. Genetically modified versions of these proteins have been successfully implied in *optogenetics* to control defined events at distinct times in intact biological systems<sup>3</sup>. Furthermore, small native biomolecules such as endogenous hormones and drugs have been equipped with photoresponsive units and been applied to a large variety of targets, including G-protein coupled receptors (GPCRs), ion channels and enzymes<sup>4-6</sup>. This relatively new and vivid field was dubbed *photopharmacology*, as it implies the use of synthetic photoswitches or photopharmaceuticals to control biological function and together with optogenetics it has become a major frontier in scientific research.

Pharmacology has come a long way from magical and natural remedies of ancient medicine over iatrochemistry to modern pharmacology<sup>7</sup>. Crucial for therapeutic efficacy of modern pharmaceuticals is the correct diagnosis and an appropriate choice of the drug<sup>8</sup>. Success of the therapy depends on the correct induction of appropriate drug concentrations in the target organ or tissue, whereby the therapeutic window (the gap between effective and toxic levels) is mostly narrow. Distinct diffusion rates and rapid drug elimination lead to decreased efficacy after high starting concentrations and make it challenging to hit and maintain the designated drug concentration. Moreover, after administration a drug may diffuse to the whole organism *via* the bloodstream and lead to off-target effects. Another major issue is drug resistance, especially in the light of elevating numbers of antibiotic resistant bacteria. Photopharmacology is a promising attempt to overcome these issues by increasing the selectivity of drugs through reversible switching between an active or inactive state and thus enabling targeting of drug action only to the tissue of interest. Using light as input signal is not only reasonable because of its high spatiotemporal precision, but also due to its non-invasiveness and non-toxicity. Intense focus on the optimization of photoswitches in the recent years has yielded a remarkable library of compounds with far red-shifted absorption

characteristics<sup>9-12</sup>. Shifting the switching wavelengths of the photoswitch to red/IR light is a necessity to achieve deep tissue penetration for non-invasive photopharmacology, without the need to ingest or implement a light source into the patient. Introducing the recent ground-breaking and basic research in this field<sup>13-17</sup> to clinical studies will be the next big leap forward and possibly help to establish photopharmacology as a new method for clinical treatment.

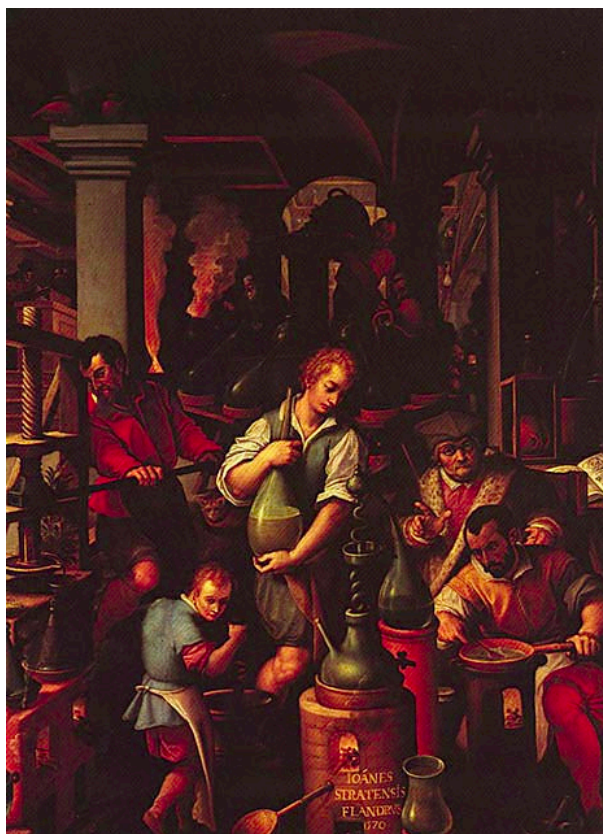


**Figure 1: Giovanni Stradano – Il laboratorio dell'alchemista.** The workshop of an alchemist, sixteenth century (Firenze, Palazzo Vecchio)<sup>18</sup>.

Besides optogenetics and photopharmacology pioneering work using photochromic compounds in biomolecules was the incorporation of azobenzenes into the side chain of polypeptides to photomodulate conformational states of poly- $\alpha$ -amino acids<sup>19</sup>. Since then, various chromopeptides have been introduced as model systems for experimental protein folding studies<sup>20-26</sup>. Although these model peptides comprise building blocks which are not constituents of any natural biomolecule, these studies have helped to bridge the gap between experimental and theoretical results. The verification or falsification of theoretical predictions based on experimental data is vital to develop precise theoretical descriptions<sup>20</sup>. The complexity and evolution of processes involved in protein folding and signaling are one of the great mysteries in biology and have fascinated generations of researchers. Protein misfolding and aggregation is correlated with many diseases, such as the neurodegenerative and age-related Alzheimer's and Creutzfeldt-Jakob's disease<sup>27</sup>, and our ageing population urges the need for a deeper understanding of these maladies.

This work comprises new studies in the mentioned fields and is divided into three parts. PART I outlines the design and synthesis of known and new photoswitches, which were used in the projects described in PART II and PART III. PART II thereby pictures the projects conducted in the field of pharmacology and photopharmacology, while latter focuses on structural biology and peptide folding.

PART I

PHOTOSWITCHES:

DESIGN AND SYNTHESIS

## PART I – PHOTOSWITCHES: DESIGN AND SYNTHESIS

### 1 AZOBENZENES AS MOLECULAR SWITCHES

#### 1.1 PRINCIPLES OF OPTICAL CONTROL

Sun light is the ubiquitous donor of energy for many living organisms and it triggers several processes in plants (photosynthesis, phototaxis), phototrophic prokaryotes (light-energy conversion through ion pumps) and animals (vision, circadian timing)<sup>12</sup>. Some of these responses, like phototactical movement or visual responses involve the absorption of light and conversion into an electrical signal (phototransduction). In the visual cycle of mammals, visible light energy induces the conformational isomerization of the chromophore 11-*cis*-retinal (*cis*-**1.1**), which is bound to the GPCR opsin and forms the photosensory rhodopsin receptor complex in the rod and cone cells of the eye. The photoisomerization of receptor bound *cis*-**1.1** to rigid all-*trans*-retinal (*trans*-**1.1**) (Figure 1.1) leads to dissociation of *trans*-**1.1** from the receptor and activates G-protein and subsequent neuronal signaling and ultimately vision<sup>28,29</sup>. Special emphasis lies on the regulation of these processes by light in the visible region of the solar spectrum, which is harmless compared to UV light. Latter is typically phototoxic to cells, absorbed nonselectively by any chromophores and exhibits weak tissue penetration<sup>30</sup>.

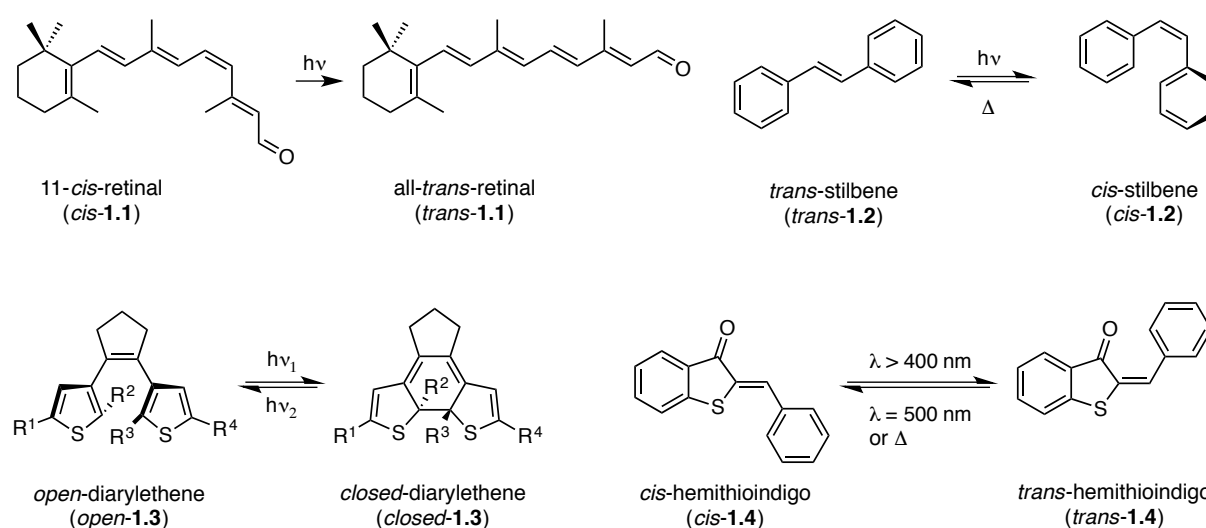


**Figure 1.1: Examples for molecular switches.** Shown are the photoisomerizations of *cis/trans*-**1.1**, *cis/trans*-stilbene **1.2**, *open*- and *closed*-DAE **1.3** and *cis/trans*-HTI **1.4** (ref. 31).

Since many decades' researchers have been inspired and guided by nature's design principles and have developed many synthetic photosensitive systems, ranging from photovoltaic cells<sup>32</sup> and photochemical synthesis<sup>33,34</sup> to optogenetics with protein-engineered rhodopsins<sup>3,35–37</sup> and photopharmacology<sup>4,16,38</sup>. These systems rely on photochromic molecules based on biological chromophores or industrial dyes and comprise molecular switches such as stilbenes<sup>39,40</sup>, diarylethenes (DAEs)<sup>41–43</sup>, hemithioindigos (HTIs)<sup>31,44–46</sup> and azobenzenes<sup>47–52</sup>, with several more not mentioned here (Figure 1.1). Although most of these

chromophores have been successfully used for biological and nonbiological applications, azobenzenes, despite being one of the oldest photoswitch class, still offer the largest range of activation wavelengths and photoactivated states, and their versatile derivatization possibilities enables tuning of their spectral properties depending on the application. For this reason, azobenzene or azobenzene based photoswitches were exclusively used throughout this work and the following chapters will focus on the photochemical and photophysical properties of known and new azobenzene derivatives.

### 1.1.1 AZOBENZENE

Azobenzene (**1.5**), the core structure of several reliable and cheap dyes, consists of two phenyl groups which are linked through a diazene bridge and photoisomerization with UV light ( $\lambda = 350\text{-}380\text{ nm}$ ) or blue light ( $\lambda = 430\text{-}480\text{ nm}$ ) leads to *trans*  $\rightarrow$  *cis* or *cis*  $\rightarrow$  *trans* isomerization, respectively (Figure 1.2). The isomerization events occur very fast on the picosecond timescale, with high quantum yields and minimal degradation/photo bleaching even after many cycles. This prevents the formation of triplet states and formation of cell damaging reactive oxygen species (ROS) by singlet oxygen avoided, which enables biocompatibility<sup>4</sup>.

While *cis*-**1.5** formation can also be induced by mechanical stress<sup>53</sup> or electrostatic stimulation<sup>54,55</sup>, *trans*-**1.5** forms spontaneously in the dark due to its higher thermodynamic stability. The thermal relaxation thereby is significantly slower than the photoisomerization, thus separating both process in time<sup>47</sup>. In unsubstituted azobenzene the thermal relaxation yields up to >99.99% of the *trans*-isomer, but light-induced isomerization produces a photostationary state (PSS) with maximal ~80% of the *cis* or ~95% of the *trans*-form<sup>56</sup>. The formation of this PSS is due to the distinct, but overlapping absorption spectra of *cis/trans*-**1.5**. The *trans*-isomer exhibits a strong  $\pi\text{-}\pi^*$  transition at 316 nm ( $\epsilon = 22000\text{ L}\cdot\text{M}^{-1}\cdot\text{cm}^{-1}$ ) and a weak, symmetry-forbidden  $n\text{-}\pi^*$  band near 440 nm ( $\epsilon = 440\text{ L}\cdot\text{M}^{-1}\cdot\text{cm}^{-1}$ ). The *cis*-isomer has a stronger, formally not forbidden  $n\text{-}\pi^*$  transition near 440 nm ( $\epsilon = 1250\text{ L}\cdot\text{M}^{-1}\cdot\text{cm}^{-1}$ ) and shorter wavelength bands at 280 and 250 nm. Despite the rather low extinction coefficient, irradiation of the  $n\text{-}\pi^*$  band leads to complete *cis*  $\rightarrow$  *trans*-isomerization<sup>57</sup>.

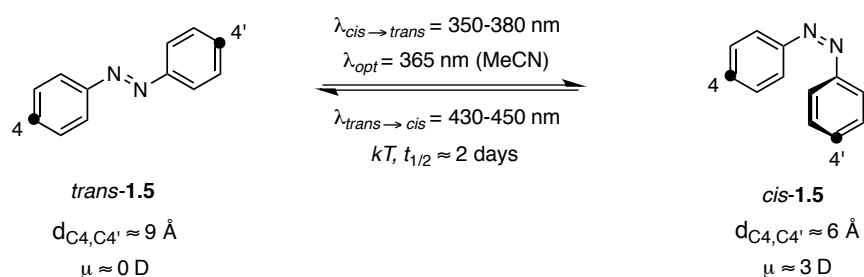


**Figure 1.2: Azobenzene (1.5) isomerization.** Basic parameters of the *cis*  $\rightarrow$  *trans* and *trans*  $\rightarrow$  *cis* photoisomerization of **1.5** (ref. 4).

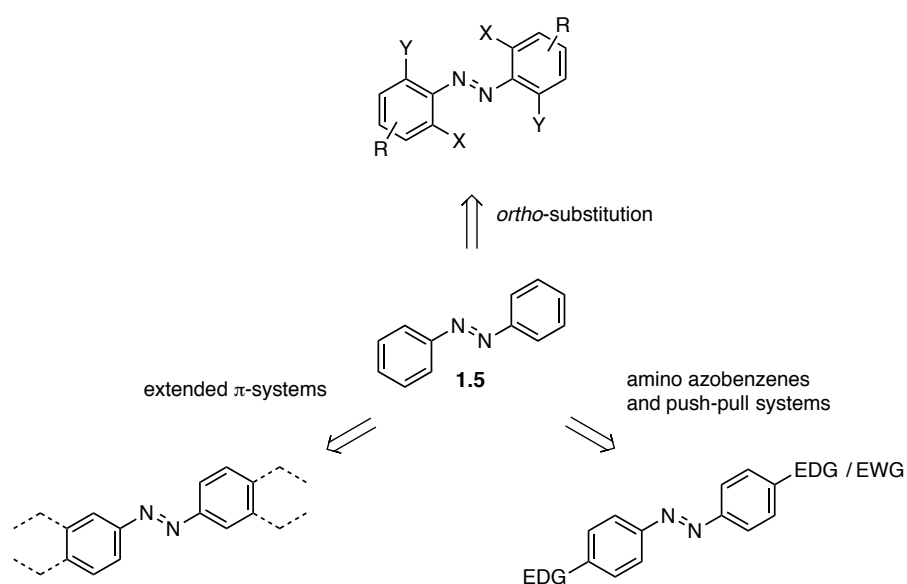
Both phenyl rings in *trans*-**1.5** are slightly twisted  $17^\circ$  around the  $\text{N}=\text{N}$ -bond and form a planar structure with a dipole moment near zero. In the *cis*-isomer, both phenyl rings are twisted  $\sim 55^\circ$  out of the  $\text{N}=\text{N}$ -bond plane and exhibit a dipole moment of  $\mu = 3\text{ D}$ . Besides these changes, there is a distance alteration

of  $\sim 3.5$  Å between the two *para*-positioned 4- and 4'-carbon atoms of the two phenyl rings in both isomers<sup>58,59</sup>. Although changes in dipole moment and compactness of the azobenzene structure upon isomerization are remarkable, it is this end-to-end distance shift which is the dominant feature for the utilization of these photoswitches in biological applications.

The most important properties of azobenzene photoswitches for controlling biological processes are (i) the photoisomerization wavelengths must be compatible with cells and tissues ( $> 400$  nm), (ii) the isomerization should be effective with a sufficient rate and capability of undergoing many switching cycles, (iii) depending on the application the conformational shift or end-to-end distance change upon isomerization has to be large enough to affect the activity or the function of the target biomolecule, (iv) while simultaneously being small enough to mimic the template compound or be noninvasively incorporated into the target molecule. Furthermore, (v) the photoswitch should be stable in the cellular environment and unsusceptible towards modification or degradation, for example through reduction by glutathione. These properties can be tweaked by introducing different substituents to the azobenzene core and the next chapter will provide a brief overview of the most recent advances.

### 1.1.2 TUNING THE SPECTRAL PROPERTIES OF AZOBENZENE

The most demanding aspect of biological photoswitches is achieving switching wavelengths in the non-toxic and tissue penetrating far red/IR region, while maintaining fast and robust switching, high isomerization rates and distinctively stable isomers. The red-shifting of the isomerization wavelengths is amenable by three general approaches; the first and most prominent method is to alter the intrinsic molecular design of the photoswitch to lower the HOMO-LUMO gap for direct photoexcitation. The second strategy relies on indirect photoexcitation through energy transfer of sensitizers, e.g. triplet photosensitizers, or multiphoton antennae, which absorb long-wavelength energy of one or multiple quanta and transfer it to the photoswitch. The last method utilizes electrochemical or long-wavelength induced oxidation/reduction through electron transfer to/from a sensitizer to drive the isomerization<sup>12</sup>. Engineering of the HOMO-LUMO gap affects the energy needed for the  $\pi$ - $\pi^*$  transition, i.e. the energy needed for *trans*  $\rightarrow$  *cis* isomerization, and lowering of this excitation energy can be classically achieved by extending the  $\pi$ -electron system with aromatic residues or through introduction of electron-donating (EDG) or electron-withdrawing (EWG) groups in *ortho/para*-position to the azo-bridge (Scheme 1.1). Although an extended  $\pi$ -system may result in a great red-shift of the  $\pi$ - $\pi^*$  transition, this does not necessarily influence the absorption wavelengths of the  $n$ - $\pi^*$  transition. Thus, the two bands can overlap leading to a shifted, "early" PSS and reduced isomerization rates with lower selectivity. In addition, tweaking of the photochromic molecule's electronic system may also result in shorter or longer half-lives of the thermal relaxation rate due to a diminished N=N-double bond character or stabilized dipoles in the transition states, respectively<sup>51,60</sup>.



**Scheme 1.1: Tuning of the azobenzene (1.5) electronic system.** Overview of the three approaches for HOMO-LUMO gap engineering for the red-shifting of photoconversion wavelengths in the direct photoexcitation of **1.5**.

### 1.1.3 MODIFYING AZOBENZENE WITH SUBSTITUENTS

There are diverse methods to synthesize azobenzenes, ranging from classical azo-coupling over *Mill's reaction* to hydrazine cross-coupling and oxidation<sup>4,61</sup>. This offers various approaches for azobenzene derivatization and many substituted azobenzene photoswitches have been synthesized and published so far. The introduction of *para*-amino groups as EDGs or the incorporation of five-membered aromatic heterocycles not only leads to a red-shift of the absorption bands, but also increases the solubility in physiologically relevant aqueous media (Figure 1.3). Thereby, the solvent has a large influence on the photophysical properties and the photoswitches should be adjusted accordingly. For example, the electron-donating amino groups in *ortho*-position in compounds **1.10** – **1.13** facilitate a further red-shift of the absorption bands, but at the expense of bistability<sup>56,62,63</sup>.

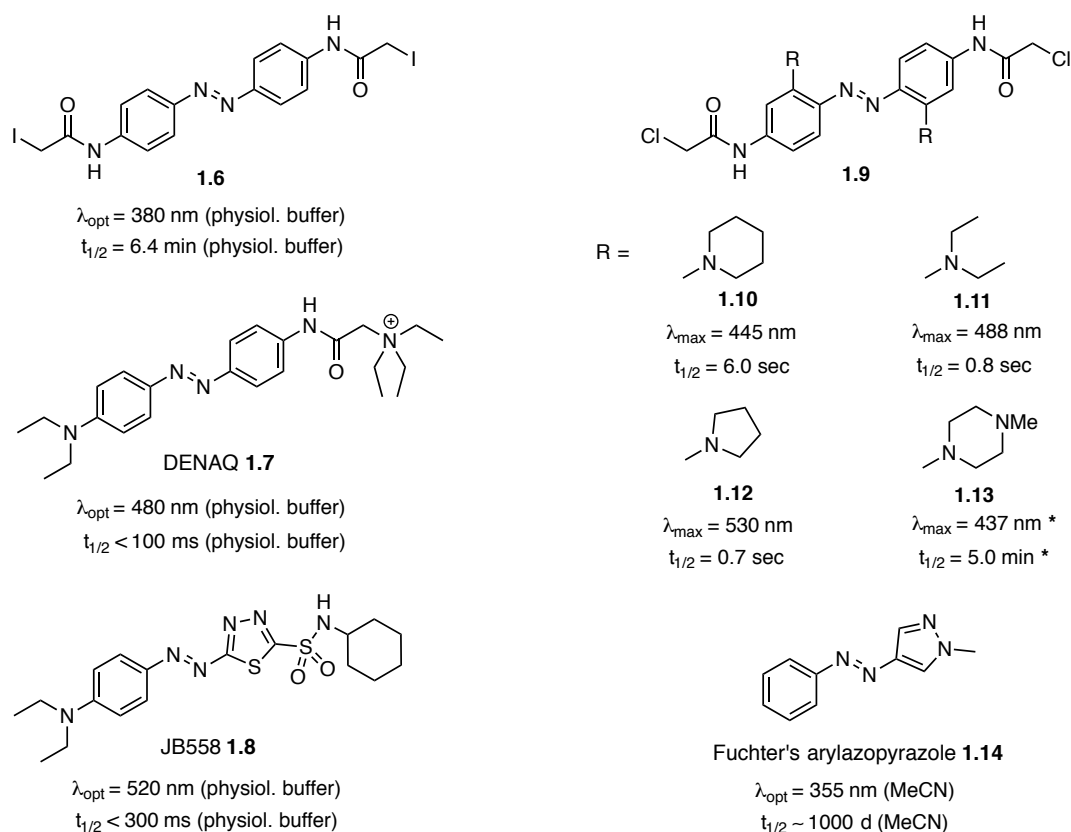


**Figure 1.3: Modified azobenzene derivatives and their photophysical properties.** Optimal photoswitching wavelengths for the *trans* → *cis* isomerization and thermal relaxation half-lives of bis(*para*-iodoacetamido)-azobenzene (**1.6**) crosslinker for incorporation *via* cysteine side chains<sup>64,65</sup>, DENAQ **1.7** for the restoration of visual responses<sup>66</sup> and the photochromic sulfonylurea JB558 **1.8** (ref. 67) under physiological conditions, *i.e.* phosphate buffered saline (PBS) or HEPES-Krebs-Ringer buffer (HKS). Absorption maxima and thermal relaxation half-lives for bis(*para*-chloroacetamido)-azobenzene (**1.9**) *ortho*-substituted with piperidin (**1.10**), diethylamine (**1.11**) and pyrrolidine (**1.12**) in PBS, and piperazine (**1.13**) in \*70% MeCN / 30% PBS solution<sup>56,62</sup>. Long-lived half-life of the *cis*-isomer in Fuchter's arylazopyrazole **1.14** (ref. 68).

The introduction of a pair of *ortho*-methoxy groups leads to a red-shifted  $\pi$ - $\pi^*$  transition, while the occupation of all four *ortho*-positions with methoxy substituents causes a red-shift of the  $\pi$ - $\pi^*$  and  $n$ - $\pi^*$  bands, yielding the chromophore **1.15** with photoswitching wavelengths exclusively in the visible spectrum and a long-lived *cis*-state under physiological conditions ( $t_{1/2} = 12 \text{ hrs}$  at  $40 \text{ }^\circ\text{C}$  in PBS)<sup>48</sup>. Nevertheless, a drawback is the impaired stability towards intracellular glutathione reduction, rendering these compounds unsuitable for biological applications. Alternatively, electron-poor azobenzenes with electron-withdrawing *ortho*-halogeno substituents are resistant to glutathione reduction, have clearly separated *cis*- and *trans*- $n$ - $\pi^*$  bands in the visible spectrum and longer thermal half-lives (Figure 1.4)<sup>12,49,69</sup>. *Para*-positioned electron-donating substituents in these compounds narrow the gap between the two  $n$ - $\pi^*$  bands, while electron-withdrawing substituents, *e.g.* ester groups as in compound **1.18**, increase this gap up to 50 nm and lead to compounds with high photoconversion and remarkable thermal half-lives of the *cis*-isomer<sup>69</sup>.

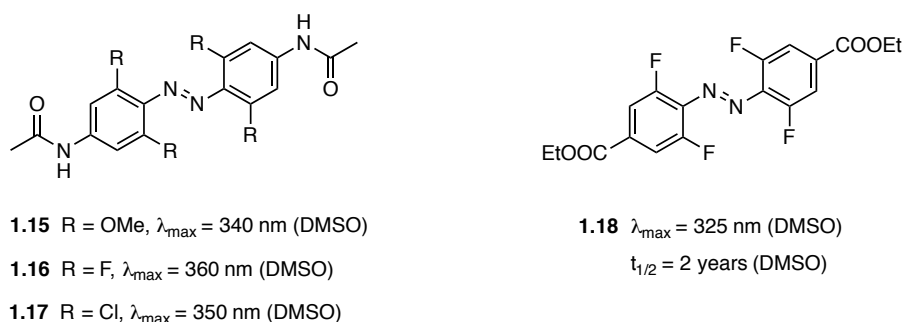
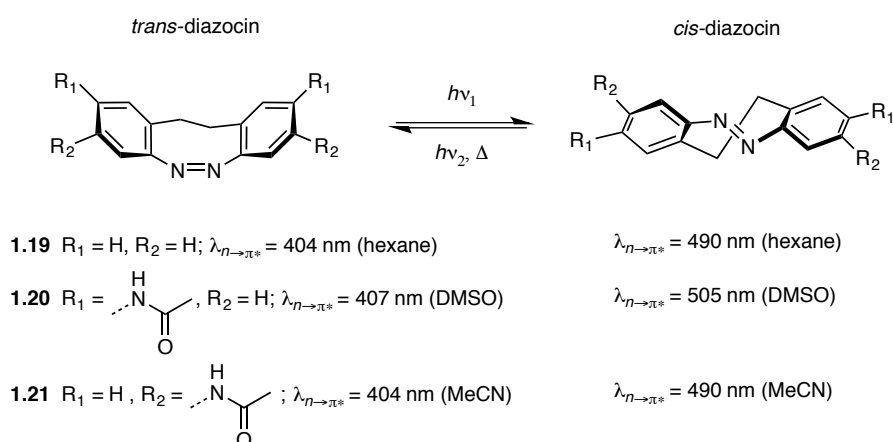


**Figure 1.4: Shifting of maximale absorption in azobenzenes with *ortho*-substituents.** Amino azobenzenes with electron-donating methoxy groups (**1.15**) or fluoro (**1.16**) and chloro (**1.17**) substituents in *ortho*-position show red-shifted transition bands, high photoconversion rates and bistability<sup>56,69,70</sup>. Electron-withdrawing ester groups in tetrafluoro compound **1.18** exhibit long thermal half-lives<sup>69</sup>.

### 1.1.4 MODIFYING THE AZOBENZENE CORE

Introducing substituents can be easily used to alter the electronic and therefore photophysical properties of azobenzene, but it is also possible to modify the azobenzene core structure. As seen for the compounds **1.8** and **1.14** in the preceding chapter, the integration of aromatic heterocycles greatly influences photoswitching wavelengths and thermal half-lives. Another series involves bridged azobenzene chromophores that are based on diazocin (**1.19**). Although this structure has already been discovered over one century ago<sup>71</sup>, it was only recently that it was evaluated, modified and employed as a photoswitch<sup>68,72,73</sup>. These cyclic azobenzenes show large separations of the *cis/trans*-isomer  $n-\pi^*$  bands due to geometrical constraints and can be switched, in contrast to unsubstituted azobenzene, in both directions by irradiation of these bands (blue or green light). One of the most interesting features of these chromophores is the inversion of the thermal stability of both isomers, meaning the *cis*-isomer is thermally more stable than the *trans*-form. Amino substituents in *ortho*- or *para*-position to the N=N-bridge influence the red-shift and separation of the *cis/trans*- $n-\pi^*$  bands, thermal half-lives and photoconversion rates (Scheme 1.2). While the latter is >90% for unsubstituted diazocin **1.19**, bis(*para*-acetamido) compound **1.20** only shows 70% and bis(*ortho*-acetamido) compound **1.21** 53% photoconversion rates<sup>73–75</sup>.



**Scheme 1.2: Bridged azobenzene compounds.** Photoswitching wavelengths of the  $n-\pi^*$  transition bands of diazocin **1.19** and related compounds **1.20** and **1.21** (ref. 73, 75).

### 1.1.5 METHODS OF AZOBENZENE IMPLEMENTATION AND PHOTOCONTROL

The optical control over the structure and function of peptides with azobenzenes can be achieved by several ways, including i) introduction of a chromophore into the peptide backbone by extension or substitution of parts of the amino acid sequence, and ii) through attachment *via* reactive side chains or side chain modifications. Photoswitches implied in the first method include molecules with amino and carboxy functional groups and azobenzene-modified natural amino acids.

The term amino acid photoswitch already reveals the nature of attachment for these chromophores: they contain an amino and carboxyl functional group for incorporation into the backbone/sequence of peptides and proteins. This can be done synthetically through solid-phase peptide synthesis<sup>56</sup>, or *in cellulo* through expanding the genetic code with modified transfer RNA (tRNA)/aminoacyl-tRNA pairs<sup>76-78</sup>. Thereby the former approach allows site-specific substitution of amino acids in the primary sequence without severely affecting the overall function and potency towards the target. Moreover, if the photoswitch is to be integrated into *de novo* peptides, e.g. small photoswitchable model systems for structural biology, the primary sequence can be designed based on the application. To access these optical responsive amino acids the azobenzene unit can be i) functionalized with the amino and carboxyl functional groups, ii) attached directly or through a linker to an amino acid functional group (*i.e.*  $\epsilon$ -amino group of lysine), or iii) introduced *via* the aromatic side chain of phenylalanine and tyrosine.

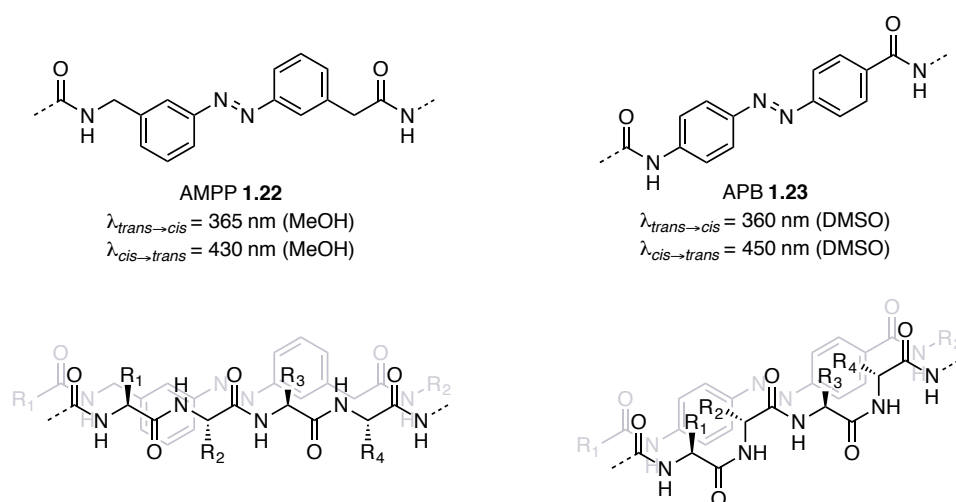


**Figure 1.5: Peptide backbone photoswitches AMPP and APB.** Structures and photoswitching wavelengths of AMPP **1.22** (ref. 25) and **1.23** (ref. 79) with adjacent amino acids (C=O, NH and dashed lines). Overlay of peptide backbone over chromophore structure **1.22** and **1.23** shows that both compounds span four amino acids: Thereby latter structure is twisted and more rigid than the former one.

Examples of this the first approach are provided by the chromophores 3-[3-(aminomethyl)phenylazo]-phenylacetic acid (AMPP, **1.22**)<sup>20,25,80</sup> and 4-[4-(amino)phenylazo]benzoic acid (APB, **1.23**)<sup>79,81</sup>, which are both inserted into the peptide backbone (Figure 1.5). Photoswitching wavelengths are similar for both compounds, with a slight red-shift for the *cis*  $\rightarrow$  *trans* isomerization in APB **1.23**. Furthermore, both azobenzenes exhibit high photoconversion rates (>90% and 75% for **1.22** and **1.23**, respectively) and good bistability. The *meta*-amino/carboxyl groups in AMPP **1.22** are connected *via* two methylene groups, which

act as flexible spacers and facilitate the adoption of native peptide structures. In contrast, APB **1.23** comprises a more rigid and twisted structure, where the *N*- and *C*-terminal amide bonds are directly attached to the azobenzene core. This leads to an overall increase of the photoinduced conformational shift between the *cis/trans*-isomers of APB-peptides. Although this might seem advantageous, it can also suppress the formation of native conformations in small linear peptides. Thus, this photoswitch was mainly used in cyclic peptides<sup>79,81</sup>. The substitution of amino acids in the peptide backbone with photoswitches represents a rather invasive approach for receiving photochromic peptides and often leads to a reduced potency towards the biological target, e.g. in case of peptidic drugs. This can be circumvented by incorporating the photoswitch as an amino acid side chain modification. In the photoswitchable amino acid (*S*)-3-(4-(phenyldiazenyl)phenyl)propanoic acid (AzoPhe, **1.24**) the azobenzene structure is connected via a side chain *para*-extension of the aromatic ring in phenylalanine or tyrosine (Figure 1.6). While this photoswitch can be incorporated into peptides by a single amino acid exchange, the structural changes provoked by *cis/trans*-isomerization are less pronounced than in backbone-functionalized photoswitchable peptides. This is obviously due to sterical rearrangement of the azobenzene in the side chain, rather than large structural shifts of the peptide secondary structure. Nevertheless, AzoPhe **1.24** and related photoswitches were successfully integrated and used to optically control protein function<sup>82,83</sup>.

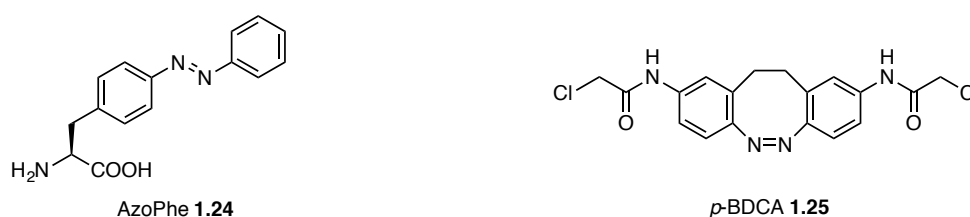


**Figure 1.6: Side chain amino acid and crosslinker photoswitches AzoPhe **1.24** and *p*-BDCA **1.25**.** Structures and photoswitching wavelengths of **1.24** (ref. 82, 83) and **1.25** (ref. 64, 73).

Another approach utilizes photoswitchable crosslinkers which are fused onto the peptide through reactive groups, *i.e.* reactive cysteine residues. A recent example is the photoswitchable crosslinker (*Z*)-*N,N'*-(11,12-dihydrodibenzo[*c,g*][1,2]diazocine-2,9-diyl)bis(2-chloroacetamide) (*p*-BDCA, **1.25**), which possess two chloroacetamido groups in *para*-position to the azo bridge and can be reacted with two thiol groups of distal cysteines (Figure 1.5). The photoswitch thus acts as a conformational bridge that enables the optical control of the distance between both cysteine residues. Since  $\alpha$ -helical structures need defined distances between involved residues, the distance change upon isomerization in crosslinked peptides was used to optically control the helix content<sup>64,73</sup>.

## 1.2 RESULTS

This chapter pools the results for all photoswitches that were designed and synthesized during this work, providing an overview of the applied synthesis strategies. Detailed information on synthesis, reagents and conditions, as well as experimental and spectral data can be found within the EXPERIMENTAL section. The photoswitches can be divided into two groups: azobenzene modified amino acids and crosslinkers (Figure 1.7).

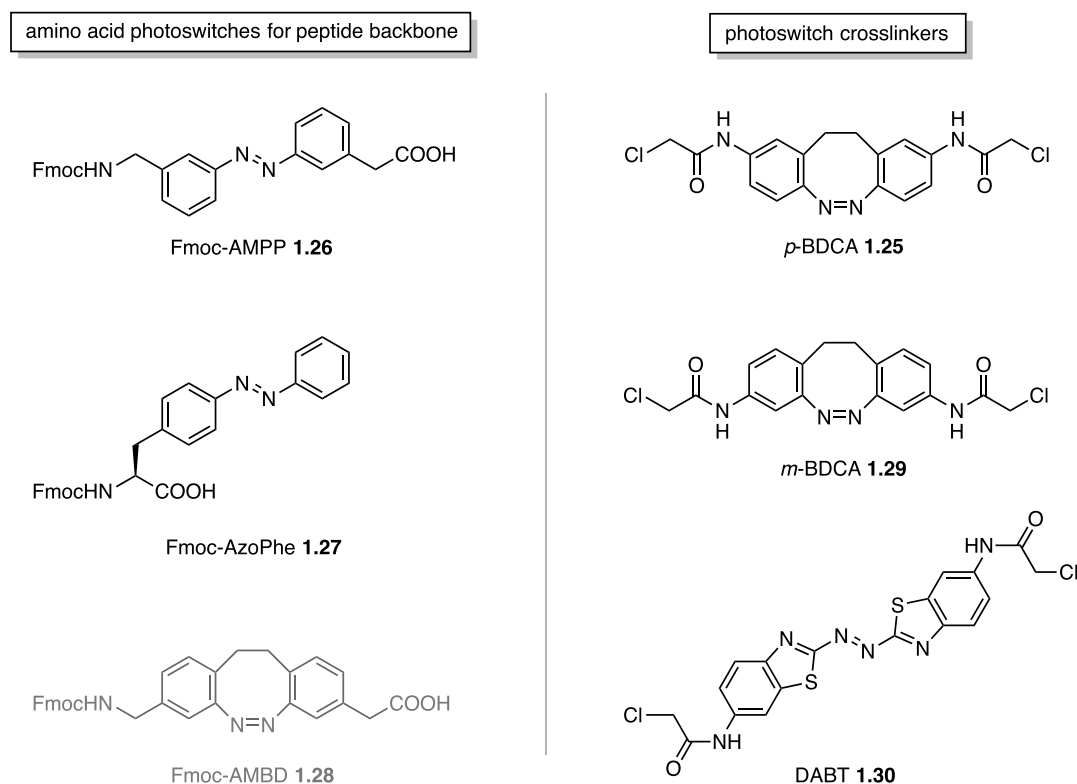
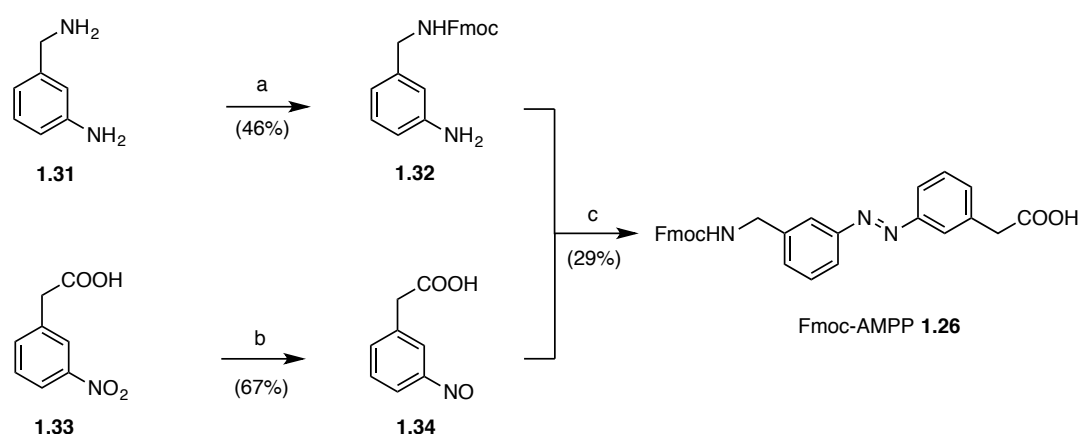


**Figure 1.7: Overview of the synthesized photoswitches.** Left: chromophoric amino acids Fmoc-AMPP **1.26**, Fmoc-AzoPhe **1.27** and Fmoc-AMBD **1.28** as building blocks for Fmoc-supported solid-phase peptide synthesis. Right: photoswitch crosslinkers *p*-BDCA **1.25**, *m*-BDCA **1.29** and DABT **1.30**. Photoswitches are shown in black (successfully synthesized) or gray (still being retrieved).

Compounds belonging to the the first group comprise photoswitches with amino and carboxylic acid functions and can be used as amino acid substitutes in peptide synthesis. The amino groups are thereby Fmoc-protected, which facilitates implementation in Fmoc-supported solid-phase peptide synthesis (SPPS). In contrast, the crosslinker photoswitches possess two chloroacetamido groups at the aromatic core, which can react with nucleophilic thiols of cysteines. From the first group of photoswitches the successful synthetic strategy towards two published Fmoc-photoswitch chromophores 2-(3-(((9*H*-fluoren-9-yl)methoxy)carbonyl)amino)methyl)phenyl)diazen-yl)phenyl)acetic acid (Fmoc-AMPP, **1.26**)<sup>21,25,80</sup> and (S)-2-(((9*H*-fluoren-9-yl)methoxy)carbonyl)-amino)-3-(4-(phenyldiazenyl)-phenyl)-propanoic acid (Fmoc-AzoPhe, **1.27**)<sup>78</sup> is shown, as well as the synthesis towards the ethylene-bridged AMPP analog 2-(8-(((9*H*-fluoren-9-yl)methoxy)carbonyl)amino)methyl)-11,12-dihydrodibenzo-[*c,g*][1,2]diazocin-3-yl)acetic acid (Fmoc-AMBD, **1.28**). It should be noted that the aspired chromophore **1.28** has not yet been obtained and

is still subject to design and synthetic optimizations. From the second group of photoswitches the successful synthesis of the known photoswitch crosslinker *N,N'*-(11,12-dihydrodibenzo[*c,g*][1,2]diazocine-2,9-diyl)bis(2-chloroacetamide) (*p*-BDCA, **1.25**)<sup>73</sup>, as well as the synthesis of the bis(chloroacetamido) analog of crosslinker **1.21**, *N,N'*-(11,12-dihydrodi-benzo[*c,g*][1,2]diazocine-3,8-diyl)bis(2-chloroacetamide) (*m*-BDCA, **1.29**), is shown. Furthermore, the synthesis of the novel photoswitch crosslinker based on azobenzothiazole, *N,N'*-(diazene-1,2-diylbis(benzo[*d*]thiazole-2,6-diyl))bis(2-chloroacetamide) (DABT, **1.30**), is presented and the photochromic properties are discussed.

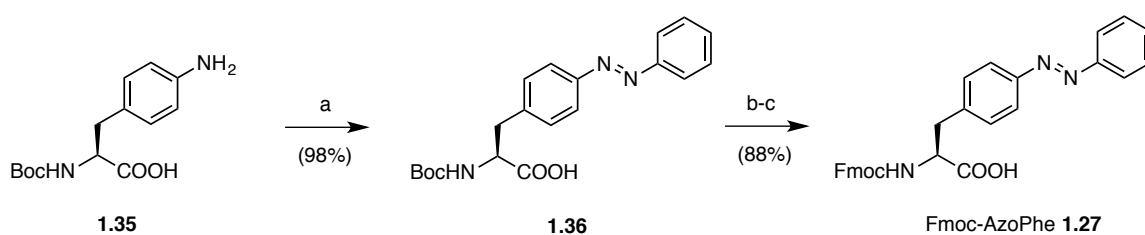
### 1.2.1 SYNTHESIS OF FMOC-AMPP 1.26



**Scheme 1.3: Synthesis of Fmoc-AMPP 1.26.** Reagents and conditions: a) Fmoc-OSu, DMF/MeCN (1:5), rt, 4 hrs (46%); b)  $\text{NH}_4\text{Cl}$ , zinc, 2-methoxyethanol, 0 °C  $\rightarrow$  rt, 30 min;  $\text{FeCl}_3 \cdot 6 \text{H}_2\text{O}$ , EtOH/ $\text{H}_2\text{O}$  (5:1), 0 °C  $\rightarrow$  rt, 90 min (67%) and c) AcOH, rt, 24 hrs, (29%).

The synthesis of Fmoc-AMPP **1.26** was adapted from *Dong et al.*<sup>80</sup>, who themselves optimized the original strategy from *Aemissegger et al.*<sup>25</sup>. It is a fast three step synthesis, which involves the classical *Mill's reaction*<sup>61</sup> between an amino and nitroso compound to generate the asymmetrically substituted azobenzene **1.26** (Scheme 1.3). In a first step the benzylic amino group in 3-(aminomethyl)aniline (**1.31**) was Fmoc-protected with *N*-(9-fluorenylmethoxycarbonyloxy)-succinimide (Fmoc-OSu) to yield compound **1.32**. In the next step, 2-(3-nitrophenyl)acetic acid (**1.33**) was first reduced with zinc to hydroxylamine and subsequently oxidized with  $\text{FeCl}_3$  to form nitroso compound **1.34**. Both compounds **1.32** and **1.34** were then reacted with each other to form the desired Fmoc-AMPP **1.26**. Spectral and photophysical data of this chromophore incorporated into peptides can be found in the publications of *Aemissegger*, *Dong* and *Podewin et al.*<sup>21,25,80</sup>.

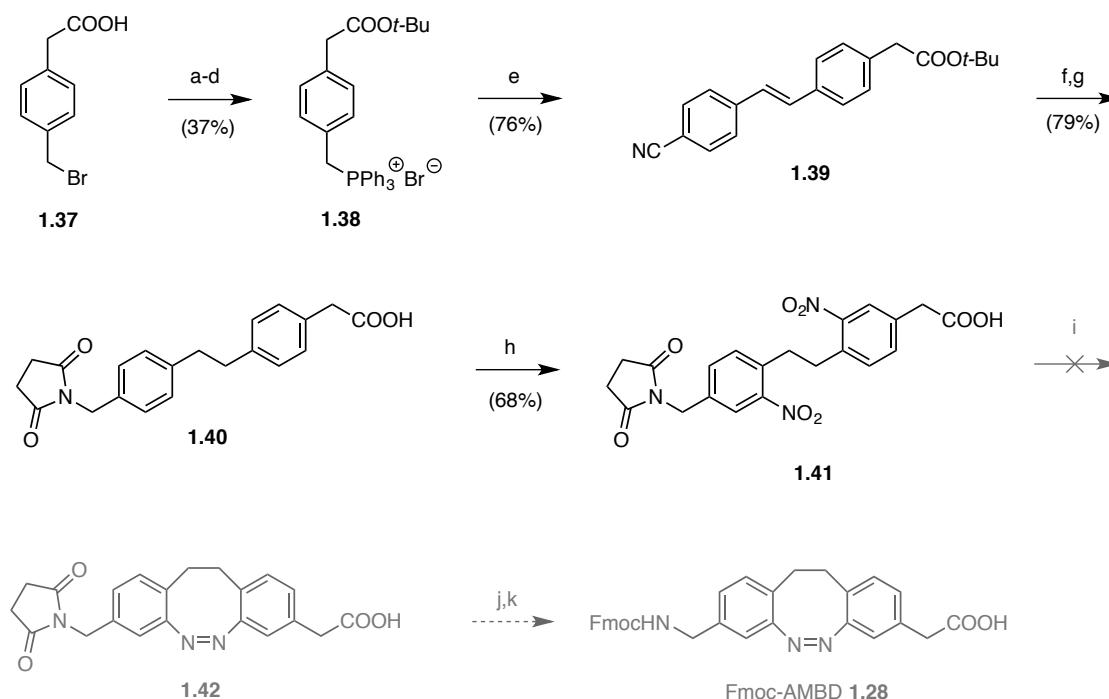
## 1.2.2 SYNTHESIS OF FMOC-AZOPHE 1.27



**Scheme 1.4: Synthesis of Fmoc-AzoPhe 1.27.** Reagents and conditions: a) PhNO, AcOH, 25 hrs, rt (98%); b) TFA, CH<sub>2</sub>Cl<sub>2</sub>, 18 hrs, rt and c) Fmoc-Cl, dioxane, 0 °C/1 hr → rt/72 hrs (88%).

The chromophore **1.27** was synthesized following the protocol of *Bose et al.*<sup>78</sup>, in which commercial available *L-N-tert-butoxycarbonyl-para-phenylalanine* (**1.35**) was reacted with nitrosobenzene to form *N-(tert-butoxycarbonyl)-L-phenylalanine-4'-azobenzene* (**1.36**) (Scheme 1.4). Deprotection of the Boc-protecting group and subsequent Fmoc-protection yielded the photoswitch amino acid Fmoc-AzoPhe **1.27** with good yields. Spectral and photophysical data to this chromophore can be found in the publication of *Bose et al.*<sup>78</sup>.

## 1.2.3 SYNTHETIC ROUTE TOWARDS FMOC-AMBD 1.28



**Scheme 1.5: Synthetic route towards Fmoc-AMBD 1.28.** Reagents and conditions: a) NBS, BPO, CCl<sub>4</sub>, 10 min, rt (92%); b) SOCl<sub>2</sub>, 110 °C, 3 hrs; c) *t*-BuOH, CH<sub>2</sub>Cl<sub>2</sub>, 0 °C/2 hrs → rt/18 hrs (78%); d) PPh<sub>3</sub>, PhMe, 120 °C, 18 hrs (52%); e) 3-Cyanobenzaldehyd, KHMDS, abs. THF, 0 °C/2 hrs → rt/20 hrs (76%); f) H<sub>2</sub>, Pd/C, THF/MeOH, 72 hrs (98%); g) succinic anhydride, AcOH, DMAP, 130 °C, 18 hrs (81%) and h) KNO<sub>3</sub>, H<sub>2</sub>SO<sub>4</sub>, 60 °C, 6 hrs (68%). Further reaction steps: i) azo coupling; j) succinimide deprotection and k) Fmoc-protection.

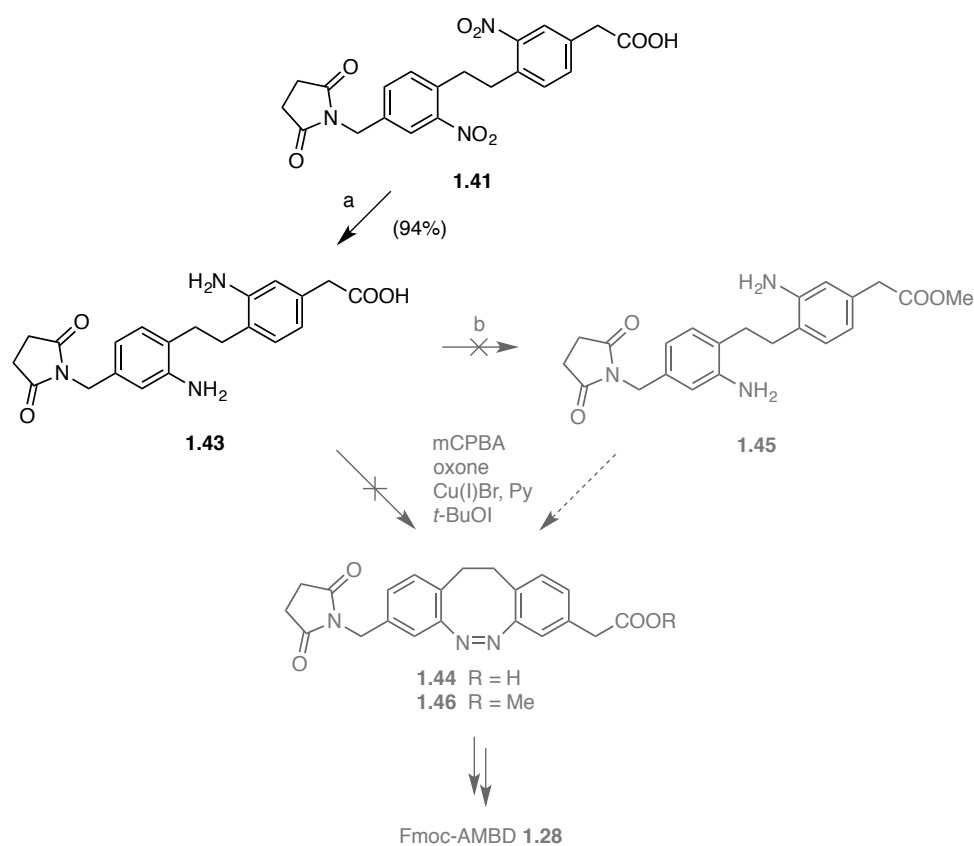
The planned synthesis of the bridged azobenzene photoswitch Fmoc-AMBD **1.28** comprised at first the construction of the ethylene bridge through a *Wittig olefination*, followed by reductive azo bridge formation and final Fmoc-protection (Scheme 1.5). Initially (steps a-d), *para*-tolylacetic acid (**1.37**) was brominated and then reacted with thionyl chloride to generate a reactive acyl chloride. Subsequent formation of the *tert*-butyl ester with *tert*-butanol and reaction with triphenylphosphine yielded the *Wittig* phosphonium salt **1.38** with an overall yield of 37%.

Compound **1.38** was then reacted with 3-cyanobenzaldehyde to form stilbene **1.39**. In the *Wittig reaction* (step e), the first step was the formation of a phosphonium ylide through treatment of the phosphonium salt **1.38** with a strong base, in this case potassium bis(trimethylsilyl)amide (KHMDs). Nucleophilic attack of the carbanion to 3-cyanobenzaldehyde then leads to formation of an intermediate betaine from which elimination delivers the desired *cis/trans*-stilbene **1.39**. Although the *cis/trans*-ratio is not of particular interest for the succeeding reactions, due to the loss of stereo information upon reduction of the stilbene double bond at a later stage, it should be noted that the obtained *cis/trans*-ratio was 1:1.7 (determined through <sup>1</sup>H-NMR). Furthermore, several strong non-nucleophilic bases such as sodium hydride, *n*-butyllithium and lithium bis(trimethylsilyl)amide (LiHMDS) have been tested, but only the use of KHMDs delivered acceptable yields of **1.39**.

The palladium on carbon (Pd/C) catalyzed hydrogenation of stilbene **1.39** in tetrahydrofuran and methanol simultaneously reduced the ethenyl bridge to ethylene and the cyano group to benzylamine. In the following step, the amino group was then protected as a succinimide to form compound **1.40**. The consequent double nitration of both phenyl rings in *meta*-position to the ethylene bridge was adapted from *Sell et al.*<sup>75</sup> and delivered the precursor azo coupling compound **1.41**.

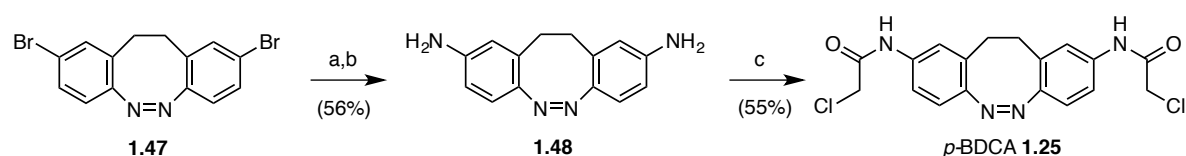
Intramolecular azo bridge formation can be achieved through reductive coupling of two nitro groups and the most frequently used protocol uses zinc as reducing agent in barium or sodium hydroxide<sup>84,85</sup>, with subsequent oxidation of the formed hydrazine intermediate. These procedures however suffer from low and irreproducible yields ranging from 2-19%. For this reason, *Sell et al.*<sup>75</sup> recently used glucose in ethanolic solution as reducing agent and achieved constant yields of >20%. Hence, for the azo bridge formation in compound **1.41** glucose under the same conditions was tried, but the bridged azobenzene product **1.42** could not be obtained. Switching to the established zinc/barium or sodium hydroxide procedure also failed to deliver the desired compound **1.42**.

A further attempt to construct the azo bridge was to change from a reductive to an oxidative coupling process, in which two intramolecular amino groups are coupled with oxidative reagents such as *meta*-chloroperoxybenzoic acid (*m*-CPBA), potassium peroxymonosulfate (Oxone<sup>®</sup>), Cu(I)Br with catalytical amounts of pyridine<sup>86</sup> or with *tert*-butyl hypoiodite (*t*-BuOI)<sup>87,88</sup> (Scheme 1.6). Therefore, dinitro compound **1.41** was hydrogenated with hydrogen and Pd/C to diamino compound **1.43**. Although the oxidative reagents were tested under different reaction conditions, all of them failed to afford product **1.44**. To rule out any interference of the free carboxylic acid in **1.44**, it was planned to transfer it into a methyl ester group. However, product **1.45** could not be obtained using thionyl chloride in methanol and at this point this synthesis route towards Fmoc-AMBD **1.28** was neglected.



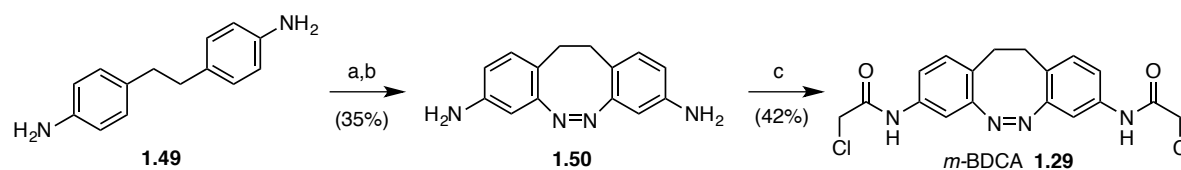
**Scheme 1.6: Oxidative coupling approach for Fmoc-AMBD 1.28.** Reagents and conditions: a)  $\text{H}_2$ , Pd/C, THF/MeOH, 48 hrs (94%) and b)  $\text{SOCl}_2$ , MeOH,  $0\text{ }^\circ\text{C} \rightarrow 75\text{ }^\circ\text{C}$ , 12 hrs. Oxidative coupling with *meta*-CPBA, Oxone, Cu(I)Br/cat. Py and *tert*-BuOI failed to afford compound **1.44** or **1.46**.

### 1.2.4 SYNTHESIS OF *p*-BDCA 1.25



**Scheme 1.7: Synthesis of *p*-BDCA 1.25.** Reagents and conditions: a)  $\text{Pd}_2\text{dba}_3$ , Xantphos, *tert*-butyl carbamate, dioxane,  $0\text{ }^\circ\text{C} \rightarrow \text{rt}$ , 90 min (80%); b)  $\text{CH}_2\text{Cl}_2$ , TFA, anisol (6:1:1), rt, 5 hrs (70%) and c) chloroacetic anhydride, pyridine, diethyl ether, 1 hr, rt (55%).

Photoswitch crosslinker *p*-BDCA **1.25** was synthesized based on bisbromo diazocin **1.47**, which was kindly provided by *D. H. Woodmansee* and *D. Trauner*. The first step was a *Buchwald-Hartwig amination* with tris(dibenzylideneacetone)dipalladium(0) ( $\text{Pd}_2\text{dba}_3$ ) and 4,5-bis(diphenylphosphino)-9,9-dimethylxanthene (Xantphos) in absolute dioxane to generate a Boc-protected bisamide, which was consequently deprotected with trifluoroacetic acid to forge bisamino diazocin **1.48** (Scheme 1.7). The last step was the reaction of **1.48** with chloroacetic anhydride to form *p*-BDCA **1.25**. Detailed spectral and photophysical data to this chromophore can be found in the publication of *Samanta et al.*<sup>73</sup>.

1.2.5 SYNTHESIS OF *m*-BDCA 1.29

**Scheme 1.8: Synthesis of *m*-BDCA 1.29.** Reagents and conditions: a)  $\text{KNO}_3$ ,  $\text{H}_2\text{SO}_4$ , 60 °C, 6 hrs, (88%); b) zinc,  $\text{Ba}(\text{OH})_2$ ,  $\text{EtOH}/\text{H}_2\text{O}$  (5:1), rt, 3 hrs (40%) and c) chloroacetic anhydride, pyridine, diethyl ether, rt, 1 hr (42%).

The first two steps of the *m*-BDCA 1.29 synthesis followed the protocol of *Sell et al.*<sup>75</sup> (Scheme 1.8). Commercially available 4,4'-(ethane-1,2-diyl)dianiline (1.49) was *meta*-nitrogenated with potassium nitrate in sulfuric acid. This was followed by a reductive azo coupling with zinc and barium hydroxide in ethanolic solution to yield bisamino diazocin 1.50 with satisfactory yield (40%). The last step involved the reaction of 1.50 with chloroacetic anhydride to form *m*-BDCA 1.29.

The UV/Vis spectra of *cis*-/*trans*-bis(*meta*-chloroacetamido) diazocin 1.29 revealed as expected similar photochromic properties to the bis(*meta*-acetamido) diazocin 1.21 (Figure 1.8)<sup>75</sup>. The UV spectrum of *cis*-1.29 exhibits a shoulder at 320 nm for the  $\pi$ - $\pi^*$  transition and a maximum at 400 nm for the  $n$ - $\pi^*$  transition. Irradiation at 405 nm leads to isomerization and generation of 51% of the *trans* isomer, as determined by  $^1\text{H-NMR}$ . The rather low conversion rate compared to unsubstituted diazocin 1.19 (>90%) probably originates from the overlapping  $\pi$ - $\pi^*$  and  $n$ - $\pi^*$  transitions. The UV spectrum of *trans*-1.29 shows a slightly shifted shoulder for the  $\pi$ - $\pi^*$  transition at 330 nm and a large shift to 490 nm for the  $n$ - $\pi^*$  transition. The distinctive separation of the latter to any other bands leads to complete back conversion to the *cis*-isomer upon irradiation with 530 nm light.

Repeated photoswitching of 1.29 with 405 and 530 nm light demonstrates the speed and reliability of isomerization and negligible photobleaching after several cycles (Figure 1.8). The observed  $\tau$ -values of  $\tau_{cis \rightarrow trans} = 98.9 \pm 3.9$  sec and  $\tau_{trans \rightarrow cis} = 60.4 \pm 4.0$  sec show a roughly 1.5x faster back conversion to the *cis*-isomer. This corresponds to the isolated  $n$ - $\pi^*$  transition of the *trans*-isomer, which enables a fast and complete *trans*  $\rightarrow$  *cis* isomerization. Detection of the thermal back-relaxation rate of 1.29 after generation of the *trans*-isomer in the PSS shows a rate of  $k_{obs} = 2.72 \times 10^{-4}$   $\text{au}_{490\text{nm}}/\text{min}$  (in DMSO at 25 °C). This is a slightly lower rate compared to  $k_{obs} = 3.58 \times 10^{-4}$   $\text{au}_{330\text{nm}}/\text{min}$  of unsubstituted azobenzene (in benzene at 0 °C)<sup>89</sup> and is similar to the thermal half-life of  $\tau_{1/2} = 46$  hrs for bis(*meta*-acetamido) diazocin 1.21 (in MeCN at 27 °C)<sup>75</sup>.

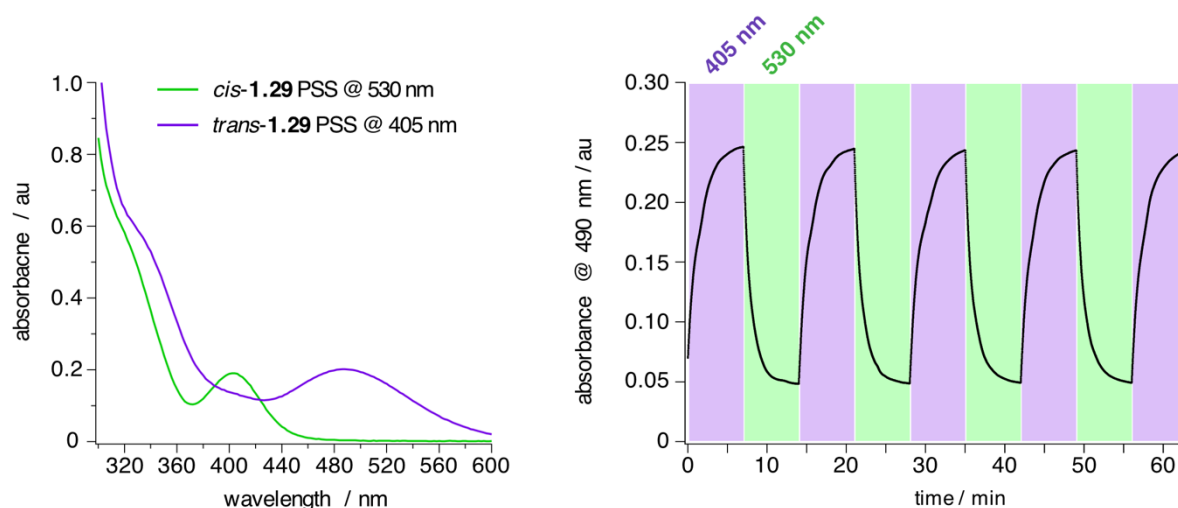
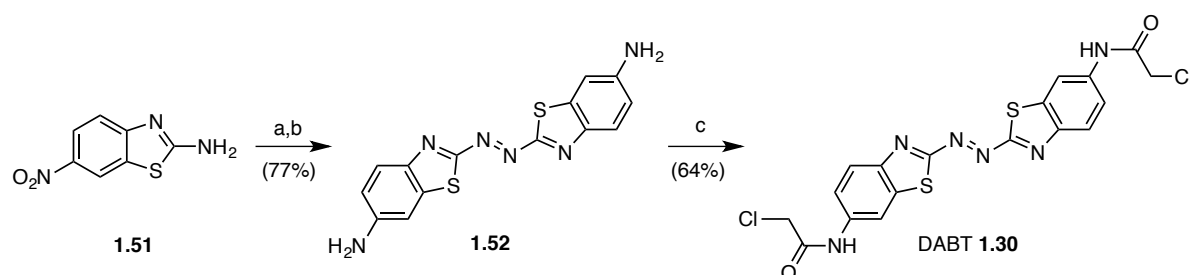


**Figure 1.8: Photophysical properties and photoswitching kinetics of *m*-BDCA **1.29**.** Left: UV/Vis spectra of *cis*-**1.29** and *trans*-**1.29** in the PSS at 530 and 405 nm, respectively (in DMSO at 25 °C). Right: switching kinetics of **1.29** for the *cis* → *trans* and *trans* → *cis* isomerization at 405 or 530 nm, respectively. Measured as absorbance change of the *trans*-**1.29** *n*- $\pi^*$  transition at 490 nm (in DMSO at 25 °C).

### 1.2.6 SYNTHESIS OF DABT **1.30**



**Scheme 1.9: Synthesis of DABT **1.30**.** Reagents and conditions: a) NaOCl solution (13%), 60 °C, 1 hr, (90%); b) NaS, THF, 80 °C, 3 hrs (86%) and c) 3-chloropropionyl chloride, DMAP, DMF, 0 °C → rt, 2 hrs (64%).

Azobenzothiazoles were first synthesized in the mid of the last century<sup>90</sup>, but their use as dyes is impeded due to the low photostability and high oxidation potential of these compounds<sup>91,92</sup>. Nevertheless, since their photophysical properties have not been properly assessed, especially with respect to their photoswitching capabilities, the azobenzothiazole crosslinker DABT **1.30** was synthesized and characterized. The synthesis of DABT **1.30** followed a fast three step route starting with commercially available 2-amino-6-nitrobenzothiazole (**1.51**), which was homo azocoupled under oxidative conditions with NaOCl to form 1,2-bis(6-nitrobenzothiazol-2-yl)diazene (**1.52**). Upon reduction with sodium sulfide and subsequent reaction with 3-chloropropionyl chloride the desired bis(chloroacetamido) azobenzothiazole **1.30** could be generated.

The UV spectra of *cis*-/*trans*-DABT **1.30** show both a very strong, red-shifted absorption band at  $\lambda_{\text{max}} = 536$  nm, with a small shoulder between 630 – 710 nm (Figure 1.9). Illumination of *trans*-**1.30** with green light (530 nm) leads to a minimal reduction of the absorption band at 536 nm, indicating the formation of the *cis*-isomer. The difference in the absorption spectra of both isomers is marginal, and no

shifting of bands could be observed. The switching kinetics were assessed through measurement of absorbance change upon illumination of the transition band at 530 nm (Figure 1.9). The isomerization rate is very fast, with the thermal *cis* → *trans* back-relaxation in the dark occurring as rapid as the corresponding light-induced *cis*-formation ( $\tau_{trans \rightarrow cis} = 274.5 \pm 33.7$  msec and  $\tau_{cis \rightarrow trans} = 289.8 \pm 40.0$  msec). Moreover, the switching was robust and no photobleaching or degradation were detected. The fast kinetics are in line with other red-shifted compounds, which also show fast photoconversion and thermal back-relaxation rates<sup>10,11</sup>. The molar extinction coefficient was determined as  $\epsilon_{530\text{ nm}} = 28400 \text{ L}\cdot\text{mol}^{-1}\cdot\text{cm}^{-1}$  (in DMSO at 25 °C) and is therewith comparable to azobenzene and other dyes<sup>93,94</sup>. The fluorescence quantum yield was determined to  $\phi = 0.5\%$  (vs. perylen-S13 standard in DMSO at 25 °C), thus **1.30** exhibits no fluorescence.

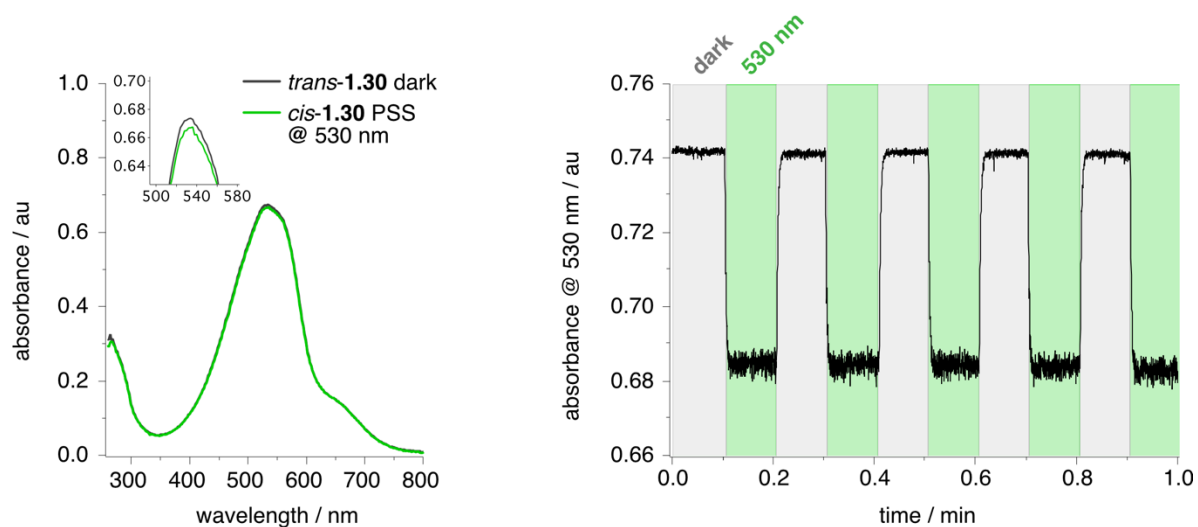


**Figure 1.9: Photophysical properties and photoswitching kinetics of DABT 1.30.** Left: UV/Vis spectra of *cis/trans*-**1.30** (in DMSO at 25 °C). Right: switching kinetics of **1.30** for the *trans* → *cis* and *cis* → *trans* thermal back-relaxation at 530 nm or in the dark, respectively. Measured as absorbance change at 530 nm (in DMSO at 25 °C).

Of the six photoswitches discussed in this chapter, AMPP **1.22**, AzoPhe **1.24**, *p*-BDCA **1.25** and *m*-BDCA **1.29** have successfully been incorporated into target peptides, however peptides containing the photoswitchable crosslinkers **1.25** and **1.29** lack preliminary results and are not discussed in detail. Thus, all the photoswitchable peptides presented in the following chapters utilized chromophores **1.26** and **1.27**. An overview of the photoswitches and the modified peptides is given in Figure 1.10.

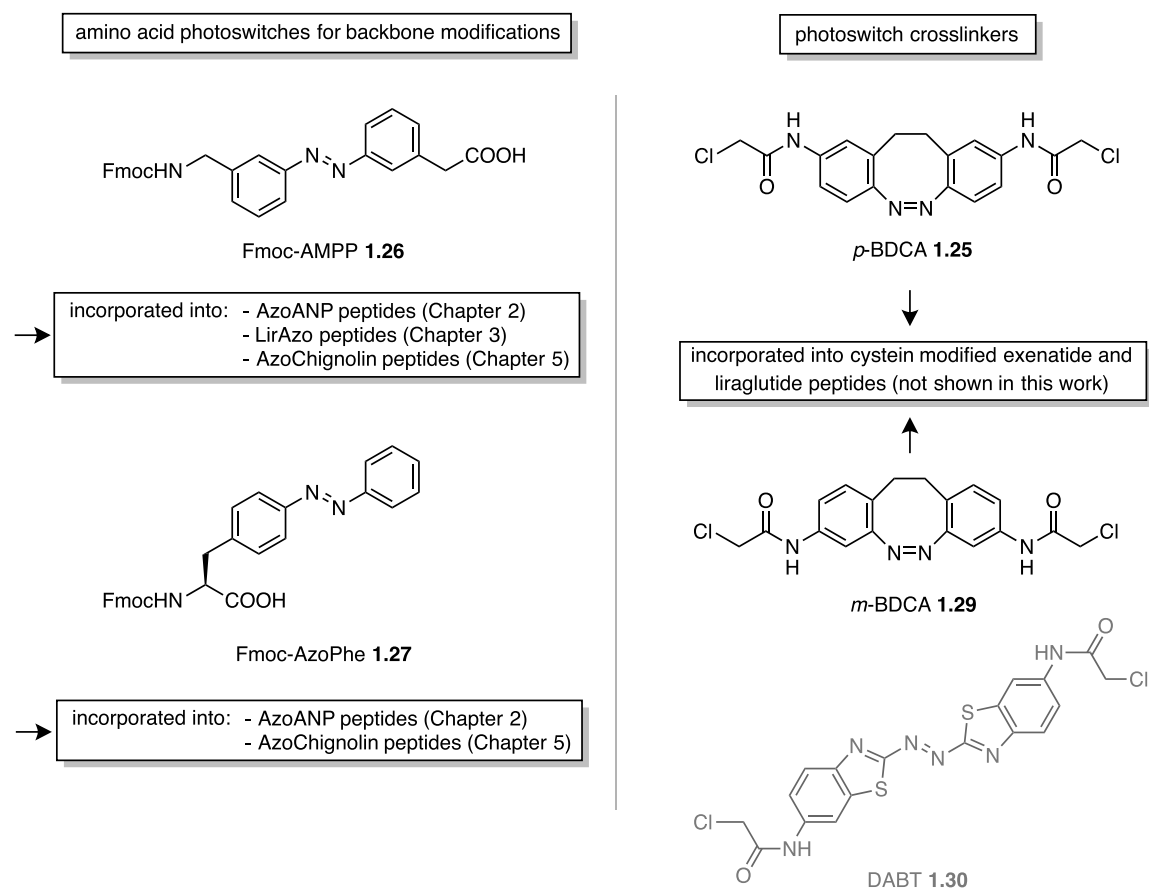
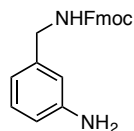


Figure 1.10: Overview of the synthesized photoswitches and the targeted peptides.

## 1.3 EXPERIMENTAL

### 1.3.1 SYNTHESIS

#### 1.3.1.1 *N*-(9-FLUORENYLMETHOXYCARBONYLOXY)-SUCCINIMIDE (**1.32**)



Chemical Formula: C<sub>22</sub>H<sub>20</sub>N<sub>2</sub>O<sub>2</sub>  
Exact Mass: 344.1525  
Molecular Weight: 344.4140

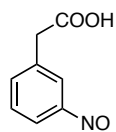
To a solution of 14.1 g (44.0 mmol, 1 eq.) Fmoc-OSu in 100 mL MeCN was added slowly a solution of 4.42 mL (44.0 mmol, 1 eq.) 3-(aminobenzyl)amine **1.31** in 6.1 mL (44.0 mmol, 1 eq.) triethylamine and 55 mL of a MeCN/DMF (10:1) mixture. The resulting solution was stirred for 4 hrs at room temperature and subsequently quenched with 50 mL water. The obtained precipitate was filtered off, washed with 50 mL of a *tert*-butyl methyl ether/trifluoroethanol (1:1) mixture and dried *in vacuo*. The product **1.32** was obtained as colorless solid (7.85 g, 22.9 mmol, 52%) and used in the next reaction without further purification.

**<sup>1</sup>H-NMR** (300 MHz, CDCl<sub>3</sub>):  $\delta$  [ppm] = 7.77 (d,  $J$  = 7.2 Hz, 2H), 7.60 (d,  $J_{\text{H1,H2}}$  = 7.4 Hz, 2H), 7.40 (t,  $J$  = 7.3 Hz, 2H), 7.31 (t,  $J$  = 7.3 Hz, 2H), 7.12 (t,  $J$  = 7.6 Hz, 1H), 6.65 (d,  $J$  = 7.6 Hz, 1H), 6.62-6.58 (m, 3H), 5.03 (bs, 1H), 4.45 (d,  $J$  = 6.9 Hz, 2H), 4.30 (d,  $J$  = 5.8 Hz, 2H), 4.24 (t,  $J$  = 7.0 Hz, 1H).

**<sup>13</sup>C-NMR** (75 MHz, CDCl<sub>3</sub>):  $\delta$  [ppm] = 156.4, 146.6, 143.9, 141.3, 139.6, 129.7, 128.7, 127.6, 127.0, 125.0, 120.1, 114.2, 114.0, 66.7, 47.3, 45.0.

**HRMS** (+EI): calc. for C<sub>22</sub>H<sub>20</sub>O<sub>2</sub>N<sub>2</sub> [M]<sup>+</sup>: 344.1525; found: 344.1596.

#### 1.3.1.2 (9H-FLUOREN-9-YL)METHYL (3-AMINO BENZYL)CARBAMATE (**1.34**)



Chemical Formula: C<sub>8</sub>H<sub>7</sub>NO<sub>3</sub>  
Exact Mass: 165.04  
Molecular Weight: 165.15

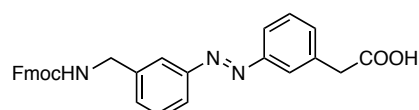
A solution of 2.50 g (13.2 mmol, 1.0 eq.) 2-(3-nitrophenyl)acetic acid (**1.33**) in 100 mL 2-methoxyethanol under an argon atmosphere was stirred for 10 min at room temperature before addition of a solution of 1.09 g (20.3 mmol, 1.5 eq.) NH<sub>4</sub>Cl in 25 mL water. The solution was cooled to 0 °C and 2.10 g (32.3 mmol, 2.5 eq.) zinc was added portionwise within 30 min. After 1 hour, the zinc was filtered off and the filtrate was added within 15 min to a 0 °C cooled solution of 11.2 g (41.4 mmol, 3.0 eq.) FeCl<sub>3</sub>·6 H<sub>2</sub>O in 120 mL of a EtOH/H<sub>2</sub>O (2:1) mixture. After stirring for 1.5 hrs, the solution was diluted with 200 mL water and extracted with 5 x 100 mL diethyl ether. The combined organic fractions were dried with magnesium sulfate and the solvent was evaporated. The crude product was purified *via* column chromatography on silica (eluent EtOAc/cHex/AcOH 10:1:0.5). The product was obtained as green-turquoise oil with 95% (2.18 g, 13.2 mmol) yield.

**<sup>1</sup>H-NMR** (400 MHz, CDCl<sub>3</sub>):  $\delta$  [ppm] = 8.16 (d,  $J_{H_4,H_5}$  = 7.5 Hz, 1H), 7.88 (d,  $J_{H_5,H_6}$  = 7.3 Hz, 1H), 7.76 (s, 1H), 7.63 (t,  $J_{H_4,H_5,H_6}$  = 7.5 Hz, 1H), 3.82 (s, 2H).

**<sup>13</sup>C-NMR** (100 MHz, CDCl<sub>3</sub>):  $\delta$  [ppm] = 176.6, 165.5, 136.2, 136.0, 129.6, 121.4, 120.5, 40.3.

**MS** (+EI) m/z: calc. for C<sub>8</sub>H<sub>7</sub>O<sub>3</sub>N [M]<sup>+</sup>: 165.04; found: 165.09.

### 1.3.1.3 3-[3-(AMINOMETHYL)PHENYLAZO]PHENYLACETIC ACID (1.26)



Chemical Formula: C<sub>30</sub>H<sub>25</sub>N<sub>3</sub>O<sub>4</sub>  
Exact Mass: 491.18  
Molecular Weight: 491.55

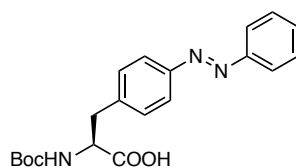
To a solution of 0.27 g (1.65 mmol, 1.0 eq.) 2-(3-nitrosophenyl)acetic acid (**1.34**) in 8.0 mL glacial acetic acid were added portionwise 0.57 g (1.65 mmol, 1 eq.) (9*H*-fluoren-9-yl)methyl (3-aminobenzyl)carbamate (**1.32**). The solution was stirred over night at room temperature, then solvent was evaporated and the crude product was purified *via* flash chromatography on silica (EtOAc/cHex/AcOH 1:1:0.01). The product was obtained as orange solid (3.83 g, 7.80 mmol, 59%).

**<sup>1</sup>H-NMR** (600 MHz, CDCl<sub>3</sub>):  $\delta$  [ppm] = 7.85-7.81 (m, 4H), 7.75 (d,  $J$  = 7.4 Hz, 2H), 7.60 (d,  $J$  = 7.1 Hz, 2H), 7.48 (t,  $J$  = 8.3 Hz, 2H), 7.42-7.36 (m, 4H), 7.30 (t,  $J$  = 7.6 Hz, 2H) 5.22 (bs, 1H), 4.51-4.47 (m, 4H), 4.24 (t,  $J_{H_9,CH_2}$  = 6.9 Hz, 1H), 3.75 (s, 2H).

**<sup>13</sup>C-NMR** (150 MHz, CDCl<sub>3</sub>):  $\delta$  [ppm] = 175.8, 156.5, 152.8, 152.7, 143.9, 141.3, 139.6, 134.7, 134.5, 132.0, 130.1, 129.5, 129.4, 127.7, 127.1, 125.0, 123.6, 122.4, 122.3, 121.4, 120.0, 66.8, 47.3, 44.8, 40.7.

**HRMS** (+EI) m/z: calc. for C<sub>22</sub>H<sub>20</sub>O<sub>2</sub>N<sub>2</sub> [M]<sup>+</sup>: 491.1845; found: 491.1845.

### 1.3.1.4 *N*-(*tert*-BUTOXYCARBONYL)-*L*-PHENYLALANINE-4'-AZOBENZENE (1.36)



Chemical Formula: C<sub>20</sub>H<sub>23</sub>N<sub>3</sub>O<sub>4</sub>  
Exact Mass: 369.17  
Molecular Weight: 369.42

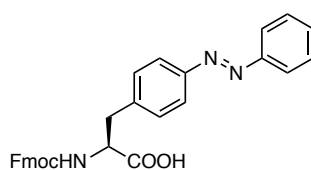
To a solution of 0.50 g (1.78 mmol, 1.0 eq.) *N*-*tert*-butoxycarbonyl-*para*-*L*-phenylalanine (**1.35**) in 50 mL glacial acetic acid was added 0.29 g (2.69 mmol, 1.5 eq.) nitrosobenzene. The solution was stirred for 24 hrs at room temperature, before 150 mL saturated sodium carbonate solution was added. The aqueous phase was extracted with 4 x 50 mL ethyl acetate. The combined organic layers were dried with magnesium sulfate and after removal of the solvent the crude product was purified *via* flash chromatography on silica gel (eluent EtOAc/cHex/AcOH 5:1:0.05). The product was obtained as orange solid with 98% (6.55 g, 1.77 mmol) yield.

**<sup>1</sup>H-NMR** (400 MHz, MeOD-d<sub>4</sub>):  $\delta$  [ppm] = 7.89 (dt, 2H, *H*<sub>9</sub>, *H*<sub>9'</sub>), 7.85 (d, *J* = 8.1 Hz, 2H, *H*<sub>6</sub>, *H*<sub>6'</sub>), 7.58-7.46 (m, 3H, *H*<sub>10</sub>, *H*<sub>10'</sub>, *H*<sub>11</sub>), 7.43 (d, *J* = 8.1 Hz, 2H, *H*<sub>5</sub>, *H*<sub>5'</sub>), 4.42 (dd, *J* = 9.3, 5.0 Hz, 1H, *H*<sub>2</sub>), 3.27 (dd, *J* = 13.8, 5.1 Hz, 1H, *H*<sub>3</sub>), 3.01 (dd, *J* = 13.8, 9.2 Hz, 1H, *H*<sub>3'</sub>) and 1.38 (s, 9H, (CH<sub>3</sub>)<sub>3</sub>).

**<sup>13</sup>C-NMR** (100 MHz, MeOD-d<sub>4</sub>):  $\delta$  [ppm] = 175.2 (COOH), 157.8 (NH-COOtBu), 154.0 (C<sub>8</sub>), 152.8 (C<sub>7</sub>), 142.5 (C<sub>4</sub>), 132.2 (C<sub>11</sub>), 131.3 (C<sub>5</sub>, C<sub>5'</sub>), 130.2 (C<sub>10</sub>, C<sub>10'</sub>), 123.8 (C<sub>6</sub>, C<sub>6'</sub>), 123.7 (C<sub>9</sub>, C<sub>9'</sub>), 80.6 (O-C(CH<sub>3</sub>)<sub>3</sub>), 56.1 (C<sub>2</sub>), 38.6 (C<sub>3</sub>) and 28.7 ((CH<sub>3</sub>)<sub>3</sub>).

**HRMS** (+ESI) *m/z*: calc. for C<sub>20</sub>H<sub>24</sub>O<sub>4</sub>N<sub>3</sub> [M+H]<sup>+</sup>: 370.1761; found: 370.1769.

### 1.3.1.5 (S,E)-2-(((9H-FLUOREN-9-YL)METHOXY)CARBONYL)AMINO)-3-(4-(PHENYLDIAZENYL)PHENYL)-PROPANOIC ACID, Fmoc-AzOPHE (1.27)



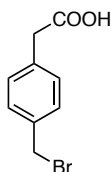
Chemical Formula: C<sub>30</sub>H<sub>25</sub>N<sub>3</sub>O<sub>4</sub>  
Exact Mass: 491.18  
Molecular Weight: 491.55

To a solution of 0.64 g (1.72 mmol, 1.0 eq.) *N*-(*tert*-butoxycarbonyl)-L-phenylalanine-4'-azobenzene (**1.36**) in 40 mL absolute dichloromethane was added 30 mL trifluoroacetic acid and the solution was stirred over night at room temperature. The solvent was evaporated and the remaining trifluoroacetic acid was co-evaporated five times with 20 mL toluene each. The product was obtained as orange solid with quant. (0.46 g, 1.71 mmol) yield and was directly employed in the next step. A solution of 0.46 g (1.71 mmol, 1.0 eq.) H<sub>2</sub>N-AzoPhe-OH in 25 mL dioxane was cooled to 0 °C and 65 mL of a 10% sodium carbonate solution and 0.57 g (1.70 mmol, 1.0 eq.) Fmoc-Cl in 30 mL dioxane was added. The mixture was stirred for 1 hour at 0 °C and subsequently stirred 72 hrs at room temperature. The reaction was triturated with 120 mL water and the aqueous phase was extracted with 3 x 100 mL dichloromethane. The aqueous phase was acidified with 1 M HCl to pH = 2 and extracted with 3 x 50 mL dichloromethane. The combined organic layers were dried with magnesium sulfate and the solvent was removed under reduced pressure. The crude product was purified *via* flash chromatography on silica (eluent cHex/EtOAc/AcOH 5:1:0.05). The product was retained as a slight-orange solid with 88% (0.73 g, 1.50 mmol) yield.

**<sup>1</sup>H-NMR** (400 MHz, DMSO-d<sub>6</sub>):  $\delta$  [ppm] = 7.91-7.77 (m, 6H, *H*-ar.), 7.67-7.23 (m, 11H, *H*-ar.), 4.32-4.08 (m, 4H, *H*<sub>2</sub>, *H*<sub>13</sub>, *H*<sub>13'</sub>, *H*<sub>14</sub>), 3.20 (dd, *J* = 13.7, 4.1 Hz, 1H, *H*<sub>3</sub>) and 2.98 (dd, *J* = 13.7, 11.0 Hz, 1H, *H*<sub>3'</sub>).

**<sup>13</sup>C-NMR** (100 MHz, DMSO-d<sub>6</sub>):  $\delta$  [ppm] = 173.1 (COOH), 155.9 (NH-COO), 152.0 (C<sub>7</sub>), 143.8, 143.7, 142.0, 140.7, 131.4, 130.2, 129.5, 127.6, 127.0, 125.2, 122.4, 120.1, 65.6 (C<sub>14</sub>), 55.2 (C<sub>2</sub>), 46.6 (C<sub>13</sub>) and 36.3 (C<sub>3</sub>).

**HRMS** (+ESI) *m/z*: calc. for C<sub>30</sub>H<sub>26</sub>O<sub>4</sub>N<sub>3</sub> [M+H]<sup>+</sup>: 492.1918; found: 492.1916.

**1.3.1.6 2-(4-(BROMOMETHYL)PHENYL)ACETIC ACID (1.53)**

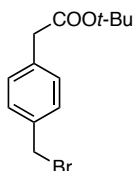
Chemical Formula: C<sub>9</sub>H<sub>9</sub>BrO<sub>2</sub>  
Exact Mass: 227.98  
Molecular Weight: 229.07

A solution of 25.6 g (171 mmol, 1.0 eq.) *para*-tolylacetic acid (**1.37**) in 300 mL carbon tetrachloride was heated to 60 °C. A mixture of 30.3 g (171 mmol, 1.0 eq.) *N*-bromosuccinimide and 2.50 g (10.3 mmol, 0.1 eq.) dibenzoylperoxide was added quickly to the reaction solution, which was then heated to 95 °C. After a short period, a white precipitate formed and the reaction was complete. After cooling 100 mL of water were added and the precipitate was filtered and washed with 700 mL warm water. The colorless solid product was dried and used in the next reaction without further purification (32.5 g, 141 mmol, 82%).

**<sup>1</sup>H-NMR** (300 MHz, DMSO-*d*<sub>6</sub>):  $\delta$  [ppm] = 10.8 (bs, 1H, COOH), 7.38 (d, *J* = 8.3 Hz, 2H, *H*<sub>2</sub>, *H*<sub>6</sub>), 7.22 (d, *J* = 8.3 Hz, 2H, *H*<sub>3</sub>, *H*<sub>5</sub>), 4.47 (s, 2H, CH<sub>2</sub>Br) and 3.55 (s, 2H, CH<sub>2</sub>COOH).

**HRMS** (+ESI) *m/z*: calc. for C<sub>9</sub>H<sub>9</sub>BrO<sub>2</sub> [M]<sup>+</sup>: 227.9786; found: 227.9764.

**R<sub>f</sub>** (cHex/EtOAc 2:1) = 0.18.

**1.3.1.7 *tert*-BUTYL 2-(4-(BROMOMETHYL)PHENYL)ACETATE (1.54)**

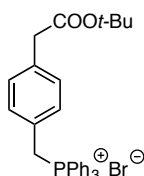
Chemical Formula: C<sub>13</sub>H<sub>17</sub>BrO<sub>2</sub>  
Exact Mass: 284.04  
Molecular Weight: 285.18

A solution of 3.00 g (13.0 mmol, 1.0 eq.) 2-(4-(bromomethyl)phenyl)acetic acid (**1.53**) in 60 mL thionylchloride was refluxed for 3 hrs at 110 °C. After cooling the excess thionylchloride was removed under reduced pressure and the residue dissolved in 5 mL dichloromethane. This solution was then slowly added to a 0 °C cooled solution of 50 mL *tert*-butanol and 10 mL dichloromethane. The reaction was kept 2 hrs at 0 °C and then allowed to warm to room temperature. After being stirred over night, the solvent was removed under reduced pressure and the residue was dissolved in 50 mL dichloromethane. The organic layer was washed with 1 x 50 mL water, 1 x 50 mL sodium bicarbonate, again with 1 x 50 mL water and then dried with magnesium sulfate. The solvent was removed and the product was received as yellow oil (2.90 g, 10.2 mmol, 78%).

**<sup>1</sup>H-NMR** (300 MHz, DMSO-*d*<sub>6</sub>):  $\delta$  [ppm] = 7.30 (m, 4H, *H*-ar.), 4.49 (s, 2H, CH<sub>2</sub>Br), 3.53 (s, 2H, CH<sub>2</sub>COOH) and 1.44 (s, 9H, CH<sub>3</sub>).

**HRMS** (+EI) *m/z*: calc. for C<sub>13</sub>H<sub>19</sub>O<sub>2</sub><sup>79</sup>Br<sub>1</sub> [M]<sup>+</sup>: 286.0391; found: 286.0414. calc. for C<sub>13</sub>H<sub>17</sub>O<sub>2</sub><sup>+</sup> [M-Br]<sup>+</sup>: 205.1229; found: 205.1186.

**R<sub>f</sub>** (cHex/EtOAc 2:1) = 0.64.

**1.3.1.8 TERT-BUTYL 2-(4-((BROMOTRIPHENYLPHOSPHANEYL)METHYL)PHENYL)-ACETATE (1.38)**

Chemical Formula: C<sub>31</sub>H<sub>32</sub>BrO<sub>2</sub>P  
 Exact Mass: 546.13  
 Molecular Weight: 547.47

A solution of 2.80 g (9.83 mmol, 1.0 eq.) *tert*-butyl 2-(4-(bromomethyl)phenyl)acetate (**1.54**) and 2.58 g (9.83 mmol, 1.0 eq.) triphenylphosphine in 100 mL toluene was heated to 120 °C and stirred over night. After cooling, the formed precipitate was filtered and washed with 2 x 100 mL chilled diethyl ether. The colorless solid product (3.18 g, 5.12 mmol, 52%) was dried and used in the next reaction without further purification.

**<sup>1</sup>H-NMR** (400 MHz, DMSO-d<sub>6</sub>): δ [ppm] = 7.93-7.89 (m, 3H, *H-p*-PPh<sub>3</sub>), 7.76-7.65 (m, 12H, *H-o/m*-PPh<sub>3</sub>), 7.10 (d, *J* = 7.8 Hz, 2H, *H2, H6*), 6.94 (dd, *J* = 8.1, 2.6 Hz, 2H, *H3, H5*), 5.23 (d, *J* = 15.6 Hz, 2H, CH<sub>2</sub>P), 3.50 (s, 2H, CH<sub>2</sub>COOH) and 1.36 (s, 9H, CH<sub>3</sub>).

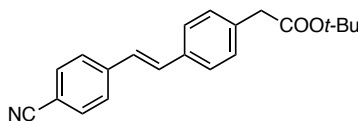
**<sup>13</sup>C-NMR** (100 MHz, DMSO-d<sub>6</sub>): δ [ppm] = 170.1 (COOt-Bu), 135.1 (C1-q), 135.0 (C-*p*-PPh<sub>3</sub>), 134.0 (C-*m*-PPh<sub>3</sub>), 133.9 (C-*m*-PPh<sub>3</sub>), 130.7 (C3, C5), 130.1 (C-*o*-PPh<sub>3</sub>), 130.0 (C-*o*-PPh<sub>3</sub>), 129.6 (C2, C6), 126.2 (C4), 118.2 (C-q-PPh<sub>3</sub>), 117.4 (C-q-PPh<sub>3</sub>), 80.2 (C-q-*t*-Bu), 41.1 (CH<sub>2</sub>COOt-Bu), 28.1 (CH<sub>2</sub>PPh<sub>3</sub>) and 27.6 (CH<sub>3</sub>).

**IR:** ν [ppm] = 2876 (w), 2781 (w), 1715 (m), 1516 (w), 1436 (m), 1372 (w), 1288 (m), 1154 (s), 1111 (s), 996 (w), 944 (w), 881 (w), 837 (m), 748 (s), 718 (s), 685 (s).

**MS** (+EI) *m/z* (rel. intensity): calc. for C<sub>31</sub>H<sub>32</sub>O<sub>2</sub>P [M]<sup>+</sup>: 467.21; found: 467.16.

**Elemental analysis** [%]: calc. (C<sub>31</sub>H<sub>32</sub>BrO<sub>2</sub>P): C 68.01, H 5.89, Br 14.60; found: C 67.84, H 5.84, Br 13.73.

**Melting point:** 219 – 221 °C.

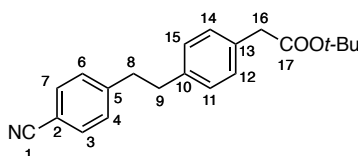
**1.3.1.9 TERT-BUTYL 2-(4-(4-CYANOSTYRYL)PHENYL)ACETATE (1.39)**

Chemical Formula: C<sub>21</sub>H<sub>21</sub>NO<sub>2</sub>  
 Exact Mass: 319.16  
 Molecular Weight: 319.40

A suspension of 7.50 g (13.7 mmol, 1.0 eq.) *tert*-butyl 2-(4-((bromotriphenyl-λ<sup>5</sup>-phosphaneyl)methyl)phenyl)acetate (**1.38**) in 40 mL of absolute tetrahydrofuran under argon atmosphere was stirred for 10 min at room temperature and then cooled to 0 °C. A 0.5 M solution of potassium bis(trimethylsilyl)amide (KHMDS) (2.73 g, 13.7 mmol, 1.0 eq.) in 27.4 mL abs. tetrahydrofuran and a solution of 1.80 g (13.7 mmol, 1.0 eq.) 4-cyanobenzaldehyde in 10 mL abs. tetrahydrofuran, both kept under argon atmosphere, were prepared in dried flasks. At first, the KHMDS solution was added to the cooled solution of **1.38** over a period of 15 min. The immediate formation of the ylide was indicated by a dark red color of the solution. After stirring for an additional 15 min, the 4-cyanobenzaldehyde solution

was added swiftly. The solution was then stirred for 2 hrs at 0 °C, subsequently warmed to room temperature and stirred over night. The reaction was aborted through addition of 100 mL of 1 M ammonium chloride solution and the organic solvent was removed under reduced pressure. The aqueous layer was extracted with 3 x 100 mL ethyl acetate and the united organic layers were dried with magnesium sulfate and the solvent removed under reduced pressure. The crude product was purified *via* flash chromatography on silica (eluent cHex/EtOAc 4:1) to give the slight yellow solid product (3.34 g, 10.5 mmol, 76%) as *cis/trans* (1:1.7) isomer mixture.

NMR atom numbering:



**<sup>1</sup>H-NMR** (400 MHz, CDCl<sub>3</sub>): ***cis*-1.39**  $\delta$  [ppm] = 7.48 (d,  $J$  = 8.6 Hz, 2H,  $H_{11}$ ,  $H_{13}$ ), 7.32 (d,  $J$  = 8.3 Hz, 2H,  $H_{10}$ ,  $H_{14}$ ), 7.30 (d,  $J$  = 8.4 Hz, 2H,  $H_4$ ,  $H_6$ ), 7.15 (d,  $J$  = 8.2 Hz, 2H,  $H_1$ ,  $H_3$ ), 6.54 (d,  $J$  = 12.3 Hz, 1H,  $H_7$ ), 6.27 (d,  $J$  = 12.3 Hz, 1H,  $H_8$ ), 3.50 (s, 2H,  $CH_2$ ) and 1.44 (s, 9H,  $CH_3$ ). ***trans*-1.39**  $\delta$  [ppm] = 7.61 (d,  $J$  = 8.6 Hz, 2H,  $H_{11}$ ,  $H_{13}$ ), 7.56 (d,  $J$  = 8.3 Hz, 2H,  $H_{10}$ ,  $H_{14}$ ), 7.48 (d,  $J$  = 8.4 Hz, 2H,  $H_4$ ,  $H_6$ ), 7.29 (d,  $J$  = 8.2 Hz, 2H,  $H_1$ ,  $H_3$ ), 7.19 (d,  $J$  = 16.3 Hz, 1H,  $H_7$ ), 7.06 (d,  $J$  = 16.3 Hz, 1H,  $H_8$ ), 3.54 (s, 2H,  $CH_2$ ) and 1.45 (s, 9H,  $CH_3$ ).

**<sup>13</sup>C-NMR** (100 MHz, CDCl<sub>3</sub>): ***cis*-1.39**  $\delta$  [ppm] = 170.7 (COOt-Bu), 142.2 (C<sub>9</sub>), 134.8 (C<sub>5</sub>), 134.5 (C<sub>2</sub>), 133.1 (C<sub>7</sub>), 132.2 (C<sub>11</sub>, C<sub>13</sub>), 129.6 (C<sub>4</sub>, C<sub>6</sub>), 129.5 (C<sub>1</sub>, C<sub>3</sub>), 128.9 (C<sub>10</sub>, C<sub>14</sub>), 128.3 (C<sub>8</sub>), 119.0 (C<sub>16</sub>), 110.5 (C<sub>12</sub>), 81.0 (C<sub>20</sub>), 42.4 (C<sub>15</sub>) and 28.1 (CH<sub>3</sub>). ***trans*-1.39**  $\delta$  [ppm] = 170.7 (COOt-Bu), 141.9 (C<sub>9</sub>), 135.2 (C<sub>2</sub>), 135.0 (C<sub>5</sub>), 132.5 (C<sub>11</sub>, C<sub>13</sub>), 132.1 (C<sub>7</sub>), 129.8 (C<sub>1</sub>, C<sub>3</sub>), 127.1 (C<sub>4</sub>, C<sub>6</sub>), 126.9 (C<sub>10</sub>, C<sub>14</sub>), 126.6 (C<sub>8</sub>), 119.1 (C<sub>16</sub>), 110.6 (C<sub>12</sub>), 81.1 (C<sub>20</sub>), 42.5 (C<sub>15</sub>) and 28.1 (CH<sub>3</sub>).

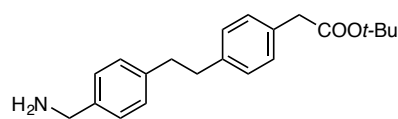
**IR:**  $\nu$  [ppm] = 3050 (w), 1728 (w), 1590 (w), 1483 (w), 1437 (m), 1189 (m), 1116 (s), 997 (w), 753 (w), 694 (vs).

**HRMS** (+EI)  $m/z$ : calc. for C<sub>21</sub>H<sub>21</sub>NO<sub>2</sub> [M]<sup>+</sup>: 319.1572; found: 319.1564. Calc. for C<sub>17</sub>H<sub>13</sub>NO<sub>2</sub><sup>+</sup> [M-*t*-Bu+H]<sup>+</sup>: 263.0946; found: 263.1012.

**Elemental analysis** [%]: calc. (C<sub>21</sub>H<sub>21</sub>NO<sub>2</sub>): C 78.97, H 6.63, N 4.39; found: C 78.78, H 6.76, N 4.34.

**R<sub>f</sub>** (cHex/EtOAc 3:1) = *trans* 0.64; *cis* 0.58.

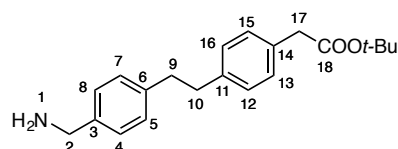
**Melting point:** 150 – 152 °C.

**1.3.1.10** *tert*-BUTYL 2-(4-(4-(AMINOMETHYL)PHENETHYL)PHENYL)ACETATE (**1.55**)

Chemical Formula: C<sub>21</sub>H<sub>27</sub>NO<sub>2</sub>  
 Exact Mass: 325.20  
 Molecular Weight: 325.45

In a large flask a solution of 9.20 g (28.8 mmol, 1.0 eq.) *tert*-butyl 2-(4-(4-cyanostyryl)phenyl)acetate (**1.39**) in mixture of 200 mL methanol/tetrahydrofuran (1:1) was prepared. To this solution 800 mg palladium on charcoal was added and the reaction flask was evacuated and purged three times with hydrogen through a mounted hydrogen balloon. The solution was stirred 36 hrs at room temperature and subsequently filtered through Hyflo<sup>®</sup> celite. The celite was rinsed with 100 mL methanol and the resulting filtrate was removed under reduced pressure. The product was obtained as colorless crystalline solid with almost quantitative yield (9.14 g, 28.1 mmol, 98%) and was used directly in the next reaction without further purification.

NMR atom numbering:



**<sup>1</sup>H-NMR** (400 MHz, DMSO-d<sub>6</sub>): δ [ppm] = 7.21 (m, 2H, *H*-ar.), 7.16 (m, 4H, *H*-ar.), 3.66 (s, 2H, *H*<sub>2</sub>), 3.49 (s, 2H, *H*<sub>17</sub>), 2.83 (s, 4H, *H*<sub>9</sub>, *H*<sub>10</sub>) and 1.39 (s, 9H, *CH*<sub>3</sub>).

**<sup>13</sup>C-NMR** (100 MHz, DMSO-d<sub>6</sub>): δ [ppm] = 172.6 (*COOt*-Bu), 141.6 (*C*<sub>6</sub>-q), 133.9 (*C*<sub>3</sub>-q), 130.7 (*C*<sub>11</sub>-q), 132.2 (*C*<sub>14</sub>-q), 129.0 (*C*<sub>4</sub>, *C*<sub>8</sub>), 128.3 (*C*<sub>5</sub>, *C*<sub>7</sub>), 128.0 (*C*<sub>12</sub>, *C*<sub>16</sub>), 126.9 (*C*<sub>13</sub>, *C*<sub>15</sub>), 45.4 (*C*<sub>2</sub>), 41.3 (*C*<sub>17</sub>), 36.8 (*C*<sub>9</sub>), 36.7 (*C*<sub>10</sub>) and 27.7 (*CH*<sub>3</sub>).

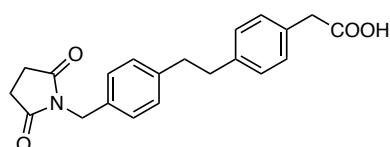
**IR:** ν [ppm] = 2981 (w), 2916 (w), 2226 (m), 1731 (s), 1606 (w), 1517 (w), 1455 (w), 1412 (w), 1368 (m), 1340 (m), 1226 (m), 1150 (s), 1021 (w), 938 (w), 872 (m), 828 (m), 744 (m), 721 (w), 691 (w).

**HRMS** (+ESI) *m/z*: calc. for C<sub>21</sub>H<sub>28</sub>O<sub>2</sub>N [M+H]<sup>+</sup>: 326.2115; found: 326.2167.

**Elemental analysis** [%]: calc. (C<sub>21</sub>H<sub>27</sub>NO<sub>2</sub>): C 77.50, H 8.36, N 4.30; found: C 77.24, H 8.37, N 4.26.

**R<sub>f</sub>** (cHex/EtOAc 1:1) = 0.01.

**Melting point:** 101 – 102 °C.

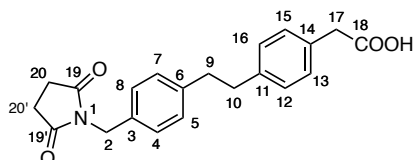
**1.3.1.11** 2-(4-(4-((2,5-DIOXOPYRROLIDIN-1-YL)METHYL)PHENETHYL)PHENYL)ACETIC ACID (**1.40**)

Chemical Formula: C<sub>21</sub>H<sub>21</sub>NO<sub>4</sub>  
 Exact Mass: 351.1471  
 Molecular Weight: 351.4020

To a solution of 2.60 g (8.00 mmol, 1.0 eq.) *tert*-butyl 2-(4-(4-(aminomethyl)phenethyl)phenyl)acetate (**1.55**) and 1.62 g (16.0 mmol, 2.0 eq.) succinic anhydride in 25 mL acetic acid was added a catalytic

amount of 4-(dimethylamino)pyridine. The solution was heated to 130 °C and stirred for 42 hrs. After cooling, the solvent was removed under reduced pressure and the residue was dissolved in 100 mL dichloromethane. The organic layer was washed with 1 x 100 mL sodium bicarbonate solution and 1 x 100 mL brine and then dried with magnesium sulfate. The product was yielded as colorless solid (2.27 g, 6.46 mmol, 81%) and was used in the next reaction without the need for further purification.

NMR atom numbering:



**<sup>1</sup>H-NMR** (400 MHz, CDCl<sub>3</sub>):  $\delta$  [ppm] = 7.31 (d,  $J$  = 8.0 Hz, 2H,  $H_4$ ,  $H_8$ ), 7.20 (d,  $J$  = 8.2 Hz, 2H,  $H_{13}$ ,  $H_{15}$ ), 7.15 (d,  $J$  = 8.2 Hz, 2H,  $H_{12}$ ,  $H_{16}$ ), 7.13 (d,  $J$  = 8.2 Hz, 2H,  $H_5$ ,  $H_7$ ), 4.63 (s, 2H,  $H_2$ ), 3.62 (s, 2H,  $H_{17}$ ), 2.87 (s, 4H,  $H_9$ ,  $H_{10}$ ) and 2.70 (s, 4H,  $H_{20}$ ,  $H_{20'}$ ).

**<sup>13</sup>C-NMR** (100 MHz, CDCl<sub>3</sub>):  $\delta$  [ppm] = 177.0 (C19, C19'), 177.0 (C18), 141.7 (C6-q), 140.9 (C11-q), 133.6 (C3-q), 131.1 (C14-q), 129.0 (C4, C8), 129.5 (C13, C15), 129.2 (C4, C8), 128.8 (C12, C16), 128.7 (C5, C7), 42.3 (C2), 40.6 (C17), 37.5 (C9, C10) and 28.4 (C20, C20').

**IR:**  $\nu$  [ppm] = 2921 (m), 1702 (s), 1606 (m), 1513 (m), 1414 (s), 1337 (m), 1245 (s), 1170 (s), 891 (m), 815 (m), 668 (m).

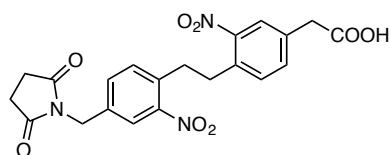
**HRMS** (+EI)  $m/z$ : calc. for C<sub>21</sub>H<sub>21</sub>NO<sub>4</sub> [M]<sup>+</sup>: 351.1471; found: 351.1154.

**Elemental analysis** [%]: calc. (C<sub>21</sub>H<sub>21</sub>NO<sub>4</sub>): C 71.78, H 6.02, N 3.99; found: C 71.32, H 6.11, N 3.96.

**R<sub>f</sub>** (cHex/EtOAc 3:1) = 0.1.

**Melting point:** 85 – 91 °C.

### 1.3.1.12 2-(4-(4-((2,5-DIOXOPYRROLIDIN-1-YL)METHYL)-2-NITROPHENETHYL)-3-NITROPHENYL)ACETIC ACID (1.41)

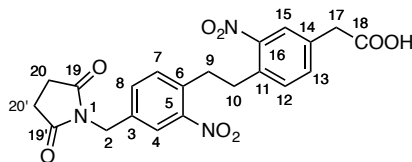


Chemical Formula: C<sub>21</sub>H<sub>19</sub>N<sub>3</sub>O<sub>8</sub>  
Exact Mass: 441.12  
Molecular Weight: 441.40

To 20 mL of sulfuric acid was added 1.56 g (3.83 mmol, 1.0 eq.) 2-(4-(4-((2,5-dioxopyrrolidin-1-yl)methyl)phenyl)phenyl)acetic acid (**1.40**) and the solution was stirred until the solid was dissolved (1 hr). To the solution was added portionwise 0.79 g (7.85 mmol, 2.1 eq.) potassium nitrate and then it was heated to 60 °C and stirred for 6 hrs. After cooling, the solution was poured into 100 mL of ice water and

the precipitate was filtered, washed with 1 x 100 mL water and dried. The product was yielded as pale brown solid (1.15 g, 2.60 mmol, 68%) and used in the next reaction without further purification.

NMR atom numbering:



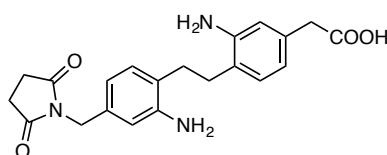
**<sup>1</sup>H-NMR** (200 MHz, DMSO-*d*<sub>6</sub>):  $\delta$  [ppm] = 7.83 (m, 2H, *H*<sub>4</sub>, *H*<sub>15</sub>), 7.50 (m, 4H, *H*<sub>6-8</sub>, *H*<sub>11-13</sub>), 4.60 (s, 2H, *H*<sub>2</sub>), 3.70 (s, 2H, *H*<sub>17</sub>), 3.08 (s, 4H, *H*<sub>9</sub>, *H*<sub>10</sub>) and 2.67 (s, 4H, *H*<sub>20</sub>, *H*<sub>20'</sub>).

**IR:**  $\nu$  [ppm] = 1702 (m), 1543 (s), 1401 (w), 1349 (m), 1170 (m), 912 (w), 820 (w), 722 (w), 667 (w).

**HRMS** (+ESI) *m/z*: calc. for C<sub>21</sub>H<sub>19</sub>N<sub>3</sub>O<sub>8</sub> [M+H]<sup>+</sup>: 442.1245; found: 442.1245.

**Melting point:** 99 – 104 °C.

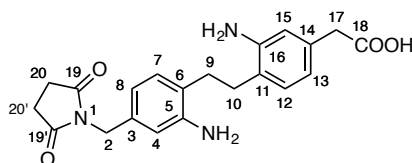
### 1.3.1.13 2-(3-AMINO-4-(2-AMINO-4-((2,5-DIOXOPYRROLIDIN-1-YL)METHYL)PHEN-ETHYL)PHENYL)ACETIC ACID (1.43)



Chemical Formula: C<sub>21</sub>H<sub>23</sub>N<sub>3</sub>O<sub>4</sub>  
Exact Mass: 381.17  
Molecular Weight: 381.43

In a large flask a solution of 1.00 g (2.88 mmol, 1.0 eq.) 2-(4-(4-((2,5-dioxopyrrolidin-1-yl)methyl)-2-nitrophenethyl)-3-nitrophenyl)acetic acid (**1.41**) in a mixture of 50 mL methanol/tetrahydrofuran (1:1) was prepared. To this solution 200 mg palladium on charcoal was added and the reaction flask was evacuated and purged three times with hydrogen through a mounted hydrogen balloon. The solution was stirred 24 hrs at room temperature and subsequently filtered through Hyflo<sup>®</sup> celite. The celite was rinsed with 50 mL methanol and the resulting filtrate was removed under reduced pressure. The product was obtained as colorless crystalline solid with almost quantitative yield (1.03 g, 2.71 mmol, 94%) and was used directly in the next reaction without further purification.

NMR atom numbering:

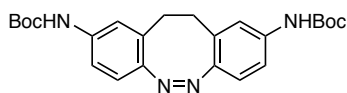


**<sup>1</sup>H-NMR** (400 MHz, DMSO-*d*<sub>6</sub>):  $\delta$  [ppm] = 7.32 (d, *J* = 7.9 Hz, 1H, *H*<sub>12</sub>), 7.26 (d, *J* = 7.9 Hz, 1H, *H*<sub>7</sub>), 7.13 (d, *J* = 1.8 Hz, 1H, *H*<sub>15</sub>), 7.08 (dd, *J* = 7.9, 1.7 Hz, 1H, *H*<sub>13</sub>), 7.03 (d, *J* = 1.8 Hz, 1H, *H*<sub>4</sub>), 6.97 (dd, *J* = 7.9, 1.8 Hz, 1H, *H*<sub>8</sub>), 4.49 (s, 2H, *H*<sub>2</sub>), 3.56 (s, 2H, *H*<sub>17</sub>), 2.80 (s, 4H, *H*<sub>9</sub>, *H*<sub>10</sub>) and 2.69 (s, 4H, *H*<sub>20</sub>, *H*<sub>20'</sub>).

**<sup>13</sup>C-NMR** (100 MHz, DMSO-*d*<sub>6</sub>):  $\delta$  [ppm] = 177.9 (C19, C19'), 172.9 (C18), 136.5 (C5-q), 135.3 (C3-q), 134.5 (C14-q), 133.8 (C16-q), 131.4 (C11-q), 130.6 (C6-q), 127.2 (C13), 123.6 (C8), 122.7 (C15), 119.7 (C4), 41.3 (C2), 40.6 (C17), 30.0 (C9), 29.7 (C10) and 28.6 (C20, C20').

**HRMS** (+ESI) *m/z*: calc. for C<sub>21</sub>H<sub>23</sub>N<sub>3</sub>O<sub>4</sub> [M+H]<sup>+</sup>: 382.1761; found: 382.1783.

#### 1.3.1.14 (Z)-Di-*tert*-butyl (11,12-dihydrodibenzo[*c,g*][1,2]diazocine-2,9-diyl)dicarbamate (**1.56**)



Chemical Formula: C<sub>24</sub>H<sub>30</sub>N<sub>4</sub>O<sub>4</sub>  
Exact Mass: 438.23  
Molecular Weight: 438.53

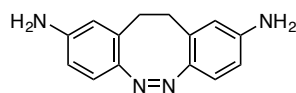
Xanthphos (6.6 mg, 11.5  $\mu$ mol, 10 mol%) and Pd<sub>2</sub>dba<sub>2</sub> (5.25 mg, 5.73  $\mu$ mol, 5 mol%) were transferred into a purged 10 mL Schlenk tube under argon atmosphere. The tube walls were washed down with 1.5 mL absolute dioxane, sealed, and both compounds could complex over 30 min at room temperature. *Tert*-butyl carbamate (85 mg, 0.75 mmol, 5.0 eq.), bisbromo diazocin **1.47** (42 mg, 14.7 mmol, 1.0 eq.), and cesium carbonate (286 mg, 0.882 mmol, 6.0 eq.) were added and an additional 1.5 mL of absolute dioxane was used to wash down the sides of the tube. The reaction vial was kept under argon pressure and heated to 100 °C for 15 min. After that the reaction vessel was sealed and kept at 100 °C for further 90 min. The reaction was cooled to room temperature and after addition of 15 mL water and 15 mL ethyl acetate the phases were thoroughly mixed, separated, and the aqueous layer was again extracted with 2 x 15 mL portions of ethyl acetate. The combined organic layers were washed with 2 x 15 mL portions of sodium bicarbonate, 3 x 15 mL portions of brine, dried with magnesium sulfate, filtered and concentrated *in vacuo*. The resulting crude product was purified on silica (eluent 0  $\rightarrow$  50% EtOAc/DCM) to yield 51.2 mg (11.7 mmol, 80%) of the pure product as a yellow green solid.

**<sup>1</sup>H-NMR** (600 MHz, CDCl<sub>3</sub>):  $\delta$  [ppm] = 7.14 (s, 2H, H1, H10), 7.04 (dd, *J* = 8.5, 2.3 Hz, 2H, H3, H8), 6.78 (d, *J* = 8.5 Hz, 2H, H4, H7), 2.04 (s, 4H, H13, H13') and 1.48 (s, 18H, CH<sub>3</sub>).

**<sup>13</sup>C-NMR** (150 MHz, CDCl<sub>3</sub>):  $\delta$  [ppm] = 122.4 (C4, C7), 114.3 (C1, C10), 112.4 (C3, C8) and 28.2 (C13, C13').

**HRMS** (+EI) *m/z*: calc. for C<sub>24</sub>H<sub>31</sub>N<sub>4</sub>O<sub>4</sub><sup>+</sup> [M+H]<sup>+</sup>: 439.2340; found: 439.2344. Calc. for C<sub>24</sub>H<sub>33</sub>N<sub>5</sub>O<sub>4</sub><sup>+</sup> [M+NH<sub>4</sub>]<sup>+</sup>: 456.2605; found: 456.2610.

#### 1.3.1.15 (Z)-11,12-Dihydrodibenzo[*c,g*][1,2]diazocine-2,9-diamine (**1.48**)



Chemical Formula: C<sub>14</sub>H<sub>14</sub>N<sub>4</sub>  
Exact Mass: 238.12  
Molecular Weight: 238.29

To a solution of 40.0 mg (0.92 mmol, 1.0 eq.) (*Z*)-di-*tert*-butyl (11,12-dihydrodibenzo[*c,g*][1,2]-diazocine-2,9-diyl)-dicarbamate (**1.56**) in 10 mL dichloromethane was added 0.5 mL anisole. After addition of 0.5 mL of trifluoroacetic acid the solution was stirred for 5 hrs at room temperature. The reaction was quenched by addition to an ice-cold sodium bicarbonate solution, the organic layer was separated and the aqueous phase was extracted with 2 x 10 mL dichloromethane. The united organic layers were dried with

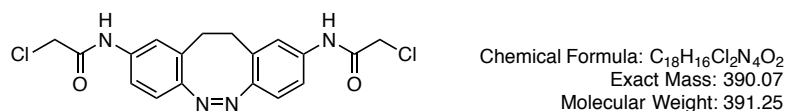
magnesium sulfate and the solvent was removed under reduced pressure. The crude product was purified via flash chromatography on silica (eluent DCM/MeOH 1:0 → 1:0.1) to give 15.4 mg (0.64 mmol, 70%) of the solid red product.

**<sup>1</sup>H-NMR** (400 MHz, DMSO-*d*<sub>6</sub>):  $\delta$  [ppm] = 6.54 (d, *J* = 8.3 Hz, 2H, *H*<sub>4</sub>, *H*<sub>7</sub>), 6.34 (dd, *J* = 8.4, 2.3 Hz, 2H, *H*<sub>3</sub>, *H*<sub>8</sub>), 5.07 (bs, 4H, *NH*<sub>2</sub>) and 6.22 (d, *J* = 2.4 Hz, 2H, *H*<sub>1</sub>, *H*<sub>10</sub>).

**<sup>13</sup>C-NMR** (100 MHz, DMSO-*d*<sub>6</sub>):  $\delta$  [ppm] = 156.3 (C5-q, C6-q), 144.1 (C3-q, C8-q), 130.3 (C1, C10), 118.3 (C11-q, C12-q), 113.9 (C2, C9), 105.1 (C4, C7) and 32.0 (C13).

**HRMS** (+EI) *m/z*: calc. for C<sub>14</sub>H<sub>15</sub>N<sub>4</sub><sup>+</sup> [M]<sup>+</sup>: 239.1291; found: 239.1291.

### 1.3.1.16 (Z)-N,N'-(11,12-DIHYDRODIBENZO[C,G][1,2]DIAZOCINE-2,9-DIYL)BIS(2-CHLOROACETAMIDE) (1.25)

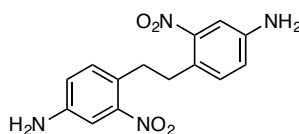


A solution of 30.1 mg (126  $\mu$ mol, 1.0 eq.) (Z)-11,12-dihydrodibenzo[c,g][1,2]diazocine-2,9-diamine (**1.48**) in 1.8 mL pyridine and 2.0 mL abs. tetrahydrofuran was kept under argon and was cooled to 0 °C. To this cold solution was added dropwise a solution of 85.8 mg (505  $\mu$ mol, 4.0 eq.) chloroacetic anhydride in 2.0 mL abs. tetrahydrofuran. The solution was warmed to room temperature and stirred for 1 hr. The solvents were removed under reduced pressure and the remaining oily residue was diluted with 10 mL ethyl acetate. The organic phase was washed with 2 x 10 mL water, dried with magnesium sulfate and evaporated. The crude product was purified through semi-preparative RP-HPLC with a water/acetonitrile gradient of 90:10 → 0:80 in 40 min and lyophilized to yield the product as fine yellow powder (27.1 mg, 69.3  $\mu$ mol, 55%).

**<sup>1</sup>H-NMR** (400 MHz, DMSO-*d*<sub>6</sub>):  $\delta$  [ppm] = 10.3 (s, 2H, *NH*), 7.35 (m, 4H, *H*<sub>1</sub>, *H*<sub>3</sub>, *H*<sub>8</sub>, *H*<sub>10</sub>), 6.34 (d, *J* = 9.0 Hz, 2H, *H*<sub>4</sub>, *H*<sub>7</sub>), 4.18 (s, 4H, CH<sub>2</sub>Cl) and 2.77 (m, 4H, *H*<sub>13</sub>, *H*<sub>13'</sub>).

**<sup>13</sup>C-NMR** (100 MHz, DMSO-*d*<sub>6</sub>):  $\delta$  [ppm] = 120.3 (C3, C8), 120.0 (C4, C7), 118.1 (C1, C10), 43.8 (CH<sub>2</sub>Cl), 31.5 (C13) and 31.4 (C13').

**HRMS** (+EI) *m/z*: calc. for C<sub>18</sub>H<sub>17</sub>Cl<sub>2</sub>N<sub>4</sub>O<sub>2</sub><sup>+</sup> [M+H]<sup>1+</sup>: 391.0723; found: 391.0724.

**1.3.1.17 4,4'-(ETHANE-1,2-DIYL)BIS(3-NITROANILINE) (1.57)**

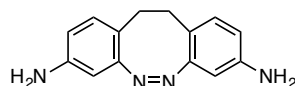
Chemical Formula: C<sub>14</sub>H<sub>14</sub>N<sub>4</sub>O<sub>4</sub>  
 Exact Mass: 302.10  
 Molecular Weight: 302.29

5.00 g (24.0 mmol, 1.0 eq.) 4,4'-(ethane-1,2-diyl)dianiline (**1.49**) was dissolved in 40 mL sulfuric acid and heated to 60 °C. 5.26 g (52.0 mmol, 2.2 eq.) freshly grounded potassium nitrate was dissolved in 45 mL sulfuric acid and then slowly added to the first solution. The reaction was then kept at 60 °C for 6 hrs. The solution was poured into 200 mL of ice water and made basic with aqueous ammonia solution (32%). The formed precipitate was filtered off, washed with 500 mL water and dried to afford the product as red orange solid (7.20 g, 23.6 mmol, 99%).

**<sup>1</sup>H-NMR** (400 MHz, DMSO-d<sub>6</sub>):  $\delta$  [ppm] = 7.06 (d,  $J$  = 2.4 Hz, 2H,  $H_2$ ), 6.99 (d,  $J$  = 8.3 Hz, 1H,  $H_5$ ), 6.78 (dd,  $J$  = 8.3, 2.4 Hz, 2H,  $H_5$ ), 5.58 (s, 4H,  $H$ -NH<sub>2</sub>) and 2.86 (s, 4H,  $H_7$ ).

**<sup>13</sup>C-NMR** (100 MHz, DMSO-d<sub>6</sub>):  $\delta$  [ppm] = 149.9 (C3), 148.6 (C1), 136.7 (C3), 132.9 (C5), 121.8 (C4), 119.2 (C6), 108.4 (C2) and 33.2 (C7).

**HRMS** (+EI)  $m/z$ : calc. for C<sub>14</sub>H<sub>14</sub>N<sub>4</sub>O<sub>4</sub><sup>+</sup> [M]<sup>+</sup>: 302.1015; found: 302.1015. Calc. for C<sub>14</sub>H<sub>10</sub>N<sub>2</sub>O<sub>2</sub><sup>+</sup> [M-NO<sub>2</sub>]<sup>+</sup>: 256.1086; found: 256.1067.

**1.3.1.18 (Z)-11,12-DIHYDRODIBENZO[C,G][1,2]DIAZOCINE-3,8-DIAMINE (1.50)**

Chemical Formula: C<sub>14</sub>H<sub>14</sub>N<sub>4</sub>  
 Exact Mass: 238.12  
 Molecular Weight: 238.29

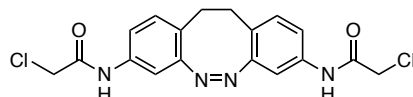
A solution of 1.00 g (3.31 mmol, 1.0 eq.) 4,4'-(ethane-1,2-diyl)bis(3-nitroaniline) (**1.57**) in 200 mL of ethanol was heated to 40 °C. Then a solution of 4.20 g (13.3 mmol, 4.0 eq.) Ba(OH)<sub>2</sub> · 6 H<sub>2</sub>O in 40 mL water was added, followed by the portionswise addition 3.40 g (52.0 mmol, 15.6 eq.) zinc. The solution was kept 3 hrs under reflux (80 °C) and after cooling was filtered through celite to remove the zinc. After removal of the solvent under reduced pressure, the crude product was purified via flash chromatography on silica (eluent cHex/EtOAc 1:2) to give 0.33 g (1.40 mmol, 40%) of the solid yellow orange product.

**<sup>1</sup>H-NMR** (400 MHz, CDCl<sub>3</sub>): **cis-1.50**  $\delta$  [ppm] = 6.73 (d,  $J$  = 8.1 Hz, 2H,  $H_1$ ,  $H_{10}$ ), 6.34 (dd,  $J$  = 8.1, 2.4 Hz, 1H,  $H_2$ ,  $H_9$ ), 6.40 (d,  $J$  = 2.4 Hz, 2H,  $H_4$ ,  $H_7$ ) and 2.70 (m, 4H,  $H_{13}$ ,  $H_{13}'$ ). **trans-1.50**  $\delta$  [ppm] = 6.76 (d,  $J$  = 8.2 Hz, 2H,  $H_1$ ,  $H_{10}$ ), 6.48 (dd,  $J$  = 8.1, 2.4 Hz, 1H,  $H_2$ ,  $H_9$ ), 6.34 (dd,  $J$  = 8.3, 2.4 Hz, 1H,  $H_4$ ), 6.34 (dd,  $J$  = 8.3, 2.4 Hz, 1H,  $H_7$ ) and 2.90 (m, 4H,  $H_{13}$ ,  $H_{13}'$ ).

**<sup>13</sup>C-NMR** (100 MHz, CDCl<sub>3</sub>): **cis-1.50**  $\delta$  [ppm] = 156.3 (C5-q, C6-q), 144.1 (C3-q, C8-q), 130.3 (C1, C10), 118.3 (C11-q, C12-q), 113.9 (C2, C9), 105.1 (C4, C7) and 31.0 (C13). **trans-1.50**  $\delta$  [ppm] = 146.5 (C5-q, C6-q), 145.3 (C3-q, C8-q), 131.4 (C1, C10), 121.5 (C11-q, C12-q), 116.9 (C2, C9), 114.1 (C7), 108.0 (C4) and 31.0 (C13).

**HRMS** (+EI)  $m/z$  (rel. intensity): calc. for  $C_{14}H_{13}N_2^{3+}$   $[M-2NH_2+3H]^{3+}$ : 209.1062; found: 209.1078. Calc. for  $C_{14}H_{14}N_4^+$   $[M]^+$ : 238.1218; found: 238.1213.

**1.3.1.19 (Z)-N,N'-(11,12-Dihydrodibenzo[c,g][1,2]diazocine-3,8-diyl)bis(2-chloroacetamide)**  
**(1.29)**



Chemical Formula:  $C_{18}H_{16}Cl_2N_4O_2$   
Exact Mass: 390.07  
Molecular Weight: 391.25

A solution of 37.3 mg (156  $\mu$ mol, 1.0 eq.) (Z)-11,12-dihydrodibenzo[c,g][1,2]diazocine-3,8-diamine (**1.50**) in 1.8 mL pyridine and 2.0 mL absolute tetrahydrofuran was kept under argon atmosphere and was cooled to 0 °C. To this cold solution was added dropwise a solution of 107 mg (630  $\mu$ mol, 4.0 eq.) chloroacetic anhydride in 2.0 mL absolute tetrahydrofuran. The solution was warmed to room temperature and stirred for 1 hr. The solvents were removed under reduced pressure and the remaining oily residue was diluted with 10 mL ethyl acetate. The organic phase was washed with 2 x 10 mL water, dried with magnesium sulfate and evaporated. The crude product was purified through semi-preparative RP-HPLC with a water/acetonitrile gradient of 90:10  $\rightarrow$  0:80 in 40 min and lyophilized to yield the product as fine yellow powder (25.7 mg, 65.7  $\mu$ mol, 42%).

**$^1H$ -NMR** (400 MHz, DMSO- $d_6$ ):  $\delta$  [ppm] = 10.2 (s, 2H,  $H$ -NH), 7.11 (dd,  $J$  = 8.2, 2.2 Hz, 2H,  $H_2$ ,  $H_9$ ), 7.08 (d,  $J$  = 2.1 Hz, 2H,  $H_4$ ,  $H_7$ ), 6.96 (d,  $J$  = 8.2 Hz, 2H,  $H_1$ ,  $H_{10}$ ), 4.10 (s, 4H,  $H$ -CH $_2$ Cl) and 2.67 (m, 4H,  $H_{13}$ ,  $H_{13}'$ ).

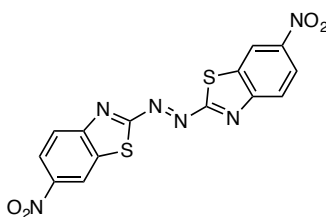
**$^{13}C$ -NMR** (100 MHz, DMSO- $d_6$ ):  $\delta$  [ppm] = 130.8 (C1, C10), 118.4 (C2, C9), 109.0 (C4, C7), 44.0 (CH $_2$ Cl) and 30.8 (C13).

**IR:**  $\nu$  [ppm] = 3292 (m), 3003 (w), 2956 (w), 1657 (s), 1582 (s), 1520 (s), 1401 (s), 1276 (m), 1251 (m), 1138 (w), 970 (w), 878 (m), 844 (m), 776 (s), 699 (m).

**HRMS** (+ESI)  $m/z$  (rel. intensity): calc. for  $C_{18}H_{20}O_2N_5Cl_2^+$   $[M+NH_4]^+$ : 408.0994; found: 408.0990 (100). Calc. for  $C_{18}H_{17}O_2N_4Cl_2^+$   $[M+H]^+$ : 391.0723; found: 391.0726 (46).

**$R_t$**  (an. RP-HPLC, Luna column, water/acetonitrile gradient 90:10  $\rightarrow$  0:80 in 40 min):  $t$  [min] = 25.6 min.

**Melting point:** 233 – 236 °C.

**1.3.1.20 (E)-1,2-Bis(6-nitrobenzo[D]thiazol-2-yl)diazene (1.52)**

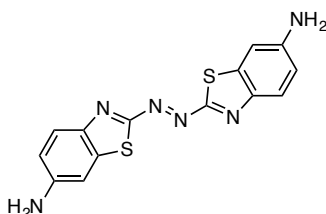
Chemical Formula: C<sub>14</sub>H<sub>8</sub>N<sub>6</sub>O<sub>4</sub>S<sub>2</sub>  
 Exact Mass: 385.99  
 Molecular Weight: 386.36

A suspension of 1.00 g (2.60 mmol, 1.0 eq.) 2-amino-6-nitrobenzothiazole (**1.51**) in 50 mL sodium hypochlorite solution (13%) was heated to 60 °C for 1 hr. The reaction could cool down and the red precipitate was filtered off, washed with 3 x 50 mL water and 3 x 50 mL diethyl ether and dried. The crude red product was received as red solid (830 mg, 2.15 mmol, 90%) and due to the low solubility, it was directly used in the next reaction.

**IR:**  $\nu$  [ppm] = 3098 (w), 1566 (m), 1511 (s), 1347 (s), 1279 (m), 1198 (m), 1122 (m), 1042 (w), 915 (m), 896 (m), 839 (m), 752 (m), 720 (m).

**HRMS** (+EI)  $m/z$  (rel. intensity): calc. for C<sub>14</sub>H<sub>7</sub>N<sub>5</sub>O<sub>3</sub>S<sub>2</sub><sup>+</sup> [M-NO+H]<sup>+</sup>: 356.9990; found: 357.9819 (35).

**Melting point:** >300 °C.

**1.3.1.21 (E)-2,2'-(Diazene-1,2-diyl)bis(benzo[D]thiazol-6-amine) (1.58)**

Chemical Formula: C<sub>14</sub>H<sub>10</sub>N<sub>6</sub>S<sub>2</sub>  
 Exact Mass: 326.04  
 Molecular Weight: 326.40

To a solution of 2.00 g (5.18 mmol, 1.0 eq.) (*E,Z*)-1,2-bis(6-nitrobenzo[d]thiazol-2-yl)diazene (**1.52**) in 125 mL tetrahydrofuran was added 5.02 g (41.4 mmol, 8.0 eq.) sodium sulfide in 20 mL water. The solution was heated to 80 °C and stirred for 3 hrs. After cooling the solution was made basic with 200 mL sodium hydrogencarbonate solution (10%) and the precipitate was filtered off, washed with 2 x 200 mL water and dried. The received product was a dark blue solid (1.46 g, 4.47 mmol, 86%) and was used directly in the next reaction without further purification.

**<sup>1</sup>H-NMR** (400 MHz, DMSO-d<sub>6</sub>):  $\delta$  [ppm] = 7.79 (d,  $J$  = 8.9 Hz, 2H, *H*8), 7.04 (d,  $J$  = 2.3 Hz, 2H, *H*5), 6.89 (dd,  $J$  = 9.0, 2.0 Hz, 2H, *H*7) and 6.40 (s, 4H, *H*-NH<sub>2</sub>).

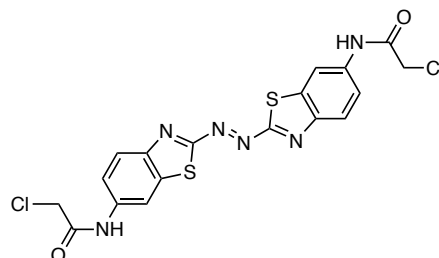
**<sup>13</sup>C-NMR** (100 MHz, DMSO-d<sub>6</sub>):  $\delta$  [ppm] = 151.5 (C2), 146.2 (C4-q), 138.6 (C6-q), 126.7 (C8), 117.2 (C7) and 103.6 (C5).

**IR:**  $\nu$  [ppm] = 3406 (w), 3306 (w), 3200 (w), 1631 (m), 1592 (m), 1544 (m), 1475 (m), 1428 (m), 1337 (m), 1280 (s), 1202 (s), 1131 (s), 915 (s), 850 (s), 804 (s), 695 (s).

**HRMS** (+EI) *m/z*: calc. for  $C_{14}H_{10}N_4S_2^{2+}$  [ $M-2NH_2+2H$ ] $^{2+}$ : 298.0336; found: 298.0313. Calc. for  $C_{14}H_{10}N_6S_2^+$  [ $M$ ] $^+$ : 326.0408; found: 326.0395.

**Melting point**: >300 °C.

### 1.3.1.22 (*E*)-*N,N'*-(DIAZENE-1,2-DIYL)BIS(BENZO[D]THIAZOLE-2,6-DIYL)BIS(2-CHLOROACETAMIDE) (**1.30**)



Chemical Formula:  $C_{18}H_{12}Cl_2N_6O_2S_2$   
Exact Mass: 477.98  
Molecular Weight: 479.35

100  $\mu$ L (1.25 mmol, 4 eq.) of chloroacetyl chloride in 5 mL dimethylformamide was cooled to 0 °C. A solution of 100 mg (0.31 mmol, 1.0 eq.) (*E*)-2,2'-(diazene-1,2-diyl)bis(benzo[d]thiazol-6-amine) (**1.58**) in 5 mL DMF and 173  $\mu$ L triethylamine (1.25 mmol, 4.0 eq.) was added dropwise to the cooled first solution. The reaction could warm to room temperature and was subsequently stirred for 2 hrs. The reaction was stopped by addition of 50 mL water and the solution was acidified with 2 M HCl. The precipitated product was filtered off, washed with 2 x 50 mL water and dried. The crude product was purified through flash chromatography on silica (eluent 0  $\rightarrow$  50% EtOAc/DCM) and the pure product was received as a dark purple solid (92.0 mg, 0.21 mmol, 64%).

**$^1H$ -NMR** (400 MHz, DMSO- $d_6$ ):  $\delta$  [ppm] = 10.8 (s, 1H, *H*-NH), 8.57 (d, *J* = 8.2, 2.2 Hz, 2H, *H*8), 8.17 (d, *J* = 9.0 Hz, 2H, *H*5), 7.67 (d, *J* = 9.0, 2.2 Hz, 2H, *H*7) and 4.32 (s, 4H, *H*-CH<sub>2</sub>Cl).

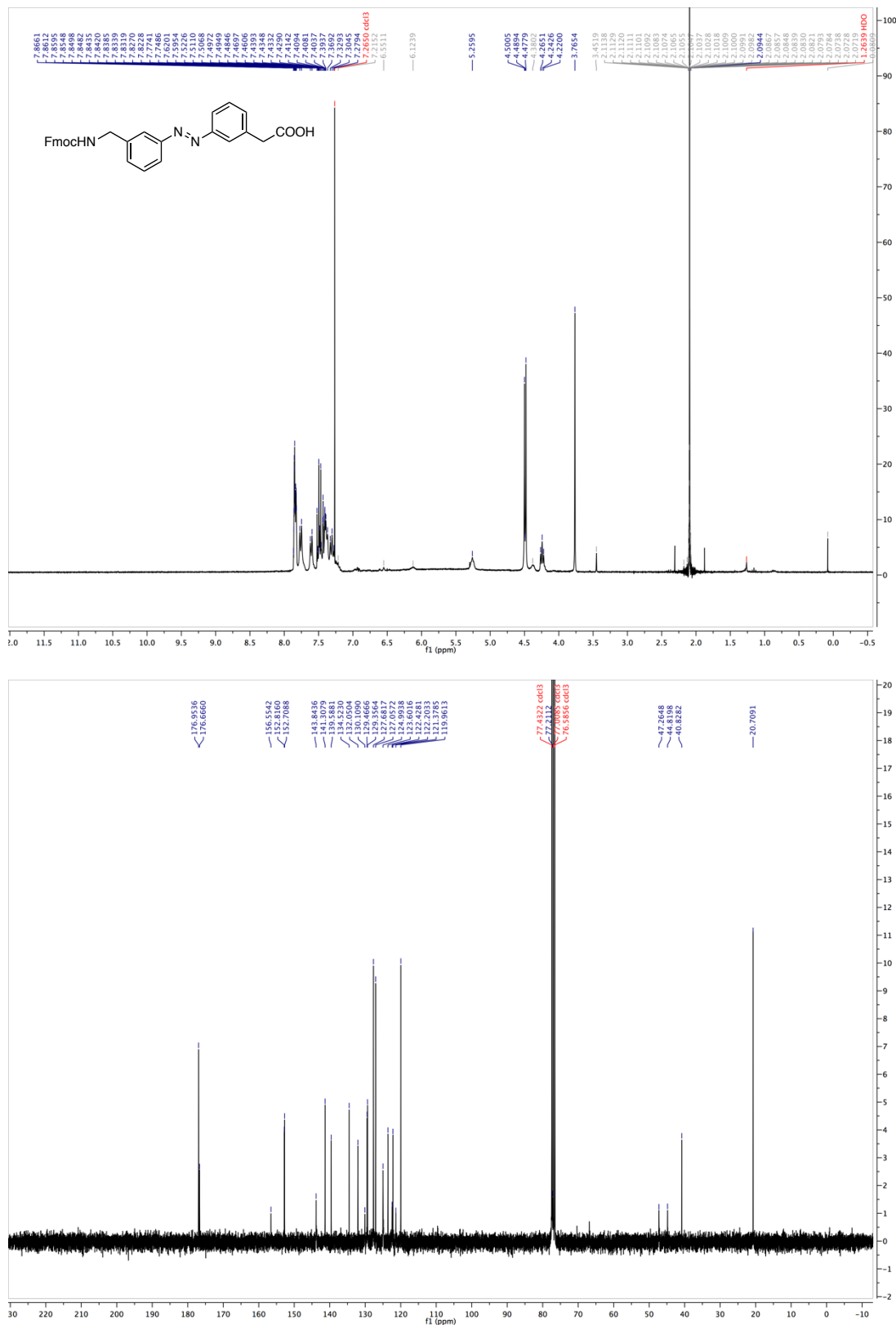
**$^{13}C$ -NMR** (100 MHz, DMSO- $d_6$ ):  $\delta$  [ppm] = 172.4 (C2), 165.6 (C=O), 149.8 (C9), 139.9 (C6), 136.6 (C4), 126.5 (C8), 120.7 (C7), 112.3 (C5) and 44.0 (CH<sub>2</sub>Cl).

**IR**:  $\nu$  [ppm] = 3256 (w), 1684 (s), 1602 (s), 1567 (s), 1529 (s), 1480 (s), 1402 (s), 1336 (m), 1289 (m), 1253 (m), 1130 (s), 869 (m), 816 (m), 784 (m), 689 (m).

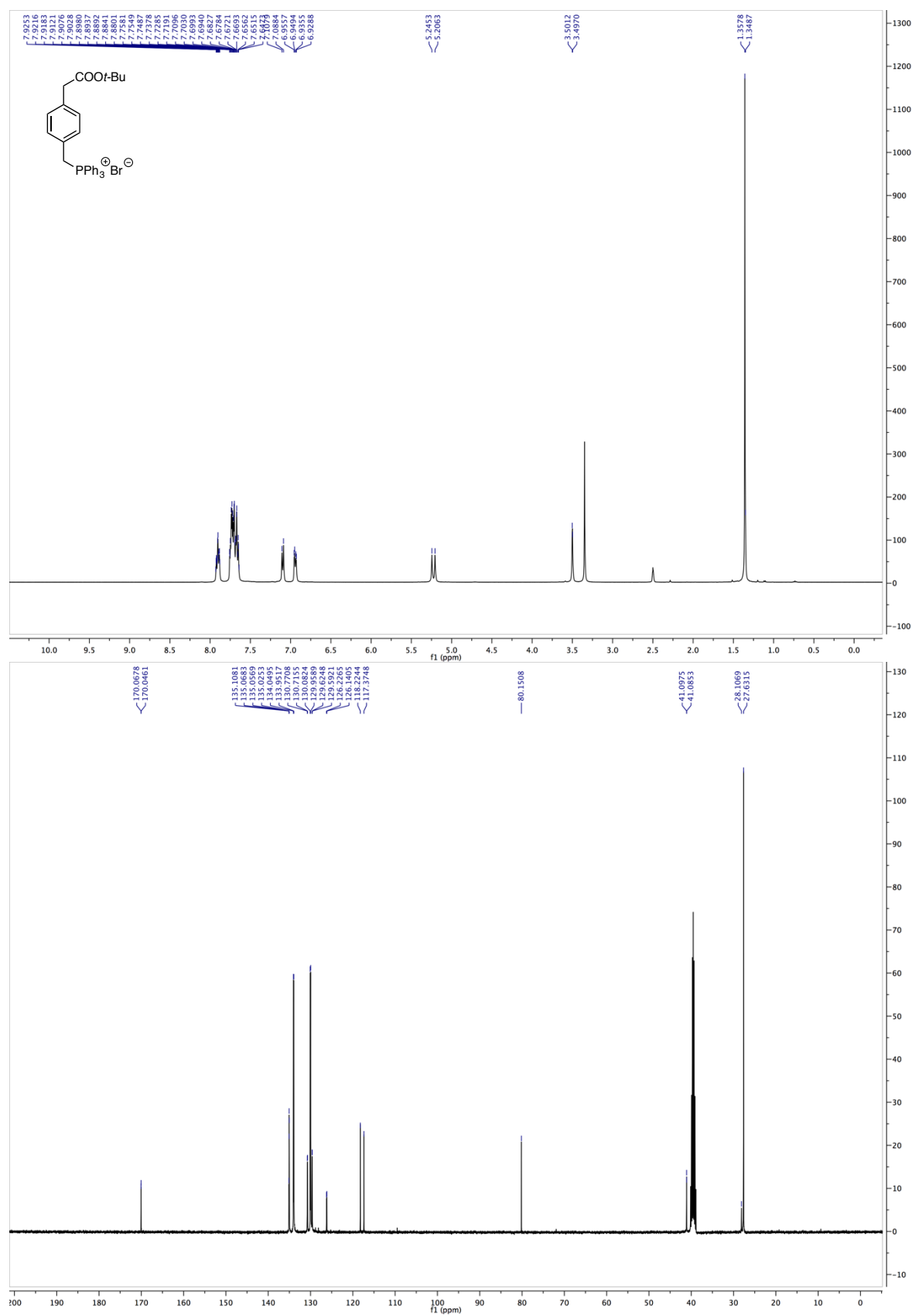
**HRMS** (+ESI) *m/z* (rel. intensity): calc. for  $C_{18}H_{13}Cl_2N_6O_2S_2^+$  [ $M+H$ ] $^+$ : 478.9913; found: 478.9920.

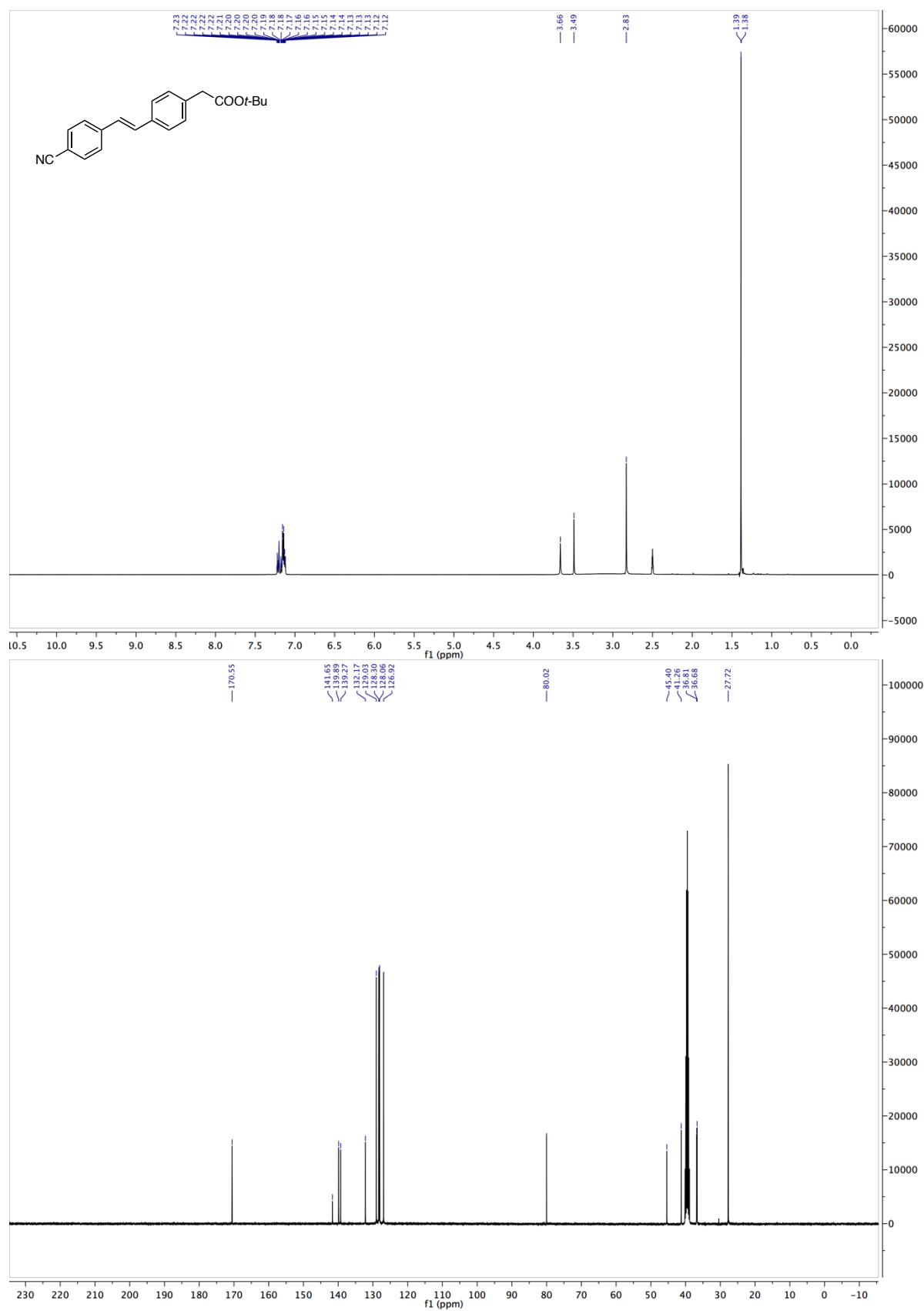
**Melting point**: >300 °C.

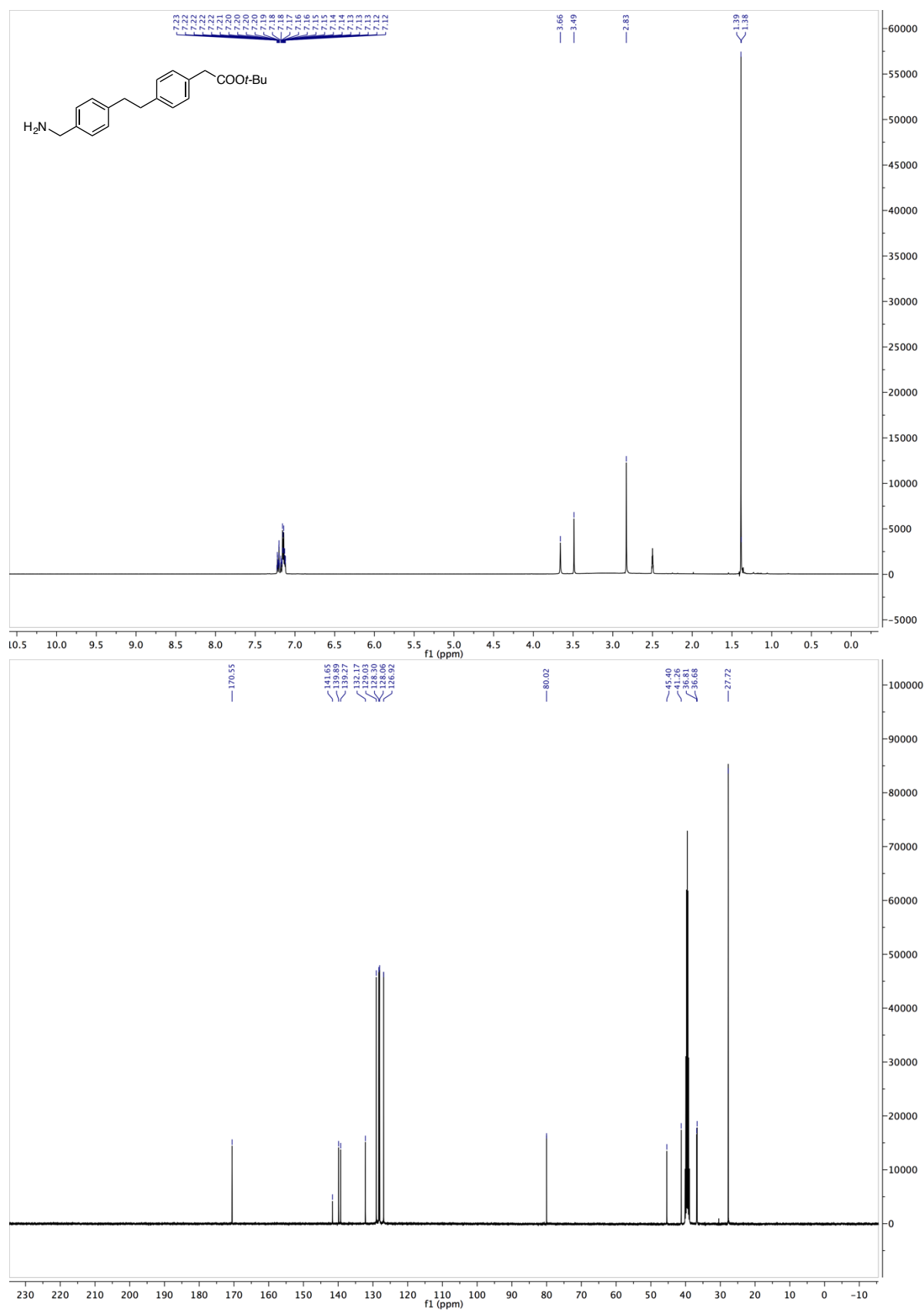
## 1.3.2 SPECTRAL DATA

1.3.2.1  $^1\text{H}$ - AND  $^{13}\text{C}$ -NMR SPECTRA OF AMPP, 3-[3-(AMINOMETHYL)PHENYLAZO]-PHENYLACETIC ACID (1.26)

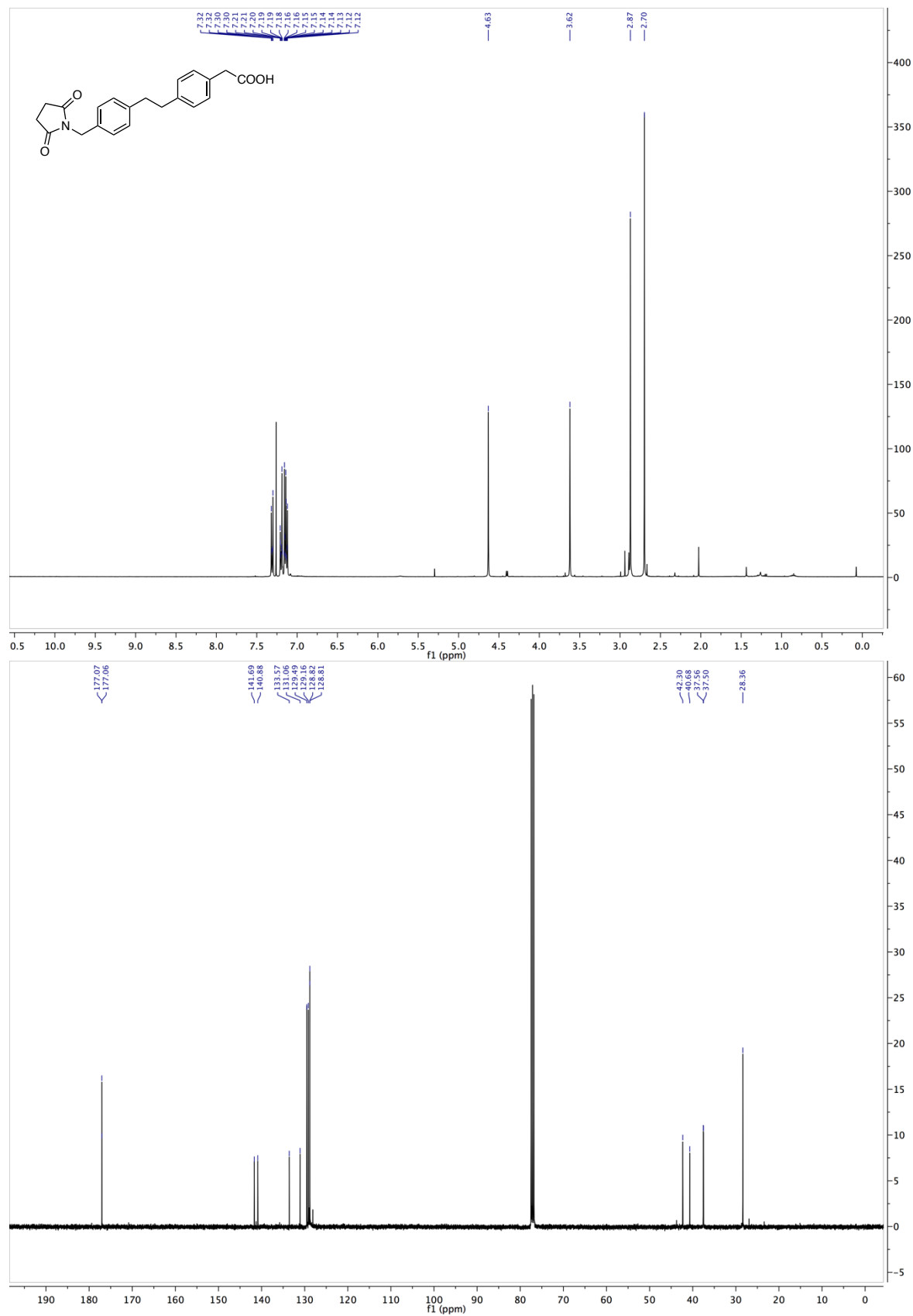
### 1.3.2.2 <sup>1</sup>H- AND <sup>13</sup>C-NMR SPECTRA OF *TERT*-BUTYL 2-(4-((BROMOTRIPHENYLPHOSPHANEYL)-METHYL)PHENYL)ACETATE (1.38)



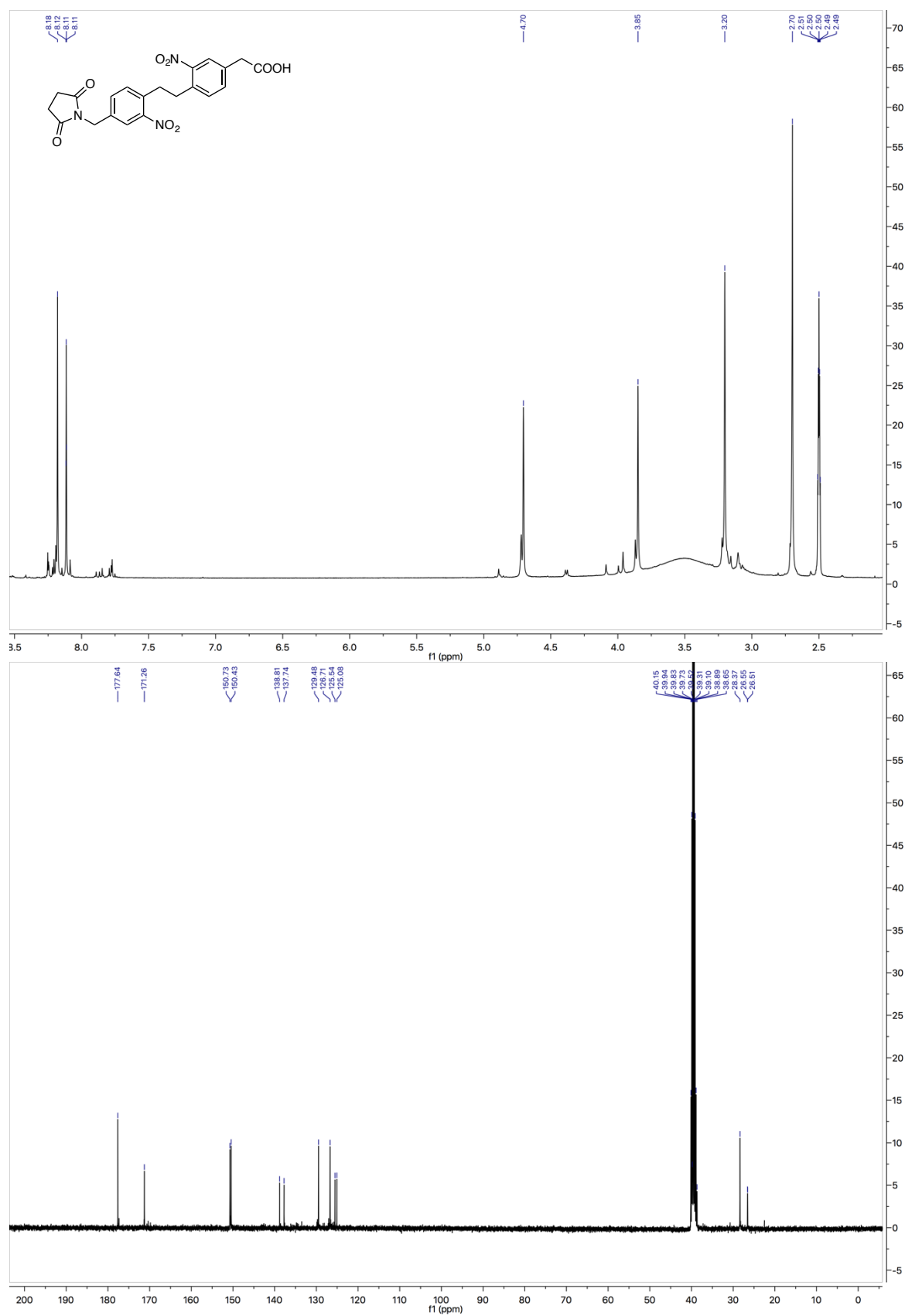
1.3.2.3  $^1\text{H}$ - AND  $^{13}\text{C}$ -NMR SPECTRA OF *TERT*-BUTYL 2-(4-(4-CYANOSTYRYL)PHENYL)ACETATE (1.39)

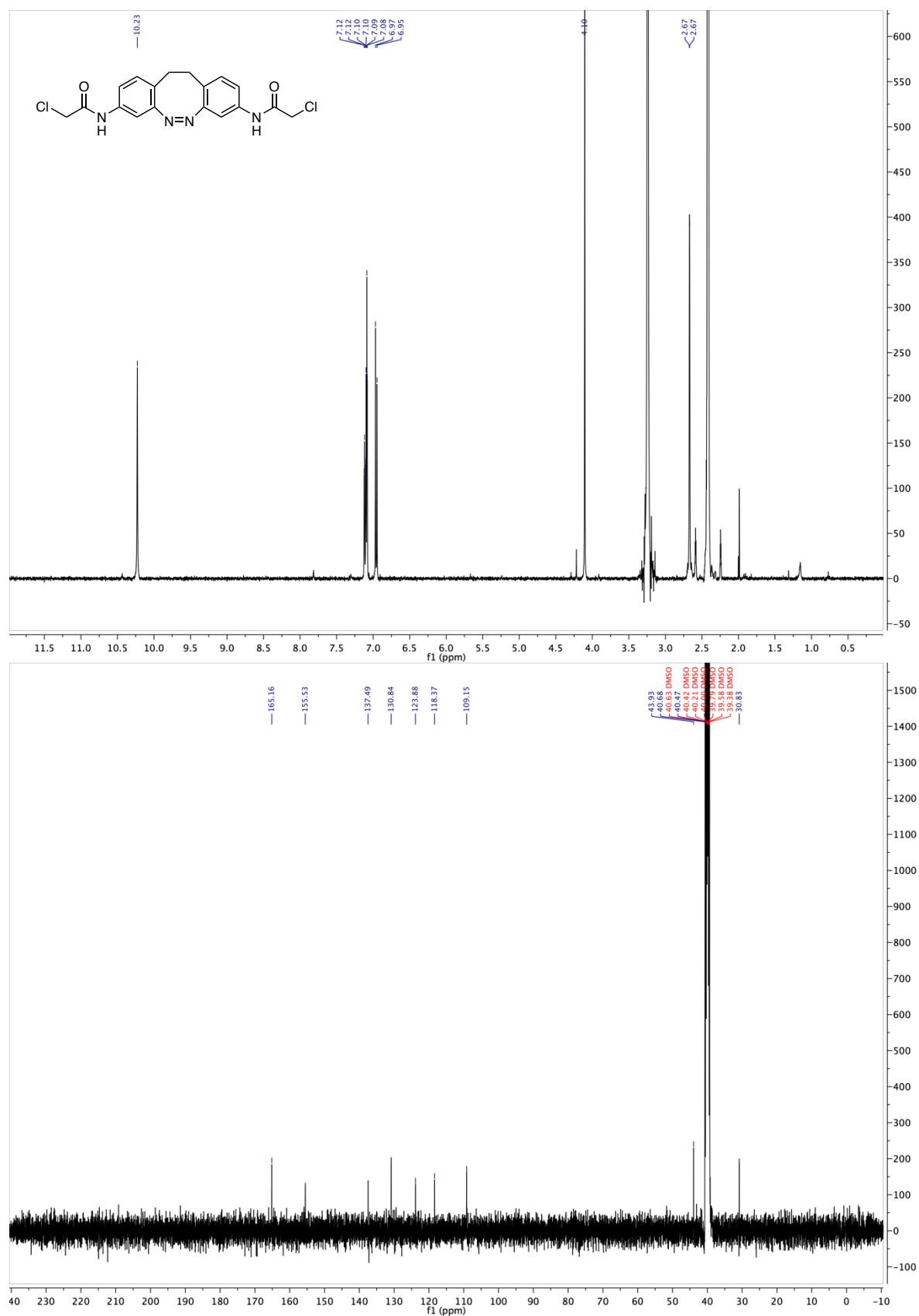
**1.3.2.4  $^1\text{H}$ - AND  $^{13}\text{C}$ -NMR SPECTRA OF *TERT*-BUTYL 2-(4-(4-(AMINOMETHYL)PHENETHYL)-PHENYL)-ACETATE (1.55)**

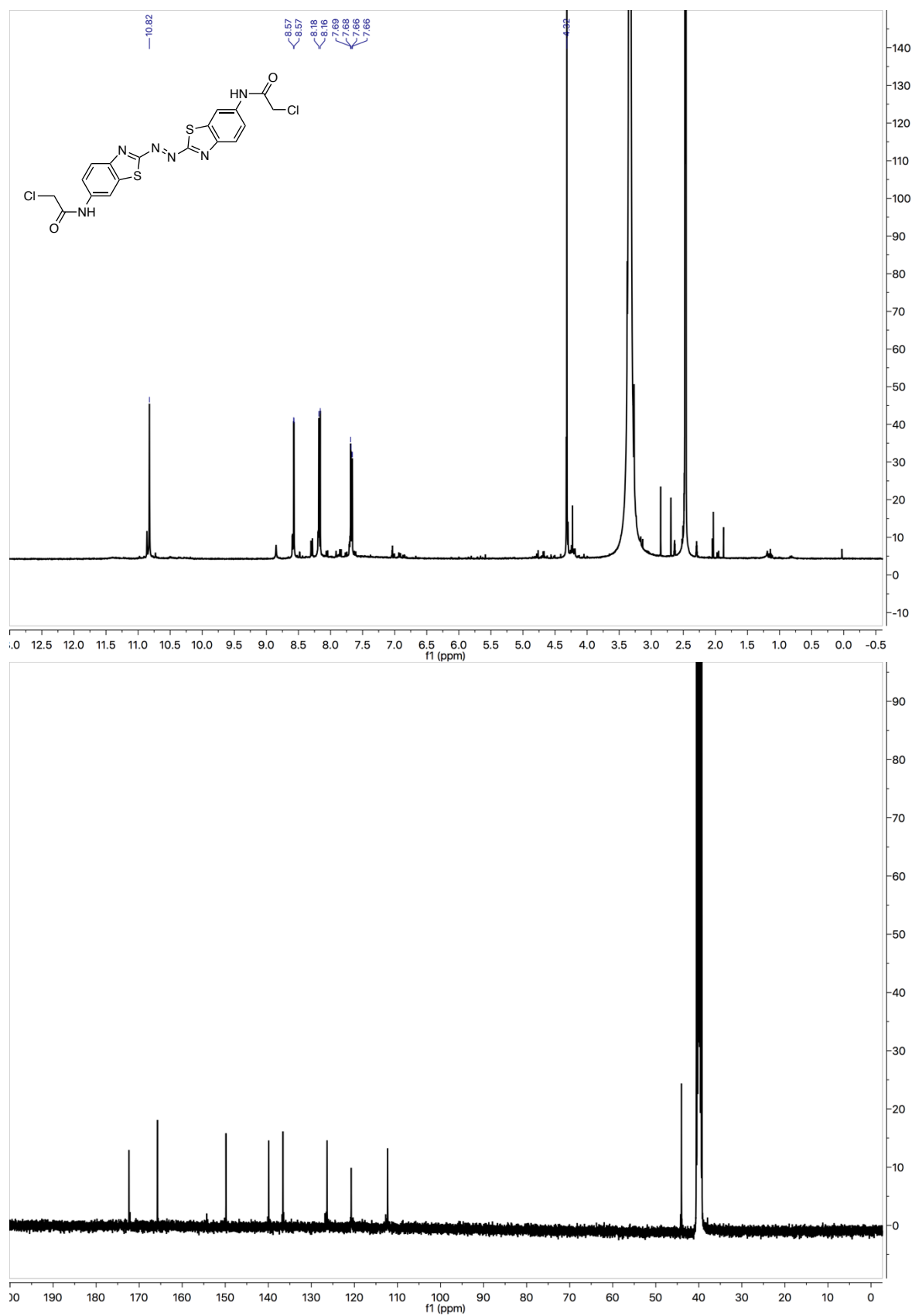
### 1.3.2.5 $^1\text{H}$ - AND $^{13}\text{C}$ -NMR SPECTRA OF 2-(4-(4-((2,5-DIOXOPYRROLIDIN-1-YL)METHYL)-PHENETHYL)PHENYL)ACETIC ACID (1.40)



### 1.3.2.6 $^1\text{H}$ - AND $^{13}\text{C}$ -NMR SPECTRA OF 2-(4-(4-((2,5-DIOXOPYRROLIDIN-1-YL)METHYL)-2-NITROPHENETHYL)-3-NITROPHENYL)ACETIC ACID (1.41)



**1.3.2.7  $^1\text{H}$ - AND  $^{13}\text{C}$ -NMR SPECTRA OF *M*-BDCA, (*Z*)-*N,N'*-(11,12-DIHYDRODIBENZO-[*C,G*][1,2]-DIAZOCINE-3,8-DIYL)BIS(2-CHLOROACETAMIDE) (1.29)**

**1.3.2.8  $^1\text{H}$ - AND  $^{13}\text{C}$ -NMR SPECTRA OF ACTA, (*E*)-*N,N'*-(DIAZENE-1,2-DIYL)BIS(BENZO-[*D*]THIAZOLE-2,6-DIYL)BIS(2-CHLOROACETAMIDE) (1.30)**

PART II  
PHOTOPHARMACOLOGY

## PART II: PHOTOPHARMACOLOGY AND TETHERED PHARMACOLOGY

The world as we know it today would not exist if it was not for the invention and advancement of pharmacotherapy<sup>7,97</sup>. It improves the everyday life of millions of people and is a major driving force for medicinal development and progress. Despite significant improvements to drug reliability, selectivity and therapy over the preceding centuries, there are still many issues remaining in pharmacotherapy that need to be addressed. Two major complications are the low selectivity of many therapeutically used drugs<sup>98</sup> and the risk of forming drug resistance<sup>5,99,100</sup>. Especially the latter, in view of mankind's failure of a sustainable use of antibiotics leading to raising numbers of resistant bacteria strains, has increasingly become a public and governmental health care focus<sup>99,101,102</sup>. The low selectivity of drugs can lead to severe side effects, limits the desired efficacy at the targeted site of action and raises challenges for drug administration<sup>17,98</sup>. Moreover, it causes a lowered toxicity threshold and leads to narrowing of the therapeutic window, which in turn prevents usage of optimal drug dosage<sup>5,103</sup>. This has far-reaching consequences for present drug development, as an estimated 85% of small molecule drugs are discarded due to insufficient selectivity<sup>104</sup>. This means many pharmaceuticals, although attractive and powerful candidates for pharmacotherapy, are not considered for further development only due to their low selectivity. Furthermore, recent systems biology studies also suggest the rethinking of pharmaceuticals as exquisitely selective compounds, but as multitarget network drugs simultaneously acting on several sites and tissues. Multitargeting drugs were shown, although case dependent, to exhibit higher clinical efficacy compared to single target drugs<sup>8</sup>. These polypharmacology findings complicate future developments in pharmacotherapy once more, as they show the demand for dynamically-selective, multiple system targeting drugs, which orchestrate complex physiological responses without triggering side effects.

The reason for poor drug selectivity often lies in their affinity for other targets and uncontrolled drug activity in space and time, *e.i.* antibiotic activity outside the desired field of action. Although there are ways to reach higher selectivity, *i.e.* local administration of the drugs like in ophthalmology<sup>105</sup>, or choosing targets which are exclusively expressed in selected tissues or overexpressed in certain diseases<sup>17,106</sup>, these approaches are not generally amenable. The targeted systems are normally expressed in several organs throughout the organism and disease related overexpression of drug targets is not a reliable drug targeting device, as seen for the severe side effects caused by many cancer therapeutics<sup>107–109</sup>.

Currently, there are three major fields that utilize light to control physiological responses and/or drug actions, namely optogenetics<sup>3,110,111</sup>, photodynamic therapy<sup>112,113</sup> and photopharmacology<sup>4,5,17</sup> (Figure II.1). Optogenetics makes use of natural occurring photoresponsive proteins such as bacteriorhodopsins, halorhodopsins or flavoproteins<sup>36,114,115</sup>. This method was successfully used to restore visual responses in blind retinæ<sup>6</sup> and to control the brain function<sup>3,116</sup> and the movement of animals<sup>37,117</sup>. Since genetic manipulation is a necessity for optogenetics, they are currently limited to being research tools for the understanding of biological processes. Photodynamic therapy deploys photosensitive dyes that transfer energy from their excited triplet states after illumination with visible light to triplet oxygen, to generate singlet oxygen ( $^3\text{O}_2 \rightarrow ^1\text{O}_2$ ). The formation of singlet oxygen as reactive oxygen species (ROS) leads to cell

damage and death in photosensitizer containing and surrounding cells. The targeted destruction of cells limits this method to applications where cell death is desirable, for example in cancer therapy or the treatment of infected tissue<sup>118</sup>.

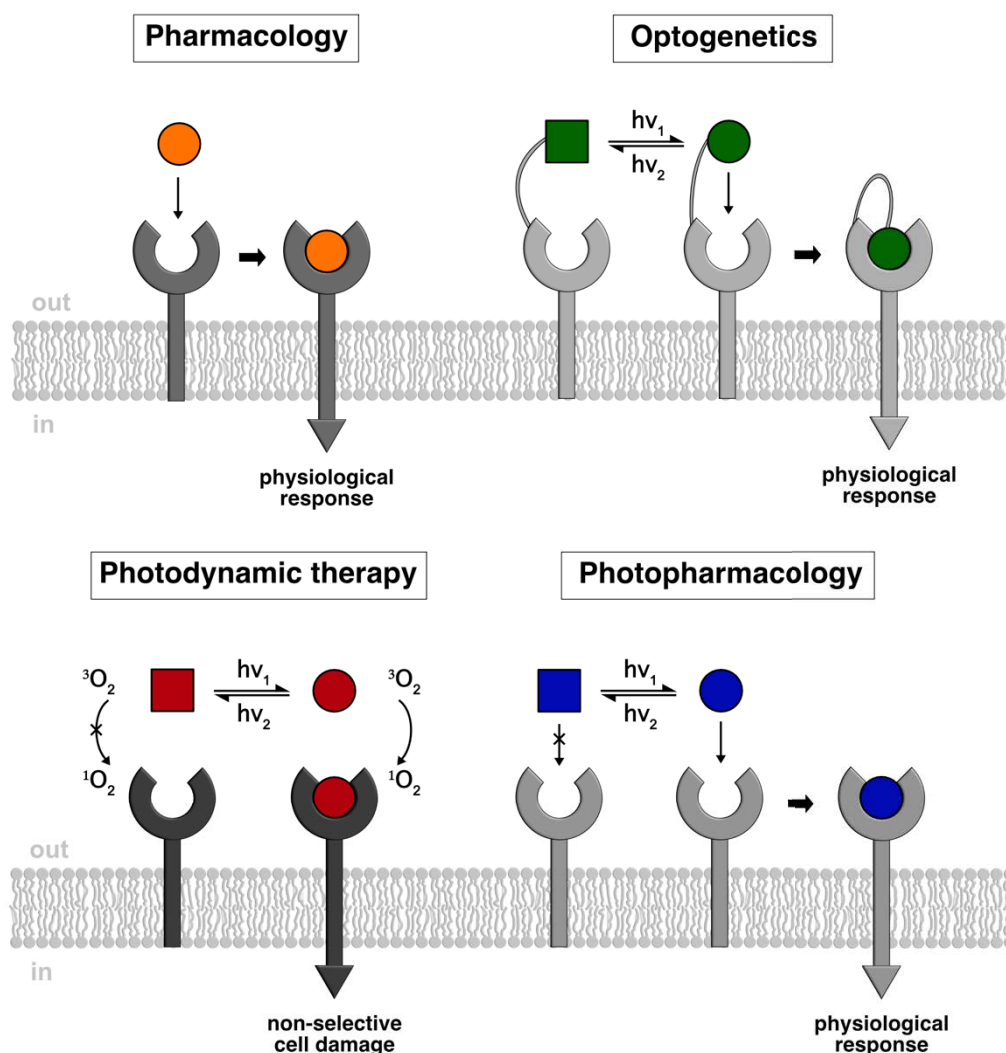


**Figure II.1: Principles of photocontrol.** Pharmacology relies on the use of pharmacophores, without any basic requirements for compound activation. Optogenetics relies on the use of genetically modified receptors (in this example with a tethered chromophore) furnishing the receptor with light responsiveness. Prerequisite for this method is the genetic modification of the receptor. Photodynamic therapy utilizes dyes which relax from their light-induced excited state through conversion of triplet oxygen to highly cytotoxic singlet oxygen. Requirements for this method are light for dye excitation and oxygen. Photopharmacology uses chromophores which become active or inactive upon illumination, thus light is needed.

Photopharmacology is an approach to circumvent the drawbacks of classical pharmaceuticals, by harnessing the high precision of light in space and time to achieve control over drug action. This control is extended by the possibility to tune the timing, wavelength and intensity of the delivered light, enabling precise drug dosage in four dimensions. Furthermore, light is orthogonal to most chemical and biological reactions and is non-invasive and non-toxic in the visible and IR spectrum<sup>4,56,119</sup>. The near-infrared phototherapeutic window ranges from 650 – 900 nm and is framed by the short-wavelength absorption of

hemoglobin and the longer-wavelength absorption of water<sup>120-122</sup>. A further decisive factor is the penetration depth of light into the tissue, which is limited by absorption through endogenous chromophores or light scattering<sup>5</sup>. The predicted penetration depths of light of 630 or 800 nm are 1 and 2 cm, respectively<sup>123</sup>. This shows the limitation and challenges of non-invasive photopharmacology towards easily light accessible targets such as skin or eyes. However, the accessibility for photopharmacotherapy on subjacent tissue was also demonstrated through light delivery by an optical fibre inserted through a small incision<sup>124</sup>.

But not all relevant drug targets are amenable to a photopharmacological approach. The recently introduced term photodrugability<sup>17</sup>, which was inspired by the term druggability, describes the different accessibilities and responsiveness of drug targets<sup>125</sup>. It furthermore prescribes rules for the choice of targets and classifies them into five categories. The targets thereby must be i) accessible by light, ii) be responsive to the light induced structural changes of the pharmacophore and iii) should be localized in a way to benefit from the spatiotemporal precision of light. Based on these conditions and the existing categorization for photodynamic therapy, photodrugable targets can be classified into five groups (Table II.1)<sup>17</sup>.

**Table II.1:** Different classes of photodrugable targets.

<b>Class 1:</b>	easy accessible, <i>e.i.</i> skin <sup>126</sup> and ophthalmology <sup>127</sup>
<b>Class 2:</b>	accessible by endoscopy, <i>e.i.</i> gastrointestinal tract <sup>128</sup> , mouth and throat <sup>129</sup> , respiratory system <sup>130</sup> , biliary tract <sup>131</sup> and bladder <sup>132,133</sup>
<b>Class 3:</b>	accessible through the skin without incision, <i>e.i.</i> testicles <sup>134</sup> , thyroid <sup>135</sup> and lymph nodes
<b>Class 4:</b>	accessible through a minor incision, <i>e.i.</i> pancreas <sup>136</sup> , prostate <sup>137</sup> , liver <sup>138</sup> , blood vessels, glands, muscles and bones
<b>Class 5:</b>	only accessible through a major incision, <i>e.i.</i> brain <sup>139</sup> and bone marrow

There are different methods and modes of application postulated for photopharmaceuticals that are dependent on the target class, duration of the treatment/therapy and the type of the pharmacophore used. Administration scenarios depict the behavior of a drug in the body and comprise four time frames: i) distribution, ii) action, iii) clearance and iv) environment (Figure II.2)<sup>5,7</sup>. These scenarios can be split into two groups; the first group comprises photoswitchable drugs with binary attributes (Figure II.2 A-E), and the second group implies photoswitchable drugs with controllable half-lives (Figure II.2 F-J)<sup>5</sup>. The binary or bistable chromophores belonging to the first group can be discretely switched between an "ON" and "OFF" state. This facilitates the administration of an inactive compound, which is then activated at the target site, stays active during the action period and is then inactivated for clearance from the body to the environment (Figure II.2 C).

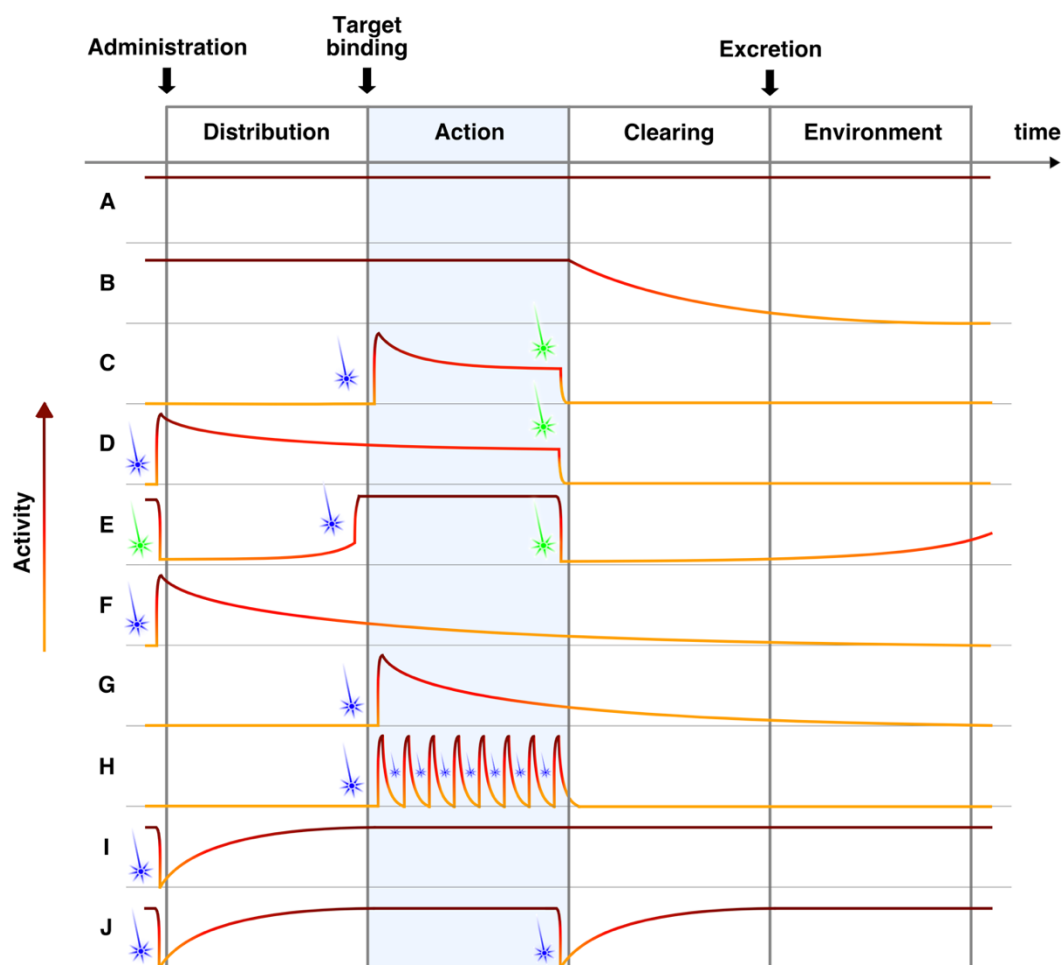


**Figure II.2: Photopharmaceutical administration scenarios.** Activity profiles for A-E) Binary photoswitchable drugs and F-J) photoswitchable drugs with controlled half-lives. A) Non-metabolisable drug. B) Metabolisable drug. C) Photopharmacophore with selective light-induced activation at the site of action and deactivation after the action phase for clearance. D) Photoswitchable drug which is pre-illuminated before use and deactivated after activity phase for clearance. E) Inactivation of a photoswitchable drug before administration, activation at the site of action followed by inactivation for clearance. F) Pre-activation of a photopharmacophore with defined half-life of the active isomer prior to administration. G) Activation of a photopharmacophore with defined half-life of the active isomer at the active site. H) Continuous cycled activation of a photoswitchable drug with short lived stability during action phase. I) Inactivation of a photoswitchable drug before administration, which returns to its active state before the action phase. J) Inactivation of a photoswitchable drug before administration, which returns to its active state before the action phase and is inactivated thereafter again for clearance. The illustration of the activity profiles was adapted and alternated based on ref. 5.

Further possibilities are the use of slowly backrelaxing preactivated or inactivated drugs, which can then be activated at the target site and inactivated after the action period (Figure II.2 D, E). The use of preactivated compounds is in general not desirable, as it can lead to off-target effects that should be circumvented through photopharmacology. However, this is also strongly dependent on the target tissue. Examples for bistable photoswitchable drugs are the chromopeptides AzoANP<sup>140</sup> and LirAzo<sup>16</sup>, which are stable in their *cis*-state for several hours and thus can be administered as active or inactive compounds. The situation is different for chromophores with short-lived half-lives, as one can activate the drug prior to administration or directly at the target site without the need for inactivation before clearance. This is beneficial for preventing the build up of active compounds in the environment (Figure II.2 F, G). For

compounds with very short-lived active states this auto-inactivation means that they must be repeatedly switched “ON” or kept active through constant illumination (Figure II.2 H). Compounds that can be inactivated prior to administration offer the possibility to distribute inactive compound to the target, which then slowly turns “ON” (Figure II.2 I) or can be turned “OFF” again for clearance (Figure II.2 J). However, in the sense of preventing the build-up of drugs in the environment after clearance, the latter two administration scenarios are less desirable.

Based on these scenarios many therapeutically valuable targets have been developed and evaluated for a photopharmaceutical or optogenetical approach and corresponding photoswitchable drugs, for example photochromic ligands (PCLs) and photoswitchable tethered ligands (PTLs)<sup>4</sup>. While the former act as normal ligands that bind, and dissociate from the orthosteric site of the target receptor, PTLs are covalently bound to the receptor in close proximity of the active site and reversibly stimulate or inhibit receptor signaling. The PTL approach thereby offers high precision of targeting because the bioconjugation motif, often an engineered cysteine for attachment of the PTL *via* reaction with a maleimide, can be genetically encoded on the target protein and expressed in cells of interest<sup>141,142</sup>. Since this cysteine-maleimide approach is very unselective towards native cysteine groups, and maleimide tends to hydrolyze and bind to glutathione under physiological conditions, novel more precise bioconjugation techniques have been developed recently.

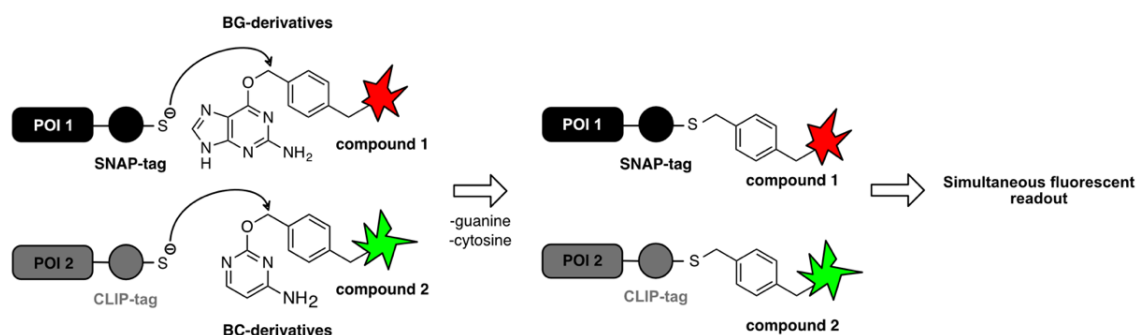


**Figure II.3: Principle of SNAP- and CLIP-tag bioconjugation for simultaneous labeling and imaging.** The SNAP-tag functionalized protein of interest 1 (POI 1) can be labeled with BG-derivatives carrying the label of interest (compound 1) through nucleophilic attack of the reactive cysteine located on the SNAP-tag on the benzylic BG position. Similarly, CLIP-tag functionalized POI 2 can be labeled with BC-derivatives carrying the label of interest (compound 2). If compound 1 and 2 are different fluorescent dyes simultaneous fluorescence imaging is possible. Adapted and modified based on ref. 143.

These approaches mainly utilize self-labeling tags, self-labeling proteins or enzyme-mediated labeling of tags to covalently attach the labeling compound to the protein of interest<sup>142</sup>. Especially the self-labeling proteins are of great interest for tethered photopharmacology, because this approach is not only applicable to many receptor types, but also allows usage of labeling techniques including fluorescent labeling to monitor conformational dynamics of GPCRs<sup>144</sup> and receptor trafficking<sup>145</sup>. The widely-used SNAP-tag is a 20 kDa engineered version of the human *O*<sup>6</sup>-alkylguanine DNA alkyltransferase (AGT) DNA repair protein domain<sup>146</sup>. It can be attached to the protein of interest, for example at the extracellular *N*-terminal end of transmembrane receptors, and binds selectively to labeling compounds bearing a *O*<sup>6</sup>-benzylguanine group

(BG-derivatives). Similarly, the more recent CLIP-tag functions likewise as AGT-based tag, but binds selectively to *O*<sup>2</sup>-benzylcytosine groups (BC-derivatives)<sup>143</sup>. This allows the simultaneous labeling and fluorescent imaging of two proteins of interest and enables the concurrent determination of cellular localization and the monitoring of different generations of proteins (Figure II.3). Other self-labeling protein domains comprise the Halo-tag<sup>147</sup>, an engineered haloalkane dehalogenase which binds to chloroalkane derivatives, and amino acid sequences which can be modified using external enzymes<sup>148</sup>.

As previously described in PART I: PHOTOSWITCHES, there is a large variety of azobenzene based photoswitchable drugs, and tuning of the tightly correlating switching wavelengths and thermal reversion rates is a tricky task. In principle, the perfect spectral parameters for two isomers of a photopharmacophore would be red-shifted (>600 nm), distinct absorption wavelengths with high molar extinction coefficients. Ideally, the high conversion rates would lead to complete depletion of one isomer upon illumination and *vice versa*, yielding 100% of the absorbing isomer in the photostationary state (PSS). Normal conversion rates are between 80-95% for the absorbing isomer in the PSS, with quantum yields in the range of 0.2-0.5<sup>4</sup>. However, low PSS conversion rates, for example 50/50 or even 40/60, do not necessarily render these compounds unsuitable as photoswitchable drugs. This is due to the nonlinear nature of biological systems, where already single stimulations can trigger largely amplified signaling cascades and small changes in receptor activation upon ligand switching can lead to altered physiological responses<sup>149</sup>. This applies particularly to neuronal systems, but also to single cells and GPCR signaling cascades<sup>4</sup>. Although no photopharmacophore has yet been developed to take the next step towards preclinical treatment evaluation, a prerequisite for successful photoswitchable drugs will be an easy amenability and a cost-effective synthesis to meet the challenges of a large-scale drug synthesis.

Some prominent examples of optogenetic and photopharmacological research tools and drug candidates comprise PCLs and PTLs for the photocontrol of ionotropic (permeable to ions such as K<sup>+</sup>, Na<sup>+</sup> and Ca<sup>2+</sup>) and metabotropic (membrane receptors activated by ligands, *e.i.* GPCRs and receptor tyrosine kinases) receptors. The transmembrane channel proteins are important for the generation of action potentials and thus control and propagate neuronal communication<sup>150</sup>. An example for the control of neuronal signaling is presented by PTL MAQ **II.1** (maleimide-azobenzene-quaternary ammonium)<sup>15</sup>, a photoswitchable tethered potassium channel blocker (Figure II.4). This photoswitch, which comprises a quaternary ammonium unit that is known to block potassium channels by binding to the extracellular side of the pore and to the channel of the so called "inner pore", was attached to a genetically engineered *Shaker* potassium channel (pdb: 18l8)<sup>151</sup> *via* cysteine-maleimide coupling. This synthetic photoisomerizable azobenzene-regulated K<sup>+</sup> channel (SPARK) was successfully used to optically control neuronal firing in dissociated neurons heterologously expressing the receptor, and was one of the first publications in the field of optogenetics<sup>15</sup>. Further examples for the optical control of ion channels are the PCLs 4-GluAzo **II.2** (ref. 152) and ATA-3 **II.3** (ref. 153), both agonists for the ionotropic kainate and AMPA receptors. The **II.4** design is based on the crystal structure of the ligand 4-(*R*)-methyl glutamate bound to the clamshell-like ligand binding domain of the kainate receptor GluK2 (pdb: 1sd3). It behaves as an agonist in its *trans*-form in the dark-adapted state or with 500 nm irradiation and becomes inactive upon *cis*-isomer accumulation

with 380 nm light. This functions by changing the degree of closure of the clamshell lips, which defines receptor activation. In its stretched *trans*-form the azobenzene moiety of **II.2** points out of the closed clamshell lips, while it forces them to open in its angled *cis*-form. Thus, this small molecular switch enables control over the whole receptor<sup>4,152</sup>. **II.3** is a photochromic ligand for the AMPA receptor GluA2 that was also designed based on the ligand-bound receptor crystal structure and shows a similar receptor control mechanism<sup>153</sup>. Another striking example is the optical control of insulin secretion using the PCL JB253 **II.4** (ref. 38). This photochromic sulfonylurea targets the ATP-sensitive potassium channels ( $K_{ATP}$ ) that control  $K^+$  efflux in pancreatic beta cells. Upon activation with blue light and accumulation of the *cis*-form the  $K_{ATP}$  channels are blocked, which results in the depolarization of the cell, opening of voltage-dependent  $Ca^{2+}$  channels (VDCC) and  $Ca^{2+}$  influx into the cell. This triggers various downstream signaling processes which ultimately lead to the exocytosis of insulin. The beforehand mentioned pharmacophore JB558 **1.8** is a red-shifted version of **II.4** and allows to remotely control pancreatic beta cell activity<sup>10</sup>.

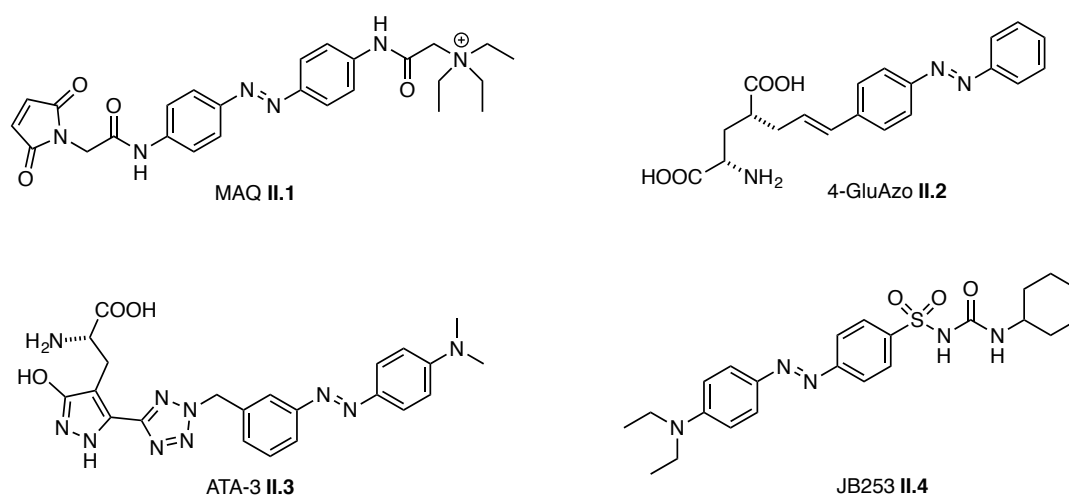


**Figure II.4: Examples for PCLs and PTLs for photopharmacological applications.** Shown are the PTL MAQ **II.1** (ref. 15) with maleimide and quaternary amino unit, the ionotropic glutamate receptor PCLs 4-GluAzo **II.2** (ref. 152) and ATA-3 **II.3** (ref. 153) and the photochromic sulfonylurea JB253 **II.4** (ref. 38).

There are many more azobenzene based PCLs and PTLs addressing various targets, and this growing library of photopharmaceuticals has not only contributed to the understanding of biological signaling, but also helped to promote the feasibility of these molecular machines. In the subsequent chapters of this work the reader will find our newest advances and developments in the field of photoswitchable hormones and tethered ligands.

## 2 OPTICAL CONTROL OF THE NATRIURETIC PEPTIDE RECEPTOR A USING A PHOTOSWITCHABLE HORMONE (AZOANP)

This work has been submitted to *Chemical Science* on the 15<sup>th</sup> November 2016.

The term hormone describes signaling molecules produced by and secreted from the endocrine gland, which releases the substances into the bloodstream. Hormones can be divided into three main classes: lipid-derived, amino acid-derived and peptide hormones. Animal organisms use these molecules to communicate between different organs to control and regulate physiological responses and behavioral actions. In this way, they affect many vital functions such as metabolism, digestion, sleep, respiration, growth, movement and reproduction, just to name a few. Endogeneous peptide hormones are short peptides or small proteins and among which one can find many familiar representatives such as insulin, oxytocin, vasopressin, and the three natriuretic peptides ANP (atrial natriuretic peptide), BNP (B-type natriuretic peptide) and CNP (C-type natriuretic peptide). While ANP and BNP act as endocrine hormones with natriuretic, diuretic and vasorelexant properties, CNP functions in an autocrine/paracrine fashion to induce vasorelaxation and vascular remodeling, and to regulate bone growth<sup>154,155</sup>. The natriuretic peptides target the three natriuretic peptide receptors A, B and C (NPR-A, NPR-B and NPR-C). NPR-A, which is targeted by ANP and BNP, as well as NPR-B, targeted by CNP, are membrane-bound guanylyl cyclases and belong to the class of receptor-linked enzymes. By contrast, NPR-C is a clearance receptor without intracellular guanylyl cyclase domain to which all three natriuretic peptides bind.

The activators of receptor-linked enzymes are normally small to medium sized proteins, with few known small molecule effectors, which makes these enzymes hard to conquer from a photopharmacological point of view. Nevertheless, the following manuscript describes the design and synthesis of a small library of photoswitchable atrial natriuretic peptides (AzoANPs), with one lead compound TOP271 **2.1**. This photochromic ANP derivative allows the optical control of NPR-A signaling and cGMP generation and was used to control vasoactive responses in mouse aorta and beta cell activity in Islets of Langerhans.

## 2.1 MANUSCRIPT: OPTICAL CONTROL OF A RECEPTOR-LINKED GUANYLYL CYCLASE USING A PHOTOSWITCHABLE PEPTIDIC HORMONE

Please do not adjust margins



Chemical Science

ARTICLE

### Optical control of a receptor-linked guanylyl cyclase using a photoswitchable peptidic hormone

Received 00th January 20xx,  
Accepted 00th January 20xx

DOI: 10.1039/x0xx00000x

www.rsc.org/

Tom Podewin,<sup>†,a</sup> Johannes Broichhagen,<sup>†,a,b</sup> Christina Frost,<sup>c</sup> Dieter Groneberg,<sup>d</sup> Helena Meyer-Berg,<sup>a</sup> Nicholas H. F. Fine,<sup>e,f</sup> Andreas Friebe,<sup>d</sup> Martin Zacharias,<sup>c</sup> David J. Hodson,<sup>e,f</sup> Dirk Trauner,<sup>\*a</sup> and Anja Hoffmann-Röder<sup>\*a</sup>

The optical control over biological function with small photoswitchable molecules has gathered significant attention in the last decade. Herein, we describe the design and synthesis of a small library of photoswitchable peptidomimetics based upon human atrial natriuretic peptide (ANP), in which the photochromic amino acid [3-(3-aminomethyl)phenylazo]phenylacetic acid (AMPP) is incorporated into the peptide backbone. The endogenous hormone ANP signals *via* the natriuretic peptide receptor A (NPR-A) through raising intracellular cGMP concentrations, and is involved in blood pressure regulation and sodium homeostasis, as well as lipid metabolism and pancreatic function. The *cis*- and *trans*-isomers of one of our peptidomimetics, termed TOP271, exhibit a four-fold difference in NPR-A mediated cGMP synthesis *in vitro*. Despite this seemingly small difference, TOP271 enables large, optically-induced conformational changes *ex vivo* and transforms the NPR-A into an endogenous photoswitch. Thus, application of TOP271 allows the reversible generation of cGMP using light and remote control can be afforded over vasoactivity in explanted murine aortic rings, as well as pancreatic beta cell function in islets of Langerhans. This study demonstrates the broad applicability of TOP271 to enzyme-dependent signalling processes, extends the toolbox of photoswitchable molecules to all classes of transmembrane receptors and utilizes photopharmacology to deduce receptor activation on a molecular level.

#### Introduction

Controlling biological function with light has been achieved using two general approaches, *viz.* optogenetics,<sup>1</sup> and photopharmacology.<sup>2,3</sup> While the first relies on the genetic introduction of light-responsive proteins, the latter describes the exogenous use of small photochromic molecules that

interact with a specific target. The advantage of photopharmacology is the precise control of cell signalling through native receptors, without necessarily introducing foreign genes. While optogenetics has successfully targeted the receptor-linked enzyme (RLE) class,<sup>4</sup> in particular receptor tyrosine kinases,<sup>5,6</sup> photopharmacology has not kept pace. One reason is that RLE ligands are usually large peptides with few known small molecule activators, making it a challenge to find a suitable “azologable”<sup>3</sup> pharmacophore. However, we and others recently reported the optical control of cell function with photoswitchable peptides,<sup>7,8</sup> an approach that is highly applicable to RLEs.

Accordingly, we focused on the natriuretic peptide receptor A (NPR-A), with its endogenous agonist atrial natriuretic peptide (ANP), as a suitable target for RLE photocontrol (Fig. 1a). The physiological actions of ANP are widespread and range from blood pressure regulation and sodium homeostasis to effects on fat metabolism and pancreatic beta cell function/survival.<sup>9–11</sup> ANP is mainly expressed and stored as inactive proANP in atrial cardiac myocytes, with lesser concentrations found in the ventricles and kidneys.<sup>6</sup> Upon secretion, primarily controlled by mechanical stimulation following atrial wall stretching,<sup>12,13</sup> proANP is rapidly cleaved by the cardiac serine protease corin to release the active 28 amino acid ANP.<sup>14</sup> The active form comprises a central 17 amino acid macrocycle linked by a disulfide bridge between Cys7 and Cys23. Upon ligand activation of NPR-A, the membrane-proximal regions of

<sup>a</sup> Department of Chemistry and Center for Integrated Protein Science, LMU Munich, 81377 Munich, Germany.

<sup>b</sup> Present address: Max-Planck Institute for Medical Research, Jahnstr. 29, 69120 Heidelberg, Germany.

<sup>c</sup> Department of Physics, Technical University of Munich, James-Frank-Str. 1, 85748 Garching, Germany.

<sup>d</sup> Julius-Maximilians-University Würzburg, Institute of Physiology, Röntgenring 9, 97070 Würzburg, Germany.

<sup>e</sup> Institute of Metabolism and Systems Research (IMSR) and Centre of Membrane Proteins and Receptors (COMPARE), University of Birmingham, Edgbaston, B15 2TT, UK.

<sup>f</sup> Centre for Endocrinology, Diabetes and Metabolism, Birmingham Health Partners, Birmingham, B15 2TH, UK.

<sup>†</sup> These authors contributed equally.

<sup>†</sup> Correspondence: Prof. Dr. Anja Hoffmann-Röder, Department of Chemistry, LMU Munich, Butenandstr. 5-13, 81377 Munich, Germany. Email: anja.hoffmann-roeder@cup.lmu.de; Prof. Dr. Dirk Trauner, Department of Chemistry, LMU Munich, Butenandstr. 5-13, 81377 Munich, Germany. Email: dirk.trauner@cup.lmu.de;

Electronic Supplementary Information (ESI) available: details on solid phase peptide synthesis and characterization of all peptides can be found here, as well as experimental details on cGMP assays, aortic tensometry, islet treatment, statistics and a detailed description of modelling and simulations. See DOI: 10.1039/x0xx00000x

‡ These authors contributed equally.

Please do not adjust margins

Please do not adjust margins

ARTICLE

Journal Name

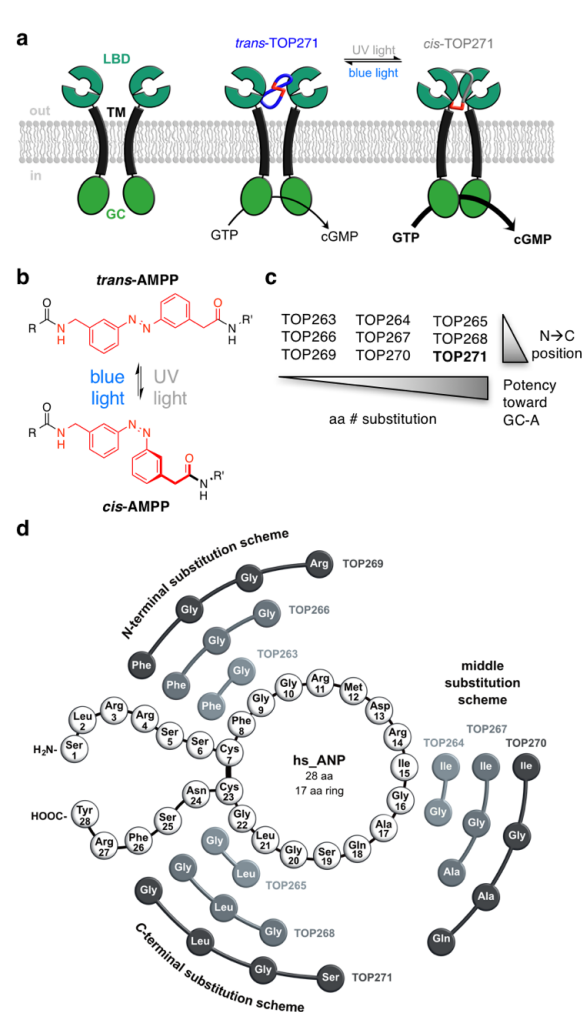


**Fig. 1:** ANP receptor and AMPP. (a) The ANP receptor links binding of and activation by a photoswitchable peptide to guanylyl cyclase activity, that is cGMP generation and subsequent vasodilation in its UV-light adapted *cis*-state. (b) The photoswitch AMPP can be toggled between its *trans*- and *cis*-isomer with blue (460 nm) and UV-light (365 nm), respectively. (c) The structure of ANP is characterized by a macrocycle that is formed by a disulfide bond between Cys7 and Cys23. Replacement of two, three or four amino acids along the ring structures leads to TOP263–271. (d) Initial assessment of AzoANP peptides TOP263–271 potency towards cGMP synthesis focuses on TOP271, where four amino acids are replaced on the C-terminal side of the macrocycle.

the monomeric receptor units undergo a global conformational change, triggering guanylyl cyclase activity. This leads to generation of cGMP, a major player in intracellular cell signalling.<sup>12</sup>

Dysregulated ANP secretion has been linked to different cardiovascular diseases, *i.e.* atrial fibrillation,<sup>15</sup> hypertension<sup>16,17</sup> and heart failure.<sup>18,19</sup> Moreover, genetic variants in or close to the ANP gene (*NPPA*) locus, which lead to increased circulating levels of plasma ANP, were shown to lower blood pressure and the risk of hypertension in healthy individuals.<sup>20,21</sup> Moreover, individuals harbouring one copy of

the G allele of rs5068 have lower likelihood of diabetes,<sup>22</sup> and ANP has been shown to increase muscle insulin sensitivity,<sup>23</sup> although whether insulin release itself is stimulated is more debated.<sup>10,24,11</sup> Such fundamental and pleiotropic actions of ANP have made its receptors an important pharmacological target, resulting in recently introduced therapies for the treatment of cardiovascular disease.<sup>25,26</sup> Despite this, many facets of ANP function and action remain elusive. Thus, novel tools for unravelling and controlling ANP/NPR-A-stimulated signalling processes would be a valuable asset.

To address this, we report the synthesis of a photochromic ligand based on human ANP that enables the photocontrol of RLE activity (Fig. 1a). The NPR-A was endowed with light-sensitivity by incorporation of the photoswitchable amino acid, [3-(3-aminomethyl)phenylazo]phenylacetic acid (AMPP)<sup>27,28</sup> into ANP, which along with related derivatives,<sup>29,30,8,31</sup> has proven to be a valuable building block for photocontrol of peptide conformation and activity (Fig. 1b). One out of nine of our synthesized photochromic ANPs (AzoANPs), termed TOP271, allowed optical control to be exerted over NPR-A activity, intracellular cGMP levels, and downstream processes using UV and blue light.

## Results and discussion

Our initial design approach was based on the substitution of amino acids in ANP by AMPP, more precisely into the peptidic backbone to induce maximal structural changes upon photoisomerization. Nine different photochromic AzoANP peptides (dubbed TOP263–271) were designed and synthesized to obtain a small library (Fig. 1c), whereby AMPP replaced either two, three or four amino acids in ANP. The substitutions, following a circular permutational fashion, were located either near the *N*- or *C*-terminus or facing the Cys7–Cys23 disulfide bridge in the native 17 amino acid cycle of ANP (see SI for details on synthesis and characterization).

At this point, it is worth noting that initial screening of cGMP accumulation returned a single compound, *i.e.* TOP271, as being the most active and most isomer-dependent peptide. Thus, we focused on characterization and investigation of this lead compound. Further details on the cGMP assays can be found under “optical control of cGMP generation”.

### Photophysical properties of AzoANP peptides TOP263–271

The photochromic AzoANP peptides including native human ANP (hsANP) were synthesized through solid-phase peptide synthesis (SPPS), characterized by high resolution mass spectrometry, and their purity assessed by reverse-phase HPLC: all were <3.7 ppm of the calculated mass and RP-HPLC revealed high purity (see SI for MS and HPLC data). The switching kinetics of all azologued peptides were determined by UV/Vis spectroscopy (TOP271 Fig. 2a–c, TOP263–270 SI Fig. 1–3 and SI Tab. 3,4). Starting with compounds in the dark-adapted state (*vide infra*), a decrease in the  $\pi\text{-}\pi^*$  and an increase in the  $n\text{-}\pi^*$  band was observed in response to UV light

Please do not adjust margins

Please do not adjust margins

Journal Name

ARTICLE

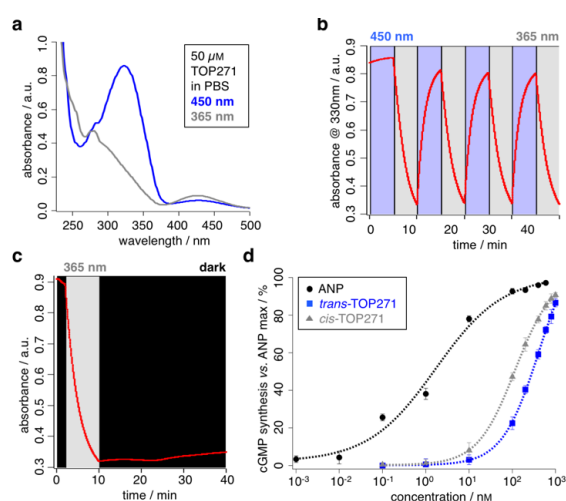


**Fig. 2:** Photodynamics and cGMP dose-response of TOP271. (a) UV/Vis spectra of *cis*- and *trans*-TOP271. (b) Reversible switching of TOP271 with UV (365 nm) and blue (460 nm) light. (c) Bistability of TOP271 when switched to the *cis*-isomer by means of UV light (365 nm) and subsequently left in the dark. (d) Dose-response of *cis*- and *trans*-TOP271 in NPR-A transfected HEK293t cells assessed by cGMP HTRF.  $EC_{50}$  values for ANP =  $2.0 \pm 0.4$  nM, *cis*-TOP271 =  $126.6 \pm 10.9$  nM and *trans*-TOP271 =  $467.9 \pm 59.4$  nM correspond to two independent assays. Values represent the mean  $\pm$  SEM.

( $\lambda = 365$  nm) (Fig. 2a), with reversion of this switching process in response to blue light ( $\lambda = 460$  nm).

As expected for an electron-poor azobenzene, all peptides were bistable (TOP271 Fig. 2c, TOP263-270 SI Fig. 3). This advantageous trait allows samples to be pre-illuminated prior to application rather than needing constant illumination. We determined the thermal *cis*→*trans* relaxation rate  $k_{obs}$  in PBS buffer. This was performed at room temperature, and because the compounds were bistable, the initial back-relaxation was obtained as a linear function (pseudo-first order) from the first 30 min after ceasing illumination. Peptides TOP263-270 showed  $k_{obs} \times 10^{-4}$  a.u.<sub>330nm</sub>/min between 0.28-2.83, with the most potent compound TOP271 being 0.98 a.u.<sub>330nm</sub>/min (see SI Table 4, compare with  $k_{obs} = 3.58 \times 10^{-4}$  a.u./min for unsubstituted azobenzene in benzene at 0 °C).<sup>32</sup> To examine the structural relations between ANP and both isomers of TOP263-271, CD spectra were recorded in 40% buffered aqueous 2,2,2-trifluoroethanol (TFE) solutions. TFE is needed for the peptides to form stabilized secondary structures instead of random coils,<sup>33</sup> and the optimal TFE concentration of 40% was determined with ANP in different aqueous buffered mixtures (SI Fig. 4). The spectra of the peptides TOP263-271 showed differences between their *cis/trans*-isomers, but remained similar to that of native ANP, with no observable trend (SI Fig. 5-7). TOP271 was subjected to further characterization for both its *cis*- and *trans*-form by NMR spectroscopy alongside ANP. The spectra were recorded in 35% aqueous TFE-d<sub>3</sub> solutions to suppress signal broadening and aggregation (see SI for NMR data on ANP and *cis/trans*-TOP271). The *cis*-TOP271 NMR spectrum showed overlapping signals and thus could not be resolved. Nevertheless, the <sup>1</sup>H

and <sup>13</sup>C chemical shift values of the *trans*-TOP271 peptide could be unambiguously identified, showing the incorporation of AMPP into the backbone of the peptide and the overall correct structure.

### Optical control of cGMP generation

To assess the most suitable peptide for further analysis, cGMP generation was measured in HEK293t cells transiently transfected with NPR-A.<sup>34</sup> cGMP is a major effector of cellular metabolism,<sup>35</sup> with effects on adipose tissue,<sup>36-38</sup> liver<sup>39,40</sup> and the brain.<sup>41</sup> Alongside nitric oxide, the natriuretic peptides are the major potentiators of cGMP generation, with downstream signalling effects on phosphodiesterases (PDEs),<sup>42</sup> cGMP-dependent protein kinases (PKGs)<sup>43</sup> and cyclic nucleotide-gated channels (CNGs).<sup>44</sup> ANP induces smooth muscle relaxation through increases in intracellular cGMP levels and activation of PKGI, which subsequently leads to a decrease in cytosolic Ca<sup>2+</sup> levels and reduced Ca<sup>2+</sup>-sensitivity of the contractile system.<sup>45,46,12</sup> Furthermore, depleting cGMP levels leads to depolarization in rods of the retina, triggering action potentials that transduce signals to perceive light.<sup>47</sup>

For testing of cGMP synthesis, each peptide was applied as the *trans*- or *cis*-isomer by keeping them either in the dark or pre-illuminating with UV light ( $\lambda = 365$  nm) for 15 minutes, respectively. Using this approach, TOP271, *i.e.* the ANP analogue where AMPP replaces four amino acids at the C-terminal end of the ring, was identified as the most promising candidate due to its highest binding affinity. In addition, a trend in the activity of these azobenzene-containing peptides was revealed: activity towards cGMP synthesis was higher the more amino acids were replaced and the closer their substitution was located to the N-terminus (Fig. 1d). Besides TOP271, only three further peptides from our small AzoANP library, TOP264, -265 and -268, showed NPR-A activation in the μM range (SI Fig. 8). The low potency of these compounds and the inactivity of the remaining photochromic ANP peptides (TOP263, -266, -267, -269 and -270) likely stems from the substitution of residues crucial for receptor binding, such as Phe8.<sup>48,49</sup>

Having identified TOP271 as the lead candidate, we attempted to access light-dependent NPR-A activity. The measured cGMP dose-responses showed that both TOP271 isomers had similar potency to native ANP ( $EC_{50,ANP} = 2.0 \pm 0.4$  nM) (Fig. 2d), but *cis*-TOP271 ( $EC_{50,cis} = 126.6 \pm 10.9$  nM) was roughly four times more potent than the *trans*-isomer ( $EC_{50,trans} = 467.9 \pm 59.4$  nM). It should be noted that, although the increase in  $EC_{50}$  seems small, signal integration and amplification of cGMP leads to more pronounced responses *in cellulo*.<sup>50</sup> With this in mind, we decided to progress TOP271 through to more relevant studies *ex vivo*.

### Optical control of smooth muscle tone and pancreatic beta cell function

Please do not adjust margins

Please do not adjust margins

ARTICLE

Journal Name

We next sought to address whether TOP271 would allow the optical control of cGMP-dependent processes in a physiologically-relevant system, *i.e.* the aortic ring preparation. The treatment of constricted aortic rings with ANP leads to a potent vasodilation, corresponding to the blood pressure reducing effect of ANP.<sup>51</sup> Accordingly, we predicted that TOP271 would allow reversible, light-controlled vasoactive responses, with *cis*-TOP271 being the stronger effector at specific concentrations. Dose-response curves were obtained for vasodilation in pre-constricted aortic rings following exposure to pre-illuminated *cis*- ( $\lambda = 365$  nm) and *trans*-TOP271 ( $\lambda = 460$  nm), and showed increased potency for the former isomer in the 100 nM to 1  $\mu$ M range (Fig. 3a, SI Fig. 9). Although this dose-response indicated a significant difference in receptor activation for 100 nM TOP271, we decided to use 400 nM TOP271 to trigger a stronger isomer-dependent vasodilation. Thus, the application of dark-adapted *trans*-TOP271 led to strong vasodilation, which was enhanced following UV ( $\lambda = 365$  nm) illumination to induce *cis*-isomerization, and again reversed after blue light ( $\lambda = 460$  nm) exposure to induce *trans*-accumulation (Fig. 3b and d). Conversely, to examine the *cis*  $\rightarrow$  *trans* isomerization cycle, pre-illuminated ( $\lambda = 365$  nm) *cis*-TOP271 was added to the organ bath, leading to a potent vasodilation (Fig. 4b and e, SI Fig. 10). Subsequent *trans*-isomer accumulation by exposure to blue light ( $\lambda = 460$  nm) elicited vasoconstriction, which again could be reversed by UV ( $\lambda = 365$  nm) illumination. Notably, the speed of the initial vasodilation was 1.5x higher for *cis*- compared to *trans*-TOP271, with the former being

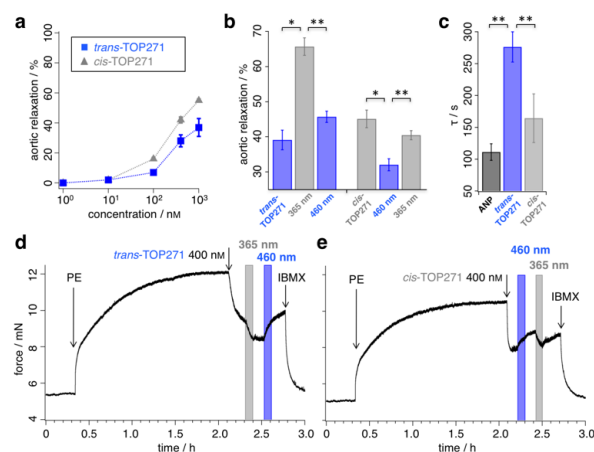


**Fig. 3:** TOP271 allows photocontrol of aortic tissue. (a) Dose-response curves for *trans*- and *cis*-TOP271. (b) Aortic relaxation for cycles in a) and b). (c)  $\tau$  of aortic relaxational responses for 17 nM ANP compared to 400 nM *trans*- and *cis*-TOP271. (d,e) Reversible photocontrol over aortic tension by application of *trans*-TOP271 (d) and *cis*-TOP271 (e) with UV/blue and blue/UV-light (365 and 460 nm) cycles, respectively. All experiments were conducted in the presence of 200  $\mu$ M *N*- $\omega$ -nitro-L-arginine methyl ester (L-NAME) and 3  $\mu$ M Diclofenac. PE = phenylephrine; IBMX = 3-iso-butyl-1-methylxanthine. (n = 6 aortic rings from 4 animals) (\* $P < 0.05$ , \*\* $P < 0.01$ , repeated measures Student's *t*-test). Values represent the mean  $\pm$  SEM.

analogous to ANP (Fig. 3c).

Insulin-secreting pancreatic beta cells express NPR-A, and ANP action is thought to provide a potential explanation for the association between cardiovascular and metabolic dysregulation.<sup>52,53</sup> We observed that native ANP dose-dependently (0.1-100 nM) suppressed beta cell function at physiologically-elevated glucose (8 mM) levels, as shown by a reduction in the amplitude of intracellular  $\text{Ca}^{2+}$  fluxes in intact islets of Langerhans. These findings could be replicated using

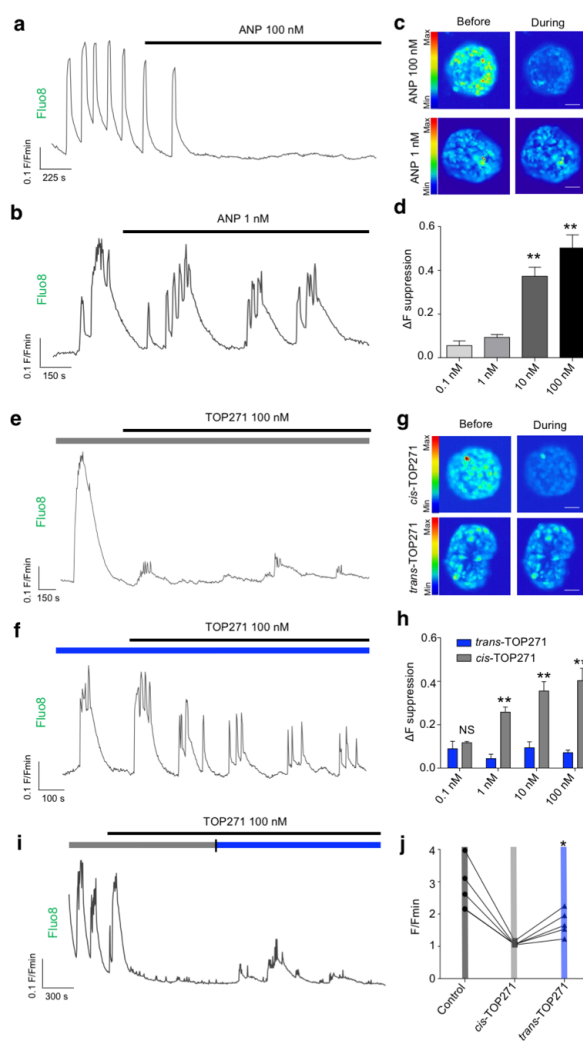


**Fig. 4:** TOP271 allows photocontrol of pancreatic beta cell function. (a-d) ANP dose-dependently suppresses  $\text{Ca}^{2+}$  response in beta cells (representative traces shown (scale bar 25  $\mu$ M) (n = 4 - 6 islets for each concentration) (\*\* $P < 0.01$ , one-way ANOVA). (g-h) *cis*-TOP271 dose-dependently inhibits  $\text{Ca}^{2+}$  spike amplitude, whereas *trans*-TOP271 is less effective at all concentrations tested (representative traces shown) (scale bar 25  $\mu$ M) (n = 4 - 6 islets for each concentration) (\*\* $P < 0.01$ , two-way ANOVA). (i-j) TOP271 allows reversible photocontrol of beta cell function, with blue (458-488 nm) light partially restoring  $\text{Ca}^{2+}$  responses (n = 5 islets) (\* $P < 0.05$ , repeated measure one-way ANOVA). Values represent the mean  $\pm$  SEM.

Please do not adjust margins

Please do not adjust margins

Journal Name

ARTICLE

UV pre-illuminated ( $\lambda = 365$  nm) *cis*-TOP271 (Fig. 4e-h), which also robustly suppressed  $\text{Ca}^{2+}$  rises from 1-100 nM. By contrast, dark-adapted *trans*-TOP271 induced only a small decrease in beta cell  $\text{Ca}^{2+}$ -spiking activity (Fig. 4e-h). Reversibility could be achieved by applying *cis*-TOP271 and then illuminating with blue light ( $\lambda = 458$ -482 nm) to induce *trans*-isomerization (Fig. 4i). Restoration of beta cell function was only partial (Fig. 4j), however, possibly due to cGMP-mediated sequestration of  $\text{Ca}^{2+}$  into internal stores such as the endoplasmic reticulum.<sup>54</sup>

Pancreatic beta cells have been shown to express NPR-A, and links exist between ANP and diabetes risk.<sup>55</sup> Indeed, ANP gene expression is increased in the ventricles of rats with reduced beta cell mass, and ANP levels are elevated during diabetes.<sup>52</sup> We were able to show that ANP dose-dependently inhibits the amplitude of beta cell  $\text{Ca}^{2+}$  rises, with significant effects at 10- and 100 nM of the peptide. Whereas *trans*-TOP271 was largely without effect, *cis*-TOP271 suppressed cytosolic  $\text{Ca}^{2+}$  fluxes and beta cell activity, and this could be partially reversed by ceasing UV illumination. The effects of ANP on beta cell function are complex and controversial. While some studies have shown that ANP inhibits  $\text{Ca}^{2+}$  levels and insulin secretion,<sup>10,24</sup> others have shown stimulatory effects.<sup>11,56</sup> This likely reflects differences in the time course of application, preparation under examination (*i.e.* dissociated vs. intact islets), stimulation state (*i.e.* low vs. high glucose) and concentration.

This likely reflects differences in the time course of application, preparation under examination (*i.e.* dissociated vs. intact islets), stimulation state (*i.e.* low vs. high glucose) and

concentration. With regards to the latter, we were able to show a bimodal relationship where low doses of ANP preferentially affect  $\text{Ca}^{2+}$  oscillation frequency without altering amplitude, whereas high doses do the opposite (SI Fig. 11). Thus, TOP271 may provide an important tool to allow ANP receptor conformation and signalling to be understood in the context of beta and other cell (dys)function.

#### Molecular dynamics simulations of ANP and *cis/trans*-TOP271

Atomic-level modelling in explicit solvent was conducted to better understand the structure/activity relationships of isomer-dependent NPR-A activation. We focused on the *in silico* structure of native ANP peptide and *cis/trans*-TOP271, both in aqueous solution and bound to the NPR-A receptor. The extra-cellular domains were modelled based on the NPR-A crystal structure (pdb: 1t34, in complex with rat ANP (rANP)),<sup>48</sup> while the receptor-bound ANP peptide and the *cis/trans*-TOP271 isomers were based on the NPR-C crystal structure (pdb: 1yk0, in complex with hsANP).<sup>49</sup> We used the latter for our structural peptide modelling to account for the Met12/Ile12 difference between ANP and rANP, respectively. In a first step, the *cis/trans*-TOP271 isomers were simulated for 200 ns in the absence of the NPR-A receptor. To compare the affinity of both isomers to adopt the bound ANP ring structure, distance restraints with respect to the ANP crystal structure were applied between all C $\alpha$ -atom pairs within the ring, neglecting the two terminal tails. The resulting restraint energy distributions show a clear difference between the

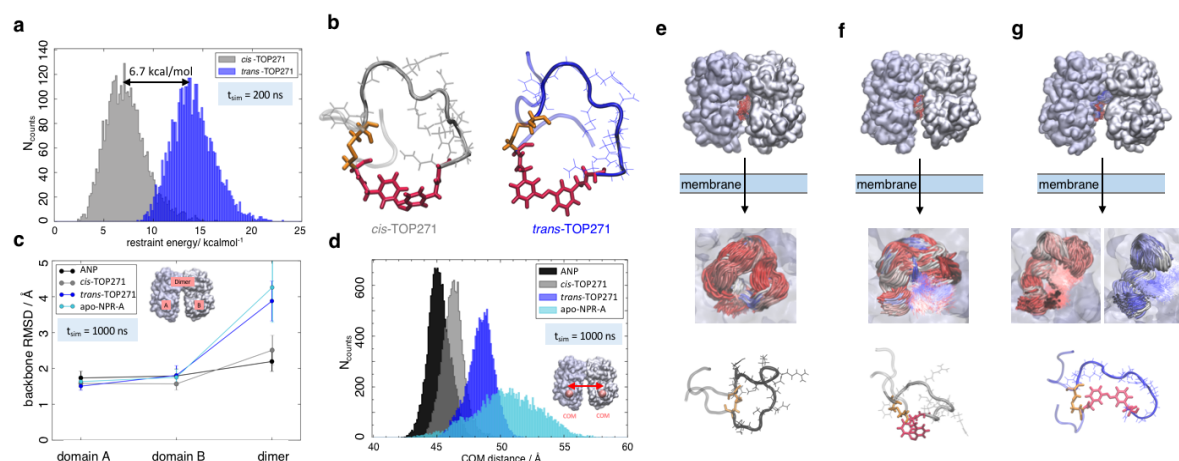


**Fig. 5:** MD simulations of ANP and TOP271. (a) Restraining energy distribution obtained from MD simulations (200 ns) of *cis*- and *trans*-TOP271 in solution, including restraints to keep the sampled conformations close to native ANP (see methods section for details). (b) Representative restrained conformations of *cis*- and *trans*-TOP271 illustrating the steric hindrance of *trans*-azobenzene to fit into the native ring structure (red: azobenzene, orange: Cys7-Cys23 disulfide bridge). (c) Mean backbone-Ca RMSD and standard deviation of the NPR-A dimer and the both receptor domains A and B after 1  $\mu$ s simulation, calculated for bound native ANP (black), bound *cis/trans*-TOP271 (gray and blue, respectively) and apo-NPR-A (cyan). The overall receptor RMSD clearly differs between native and *cis*-TOP271 vs. *trans*-TOP271 and apo-NPR-A. (d) Center-of-mass distance (orange balls and arrow) of the membrane-proximal NPR-A domains after 1  $\mu$ s simulation. For bound native ANP (black) and *cis*-TOP271 (gray) the receptor domains tend to close compared to *trans*-TOP271 and the apo-NPR-A (blue and cyan). (e, f, g) Representative NPR-A and peptide conformations for bound native ANP (e) and bound *cis/trans*-TOP271 (f and g, respectively). Top row: Isomer-dependent overall receptor geometry and binding site coverage visualized by time-superposition of the disulfide-connected isomer segment Cys7-Cys23 (red:  $\leq 300$  ns, white  $\leq 600$  ns, blue  $\leq 1000$  ns). Middle row: zoom into the time-superposition illustrates differences in the conformational ensemble of native ANP and *cis*-TOP271 vs. *trans*-TOP271 (azobenzene in line design). Bottom row: Representative isomer conformations extracted from the simulated ensemble (red: azobenzene, orange: Cys7-Cys23 disulfide bridge).

Please do not adjust margins

Please do not adjust margins

ARTICLE

Journal Name

isomers (Fig. 5a), with the energy of *trans*-TOP271 being on average 6.7 kcal/mol higher. This likely derives from the rigid, extended *trans*-azobenzene structure, which sterically prevents adoption of the native ring structure (Fig. 5b).

To elucidate the effect of the isomeric conformational differences on receptor geometry, unrestrained simulations of 1  $\mu$ s length were performed for NPR-A bound *cis/trans*-TOP271, ANP and apo-NPR-A. The overall receptor RMSD significantly differs for *cis*- and *trans*-TOP271, with the former matching ANP and the latter being similar to apo-NPR-A (Fig. 5c). These isomer-dependent differences in receptor geometry are related to a change in relative orientation of the two NPR-A dimers: while there are no ligand-dependent orientation changes in the membrane-distal domains (SI Fig. 12), the membrane-proximal domains tend to close around ANP and *cis*-TOP271, but remain more open in the case of *trans*-TOP271 (Fig. 5d-g). This is in agreement with the crystal structures of the different apo- and ligand-bound natriuretic peptide receptors, which show up to 20 Å distance change between the two C-terminal/membrane-proximal receptor domains upon ligand binding.<sup>48,49</sup> *trans*-TOP271 thereby resembles the apo-form, in which fluctuating membrane-proximal distances shift the receptor towards an open state (Fig. 5c). These changes in receptor geometry can be assigned to isomeric differences in the bound conformation. Whereas the conformations of *cis*-TOP271 are comparable to the crystal ring structure of ANP, the conformational ensemble of *trans*-TOP271 is narrower and more hairpin-like (Fig. 5e-g). The NPR-A-bound crystal structure of ANP also reveals a central pore in the 17 amino acid ring that is essential for ligand binding; only *cis*-TOP271 is able to adapt this donut like conformation, while the *trans*-isomer forms a closed structure (Fig. 5e-g).

Lastly, we attempted to quantify the twist motion of the NPR-A membrane-proximal domains upon ligand binding, which is thought to initiate intracellular GC activation.<sup>48</sup> Here, we detected a less prominent isomer-dependency for the selected twist angle of the ligand-bound receptor domains compared to apo-NPR-A (see SI Fig. 13 and SI Tab. 6). While the binding of ANP leads to a focusing of the twist angle distributions in NPR-A, bound *cis*- and *trans*-TOP271 show broader, shifted distributions and the apo-NPR-A inherits large angle fluctuations. This shows on the one hand the higher similarity of angle distributions of ANP and *cis*-TOP271 compared to *trans*-TOP271, but on the other hand also the flexibility of the apo-NPR-A membrane-proximal regions. Notably, crystal structures represent only a structural snapshot, while MD simulations cover a whole ensemble of structures and as a result we conclude that the reduced distance between the membrane-proximal domains in the ligand-bound state, and not the twisting motion of the NPR-A, is the major trigger for receptor activation.

In summary, our MD simulations showed a higher flexibility of the apo-NPR-A receptor as well as bound to *trans*-TOP271, whereas the membrane-proximal receptor domains tend to close around ANP and *cis*-TOP271. The simulations hence suggest an alternative regulation of the guanylyl cyclase activity, in which the binding of ANP and *cis*-TOP271 to NPR-A

suppresses dynamic fluctuations of the membrane-proximal domains of both receptor dimers, leading to defined ligand/receptor structures. Since in contrast to previous experiments our simulations suggest an only less prominent isomer-dependency of twisting motion of the membrane-proximal domains, we predict that our dynamic simulations deliver a more precise picture of NPR-A activation than the static crystal structure model.<sup>48</sup>

## Conclusions

In this study, we present the design, synthesis, evaluation and application of TOP271, a peptidic hormone based on ANP with a photoresponsive azobenzene unit. Acting *via* the NPR-A receptor to generate cGMP, TOP271 allows the reversible photocontrol of contraction/dilation in aortic tissue, as well as Ca<sup>2+</sup> oscillations in rodent islets of Langerhans. Although photodependent cGMP synthesis was described earlier, these approaches rely on the genetically-encoded photosensitive proteins EROS<sup>57,58</sup> or BeCycOps,<sup>59,60</sup> whereas TOP271 allows the unprecedented photocontrolled cGMP synthesis in native tissue. EROS and BeCycOps are based on bacterial flavin-containing photoreceptors and fungal rhodopsins, respectively, and can be used to induce penile erection in male rats or tactic behavior in *C. elegans* following illumination. A drawback of EROS is the residual cAMP activity, caused by the specific mutation of an adenylyl cyclase to an engineered guanylyl cyclase. BeCycOps on the other hand utilizes native guanylyl cyclase activity and was shown to specifically engage only cGMP synthesis, but requires genetic introduction. Photochromic ligands like TOP271 avoid these issues and remain exogenously applied, thereby only targeting and activating the protein of interest.

With TOP271, we could selectively and reversibly manipulate the NPR-A/cGMP signalling pathway with high spatio-temporal precision. Interestingly, the 4-fold higher potency of *cis*-TOP271 for cGMP generation detected *in vitro* in transfected HEK293t cells is sufficient to trigger a more pronounced vasodilation *ex vivo* in aortic ring tissue. Although the exact intracellular cGMP concentration is an active source of research efforts, the changes observed are in agreement to prior findings, where small changes in the concentration of this second messenger provoke a significant amplification of downstream signals.<sup>61</sup> It also showcases the robustness and applicability of TOP271, which we believe will enable precise control of hemodynamic processes, contributing to the dissection of vascular function in health and disease.

Moreover, TOP271 not only demonstrates the successful transformation of ANP into a photoswitchable peptide, but also extends the toolbox of photochromic ligands to all classes of transmembrane receptors. The incorporation of azobenzenes into peptides and proteins has been achieved in a multitude of systems in the last decade, *i.e.* in proteins of *E. coli*<sup>62,7</sup> and in short peptides with specific secondary structures such as  $\beta$ -sheet and  $\beta$ -hairpin motifs.<sup>63,30,29,27</sup> Two major possibilities should be distinguished: i) having an azobenzene as an amino acid residue and ii) having an azoswitch in the

Please do not adjust margins

Please do not adjust margins

## Journal Name

## ARTICLE

peptide backbone. While the former has been used to gain optical control over binding affinity of transcription factor and cell adhesion molecules,<sup>62,64</sup> the latter was successfully applied to the optical control of muscle contraction<sup>31</sup> and secondary structure formation.<sup>65</sup> We envision our design herein, together with AzoChig<sup>28</sup> and LirAzo,<sup>8</sup> to be highly applicable to all kinds of peptides (e.g. neuropeptides, such as oxytocin, vasopressin, kisspeptin etc.), as backbone substitution allows a larger conformational change upon isomerisation and therefore a larger change in affinity/efficacy. With recent synthetic efforts in mind,<sup>66</sup> tetra-ortho-chloro-AMPP, exhibiting red-shifted illumination wavelengths and high bistability, can be envisioned for the incorporation into target peptides. Such breadth already encompasses hairpin structures,  $\alpha$ -helices and now macrocyclic structures, but can potentially be extended to antibodies, immunogens, peptidic hormones and receptors, where fine regulation of protein function by tertiary structure stabilization/destabilization is necessary for function.<sup>67</sup> Thus, the present findings set the stage for photochromic peptides to become a mainstay for optical control of biological processes using photopharmacology.

## Acknowledgements

T.P. and C.F. were supported by the SFB749 project of the Deutsche Forschungsgemeinschaft and the Center for Integrated Protein Science Munich (CIPSM). J.B. was supported by a Studienstiftung des Deutschen Volkes PhD studentship. D.J.H. was supported by Diabetes UK R.D. Lawrence (12/0004431), EFSD/Novo Nordisk Rising Star and Birmingham Fellowships, as well as MRC Project (MR/N00275X/1), Imperial Confidence in Concept (ICiC), Wellcome Trust Institutional Support and ERC-StG (715884) Awards. D.T. was supported by an Advanced Grant from the European Research Council (268795). A.H.R. and M.Z. were supported by the SFB749 project of the Deutsche Forschungsgemeinschaft. We are very grateful to Dr. Davor Pavlovic, Dr. Fahima Syeda and Sreedha Nashitha Kabir for the planning and testing of Langendorff perfused heart experiments. We thank Dr. Ruey-Bing Yang for providing the pCMV5\_GC-A plasmid and Axel Schäfer for technical assistance.

## Notes and references

‡ All peptides are available for academic use from the Hoffmann-Röder lab upon request.

- K. Deisseroth, *Nat. Methods*, 2011, **8**, 26–29.
- W. A. Velema, W. Szymanski, and B. L. Feringa, *J. Am. Chem. Soc.*, 2014, **136**, 2178–2191.
- J. Broichhagen, J. Frank, and D. Trauner, *Acc. Chem. Res.*, 2015, **48**, 1947–1960.
- W. Costa, J. Liewald, and A. Gottschalk, *Photoswitching Proteins: Methods and Protocols (Clifton, N.J.)*, 2014, **1148**, 161–175.
- E. Reichhart, A. Ingles-Prieto, and A. Tichy, *Angew. Chem. Int. Ed.*, 2016, **55**, 6339–6342.
- S. Miyamoto and P. A. Kollman, *J. Comp. Chem.*, 1992, **13**, 952–962.
- C. Hoppmann, V. Lacey, and G. Louie, *Angew. Chem. Int. Ed.*, 2014, **53**, 3932–3936.
- J. Broichhagen, T. Podewin, H. Meyer-Berg, Y. von Ohlen, N. R. Johnston, B. J. Jones, S. R. Bloom, G. A. Rutter, A. Hoffmann-Röder, D. J. Hodson, and D. Trauner, *Angew. Chem. Int. Ed.*, 2015, **54**, 15565–15569.
- D.-R. Park, A. Shawl, T.-G. Ha, K.-H. Park, S.-Y. Kim, and U.-H. Kim, *PLoS one*, 2015, **10**, 1–20.
- B. Lee and S. Laychock, *Diabetes*, 1997, **46**, 1312–1318.
- A. Roperio, S. Soriano, E. Tuduri, L. Marroqui, N. Tellez, B. Gassner, P. Juan-Pico, E. Montanya, I. Quesada, M. Kuhn, and A. Nadal, *Endocrinology*, 2010, **151**, 3665–3674.
- L. R. Potter, S. Abbey-Hosch, and D. M. Dickey, *Endocr. Rev.*, 2005, **27**, 47–72.
- B. Edwards, R. Zimmerman, and T. Schwab, *Circ. Res.*, 1988, **62**, 191–195.
- W. Yan, F. Wu, J. Morser, and Q. Wu, *Proc. Natl. Acad. Sci. U.S.A.*, 2000, **97**, 8525–8529.
- C. Röcken, B. Peters, G. Juenemann, and W. Saeger, *Circulation*, 2002, **106**, 2091–2097.
- S. John, J. Krege, P. Oliver, and J. Hodgkin, *Science*, 1995, **267**, 679–681.
- M. Lopez, S. Wong, I. Kishimoto, S. Dubois, and V. Mach, *Nature*, 1995, **378**, 65–68.
- J. Burnett, P. Kao, D. Hu, and D. Hesser, *Science*, 1986, **231**, 1145–1147.
- M. Cowie, A. Struthers, D. Wood, and A. Coats, *Lancet*, 1997, **350**, 1347–1351.
- C. Newton-Cheh, M. G. Larson, R. S. Vasani, D. Levy, K. D. Bloch, A. Surti, C. Guiducci, S. Kathiresan, E. J. Benjamin, J. Struck, N. G. Morgenthaler, A. Bergmann, S. Blankenberg, F. Kee, P. Nilsson, X. Yin, L. Peltonen, E. Vartiainen, V. Salomaa, J. N. Hirschhorn, O. Melander, and T. J. Wang, *Nat. Genet.*, 2009, **41**, 348–353.
- V. Cannone, G. Boerrigter, A. Cataliotti, L. C. Costello-Boerrigter, T. M. Olson, P. M. McKie, D. M. Heublein, B. D. Lahr, K. R. Bailey, M. Aversa, M. M. Redfield, R. J. Rodeheffer, and J. C. Burnett, *J. Am. Coll. Cardiol.*, 2011, **58**, 629–636.
- A. Juić, P. M. Nilsson, G. Engström, B. Hedblad, O. Melander, and M. Magnusson, *PLoS ONE*, 2014, **9**, e89201.
- M. Coué, P.-M. M. Badin, I. K. Vila, C. Laurens, K. Louche, M.-A. A. Marqués, V. Bourlier, E. Mouisel, G. Tavernier, A. C. Rustan, J. E. Galgani, D. R. Joannisse, S. R. Smith, D. Langin, and C. Moro, *Diabetes*, 2015, **64**, 4033–4045.
- H. You and S. G. Laychock, *Endocrinology*, 2009, **150**, 5455–5465.
- J. McMurray, M. Packer, and A. Desai, *N. Engl. J. Med.*, 2014, **371**, 993–1004.
- Y. Saito, *J. Cardiol.*, 2010, **56**, 262–270.
- A. Aemissegger, V. Kräutler, W. F. van Gunsteren, and D. Hilvert, *J. Am. Chem. Soc.*, 2006, **127**, 2929–2936.
- T. Podewin, M. Rampp, I. Turkanovic, K. Karaghiosoff, W. Zinth, and A. Hoffmann-Röder, *Chem. Commun.*, 2015, **51**, 4001–4004.
- C. Renner and L. Moroder, *Chem. Bio. Chem.*, 2006, **7**, 868–878.
- T. Schrader, W. Schreier, T. Cordes, F. Koller, G. Babitzki, R. Denschlag, C. Renner, M. Löweneck, S.-L. Dong, P. Tavan, and W. Zinth, *Proc. Natl. Acad. Sci. U.S.A.*, 2007, **104**, 15729–15734.
- C. Hoppmann, P. Schmieder, P. Domaing, G. Vogelreiter, J. Eichhorst, B. Wiesner, I. Morano, K. Rück-Braun, and M. Beyermann, *Angew. Chem. Int. Ed.*, 2011, **50**, 7699–7702.
- E. Talaty and J. Fargo, *Chem. Commun.*, 1967, 65–66.
- M. Mimeault, A. Lean, M. Lafleur, D. Bonenfant, and A. Fournier, *Biochemistry*, 1995, **34**, 955–964.

Please do not adjust margins

Please do not adjust margins

## ARTICLE

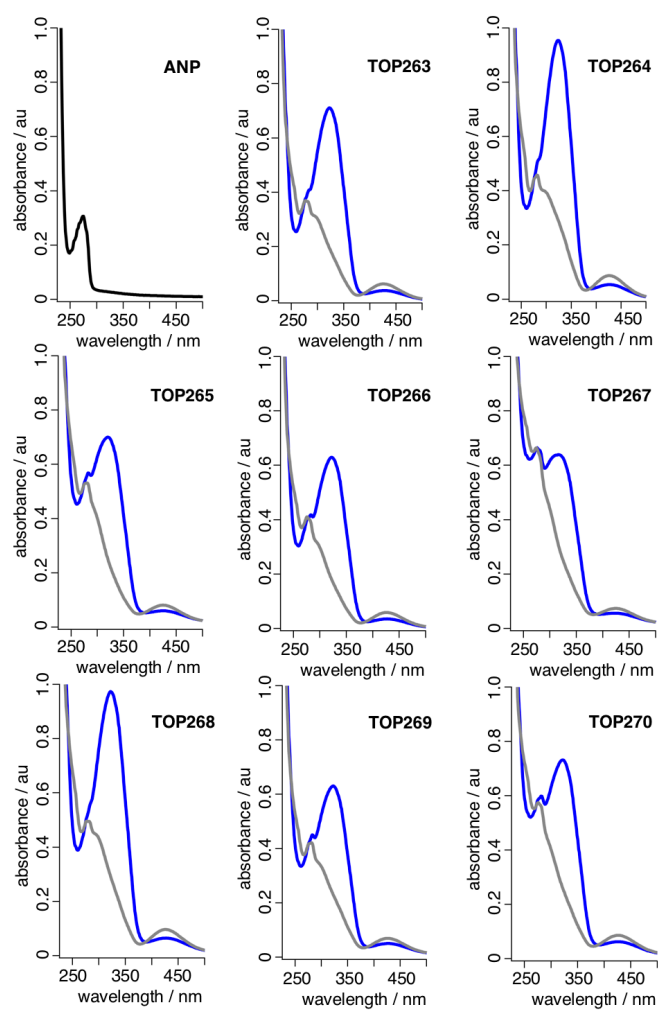
## Journal Name

- 34 Y.-C. Chao, C.-J. Cheng, H.-T. Hsieh, C.-C. Lin, C.-C. Chen, and R.-B. Yang, *Biochem. J.*, 2010, **432**, 267–273.
- 35 A. Pfeifer, A. Kilić, and L. Hoffmann, *Pharmacol. Therapeut.*, 2013, **140**, 81–91.
- 36 E. Nisoli, E. Clementi, and C. Tonello, *Br. J. Pharm.*, 1998, **125**, 888–894.
- 37 B. Haas, P. Mayer, K. Jennissen, D. Scholz, and M. Diaz, *Sci. Signal.*, 2009, **99**, 1–12.
- 38 M. Bordicchia, D. Liu, E.-Z. Z. Amri, G. Ailhaud, P. Dessi-Fulgheri, C. Zhang, N. Takahashi, R. Sarzani, and S. Collins, *J. Clin. Invest.*, 2012, **122**, 1022–1036.
- 39 A. Kiemer, N. Weber, R. Fürst, and N. Bildner, *Circ. Res.*, 2002, **90**, 874–881.
- 40 C. Moro and M. Lafontan, *Am. J. Physiol. Heart Circ. Physiol.*, 2013, **304**, 358–368.
- 41 T. Kleppisch and R. Feil, *cGMP Signalling in the Mammalian Brain: Role in Synaptic Plasticity and Behaviour*, Springer, 2009, vol. 191.
- 42 S. H. Francis, M. A. Blount, and J. D. Corbin, *Physiol. Rev.*, 2011, **91**, 651–690.
- 43 R. Feil, S. Lohmann, H. de Jonge, and U. Walter, *Circ. Res.*, 2003, **93**, 907–916.
- 44 M. Biel and S. Michalakakis, *Cyclic Nucleotide-Gated Channels*, Springer, Berlin Heidelberg, 2009, vol. 191.
- 45 A. Alioua, Y. Tanaka, M. Wallner, and F. Hofmann, *J. Biol. Chem.*, 1998, **273**, 32950–32956.
- 46 J. Schlossmann, A. Ammendola, K. Ashman, and X. Zong, *Nature*, 2000, **404**, 197–201.
- 47 K. Koch and D. Dell’Orco, *Front. Mol. Neurosci.*, 2015, **8**, 67.
- 48 H. Ogawa, Y. Qiu, C. M. Ogata, and K. S. Misono, *J. Biol. Chem.*, 2004, **279**, 28625–28631.
- 49 X. L. He, A. Dukkupati, and K. C. Garcia, *J. Mol. Biol.*, 2006, **361**, 698–714.
- 50 F. Marks, U. Klingmueller, and K. Mueller-Decker, *Cellular signal processing*, Taylor & Francis, 2009, vol. 8.
- 51 C. M. Panayiotou, R. Baliga, R. Stidwill, V. Taylor, M. Singer, and A. J. Hobbs, *Br. J. Pharmacol.*, 2010, **160**, 2045–2054.
- 52 F. Ortola, B. Ballermann, and S. Anderson, *J. Clin. Invest.*, 1987, **80**, 670–674.
- 53 H. Matsubara, Y. Mori, J. Yamamoto, and M. Inada, *Circ. Res.*, 1990, **67**, 803–813.
- 54 M.-L. Lazo-de-la-Vega-Monroy and A. Vilches-Flores, *Immunol. Endocr. Metabolic Agents Med. Chem.*, 2014, **14**, 8–14.
- 55 G. Gruden, A. Landi, and G. Bruno, *Diabetes Care*, 2014, **37**, 2899–2908.
- 56 N. Matsuura, T. Ishikawa, S. Abe, H. Yuyama, F. Sugino, K. Ishii, and K. Nakayama, *Life Sci.*, 1999, **65**, 1515–1522.
- 57 M.-H. H. Ryu, O. V. Moskvina, J. Siltberg-Liberles, and M. Gomelsky, *J. Biol. Chem.*, 2010, **285**, 41501–41508.
- 58 T. Kim, M. Folcher, M. D.-E. Baba, and M. Fussenegger, *Angew. Chem. Int. Ed.*, 2015, **54**, 5933–5938.
- 59 G. M. Avelar, R. I. Schumacher, P. A. Zaini, G. Leonard, T. A. Richards, and S. L. Gomes, *Curr. Biol.*, 2014, **24**, 1234–1240.
- 60 S. Gao, J. Nagpal, M. W. Schneider, V. Kozjak-Pavlovic, G. Nagel, and A. Gottschalk, *Nat. Commun.*, 2015, **6**, 8046.
- 61 S. H. Francis, J. L. Busch, J. D. Corbin, and D. Sibley, *Pharmacol. Rev.*, 2010, **62**, 525–563.
- 62 M. Bose, D. Groff, J. Xie, E. Brustad, and P. G. Schultz, *J. Am. Chem. Soc.*, 2006, **128**, 388–389.
- 63 T. Schrader, T. Cordes, W. Schreier, F. Koller, S.-L. Dong, L. Moroder, and W. Zinth, *J. Phys. Chem. B*, 2011, **115**, 5219–5226.
- 64 C. Hoppmann, I. Maslennikov, S. Choe, and L. Wang, *Journal of the American Chemical Society*, 2015, **137**, 11218–11221.
- 65 S. Samanta, C. Qin, A. J. Lough, and G. A. Woolley, *Angew. Chem. Int. Ed.*, 2012, **51**, 6452–6455.
- 66 D. Konrad, J. Frank, and D. Trauner, *Chem. Eur. J.*, 2016, **22**, 4364–4368.
- 67 A. V. Karginov, F. Ding, P. Kota, N. V. Dokholyan, and K. M. Hahn, *Nat. Biotechnol.*, 2010, **28**, 743–747.

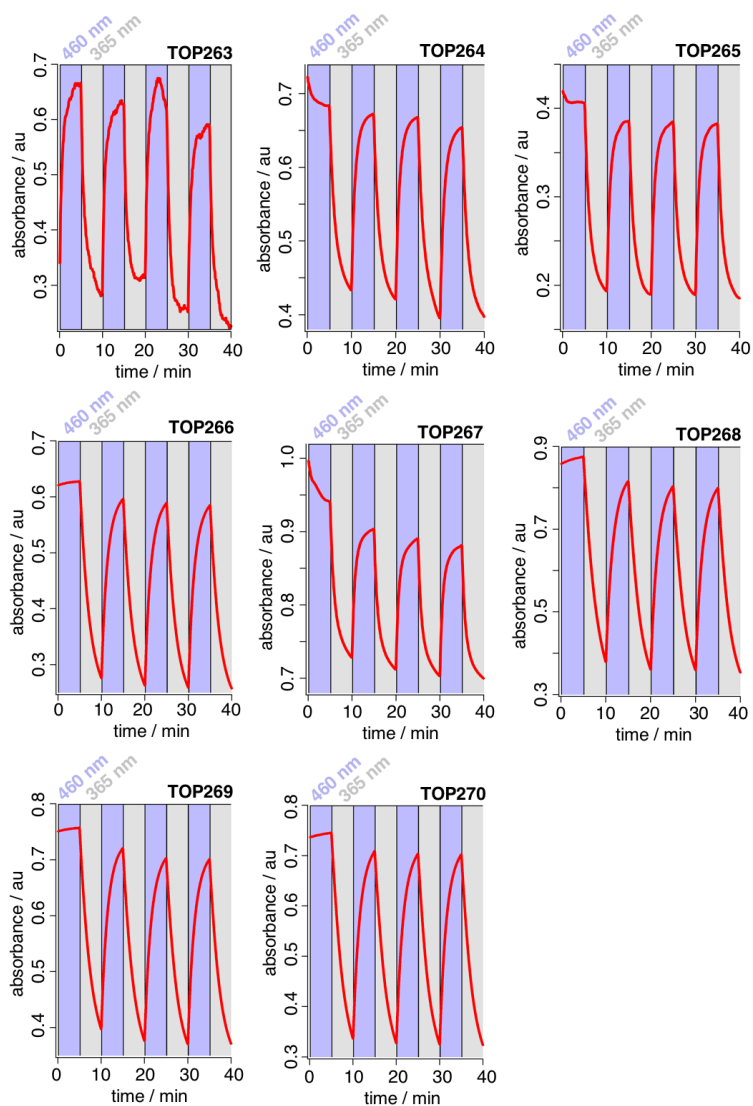
Please do not adjust margins

## 2.2 SUPPLEMENTARY FIGURES AND TABLES

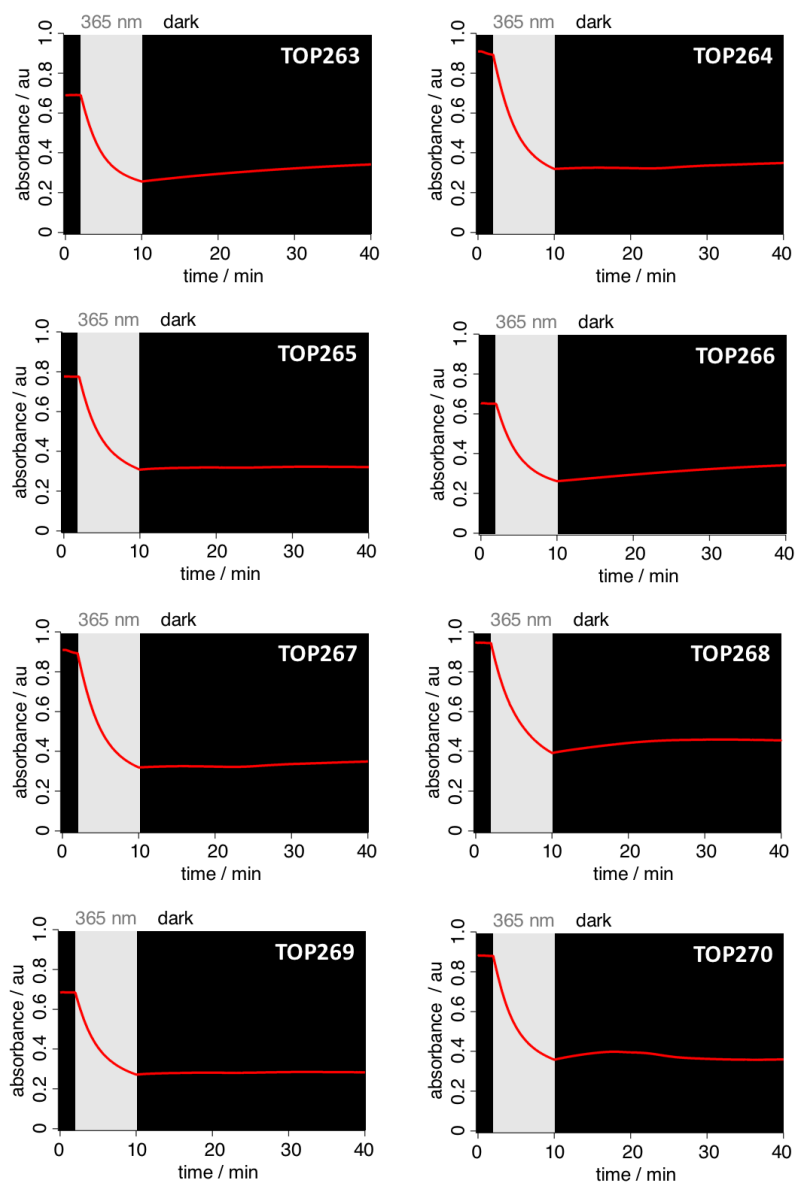
## 3. Supplementary Figures and Tables



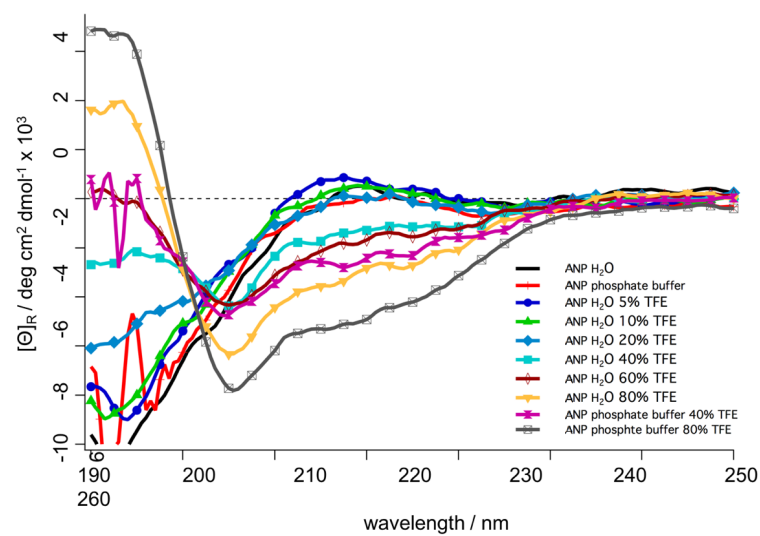
**Supplementary Figure 1:** UV/Vis spectra of ANP (black) and the *cis*- (gray) and *trans*-isomers (blue) of peptides TOP263-TOP270 in PBS buffer at approx. 50  $\mu\text{M}$  conc.; 25  $^{\circ}\text{C}$ .



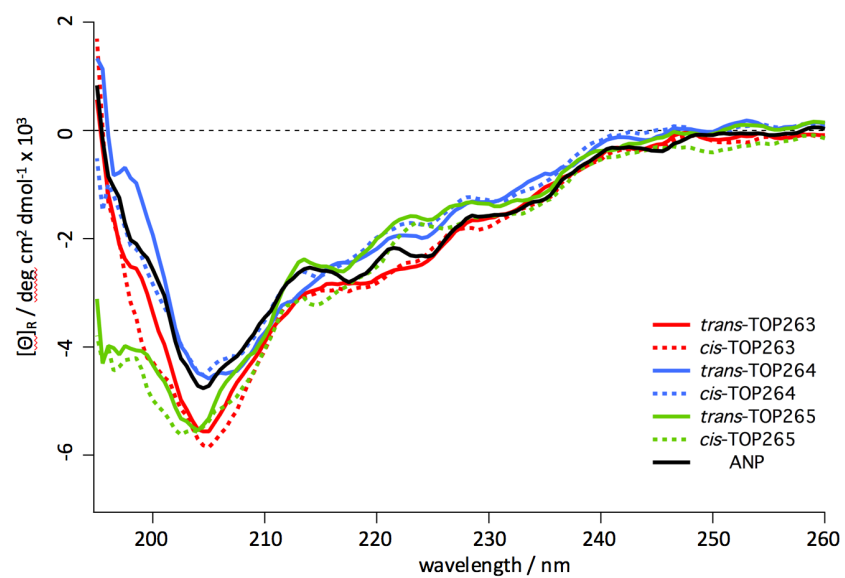
**Supplementary Figure 2:** UV/Vis switching kinetics of peptides TOP263-TOP270 in PBS buffer measured over abs. at 330 nm; 50  $\mu\text{M}$  conc.; 25  $^{\circ}\text{C}$ . Reversible *cis* $\leftrightarrow$ *trans*-isomerization was recorded by 365 (*trans* $\rightarrow$ *cis*) and 460 nm (*cis* $\rightarrow$ *trans*) illumination cycles (5 min).



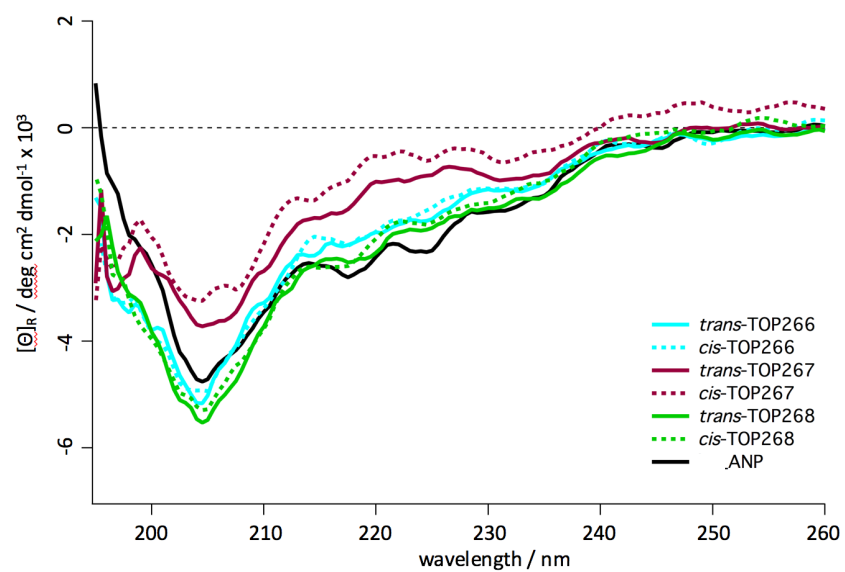
**Supplementary Figure 3:** UV/Vis bistability measurement of peptides *cis*-TOP263-TOP270 at 330 nm in PBS buffer; 25 °C.



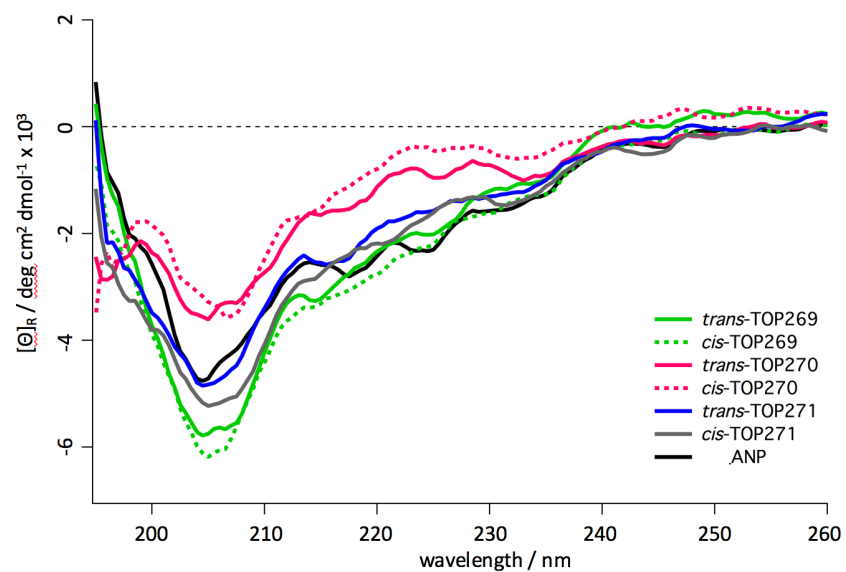
**Supplementary Figure 4:** CD spectra of ANP peptide in H<sub>2</sub>O, 20 phosphate buffer pH 5.5 and aqueous and buffered TFE (5-80%) solutions. Raising rates of TFE lead to stabilization of secondary structure domains and increase the peptide helical content, with a maximum at 80% aqueous/buffered TFE solutions.



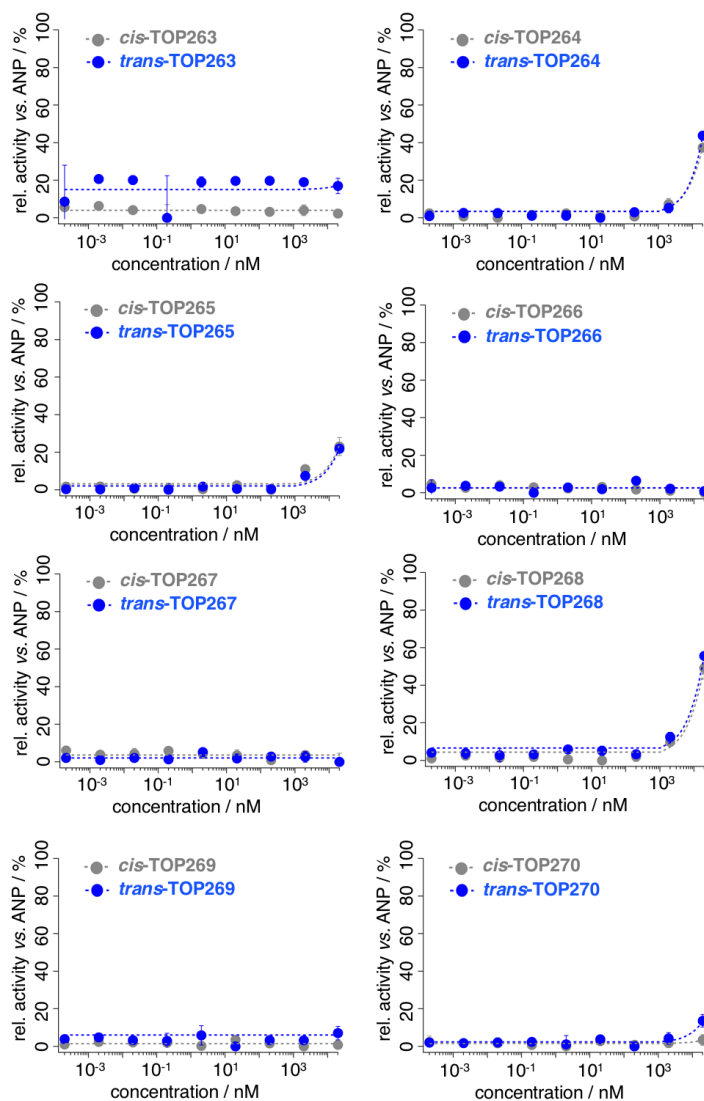
**Supplementary Figure 5:** CD spectra of the *cis/trans*-isomers of peptides TOP263, TOP264 and TOP265 with two amino acids substituted by AMPP.



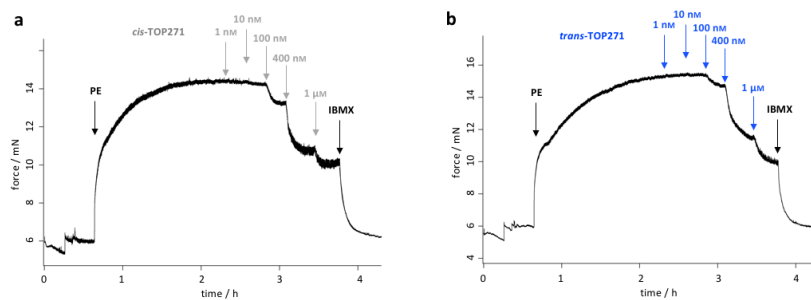
**Supplementary Figure 6:** CD spectra of the *cis/trans*-isomers of peptides TOP266, TOP267 and TOP268 with three amino acids substituted by AMPP.



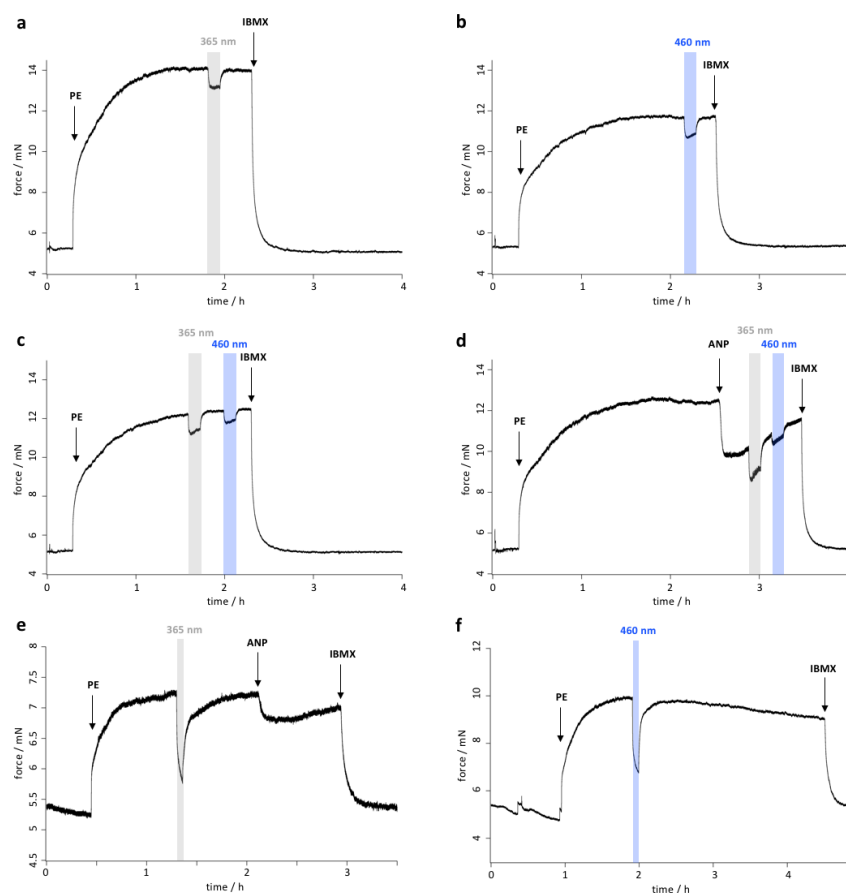
**Supplementary Figure 7:** CD spectra of the *cis/trans*-isomers of peptides TOP269, TOP270 and TOP271 with two amino acids substituted by AMPP.



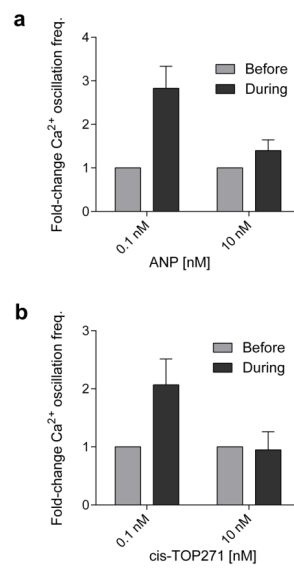
**Supplementary Figure 8:** cGMP dose-responses of peptides TOP263-270 recorded in YFP and NPR-A co-transfected HEK293t cells using a cisbio HTRF<sup>®</sup> kit.  $EC_{50}$  values of TOP264, -265 and -268 were not calculated, nor were experiments repeated due to low activation in the  $\mu$ M range.



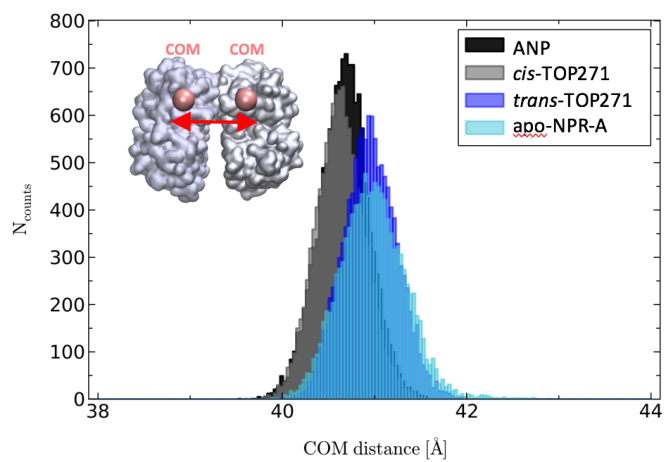
**Supplementary Figure 9:** Representative traces for aortic ring tensometry vasodilatory dose-responses recorded for *cis*- (gray, a) and *trans*-TOP271 (blue, b).



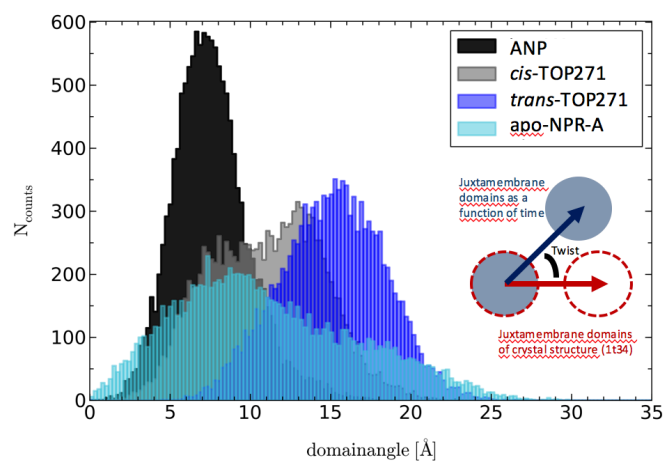
**Supplementary Figure 10:** Representative traces for aortic ring tensometry illumination control experiments showing the reversibility of UV (365 nm) and blue (460 nm) light induced vasoactive responses. Rings were precontracted with 1  $\mu$ M phenylephrine (PE) and maximally dilated with 100  $\mu$ M 3-isobutyl-1-methylxanthin (IBMX). To test the reversibility on dilated rings, 17 nM ANP was added in some cases. (a-d) Indirect illumination of the surrounding organ bath solution. (e,f) Direct illumination of the tissue. (a) Vasodilation with UV light (365 nm). (b) Vasodilation with blue light (460 nm). (c) Vasodilation with UV (365 nm) and blue light (460 nm). (d) Reversible dilational effect of UV (365 nm) and blue light (460 nm) on vasodilated rings (17 nM ANP). (e) Reversible effect of direct tissue illumination with UV light (365 nm). (f) Reversible effect of direct tissue illumination with blue light (460 nm).



**Supplementary Figure 11:** (a) Low (0.1 nM) but not high (10 nM) concentrations of ANP stimulate increases in pancreatic beta cell  $\text{Ca}^{2+}$  spiking frequency ( $n = 5-7$  islets for each concentration). b) As for a), but *cis*-TOP271 ( $n = 4-7$  islets for each concentration).



**Supplementary Figure 12:** Center-of-mass distance distribution of the membrane-distal NPR-A domains A and B after 1  $\mu$ s simulation show no significant ligand-dependence for bound native ANP (black), *cis/trans*-TOP271 (gray and blue, respectively) and apo-NPR-A (cyan).



**Supplementary Figure 13:** Twist angle distributions of the membrane-proximal NPR-A subdomains with respect to the crystal structure 1t34<sup>5</sup> indicating only a slight isomer-dependence, with the distributions of ANP and *cis*-TOP271 (black and gray, respectively) having more overlap than ANP and *trans*-TOP271 (blue).

Research Article Manuscript

**Supplementary Table 3:** Photoswitching kinetics of peptides TOP263-271.

<b>TOP263</b>	<b><math>\tau</math> (sec)</b>
<i>cis</i>	67.2 $\pm$ 3.7
<i>trans</i>	46.2 $\pm$ 2.2
<b>TOP264</b>	
<i>cis</i>	83.6 $\pm$ 1.6
<i>trans</i>	55.1 $\pm$ 1.4
<b>TOP265</b>	
<i>cis</i>	71.3 $\pm$ 1.2
<i>trans</i>	50.3 $\pm$ 0.8
<b>TOP266</b>	
<i>cis</i>	136.6 $\pm$ 1.1
<i>trans</i>	84.8 $\pm$ 0.8
<b>TOP267</b>	
<i>cis</i>	84.8 $\pm$ 6.4
<i>trans</i>	62.0 $\pm$ 4.0
<b>TOP268</b>	
<i>cis</i>	174.3 $\pm$ 7.1
<i>trans</i>	95.7 $\pm$ 2.6
<b>TOP269</b>	
<i>cis</i>	167.8 $\pm$ 8.9
<i>trans</i>	98.9 $\pm$ 3.1
<b>TOP270</b>	
<i>cis</i>	187.0 $\pm$ 6.5
<i>trans</i>	103.2 $\pm$ 2.8
<b>TOP271</b>	
<i>cis</i>	163.2 $\pm$ 5.3
<i>trans</i>	95.8 $\pm$ 0.8

Research Article Manuscript

**Supplementary Table 4:**  $k_{\text{obs}}$  of thermal *cis*→*trans* relaxation of peptides TOP263-271.

	$k_{\text{obs}} \times 10^{-4}$ a.u. / min
<b>TOP263</b>	2.825 ± 0.008
<b>TOP264</b>	0.945 ± 0.010
<b>TOP265</b>	0.316 ± 0.004
<b>TOP266</b>	2.726 ± 0.006
<b>TOP267</b>	0.942 ± 0.010
<b>TOP268</b>	2.020 ± 0.026
<b>TOP269</b>	0.275 ± 0.003
<b>TOP270</b>	1.620 ± 0.069
<b>TOP271</b>	0.975 ± 0.010

**Supplementary Table 5:**  $^1\text{H}/^{13}\text{C}$ -NMR chemical shifts of *trans*-TOP271.

Residue	$^1\text{H}$ chem. shifts [ppm]	$^{13}\text{C}$ chem. shifts [ppm]
<b>Ser1</b>	H $\alpha$ 4.09, H $\beta^*$ 3.95	C $\alpha$ 56.8, C $\beta$ 62.6
<b>Leu2</b>	NH 8.52, H $\alpha$ 4.35, H $\beta^*$ 1.55, H $\gamma$ 1.54, H $\delta\alpha$ 0.82, H $\delta\beta$ 0.86	C $\alpha$ 55.0, C $\beta$ 42.1, C $\gamma$ 26.4, C $\delta\alpha$ 23.0, C $\delta\beta$ 23.9
<b>Arg3</b>	NH 8.06, H $\alpha$ 4.26, H $\beta\alpha$ 1.79, H $\beta\beta$ 1.69, H $\gamma\alpha$ 1.54, H $\gamma\beta$ 1.55, H $\delta^*$ 3.07, H $\epsilon$ 7.07	C $\alpha$ 55.6, C $\beta$ 30.7, C $\gamma$ 26.7, C $\delta$ 42.8
<b>Arg4</b>	-	-
<b>Ser5</b>	NH 7.96, H $\alpha$ 4.29, H $\beta\alpha$ 3.62, H $\beta\beta$ 3.69	C $\alpha$ 58.1, C $\beta$ 63.3
<b>Ser6</b>	NH 7.90, H $\alpha$ 4.22, H $\beta\alpha$ 3.64, H $\beta\beta$ 3.59	C $\alpha$ 58.4, C $\beta$ 63.1
<b>Cys7</b>	NH 8.52, H $\alpha$ 4.59, H $\beta^*$ 2.72	C $\alpha$ 53.4, C $\beta$ 38.0
<b>Phe8</b>	NH 8.11, H $\alpha$ 4.56, H $\beta\alpha$ 3.11, H $\beta\beta$ 2.96, H $\delta^*$ 7.25, H $\epsilon^*$ 7.18, H $\zeta$ 7.11	C $\alpha$ 57.6, C $\beta$ 38.9, C $\delta^*$ 130.8, C $\epsilon^*$ 131.2, C $\zeta$ 129.2
<b>Gly9</b>	NH 8.18, H $\alpha\alpha$ 3.73, H $\alpha\beta$ 3.71	C $\alpha$ 44.8
<b>Gly10</b>	NH 8.14, H $\alpha\alpha$ 3.82, H $\alpha\beta$ 3.81	C $\alpha$ 44.9
<b>Arg11</b>	NH 7.66, H $\alpha$ 4.18, H $\beta\alpha$ 1.60, H $\beta\beta$ 1.49, H $\gamma^*$ 1.35, H $\delta^*$ 3.00, H $\epsilon$ 6.99	C $\alpha$ 55.2, C $\beta$ 30.5, C $\gamma$ 26.7, C $\delta$ 42.7
<b>Met12</b>	NH 7.57, H $\alpha$ 4.44, H $\beta\alpha$ 2.00,	C $\alpha$ 54.3, C $\beta$ 31.9, C $\gamma$ 31.5, C $\epsilon$ 16.0

## Research Article Manuscript

	H $\beta$ b 1.91, H $\gamma$ a 2.47, H $\gamma$ b 2.39, H $\epsilon$ * 1.98	
<b>Asp13</b>	NH 7.76, H $\alpha$ 4.47, H $\beta$ a 2.97, H $\beta$ b 2.86	C $\alpha$ 57.3, C $\beta$ 38.8
<b>Arg14</b>	NH 7.76, H $\alpha$ 4.20, H $\beta$ a 1.63, H $\beta$ b 1.52, H $\gamma$ * 1.38, H $\delta$ * 3.02, H $\epsilon$ 7.01	C $\alpha$ 55.2, C $\beta$ 30.6, C $\gamma$ 26.3, C $\delta$ 42.7
<b>Ile15</b>	NH 7.82, H $\alpha$ 3.99, H $\beta$ 1.76, H $\gamma$ 1a 1.04, H $\gamma$ 1b 1.02, H $\gamma$ 2* 0.75, H $\delta$ 1* 0.72	C $\alpha$ 61.6, C $\beta$ 37.8, C $\gamma$ 1 27.0, C $\gamma$ 2 16.5, C $\delta$ 1 11.8
<b>Gly16</b>	NH 8.09, H $\alpha$ * 3.87	C $\alpha$ 44.8
<b>Ala17</b>	NH 7.87, H $\alpha$ 4.23, H $\beta$ * 1.31	C $\alpha$ 52.4, C $\beta$ 18.5
<b>Gln18</b>	NH 8.15, H $\alpha$ 4.31, H $\beta$ a 2.12, H $\beta$ b 1.98, H $\gamma$ * 2.30	C $\alpha$ 55.7, C $\beta$ 29.1, C $\gamma$ 1 33.5
<b>AMPP</b>	NH 8.19, H2* 4.41, H4 7.66, H6 7.68, H7 7.46, H8 7.38, H12 7.73, H14 7.42, H15 7.49, H16 7.71, H17a 3.80, H17b 3.73	C2 44.9, C4 123.1, C6 123.8, C7 131.9, C8 132.5, C12 125.1, C14 134.6, C15 131.9, C16 123.8, C17 43.9
<b>Cys23</b>	NH 8.52, H $\alpha$ 4.64, H $\beta$ * 2.69	C $\alpha$ 53.2, C $\beta$ 38.1
<b>Asn24</b>	NH 7.88, H $\alpha$ 4.51, H $\beta$ a 2.98, H $\beta$ a 2.91	C $\alpha$ 57.3, C $\beta$ 39.0
<b>Ser25</b>	NH 8.24, H $\alpha$ 4.42, H $\beta$ a 3.88, H $\beta$ a 3.74	C $\alpha$ 58.1, C $\beta$ 63.5
<b>Phe26</b>	NH 7.62, H $\alpha$ 4.46, H $\beta$ a 3.02, H $\beta$ a 2.83, H $\delta$ * 7.13, H $\epsilon$ * 7.04, H $\zeta$ 7.20	C $\alpha$ 56.7, C $\beta$ 38.1, C $\delta$ * 130.7, C $\epsilon$ * 131.2, C $\zeta$ 129.3
<b>Arg27</b>	-	-
<b>Tyr28</b>	NH 7.63, H $\alpha$ 4.46, H $\beta$ a 3.02, H $\beta$ a 2.84, H $\delta$ * 7.01, H $\epsilon$ * 6.73, H $\zeta$ 7.20	C $\alpha$ 58.1, C $\beta$ 38.1, C $\delta$ * 132.7, C $\epsilon$ * 117.5

**Supplementary Table 6:** Average twist angle of NPR-A membrane-proximal domains upon ligand binding.

Twist angle	Mean / °	Stddev / °
<b>ANP</b>	7.56	2.37
<i>cis</i> - <b>TOP271</b>	10.99	3.51
<i>trans</i> - <b>TOP271</b>	15.10	3.25
<b>apo-NPR-A</b>	11.07	5.58

## 2.3 ADDITIONAL COMPOUNDS AND DATA

During this work, two additional photochromic AzoANP peptides have been designed, synthesized and tested, but they have not found their way into the final manuscript. In these two peptides, dubbed N24AzoPhe-ANP **2.2** and S25AzoPhe-ANP **2.3**, the side chain photoswitch AzoPhe **1.24** was incorporated instead of AMPP **1.22**. This implies a completely different azologization pattern, where **1.27** substitutes only a single amino acid and not two, three or four, as it is the case for the nine AzoANP peptides TOP263-270 and TOP271 **2.1**. As can be deduced from the compound abbreviations, sites for single amino acid substitutions in native ANP are Asn24 and Ser25 in peptides **2.2** and **2.3**, respectively. Asn24 and Ser25, which are located on the C-terminal tail of ANP adjacent to the disulfide bridge, were selected based on the crystal structure of a truncated ANP ligand bound to NPR-A (pdb: 1yk0). This structure revealed the position of Asn24 and Ser25 close to a hydrophobic region comprising residues Ile188, Tyr189 and Phe191 within the B-domain of NPR-A (Figure 2.1).

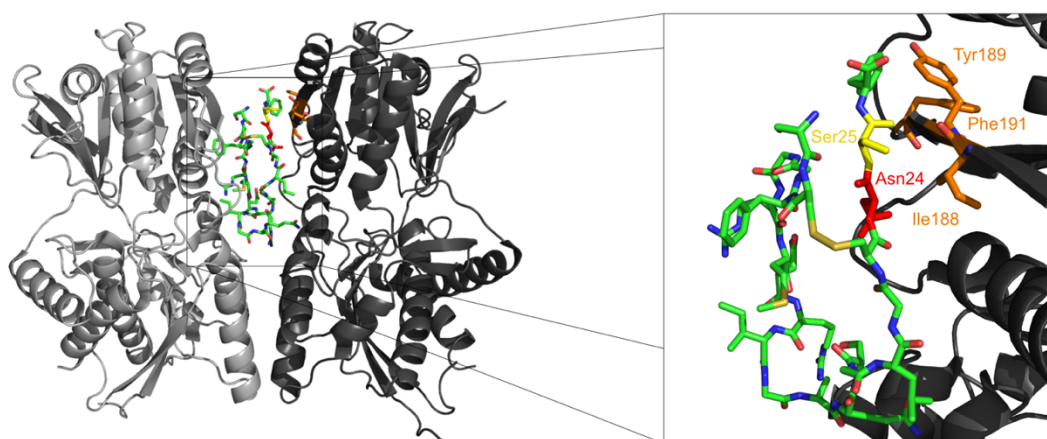


**Figure 2.1:** X-Ray crystal structure based design scheme for N24AzoPhe-ANP **2.2** and S25AzoPhe-ANP **2.3**. Left: X-ray crystal structure of both homo dimers of the NPR-A receptor (subunit A light gray, subunit B dark gray) with bound truncated ligand ANP (green) (pdb: 1yk0). Right: zoom into the ANP and NPR-A interactions with marked AzoPhe-substituted amino acids Asn24 (red) and Ser25 (yellow) of ANP and hydrophobic residues Ile188, Tyr189 and Phe191 (all orange) of the homodimer B of NPR-A.

It was anticipated that either the *cis*- or the *trans*-form of AzoPhe **1.24** would direct the exo phenyl ring of the azobenzene unit into the hydrophobic region, resulting in deviating binding affinities of both peptide isomers and a biased receptor activation. Similar to the other nine AzoANP peptides, **2.2** and **2.3** were initially assessed through detection of their photoswitching kinetics and through the measurement of cGMP synthesis dose-response curves using with NPR-A transiently transfected HEK293t cells. Both peptides showed the expected *cis/trans*-switching with 365 nm UV light or 430 nm blue light and robust switching kinetics. The observed  $\tau$ -values for the photoconversion rates were  $\tau_{trans \rightarrow cis} = 133.4 \pm 5.8$  sec and  $\tau_{cis \rightarrow trans} = 95.0 \pm 0.2$  sec for **2.2** and  $\tau_{trans \rightarrow cis} = 116.4 \pm 3.2$  sec and  $\tau_{cis \rightarrow trans} = 92.9 \pm 0.5$  sec for **2.3**, and therefore similar to the remaining AzoANP peptides.

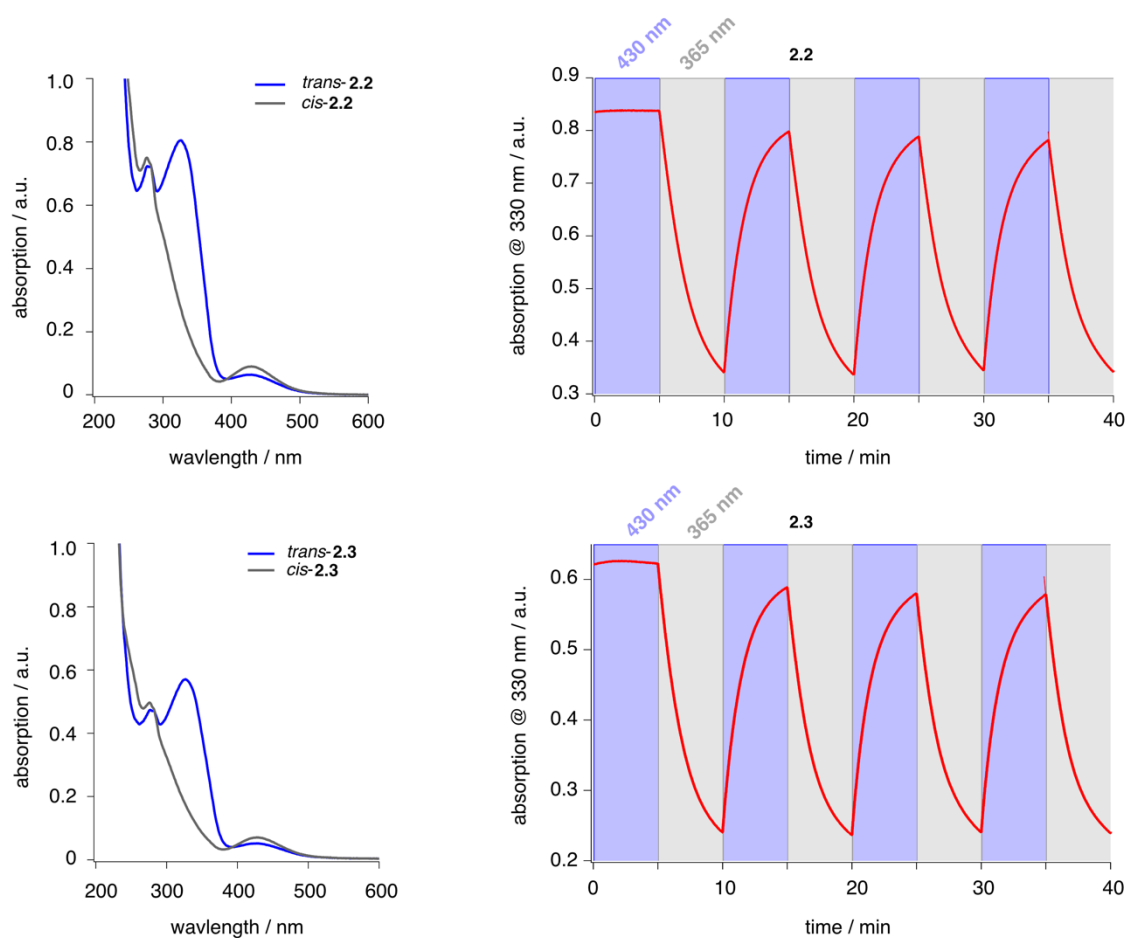


**Figure 2.2:** UV/Vis spectra and UV switching kinetics of **2.2** and **2.3**. Top left: UV/Vis spectra of *cis/trans*-**2.2**. Top right: UV switching kinetics of **2.2** measured through the absorption at 330 nm after photoswitching with 365 nm UV light (*trans* → *cis*) and 430 nm blue light (*cis* → *trans*). Bottom left: UV/Vis spectra of *cis/trans*-**2.3**. Bottom right: UV switching kinetics of **2.3** measured through the absorption at 330 nm after photoswitching with 365 nm UV light (*trans* → *cis*) and 430 nm blue light (*cis* → *trans*).

The  $EC_{50}$  values obtained for both isomers of **2.2** were  $EC_{50,cis} = 72.1 \pm 1.3$  nM and  $EC_{50,trans} = 149.0 \pm 22.5$  nM. With  $EC_{50}$  values of  $EC_{50,cis-2.3} = 207.3 \pm 9.8$  nM and  $EC_{50,trans-2.3} = 894.9 \pm 37.1$  nM both isomers of **2.3** have a weaker potency towards NPR-A than **2.2** (see table 2.1 to compare with  $EC_{50}$  of ANP and TOP271 **2.1**). However, although **2.2** is a better agonist it shows only a roughly two-fold difference in NPR-A activation between both isomers, while **2.3** has an over four-fold difference in NPR-A activation and is comparable to TOP271 **2.1**. Thus, **2.1** was chosen as the lead compound based on the large difference in receptor activation of *cis/trans*-**2.1**, together with its higher potency. Compounds **2.2** and **2.3** were dismissed, not least because of their different photoswitch substitution scheme. Nevertheless, the drop in potency and simultaneous rise in isomer-bias between **2.2** and **2.3** remains very interesting and is worth investigating through structural analysis of ligand-bound NPR-A structures.

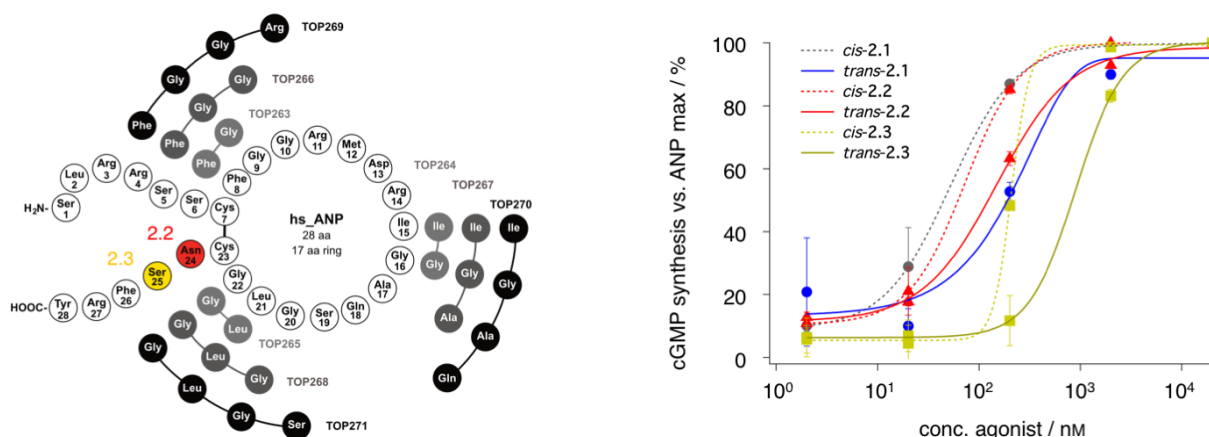


**Figure 2.3: Overview of AzoANP peptides and cGMP dose-response curves for TOP271 2.1, N24AzoPhe-ANP 2.2 and S25AzoPhe-ANP 2.3.** Left: schematic overview of the AMPP 22 substitution pattern in the AzoANP peptides TOP263-270 and TOP271 2.1, and dismissed compounds 2.2 and 2.3 with the AzoPhe 1.24 photoswitch. Right: dose-response curves of both *cis/trans*-isomers of TOP271 2.1, 2.2 and 2.3 for cGMP synthesis in with NPR-A transiently transfected HEK293t cells. Values represent mean  $\pm$  SEM ( $n = 3$  technical repeats).

**Table 2.1:  $EC_{50}$  values of peptides ANP, TOP271 2.1, N24AzoPhe-ANP 2.2 and S25AzoPhe-ANP 2.3.**

Peptide	$EC_{50}$ <i>trans</i> (nM)	$EC_{50}$ <i>cis</i> (nM)	$EC_{50}$ <i>trans/cis</i>
ANP	2.0 $\pm$ 0.4	-	-
TOP271 2.1	467.9 $\pm$ 59.4	126.6 $\pm$ 10.9	3.7 $\pm$ 0.8
N24AzoPhe-ANP 2.2	149.0 $\pm$ 22.5	72.1 $\pm$ 1.3	2.1 $\pm$ 0.3
S25AzoPhe-ANP 2.3	894.9 $\pm$ 37.1	207.3 $\pm$ 9.8	4.3 $\pm$ 0.4

## 2.4 SUMMARY AND OUTLOOK

The natriuretic peptides are important regulatory hormones in eukaryotes and involved in maintaining blood and water homeostasis and blood pressure regulation. Many cardiac diseases are associated with dysfunctional expression of natriuretic peptides through gene defects<sup>154,156</sup>, and the plasma levels of atrial (ANP) and the B-type (BNP) natriuretic peptide are used as markers for the detection of atrial fibrillation, arrhythmia and heart failure<sup>157,158</sup>. Moreover, ANP is used in many preclinical trials as treatment for heart and renal diseases, but in part with varying effects<sup>159-161</sup>. Recently, there is also growing evidence for a gut-heart axis and elevated ANP plasma levels are related with obesity and diabetes risk<sup>162-165</sup>. Although originally discovered in 1981 (ref. 166), there are many recent discoveries of the vast interactions of ANP and its natriuretic peptide receptor A (NPR-A) throughout the body, making this hormone and its receptor a worthwhile target for a photopharmacological approach. This is supported through the affiliation of the NPR-A to the class of receptor-linked enzymes, which was not amenable to photopharmacology hitherto.

To gain optical control over NPR-A signaling nine photochromic AzoANP peptides TOP263-270 and TOP271 2.1 carrying the AMPP 1.22 photoswitch, and the two peptides N24AzoPhe-ANP 2.2 and S25AzoPhe-ANP 2.3 with the AzoPhe 1.27 photoswitch, were synthesized. After initial assessment of all the AzoANP peptides and screening of cGMP synthesis in with NPR-A transiently transfected HEK293t

cells TOP271 **2.1** was selected as most suitable candidate. This compound not only showed a merely ~63x times reduced potency, which is remarkable for a native compound altered with a hydrophobic photoswitch that substitutes four amino acids, but also showed a roughly four-fold difference in NPR-A activation between the more potent *cis*-isomer and the weaker *trans*-form. This difference in potency is enough to trigger pronounced physiological responses, which was demonstrated in murine smooth muscle tissue and islets of Langerhans. Thereby it was possible to optically control the smooth muscle tone by inducing vasoactive responses, *i.e.* illumination of aortic rings with UV light led to vasodilation, while blue light provoked vasoconstriction. In islets of Langerhans ANP and *cis*-**2.1** caused complete suppression of Ca<sup>2+</sup> spiking, while *trans*-**2.1** showed no inhibitory effects. The suppression through the *cis*-isomer could be abolished by blue light illumination and *trans*-accumulation, demonstrating the reversibility of **2.1** action.

However, the complete spectrum of ANP action and function throughout the body so far remains elusive, which can easily be recognized by the contradictory results about ANP induced stimulation<sup>167-169</sup> or suppression of beta cell function<sup>170,171</sup>. Furthermore, the direct effect of ANP on heart rate and action potential is also being controversially discussed<sup>154,172,173</sup>. This shows the need for a tool to precisely control and dissect the actions of ANP in health and disease, and TOP271 **2.1** is the first PCL to successfully facilitate optical control of NPR-A signaling and subsequent physiological actions. Moreover, it provides a valuable blue print for the next generation of ANP based photopharmacophores and by being available on gram scale through amenable photoswitch and peptide synthesis, this compound has the future to become a widely used photopharmacological tool. A remaining drawback for *in vivo* applications are the photoswitching wavelengths in the UV region, but this disadvantage is currently being addressed through the design of red-shifted AMPP **1.22** photoswitch derivatives.

## 2.5 EXPERIMENTAL

This chapter lists experimental details and spectroscopic and spectrometric data of the AzoANP peptides TOP263-270, TOP271 **2.1**, N24AzoPhe-ANP **2.2** and S25AzoPhe-ANP **2.3**. Details on peptide synthesis, chemicals and methods for compounds TOP263-270 and **2.1** can be found in the SUPPORTING INFORMATION on the enclosed CD. Details on peptide synthesis for **2.2** and **2.3** can be found in this chapter, chemicals and general methods are listed in the APPENDIX.

### 2.5.1 SPECTROSCOPIC AND SPECTROMETRIC DATA OF TOP263-271

*Research Article Manuscript*

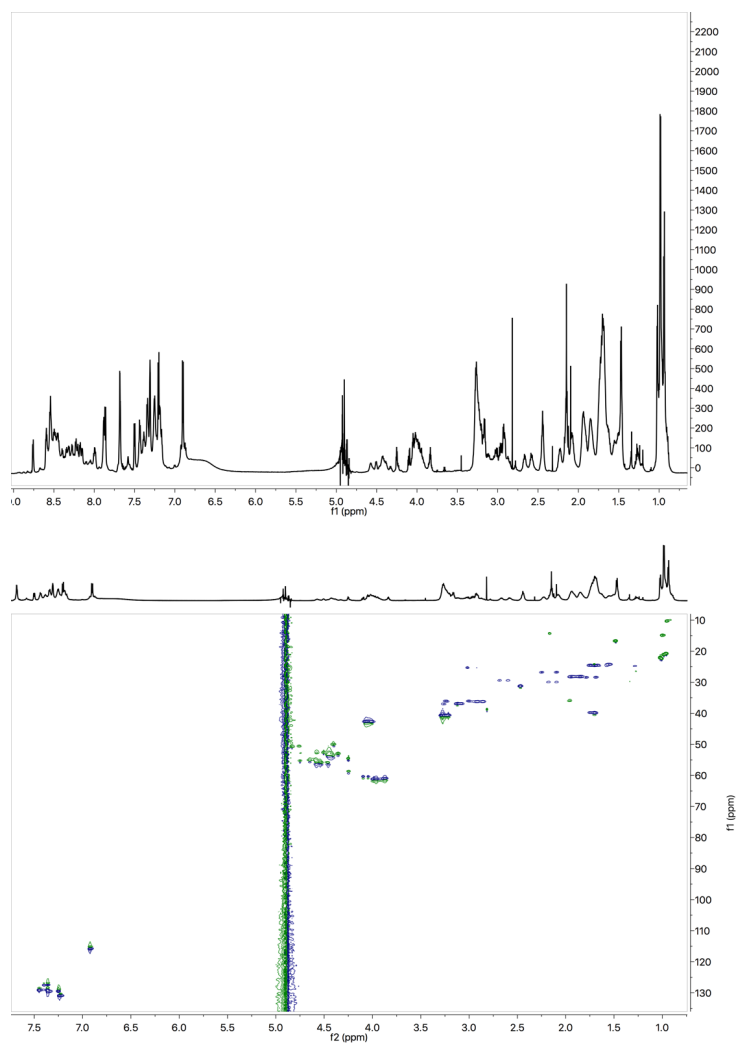
#### 1.6. HRMS-ESI of peptides TOP263-TOP271

Peptid	calc. mono isotopic mass	found mono isotopic mass	$\Delta m/m$ (ppm)
ANP	$[M+4H]^{4+} = 3084.4804$	3084.4858	-1.75
TOP263	$[M+4H+H_2O+3MeCN]^{4+} = 3273.5980$	3273.5979	0.02
TOP264	$[M+5H-CH_4N_3]^{5+} = 3148.4786$	3148.4780	1.87
TOP265	$[M+4H+Na]^{5+} = 3190.5397$	3190.5281	3.68
TOP266	$[M+2H+2NH_4+Na]^{5+} = 3148.5192$	3148.5225	-1.08
TOP267	$[M+5H-NH]^{5+} = 3079.4411$	3079.4391	0.70
TOP268	$[M+5H-NH]^{5+} = 3093.4447$	3093.4495	0.97
TOP269	$[M+4H]^{4+} = 2918.3840$	2918.3774	-2.29
TOP270	$[M+5H-H_2O]^{5+} = 2948.3868$	2948.3840	2.13
TOP271	$[M+5H-H_2O]^{5+} = 3003.4300$	3003.4323	2.25

Research Article Manuscript

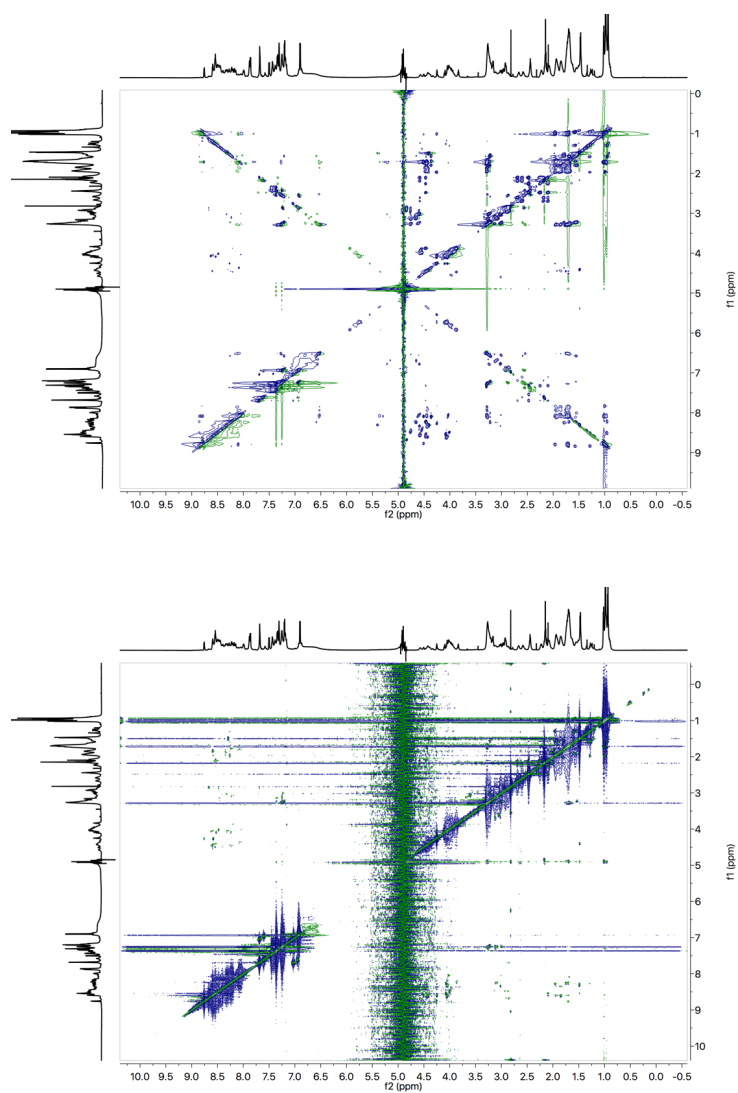
## 1.5. NMR Spectra of ANP and *cis/trans*-TOP271 peptides

### 1.5.1. ANP



$^1\text{H}$ - (top) and HSQC- (bottom) NMR spectra of ANP peptide.

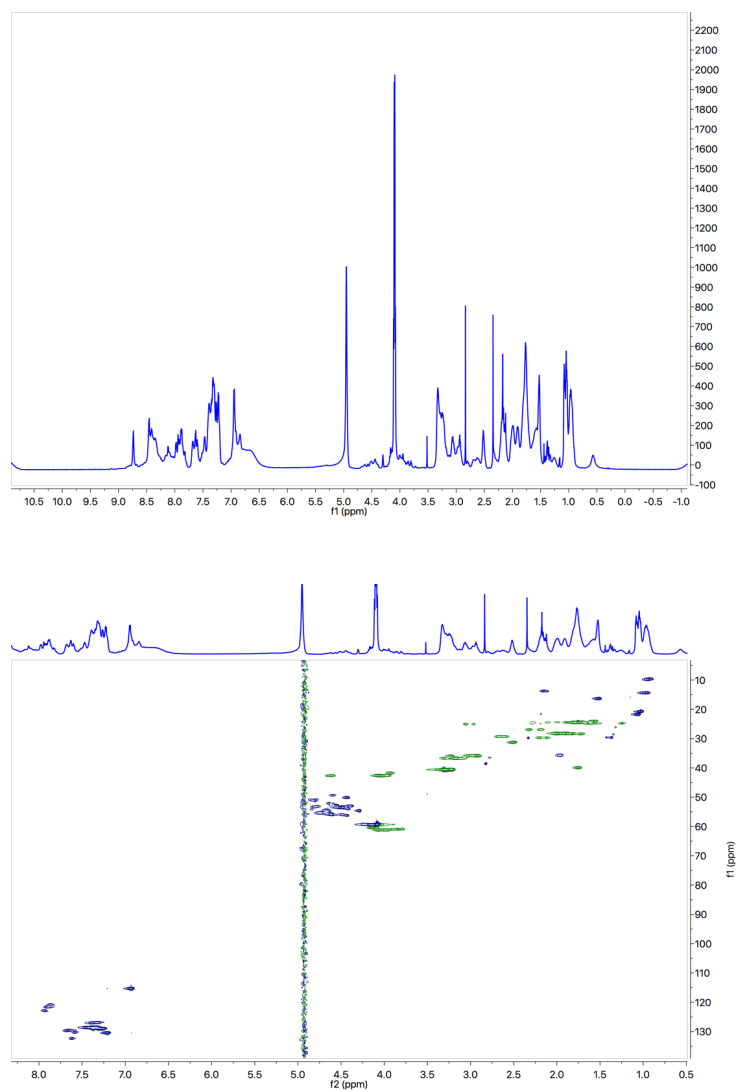
Research Article Manuscript



$^1\text{H},^1\text{H}$ -TOCSY (top) and  $^1\text{H},^1\text{H}$ -NOESY (bottom) NMR spectra of ANP peptide.

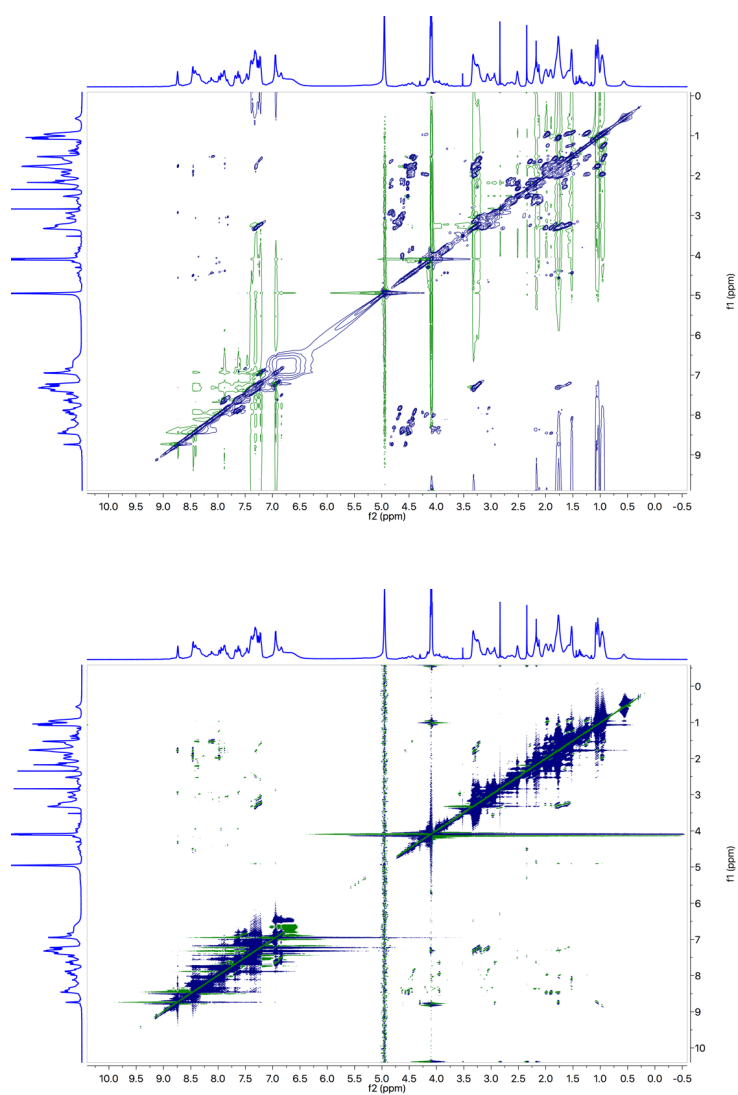
Research Article Manuscript

1.5.2. *trans*-TOP271

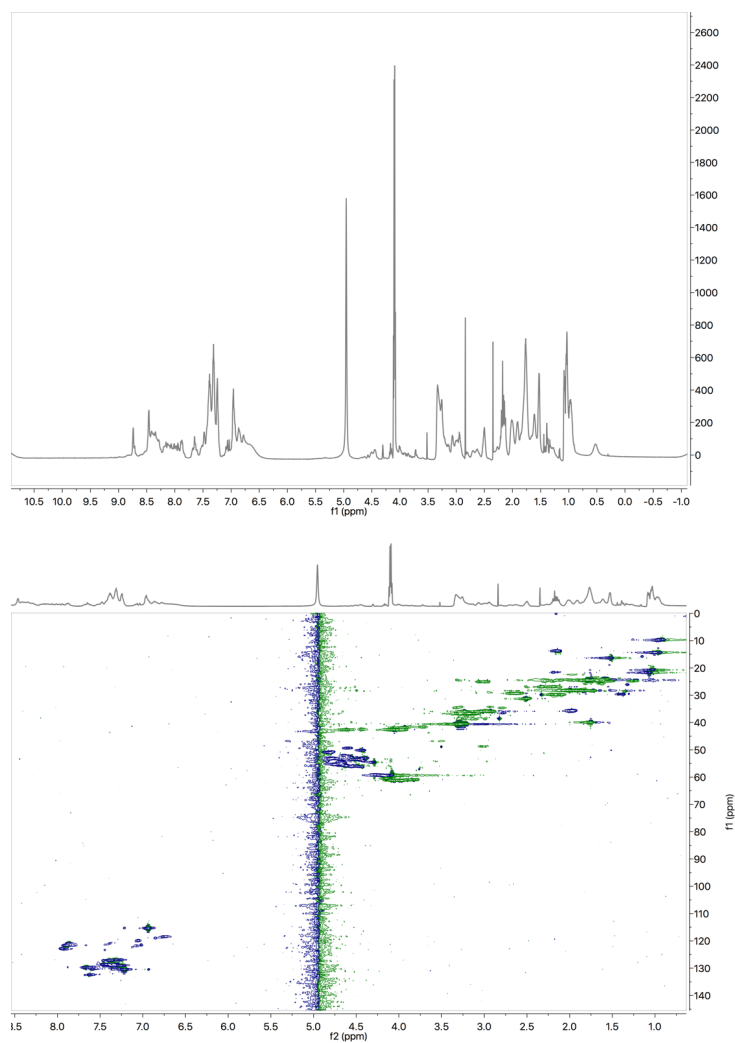


$^1\text{H}$ - (top) and HSQC- (bottom) NMR spectra of *trans*-TOP271 peptide.

Research Article Manuscript

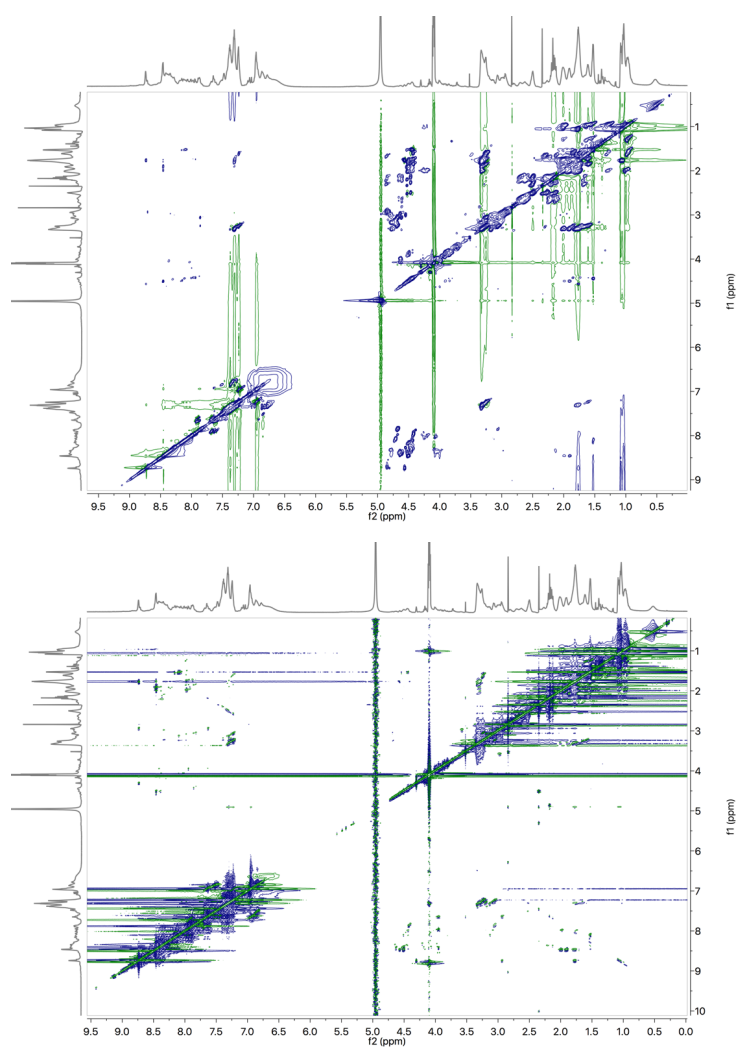


$^1\text{H}, ^1\text{H}$ -TOCSY (top) and  $^1\text{H}, ^1\text{H}$ -NOESY (bottom) NMR spectra of *trans*-TOP271. *cis*-TOP271

*Research Article Manuscript***1.5.3. *cis*-TOP271**

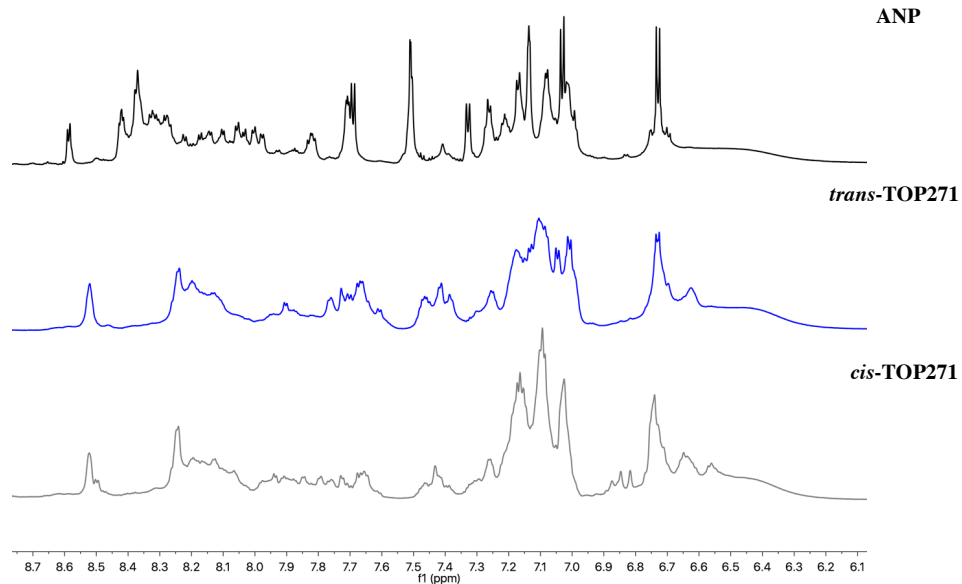
$^1\text{H}$ - (top) and HSQC- (bottom) NMR spectra of *cis*-TOP271 peptide.

Research Article Manuscript



$^1\text{H},^1\text{H}$ -TOCSY (top) and  $^1\text{H},^1\text{H}$ -NOESY (bottom) NMR spectra of *cis*-TOP271.

Research Article Manuscript



Aromatic signals from <sup>1</sup>H-NMR spectra of ANP (black) and *cis/trans*-TOP271 (blue/purple). Full assignment of chemical shifts for *trans*-TOP271 can be found in Supplementary Table 5.

## 2.5.2 EXPERIMENTAL DATA OF ADDITIONAL COMPOUNDS N24AZOPHE-ANP 2.2 AND S25AZOPHE-ANP 2.3

### 2.5.2.1 SYNTHESIS OF PEPTIDES N24AZOPHE-ANP 2.2 AND S25AZOPHE-ANP 2.3

The synthesis of peptides N24AzoPhe-ANP 2.2 and S25AzoPhe-ANP 2.3 followed the general peptide synthesis protocol stated in the APPENDIX. Table 2.2 depicts the coupling conditions of the different building blocks used for the automated peptide synthesis.

**Table 2.2: Coupling conditions for synthesis of peptides N24AzoPhe-ANP 2.2 and S25AzoPhe-ANP 2.3.**

Amino acid(s)	Coupling method	Steps	Time (sec)	Temperature (°C)	Power (W)
Fmoc-Arg(Pbf)-OH	Arg double coupling	2	Step 1: 1500 Step 2: 300	Step 1: 25 Step 2: 75	Step 1: 0 Step 2: 23
Fmoc-Cys(Trt)-OH	Single amino acid 50 °C coupling	1	480	50	23
Fmoc-AzoPhe-OH <b>1.27</b>	Photoswitch coupling	1	1800	75	23
Fmoc-Ala-OH, Fmoc-Asn(Trt)-OH, Fmoc-Glu( <i>t</i> -Bu)-OH, Fmoc-Gly-OH, Fmoc-Ile-OH, Fmoc-Leu-OH, Fmoc-Phe-OH, Fmoc-Ser( <i>t</i> -Bu)-OH, Fmoc-Tyr( <i>t</i> -Bu)-OH	Standard single amino acid coupling	1	480	75	23

## 2.5.2.2 ANALYTICAL HPLC SPECTRUM AND MASS SPECTRUM OF N24AZOPHE-ANP 2.2

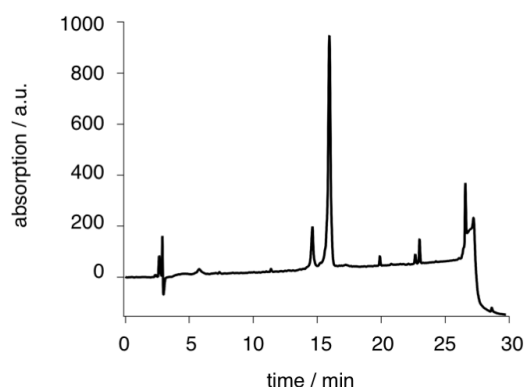


**Figure 2.4: HPLC spectrum of N24-AzoPhe-ANP 2.2.** Analytical HPLC spectrum of 2.2 with a water/acetonitrile gradient 95:5 → 20:80 in 40 min.  $R_{t,cis} = 14.6$  min,  $R_{t,trans} = 16.0$  min.

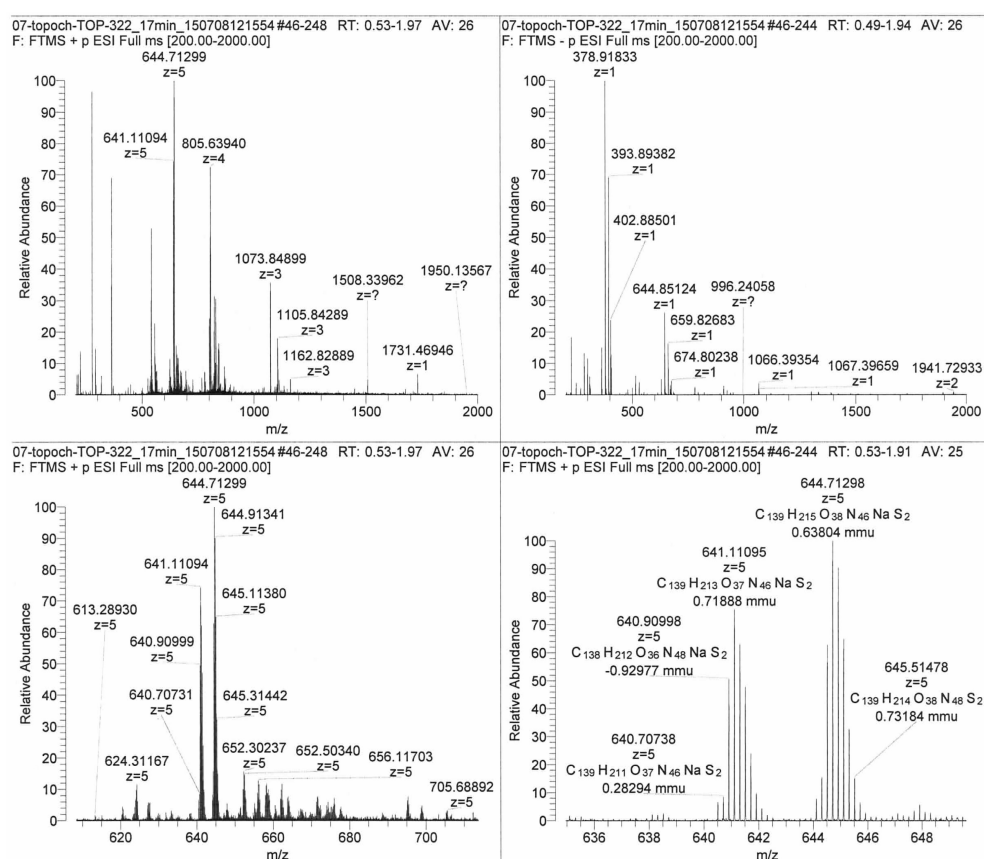


**Figure 2.5: HRMS spectrum of N24-AzoPhe-ANP 2.2.** HRMS (+ESI)  $m/z$ : calc. for  $C_{139}H_{213}O_{38}N_{45}S_2Na^3+$  [M-NH+Na+4H] $^{3+}$ : 1073.8476; found: 1073.8490. Calc. for  $C_{139}H_{214}O_{38}N_{45}S_2Na^4+$  [M-NH+Na+3H] $^{4+}$ : 805.6357; found: 805.6394.  $\Delta m = -0.45$  ppm. Calc. for  $C_{139}H_{215}O_{38}N_{45}S_2Na^5+$  [M-NH+Na+4H] $^{5+}$ : 644.7114; found: 644.7130.  $\Delta m = 0.93$  ppm.

## 2.5.2.3 ANALYTICAL HPLC SPECTRUM AND MASS SPECTRUM OF S25AZOPHE-ANP 2.3

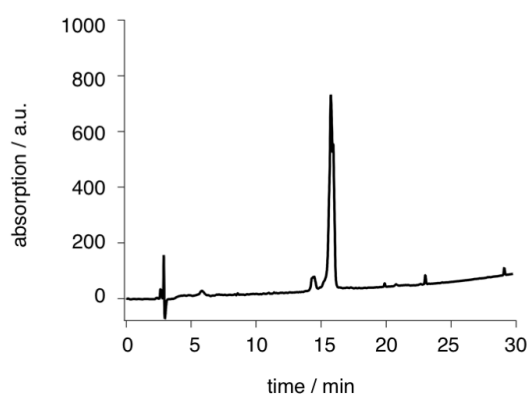


**Figure 2.6: HPLC spectrum of S25AzoPhe-ANP 2.3.** Analytical HPLC spectrum of **2.3** with a water/acetonitrile gradient 95:5 → 20:80 in 40 min.  $R_{t,cis}$  = 14.6 min,  $R_{t,trans}$  = 15.9 min.

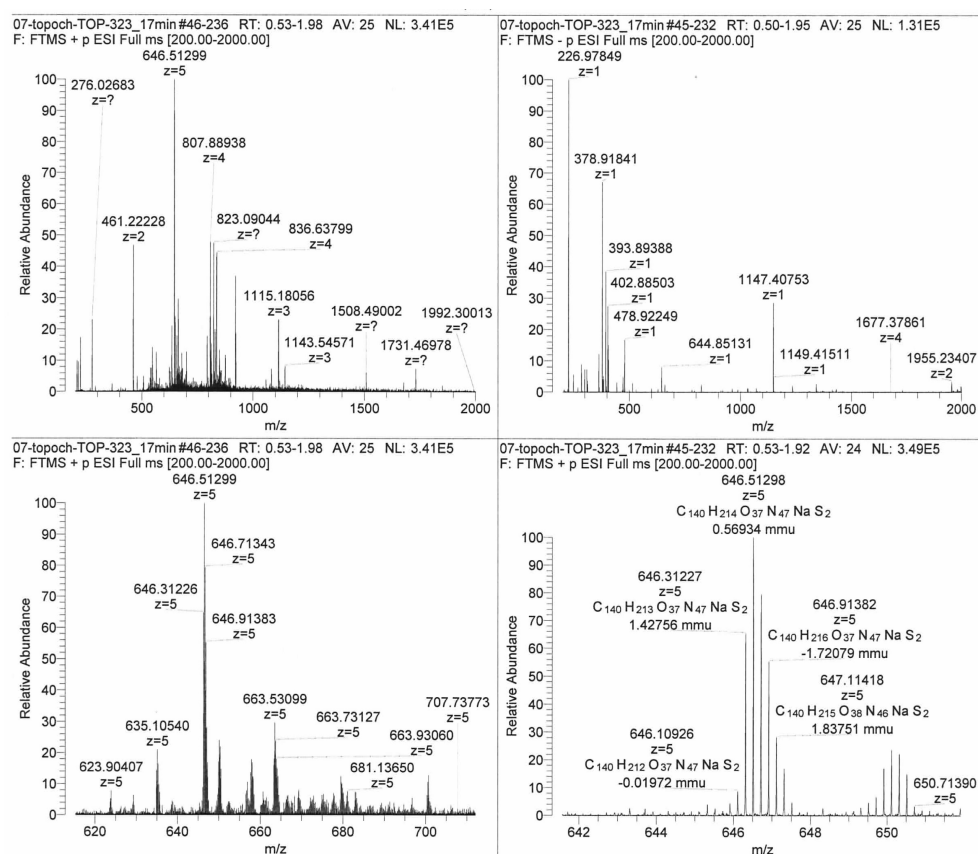


**Figure 2.7: HRMS spectrum of S25AzoPhe-ANP 2.3.** HRMS ESI from **2.3**. HRMS (+ESI) m/z: calc. for  $C_{140}H_{216}O_{38}N_{47}S_2K_3^{3+}$   $[M+3H+3K]^{3+}$ : 1115.1595; found: 1115.1806. Calc. for  $C_{140}H_{218}O_{38}N_{47}S_2^{4+}$   $[M+5H]^{4+}$ : 646.5120; found: 646.5130.  $\Delta m$  = 1.55 ppm.

### 3 OPTICAL CONTROL OF INSULIN SECRETION USING AN INCRETIN SWITCH (LIRAZO)

This work was published in *Angew. Chem. Int. Ed. Engl.* **54**, 15565-15569 (2015).

There are many diseases afflicting the human population and diabetes belongs to the severer and rapidly growing ones. In 2015 9% (415 million) of the adult population was affected by diabetes, causing 5 million victims every year (or one death every six seconds). The *International Diabetes Foundation* (IDF) predicts that the number of adult people with diabetes will rise to 10% (642 million) by 2040<sup>174</sup>. Moreover, every seventh new born child is affected by gestational diabetes and the numbers of children and young adults with diabetes are climbing. Most countries already spend 5-20% of their health expenditure on the treatment of diabetes and related diseases, which sums up to a global spending of around 650 billion USD in 2015, and is predicted to raise to nearly 800 billion USD by 2040. These numbers fiercely demonstrate the need for action against this global emergency.

But what is diabetes, and what are the causes? There are three main types of diabetes: type 1 (T1D), type 2 (T2D) and gestational diabetes. The less common variants comprise monogenic diabetes, which is due to genetic mutations, and secondary diabetes, which is triggered by complications with other diseases<sup>174</sup>. In T1D an auto-immune reaction leads to destruction of the insulin producing beta cells of the pancreas, which leaves the body completely without the hormone in charge of cellular glucose uptake and reduction of blood glucose levels. People with T1D need insulin administered every day. Gestational diabetes can affect pregnant women and elevated blood glucose levels during pregnancy can cause risks during child birth and trigger high blood pressure and foetal macrosomia. The most common form is T2D, and the following CHAPTERS 3 and 4 will focus on this type. T2D, often also referred to as type 2 diabetes mellitus, can be described as tandem between impaired cellular glucose uptake, *i.e.* insulin resistance, and deficient amounts of insulin produced by the body<sup>175-177</sup>. The pancreatic beta cells attempt to retain normoglycemia (normal blood glucose levels) and compensate the resistance by secreting more insulin, but this leads to enhanced insulin resistance in cells. In the end, the constantly raised blood glucose levels lead to a progressive death of the beta cell mass and leave the body without insulin at the final stage of T2D. The resulting complications are diverse and include heart, vascular, nerve and renal diseases<sup>178</sup>. Although the exact causes for the insulin resistance remain enigmatic, there are several risk factors related to T2D, with the most prominent being excess body weight, physical inactivity and poor nutrition<sup>174</sup>.

If T2D is diagnosed in an early stage, the reduction of body weight through sport and a healthy lifestyle and diet, together with a life-long medication can help to delay severe effects and the need for the administration of insulin as in T1D. The key here is to maintain normoglycemia to protect the beta cell mass and thus keep up the endogenous insulin production. There are several drugs used for the treatment of T2D addressing various targets, with the oldest and most prevailing ones being metformin (**3.1**)<sup>179</sup> (*e.i.*

Glucophage®) and sulfonylureas<sup>180-182</sup> (e.i. Glimeperide® (3.2)) (Figure 3.1). The biguanide metformin 3.1 acts through decreasing the hepatic glucose production (gluconeogenesis) in T2D patients, which can be three times as high as normal<sup>183</sup>, and by improving cellular insulin sensitivity<sup>184</sup>. Although this drug is the most widely prescribed medicament for T2D treatment, the mechanisms of action are not completely understood. Sulfonylureas generally boost insulin secretion by acting *via* the sulfonylurea receptors (SUR-1) in pancreatic beta cells. They block of K<sub>ATP</sub> channels which leads to depolarization of the cell, Ca<sup>2+</sup> influx and insulin excretion<sup>185</sup>.

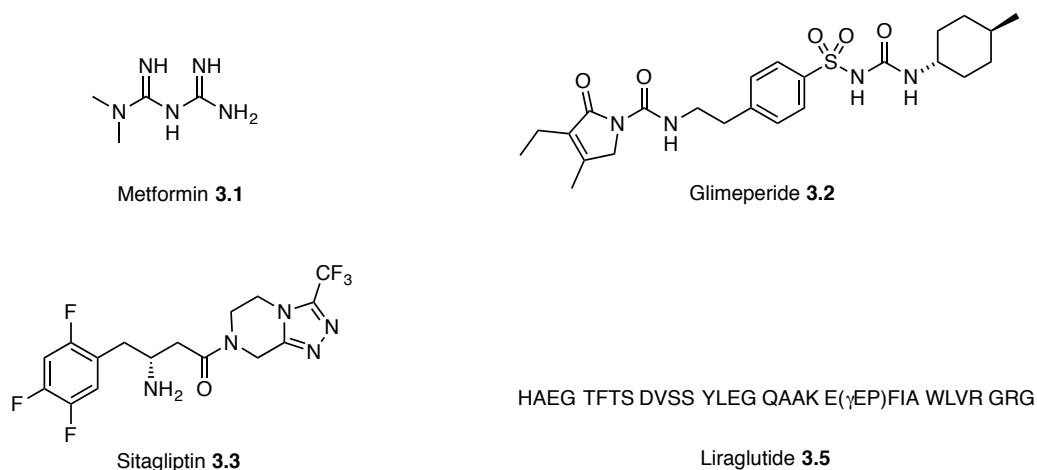


**Figure 3.1: Different drugs for the treatment of T2D.** Shown are the biguanide metformin 3.1, the sulfonylurea 3.2, the DPP-IV inhibitor sitagliptin 3.3 and the incretin mimetic liraglutide 3.5.

Other new treatment methods comprise enzymatic inhibitors of the dipeptidyl peptidase IV (DPP-IV), e.i. Sitagliptin® (3.3), and incretin mimetika such as exenatide (3.4) (Byetta®) and liraglutide (3.5) (Victoza®)<sup>186</sup>. While DPP-IV inhibitors block the enzymatic degradation of the endogenous incretin glucagon-like peptide 1 (GLP-1), incretin mimetika are long-acting variants thereof. The antihyperglycemic hormone GLP-1 is secreted in the intestinal L cells upon food intake and exerts its effects through action on the glucagon-like peptide 1 receptor (GLP-1R), thereby slowing gastric emptying, reducing food intake, boosting insulin secretion in pancreatic beta cells and suppressing glucagon secretion in pancreatic alpha cells<sup>187,188</sup>. The latter is important for maintaining normoglycemia after food intake, because ongoing secretion of glucagon would lead to continuous hepatic gluconeogenesis and high blood glucose levels. In this sense glucagon is the counterpart to insulin and both hormones are the main actors for controlling cellular energy uptake, metabolism, blood sugar levels and food intake. Upon secretion GLP-1 is rapidly cleaved as mentioned by the DPP-IV with a half-life of typically two min<sup>187,188</sup>. Liraglutide 3.5 as long-acting incretin mimeticum exerts similar effects as GLP-1<sup>189</sup>, i.e. it potently augments insulin release in a glucose-dependent manner, induces profound weight loss, slows down beta cell failure and has a half-life of thirteen hours<sup>190,191</sup>, which allows the administration of a single daily dose. The feature of incretins to only act upon permissive glucose levels reduces the risk of hyperglycemia (critical low blood glucose levels), and is a great advantage over insulin-dependent therapy. However, adverse effects have also been reported, such as gastrointestinal disturbance and nausea<sup>192,193</sup>, but also a critical increased risk of

pancreatitis<sup>194,195</sup>. Since incretins are believed to become a mainstay of T2D treatment soon, a deeper insight into the mechanism of action and into beta cell physiology is mandatory.

Thus, we set out to install a photoswitchable unit to liraglutide **3.5** to bestow the GLP-1R with light sensitivity. The resulting photoswitchable incretin mimetic dubbed LirAzo **3.6** allowed an isomer-biased control over GLP-1R action and is presented in the following article.

## 3.1 ARTICLE: OPTICAL CONTROL OF INSULIN SECRETION USING AN INCRETIN SWITCH

**Photopharmacology**

 International Edition: DOI: 10.1002/anie.201506384  
 German Edition: DOI: 10.1002/ange.201506384

## Optical Control of Insulin Secretion Using an Incretin Switch

Johannes Broichhagen, Tom Podewin, Helena Meyer-Berg, Yorrick von Ohlen, Natalie R. Johnston, Ben J. Jones, Stephen R. Bloom, Guy A. Rutter, Anja Hoffmann-Röder,\* David J. Hodson,\* and Dirk Trauner\*

**Abstract:** Incretin mimetics are set to become a mainstay of type 2 diabetes treatment. By acting on the pancreas and brain, they potentiate insulin secretion and induce weight loss to preserve normoglycemia. Despite this, incretin therapy has been associated with off-target effects, including nausea and gastrointestinal disturbance. A novel photoswitchable incretin mimetic based upon the specific glucagon-like peptide-1 receptor (GLP-1R) agonist liraglutide was designed, synthesized, and tested. This peptidic compound, termed **LirAzo**, possesses an azobenzene photoresponsive element, affording isomer-biased GLP-1R signaling as a result of differential activation of second messenger pathways in response to light. While the *trans* isomer primarily engages calcium influx, the *cis* isomer favors cAMP generation. **LirAzo** thus allows optical control of insulin secretion and cell survival.

**T**ype 2 diabetes (T2D) currently affects approximately 8% of the global adult population. This syndrome can be best described as a failure of the pancreatic beta-cell mass to adequately compensate for peripheral insulin resistance by secreting sufficient hormone.<sup>[1]</sup> The resultant dysregulated glucose and lipid metabolism underlie a range of undesirable sequelae, including heart, vascular, nerve, and renal diseases.<sup>[2]</sup> In the majority of cases, adequate control over T2D

can be achieved through lifelong medication together with diet and exercise. To this end, incretin mimetics, i.e., drugs based upon gut-derived glucose-lowering hormones, have rapidly become first-line antidiabetics for the maintenance of normoglycemia.<sup>[3]</sup> Indeed, long-acting analogues of the endogenously released incretin glucagon-like peptide-1 (GLP-1) have been shown to: 1) potently augment insulin release in a glucose-dependent manner; 2) induce profound weight loss through actions on the brain; and 3) slow down beta-cell failure through pro-survival/anti-apoptotic effects.<sup>[4]</sup> While such traits undoubtedly make the incretin class attractive candidates for the management of T2D, adverse effects have already been associated with their use, including an increased risk of pancreatitis (causality unclear),<sup>[5]</sup> gastrointestinal disturbance, and nausea.<sup>[6]</sup> Methods for targeting drug activity to the tissue of interest would thus provide a desirable refinement to the treatment of T2D with incretin mimetics. Photopharmacology is well-adapted for these purposes, since it harnesses the spatiotemporal precision of light to finely control biological processes (see Figure S1 in the Supporting Information)<sup>[7]</sup> and is applicable to the pancreas.<sup>[8]</sup>

Building on previous studies with photocontrolled chigolin, nNOS derivatives, and fluorescence reporter peptides,<sup>[9]</sup> we reasoned that optical control over the incretin axis could be afforded by installing photoresponsive elements on liraglutide, a stabilized GLP-1 analogue (Figure 1 a,b).<sup>[6,10]</sup>

[\*] Dr. J. Broichhagen,<sup>[1]</sup> M. Sc. T. Podewin,<sup>[1]</sup> H. Meyer-Berg, Prof. Dr. A. Hoffmann-Röder, Prof. Dr. D. Trauner  
 LMU Munich, Department of Chemistry and  
 Centre for Integrated Protein Science (CIPSM)  
 Butenandtstrasse 5–13, 81377 Munich (Germany)  
 E-mail: anja.hoffmann-roeder@cup.lmu.de  
 dirk.trauner@cup.lmu.de

Y. von Ohlen, N. R. Johnston, Prof. Dr. G. A. Rutter, Dr. D. J. Hodson  
 Imperial College London, Section of Cell Biology and Functional  
 Genomics, Division of Diabetes, Endocrinology and Metabolism  
 Department of Medicine  
 Hammersmith Hospital, Du Cane Road, London W12 0NN (UK)  
 E-mail: d.hodson@imperial.ac.uk

Dr. B. J. Jones, Prof. Dr. S. R. Bloom  
 Imperial College London, Section of Investigative Medicine  
 Division of Diabetes, Endocrinology and Metabolism  
 Hammersmith Hospital, Du Cane Road, London W12 0NN (UK)

[†] These authors contributed equally to the work.

Supporting information for this article (including experimental details and spectroscopic characterization) is available on the WWW under <http://dx.doi.org/10.1002/anie.201506384>.

© 2015 The Authors. Published by Wiley-VCH Verlag GmbH & Co. KGaA. This is an open access article under the terms of the Creative Commons Attribution License, which permits use, distribution and reproduction in any medium, provided the original work is properly cited.

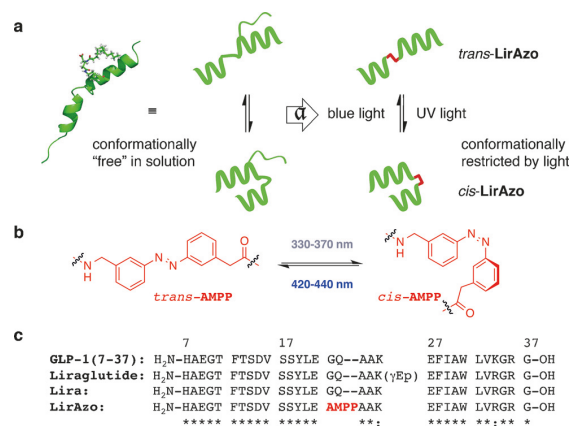


**Figure 1.** Logic, design, and primary structure of **LirAzo**. a) The liraglutide NMR structure (PDB ID: 4apd) served as a template for the synthesis of **LirAzo**, which differs in the placement of AMPP (red) between the helices (a = azologization). b) *cis*-AMPP and *trans*-AMPP are formed upon illumination with UV and blue light, respectively. c) The amino acid sequence of **LirAzo**, showing the replacement of <sup>22</sup>G–<sup>23</sup>Q by AMPP (p = palmitoyl).

To reliably access glucagon-like peptide-1 receptor (GLP-1R) photoactivation through geometric alterations to ligand structure, an azobenzene photoswitch comprising the amino acid [3-(3-aminomethyl)phenylazo]phenylacetic acid (AMPP)<sup>[9b,11]</sup> was incorporated into liraglutide. To minimize disruption to helix folding, AMPP was inserted as a bridge between the two  $\alpha$ -helices of liraglutide (PDB ID: 4apd; Figure 1a), replacing amino acids <sup>22</sup>G-<sup>23</sup>Q, to obtain **LirAzo** by solid-phase peptide synthesis (Figure 1c and Table S1 in the Supporting Information). NMR spectra were recorded with 35% aqueous [D<sub>3</sub>]trifluoroethanol to prevent aggregation, as previously reported (PDB ID: 1d0r),<sup>[12]</sup> thus providing further evidence for correct folding and in vitro behavior of **LirAzo**.

To compare **LirAzo** with liraglutide, we synthesized a benchmark peptide, termed “Lira”, in which the palmitoyl ( $\gamma$ Ep) moiety at <sup>26</sup>K was omitted. This residue, originally introduced to improve plasma binding and half-life in vivo,<sup>[6]</sup> is unnecessary for in vitro studies.

The *cis*–*trans* isomerization of **LirAzo** was initially assessed by UV/Vis spectroscopy (Figure 2a). Switching kinetics in response to blue ( $\lambda = 440$  nm; *cis*→*trans*) and UV ( $\lambda = 330$  nm; *trans*→*cis*) light were robust and fast, with no evidence of degradation or bleaching (Figure 2b; see Figure S2 and Table S2 in the Supporting Information). **LirAzo** displayed remarkable bistability when switched to its *cis* state and subsequently left in the dark (Figure 2c), thus allowing pre-illuminated **LirAzo** to be applied to tissue. GLP-1 binds the GLP-1R through interactions with both the extracellular (<sup>22</sup>G-<sup>37</sup>G) and lipid bilayer (7TM domain) portions (Figure S3).<sup>[13]</sup> From this, it can be predicted that

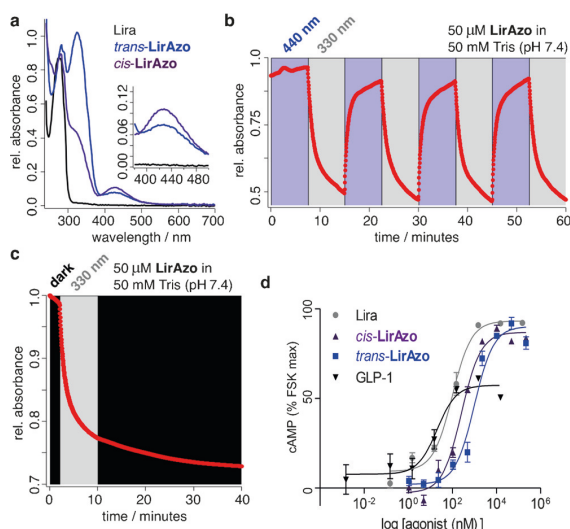


**Figure 2.** Photoisomerization and potency of **LirAzo**. a) UV/Vis spectra for *cis*- (purple) and *trans*- (blue) **LirAzo**, as well as Lira (black). Inset:  $n-\pi^*$  band expanded. b) Reversible and repeated toggling of **LirAzo** between its *cis* and *trans* isomers by using blue ( $\lambda = 440$  nm) and UV ( $\lambda = 330$  nm) light. c) Bistability of the *cis* state over 30 min. d) cAMP concentration–response studies in CHO-GLP-1R cells, determined by Promega cAMP-Glo assay. Values plotted are the mean  $\pm$  standard error of the mean (SEM;  $n = 3$  repeats).

*cis*- and *trans*-**LirAzo** divergently activate receptor signaling by altering one or both of the helical interactions, rather than providing a simple “on–off” switch.

Accompanying alterations to peptide secondary and tertiary structure were confirmed by CD spectroscopy (Figure S4). While Lira exhibits CD signals typical of  $\alpha$ -helix possession, only the *trans* isomer of **LirAzo** shows signals similar to those of Lira. *cis*-**LirAzo**, however, features diverging CD signals (weak maximum at  $\lambda = 189$  nm) consistent with the predicted (partial) helix unfolding (Figure S4a). Moreover, in the near-UV region, the signal of *cis*-**LirAzo** rises to a maximum ( $\lambda = 326$  nm) that can be assigned to the *cis*-azobenzene moiety in a chiral environment (see Figure S4b).<sup>[14]</sup> NMR spectra for Lira and **LirAzo** unambiguously demonstrate differences in AMPP and folding behavior upon *cis*–*trans* isomerization (see the Supporting Information for full NMR spectra and Table S3 for annotation). These findings are of interest, since changes in the secondary and tertiary structure dictate key pharmacological properties, including half-life, permeability, and mode of action. While the former two require complex pharmacokinetic studies, the latter can be examined by using functional in vitro assays. To determine the relative potency and specificity of **LirAzo** versus Lira, concentration–response curves were recorded for cAMP generation in CHO cells expressing the GLP-1R (CHO-GLP-1R).<sup>[15]</sup> The half maximal effective concentration ( $EC_{50}$ ) values for *cis*-**LirAzo** ( $EC_{50} = 262.0$  nM) and *trans*-**LirAzo** ( $EC_{50} = 993.6$  nM) were only slightly higher than for Lira ( $EC_{50} = 98.9$  nM) and GLP-1 ( $EC_{50} = 20.3$  nM; Figure 2d and Table S4). Together, these data suggest that the presence of AMPP does not significantly disturb ligand binding to GLP-1R.

We next sought to determine the photoswitching properties of **LirAzo** in a more relevant system, namely pancreatic beta cells, in which GLP-1 signals via cAMP and  $Ca^{2+}$  to boost insulin secretion.<sup>[16]</sup> By using intact islets of Langerhans, we confirmed that precise temporal control could be exerted over intracellular  $Ca^{2+}$  levels (Figure 3a). Whereas *trans*-**LirAzo** induced increases in the baseline amplitude and frequency of multicellular  $Ca^{2+}$  spiking, this was reduced following UV ( $\lambda = 350$  nm) illumination to induce *cis*-**LirAzo** accumulation ( $P < 0.01$ ; Figure 3b–f).

Through alternating exposure to blue ( $\lambda = 440$  nm) and UV ( $\lambda = 350$  nm) light, oscillations in beta-cell activity, which are thought to underlie insulin pulses, could be induced (Figure S5a,b). The effects of *trans*-**LirAzo** on  $Ca^{2+}$  levels were abolished by blockade of the GLP-1R with the specific antagonist exendin 9–39 (see Figure S5c,d). Furthermore, *trans*-**LirAzo** was unable to stimulate changes in beta-cell activity in the presence of non-permissive (i.e. low) glucose concentrations (Figure S5e,f), a prerequisite for proper incretin action.<sup>[4]</sup> In all cases, results in islets were recapitulated in immortalized MIN6 beta cells, which are more amenable to high-throughput assays (see Figure S5g,h). While *cis*-**LirAzo** was able to stimulate  $Ca^{2+}$  fluxes, these were only just above those observed following control injection (high glucose alone; see Figure S6).

We next determined the effects of **LirAzo** on cAMP generation, another key pathway through which incretins act

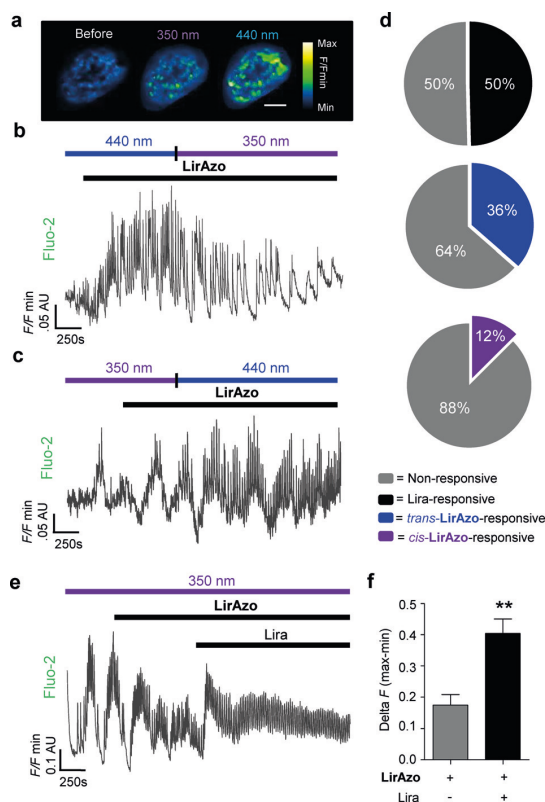


**Figure 3.** Photoswitching of ionic fluxes in pancreatic beta cells. a–c) Increases in cytosolic  $\text{Ca}^{2+}$  levels are larger in **LirAzo**-treated islets exposed to blue (*trans*) versus UV (*cis*) light ( $n = 8$  recordings). d) Pie charts showing the proportion of beta cells within intact islets that respond to Lira, *trans-LirAzo* (blue light), and *cis-LirAzo* (UV light;  $n = 8$  islets). e–f) Positive control showing stimulation of cytosolic  $\text{Ca}^{2+}$  levels following the application of Lira but not *cis-LirAzo* ( $n = 5$  recordings). Lira/**LirAzo** were applied at 150 nM in the presence of permissive ( $> 8$  mM) glucose concentration.  $**P < 0.01$  versus **LirAzo**. Values are given as the mean  $\pm$  SEM.

to amplify insulin secretion. As expected from modeling studies of GLP-1–GLP-1R binding interactions,<sup>[13a,17]</sup> *cis-LirAzo* displayed different signaling properties to the *trans* isomer. The cAMP concentration response in MIN6 beta cells was significantly left-shifted, with a higher maximal response for *cis-* compared to *trans-LirAzo* (Figure 4 a, b). Similar results were observed in CHO-GLP-1R cells (Figure S7 and Table S4). Robust signal bias, shown to be a feature of other GLP-1R agonists,<sup>[18]</sup> was present at all **LirAzo** concentrations over 4 nM (Figure 4 c). Indeed *cis-LirAzo* favored cAMP generation, while *trans-LirAzo* engaged mainly  $\text{Ca}^{2+}$  signaling. Mechanistically, both *trans-* and *cis-LirAzo* sig-

naled via the cAMP binding partners Epac2 and PKA, as well as  $\text{IP}_3$ , a second messenger that mediates the release of  $\text{Ca}^{2+}$  from the endoplasmic reticulum. However, only the former isomer was able to couple properly to ATP-sensitive  $\text{K}^+$  channel ( $K_{\text{ATP}}$ ) and voltage-dependent  $\text{Ca}^{2+}$  channel (VDCC) activity (Figure S8 a, b). By contrast, Lira triggered all signaling pathways tested, as expected (Figure S8 c). The minor effects of *cis-LirAzo* on ionic fluxes are thus mediated through liberation of  $\text{Ca}^{2+}$  from intracellular stores, whereas *trans-LirAzo* stimulates  $\text{Ca}^{2+}$  influx to support the  $\text{Ca}^{2+} \gg$  cAMP bias.

Given that **LirAzo** was able to confer light-sensitivity on GLP-1R signaling, we wondered whether it would also allow photocontrol of insulin secretion. To examine this, mouse islets were incubated with **LirAzo** and exposed to either dark or light ( $\lambda = 350$  nm). Whereas *cis-LirAzo* augmented glucose-stimulated insulin secretion equipotently to Lira (ca. 2.5-fold), *trans-LirAzo* was much less effective (ca. 1.4-fold; Figure 5 a). This was unlikely to be the result of effects on cell viability, since cytotoxicity was not detected by either dead-live or TUNEL assays following 3 hr exposure of cells to **LirAzo** (see Figure S9). Finally, only the *trans* isomer of **LirAzo** was able to offer significant protection from a 24 h glucolipotoxic insult, which induces beta-cell failure through apoptosis (Figure 5 b).

In the present study, we describe a photoswitchable GLP-1R agonist based on liraglutide, which allows unprecedented optical control of a class B GPCR and insulin secretion in pancreatic beta cells. Intriguingly, signal bias could be introduced depending on isomerization status, most likely owing to the pronounced effects of azobenzene orientation on peptide structure. This phenomenon is well-reported for the GLP-1R<sup>[15,18]</sup> and forms the basis of intense research efforts, since drug side effects may stem from presently unknown signaling interactions.<sup>[19]</sup> The GLP-1R is coupled to multiple pathways (e.g., cAMP, PKA, Epac2, ERK, and  $\beta$ -arrestin), however, orthosteric ligands can provoke different receptor conformations to engage distinct signals.<sup>[15,18]</sup> This is best exemplified by responses to oxyntomodulin, which is biased for cAMP over ERK when compared to GLP-1 7–36.<sup>[15,18]</sup>

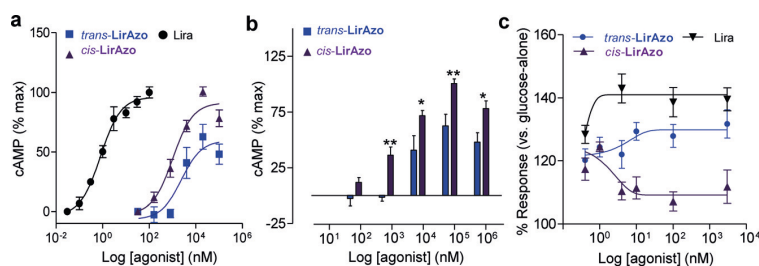


**Figure 4.** Isomer-biased signaling. a) Photoswitching of cAMP responses in MIN6 beta cells exposed to Lira, *cis-LirAzo*, or *trans-LirAzo*, as determined by Cisbio HTRF cAMP assay ( $n = 7$  repeats). b) As for (a), but showing that *cis-LirAzo* generates significantly more cAMP than *trans-LirAzo* at concentrations greater than  $10^2$  nM ( $n = 7$  repeats). c) Isomer-biased  $\text{Ca}^{2+}$  signaling is present at **LirAzo** concentrations greater than  $10^1$  nM ( $n = 8$  repeats; Lira shown as a positive control). Cells were retained in permissive ( $> 8$  mM) glucose concentration and Lira or **LirAzo** applied at 150 nM.  $*P < 0.05$ ,  $**P < 0.01$ , and NS (not significant) versus *trans-LirAzo*. Values are given as the mean  $\pm$  SEM.

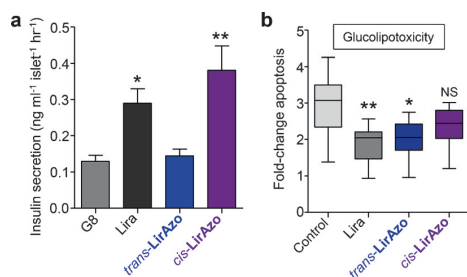


**Figure 5.** Insulin secretion and apoptosis in pancreatic beta cells. a) Lira and *cis*-LirAzo, but not *trans*-LirAzo, potentiate glucose-stimulated insulin secretion (G8; 8 mM glucose;  $n=12$  animals). Lira or LirAzo were applied at 150 nM in the presence of 8 mM glucose concentration. Values are given as the mean  $\pm$  SEM. b) Lira and *trans*-LirAzo are more protective than *cis*-LirAzo against apoptosis induced by glucolipototoxicity ( $n=8$  repeats; the mean and upper/lower quartile are shown with max/min). Lira or LirAzo were applied at 500 nM. \* $P<0.05$ , \*\* $P<0.01$  and NS (non-significant) versus G8 or control.

Such divergent effects likely arise from interactions with specific conserved polar residues.<sup>[20]</sup>

The fine control offered over GLP-1R molecular pathways by LirAzo may hence provide a novel method to tease apart the mechanisms underlying signal bias in beta cells, thereby enabling the refinement of incretin mimetics. Indeed, we were able to show here that cAMP is the major driver of incretin-potentiated insulin secretion, whereas anti-apoptotic effects are more pronounced in the presence of both cAMP and Ca<sup>2+</sup>. This has repercussions for the design of specific GLP-1R agonists, since stimulation of both pathways is likely to be beneficial for T2D treatment. While LirAzo potency was less than for native liraglutide, it should be noted that concentration–response studies in CHO and MIN6 cells do not translate well to islets of Langerhans, where the effects of GLP-1 on secretion have been detected in the low picomolar range.<sup>[21]</sup> Lastly, LirAzo demonstrated excellent bistability, which facilitates its use in biological studies by circumventing the need for complex imaging setups/expensive light sources.

In summary, LirAzo provides a blueprint for the production of anti-diabetic peptides for which light-triggered alterations to peptide folding—emanating from an azobenzene unit wedged between the helices—alters GPCR activity. We anticipate that this, or future variants, may serve as a useful tool for the functional dissection of GLP-1R signaling in health and disease.

### Acknowledgements

J.B. was supported by an EFSD Albert Renold Young Scientist Fellowship and a Studienstiftung des deutschen Volkes PhD studentship. T.P., H.M.B and N.R.J. were supported by Center for Integrated Protein Science Munich (CIPSM), Bavarian Grant for Studies and a Diabetes UK RW and JM Collins Studentship, respectively. G.A.R. was supported by Wellcome Trust Senior Investigator (WT098424A1A), MRC Programme (MR/J0003042/1), Diabetes UK Project Grant (11/0004210) and Royal Society

Wolfson Research Merit Awards. B.J.J. was funded by an MRC Clinical Research Training Fellowship. S.R.B. is funded by grants from the MRC, BBSRC, IHR, an Integrative Mammalian Biology (MB) Capacity Building Award, an FP7-HEALTH-2009-241592 EuroCHIP grant and is supported by the NIHR Imperial Biomedical Research Centre Funding Scheme. A.H.R. was supported by CIPSM and SFB 749. D.J.H. was supported by Diabetes UK R.D. Lawrence (12/0004431) and EFSD/Novo Nordisk Rising Star Fellowships, as well as an MRC project grant (MR/N00275X/1). D.J.H. and G.A.R. were supported by Imperial Confidence in Concept (ICiC) Grants. D.T. was supported by an Advanced Grant from the European Research Council (268795). We are grateful to Dr. David Stephenson and Claudia Dubler for assistance with NMR spectroscopy.

**Keywords:** beta cells · insulin · liraglutide · photopharmacology · type 2 diabetes

**How to cite:** *Angew. Chem. Int. Ed.* **2015**, *54*, 15565–15569  
*Angew. Chem.* **2015**, *127*, 15786–15790

- [1] a) F. M. Ashcroft, P. Rorsman, *Cell* **2012**, *148*, 1160–1171; b) M. Prentki, F. M. Matschinsky, S. R. Madiraju, *Cell Metab.* **2013**, *18*, 162–185.
- [2] C. J. Nolan, P. Damm, M. Prentki, *The Lancet* **2011**, *378*, 169–181.
- [3] D. J. Drucker, S. I. Sherman, F. S. Gorelick, R. M. Bergenstal, R. S. Sherwin, J. B. Buse, *Diabetes Care* **2010**, *33*, 428–433.
- [4] J. E. Campbell, D. J. Drucker, *Cell Metab.* **2013**, *17*, 819–837.
- [5] a) A. G. Egan, E. Blind, K. Dunder, P. A. de Graeff, B. T. Hummer, T. Bourcier, C. Rosebraugh, *N. Engl. J. Med.* **2014**, *370*, 794–797; b) J. J. Meier, M. A. Nauck, *Diabetologia* **2014**, *57*, 1320–1324.
- [6] a) L. B. Knudsen, P. F. Nielsen, P. O. Huusfeldt, N. L. Johansen, K. Madsen, F. Z. Pedersen, H. Thogersen, M. Wilken, H. Agerso, *J. Med. Chem.* **2000**, *43*, 1664–1669; b) J. J. Meier, *Nat. Rev. Endocrinol.* **2012**, *8*, 728–742.
- [7] a) W. A. Velema, W. Szymanski, B. L. Feringa, *J. Am. Chem. Soc.* **2014**, *136*, 2178–2191; b) J. Broichhagen, J. A. Frank, D. Trauner, *Acc. Chem. Res.* **2015**, *8*, 1947–1960.
- [8] a) J. Broichhagen, J. A. Frank, N. R. Johnston, R. K. Mitchell, K. Šmid, P. Marchetti, M. Bugliani, G. A. Rutter, D. Trauner, D. J. Hodson, *Chem. Commun.* **2015**, *51*, 6018–6021; b) J. Broichhagen, M. Schönberger, S. C. Cork, J. A. Frank, P. Marchetti, M. Bugliani, A. M. J. Shapiro, S. Trapp, G. A. Rutter, D. J. Hodson, D. Trauner, *Nat. Commun.* **2014**, *5*, 5116.
- [9] a) C. Hoppmann, S. Seedorff, A. Richter, H. Fabian, P. Schmieder, K. Rück-Braun, M. Beyermann, *Angew. Chem. Int. Ed.* **2009**, *48*, 6636–6639; *Angew. Chem.* **2009**, *121*, 6763–6766; b) C. Renner, L. Moroder, *ChemBioChem* **2006**, *7*, 868–878; c) C. Hoppmann, P. Schmieder, P. Domaing, G. Vogelreiter, J. Eichhorst, B. Wiesner, I. Morano, K. Rück-Braun, M. Beyermann, *Angew. Chem. Int. Ed.* **2011**, *50*, 7699–7702; *Angew. Chem.* **2011**, *123*, 7841–7845; d) T. Podewin, M. S. Rapp, I. Turkanovic, K. L. Karaghiosoff, W. Zinth, A. Hoffmann-Röder, *Chem. Commun.* **2015**, *51*, 4001–4004.
- [10] J. Eng, W. A. Kleinman, L. Singh, G. Singh, J. P. Raufman, *J. Biol. Chem.* **1992**, *267*, 7402–7405.
- [11] A. Aemissegger, V. Kräutler, W. F. van Gunsteren, D. Hilvert, *J. Am. Chem. Soc.* **2005**, *127*, 2929–2936.
- [12] X. Chang, D. Keller, S. Björn, J. J. Led, *Magn. Reson. Chem.* **2001**, *39*, 477–483.

- [13] a) C. R. Underwood, P. Garibay, L. B. Knudsen, S. Hastrup, G. H. Peters, R. Rudolph, S. Reedtz-Runge, *J. Biol. Chem.* **2010**, *285*, 723–730; b) L. J. Miller, Q. Chen, P. C. Lam, D. I. Pinon, P. M. Sexton, R. Abagyan, M. Dong, *J. Biol. Chem.* **2011**, *286*, 15895–15907.
- [14] G. Haberhauer, C. Kallweit, *Angew. Chem. Int. Ed.* **2010**, *49*, 2418–2421; *Angew. Chem.* **2010**, *122*, 2468–2471.
- [15] C. Koole, D. Wootten, J. Simms, C. Valant, R. Sridhar, O. L. Woodman, L. J. Miller, R. J. Summers, A. Christopoulos, P. M. Sexton, *Mol. Pharmacol.* **2010**, *78*, 456–465.
- [16] C. A. Leech, I. Dzhura, O. G. Chepurny, G. Kang, F. Schwede, H. G. Genieser, G. G. Holz, *Prog. Biophys. Mol. Biol.* **2011**, *107*, 236–247.
- [17] F. Y. Siu, M. He, C. de Graaf, G. W. Han, D. Yang, Z. Zhang, C. Zhou, Q. Xu, D. Wacker, J. S. Joseph, W. Liu, J. Lau, V. Cherezov, V. Katritch, M. W. Wang, R. C. Stevens, *Nature* **2013**, *499*, 444–449.
- [18] C. Koole, E. E. Savage, A. Christopoulos, L. J. Miller, P. M. Sexton, D. Wootten, *Mol. Endocrinol.* **2013**, *27*, 1234–1244.
- [19] C. Weston, D. Poyner, V. Patel, S. Dowell, G. Ladds, *Br. J. Pharmacol.* **2014**, *171*, 3651–3665.
- [20] D. Wootten, J. Simms, L. J. Miller, A. Christopoulos, P. M. Sexton, *Proc. Natl. Acad. Sci. USA* **2013**, *110*, 5211–5216.
- [21] a) D. J. Hodson, R. K. Mitchell, E. A. Bellomo, G. Sun, L. Vinet, P. Meda, D. Li, W. H. Li, M. Bugliani, P. Marchetti, D. Bosco, L. Piemonti, P. Johnson, S. J. Hughes, G. A. Rutter, *J. Clin. Invest.* **2013**, *123*, 4182–4194; b) M. Shigeto, M. Katsura, M. Matsuda, S. Ohkuma, K. Kaku, *J. Pharmacol. Sci.* **2008**, *108*, 274–279.

Received: July 10, 2015

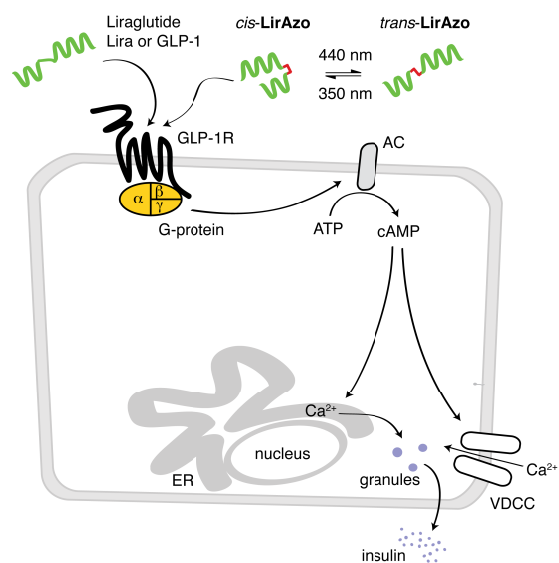
Revised: August 11, 2015

Published online: November 2, 2015

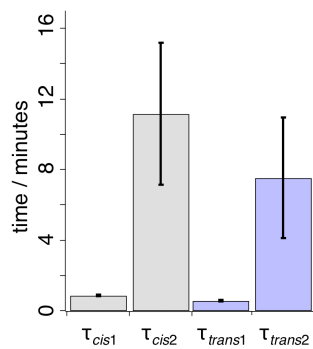
## 3.2 SUPPLEMENTARY FIGURES AND TABLES

### 3.2.1 SUPPLEMENTARY FIGURES

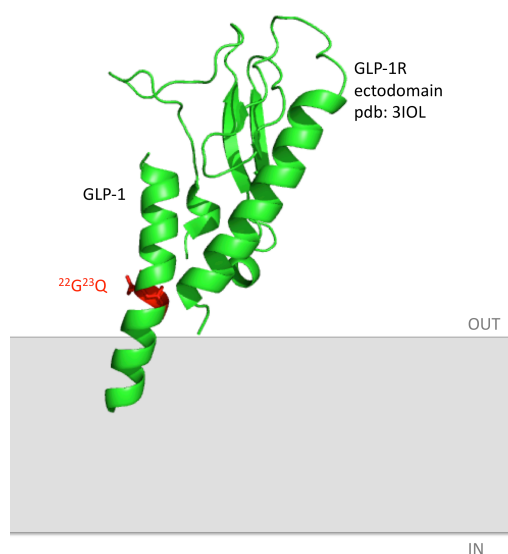
#### 3. Supplementary Figures and Tables



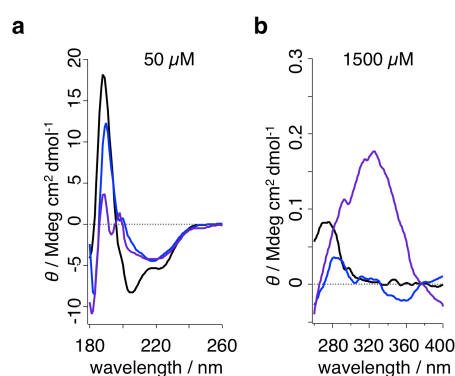
**Supplementary Figure 1:** GLP-1R signaling and stimulus-secretion coupling in the pancreatic beta-cell.



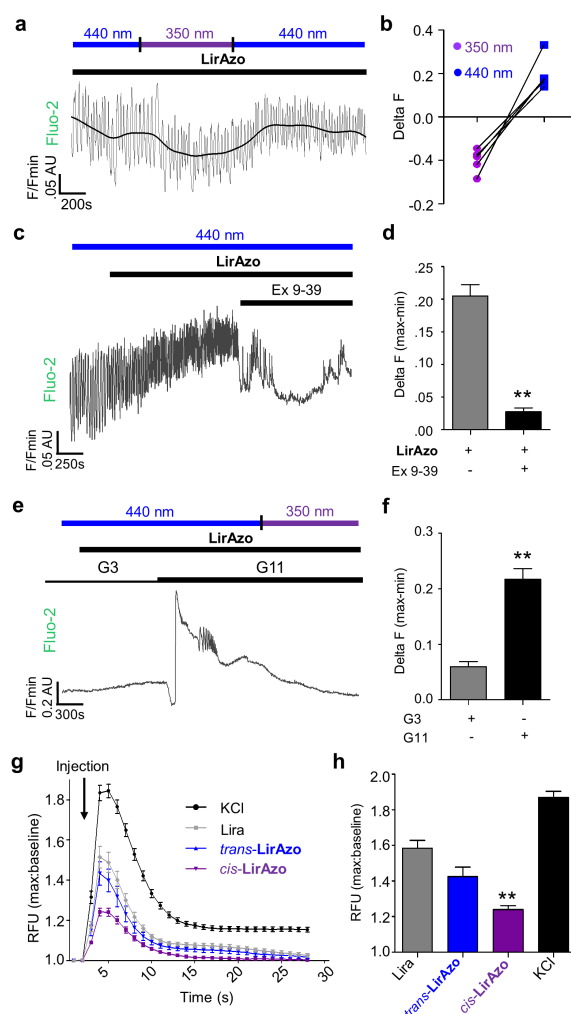
**Supplementary Figure 2: LirAzo** photoswitching kinetics. *cis*-Isomerization occurs over the minutes timescale ( $n = 4$ ). Values represent mean  $\pm$  S.D.



**Supplementary Figure 3:** GLP-1 bound to the GLP-1R ectodomain (pdb: 3iol)<sup>[4]</sup> served as an additional model for the design of **LirAzo**. GLP-1 binds to the GLP-1R ectodomain through interactions of <sup>22</sup>G-<sup>37</sup>G. Moreover, the N-terminus is believed to interact with the 7TM domain located in the lipid bilayer. Therefore, we propose that replacement of <sup>22</sup>G-<sup>23</sup>Q (highlighted in red) with AMPP will alter one or both of the helical interactions, leading to divergent class B GPCR signaling through isomer bias. To date, no crystal structure of the full GLP-1R is available. However, the homologous glucagon receptor (GCGR) has been resolved in atomic detail and used to model GLP-1 interactions depicting binding to the 7TM domain.<sup>[5]</sup> Taken together, a more detailed activation model can only be proposed using an x-ray structure of GLP-1R that highlights the specific interactions with the 7TM domain.

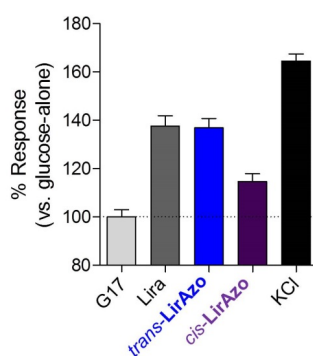


**Supplementary Figure 4:** CD spectral data of Lira and *cis/trans-LirAzo*. a) Far UV spectra and b) Near UV spectra of Lira (black), *trans-LirAzo* (blue) and *cis-LirAzo* (purple) at 50 μM and 1500 μM concentrations, respectively. Lira exhibits two minima ( $\lambda = 205$  and  $223$  nm) and a pronounced rise to a maximum ( $\lambda = 188$  nm), typical of  $\alpha$ -helix possession. Consistent with this, both *cis/trans-LirAzo* exhibit minima in the  $\lambda = 200$ - $220$  nm region. However, whereas *trans-LirAzo* displays a maximum at  $\lambda = 180$  nm, *cis-LirAzo* only shows a weak maximum ( $\lambda = 189$  nm) after a local minimum ( $\lambda = 193$  nm), consistent with (partial) helix unfolding. Moreover, in the near UV-region, the signal of *cis-LirAzo* rises to a maximum ( $\lambda = 326$  nm) that can be assigned to the *cis*-azobenzene moiety in a chiral environment.

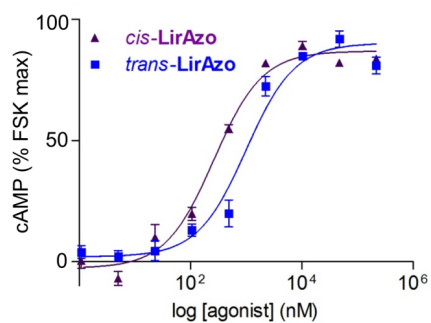


**Supplementary Figure 5:** Photoswitching of ionic fluxes in beta cells, and GLP-1R- and glucose-dependency. a) Representative trace showing reversible control of GLP-1R signaling and  $\text{Ca}^{2+}$  levels ( $n = 4$  recordings) (smoothed trace shown in black). b) As for a) but before-after plot showing reversal of *cis*-LirAzo effects following exposure to blue light to induce *trans*-isomerization ( $n = 4$  recordings). c-d) Exendin 9-39 (Ex 9-39) 150 nM abolishes *trans*-LirAzo-stimulated  $\text{Ca}^{2+}$  oscillations ( $n = 9$  recordings). e-f) *trans*-LirAzo 150 nM is unable to properly stimulate  $\text{Ca}^{2+}$  rises in the presence of low (non-permissive) glucose concentration (G3; 3 mM glucose) (G11; 11 mM glucose) ( $n = 5$  recordings). g-h)

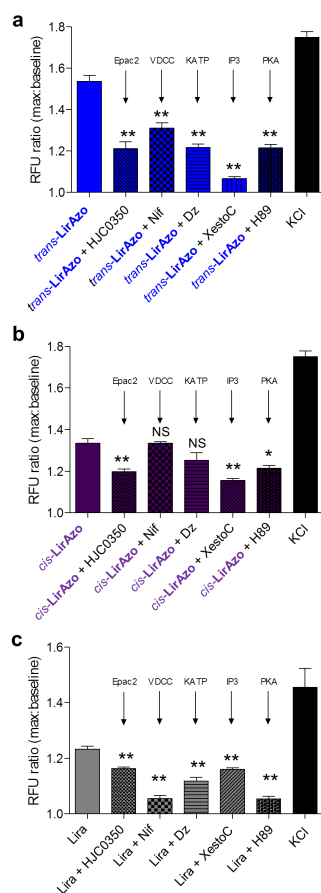
**LirAzo** allows photoswitching of  $\text{Ca}^{2+}$  in immortalized MIN6 beta cells subjected to high-throughput assays ( $n = 4$  repeats). Lira/**LirAzo** were applied at 150 nM in the presence of permissive ( $> 8$  mM) glucose concentration.  $**P < 0.01$  versus **LirAzo**/Lira. Values represent mean  $\pm$  S.E.M.



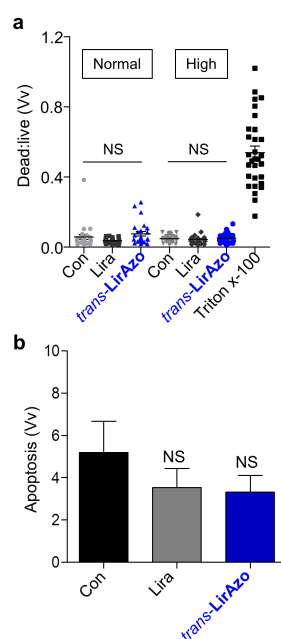
**Supplementary Figure 6:** LirAzo-stimulated  $\text{Ca}^{2+}$  rises *versus* control (*i.e.* 17 mM glucose; G17) (KCl, positive control) ( $n = 8$ ).



**Supplementary Figure 7:** Photoswitching of cAMP generation in CHO-GLP-1R cells. Identical to Figure 2d (main text), except showing only cAMP concentration-responses for *cis*- ( $EC_{50} = 262.0$  nM) and *trans*-LirAzo ( $EC_{50} = 993.6$  nM) ( $n = 3$  repeats) on a contracted x-axis, for clarity. Values represent mean  $\pm$  S.E.M.



**Supplementary Figure 8:** Isomer-dependent engagement of beta cell signaling pathways. a) Effects of *trans*-LirAzo on cytosolic  $\text{Ca}^{2+}$  rises in MIN6 beta cells are blocked by antagonists of Epac2 (HJC0350 10  $\mu\text{M}$ ), L-type  $\text{Ca}^{2+}$  channels (Nif, nifedipine 50  $\mu\text{M}$ ),  $\text{K}_{\text{ATP}}$  (Dz, diazoxide 150  $\mu\text{M}$ ),  $\text{IP}_3\text{R}$  (XestoC, Xestospongins C 10  $\mu\text{M}$ ) and PKA (H89, 10  $\mu\text{M}$ ) ( $n = 8$  repeats). b) As for a), but effects of *cis*-LirAzo are only blocked by inhibitors of Epac2,  $\text{IP}_3\text{R}$  and PKA. c) As for a) but Lira positive control showing blockade by all inhibitors. Cells were retained in permissive (> 8 mM) glucose concentration and Lira/LirAzo applied at 150 nM. *cis*- and *trans*-LirAzo were run in parallel in the same assay, and KCl used as a single positive control for a) and b). \* $P < 0.05$ , \*\* $P < 0.01$  and NS, non-significant versus LirAzo-alone. Values represent mean  $\pm$  S.E.M.



**Supplementary Figure 9: LirAzo** does not induce cytotoxicity in beta cells. a) Normal (150 nM) and high (2000 nM) concentrations of LirAzo do not alter islet viability (Triton X-100; positive control) ( $n = 20-25$  islets) (Con, control). b) Lira and *trans-LirAzo* do not induce islet cell apoptosis under normal conditions (*i.e.* 11 mM glucose-only), as determined using TUNEL staining ( $n = 8-9$  islets). NS, Non-significant *versus* control (Con). Values represent mean  $\pm$  S.E.M.

**3.2.2 SUPPLEMENTARY TABLES****Supplementary Table 2: LirAzo photoswitching kinetics**

<b>LirAzo</b>	$\tau_1$ (sec)	$\tau_2$ (min)
<i>cis</i>	51.0 $\pm$ 2.4	11.1 $\pm$ 4.0
<i>trans</i>	32.3 $\pm$ 1.6	7.5 $\pm$ 3.4

**Supplementary Table 4:**  $EC_{50}$  values for cAMP generation in CHO-GLP-1R cells. \* $P < 0.03$  and  $^{\S}P < 0.34$  versus *cis-LirAzo* (Lira; liraglutide) (Student's t-test). 95% Confidence intervals are shown in brackets.

	<i>cis-LirAzo</i>	<i>trans-LirAzo</i>	Lira
$EC_{50}$ (nM)	262.0 (199.5 to 344.1)	993.6* (681.6 to 1448)	98.93 $^{\S}$ (69.14 to 141.5)

### 3.3 ADDITIONAL COMPOUNDS AND DATA

The published photoswitchable incretin mimetic LirAzo **3.6** was only one of originally three AMPP **1.22** modified peptides, however the other two peptides LirAzo2 **3.7** and LirAzo3 **3.8** were neglected due a lack of potency and/or isomer-bias. Following the described design principles in PART I, the AMPP photoswitch **1.22** was incorporated into liraglutide by substituting either two (**3.6**), three (**3.7**) or four (**3.8**) amino acids. While **1.22** substitutes Gly22 and Gln23 in Liraglutide **3.5**, it substitutes adjacent Ala24 and Ala25 in **3.7** and **3.8**, respectively. This substitution pattern was for one reason selected based on the X-ray crystal structure of GLP-1 bound to the extracellular domain of GLP1-R (pdb: 3iol), as well as the NMR structure of liraglutide **3.5** in solution (pdb: 4apd) (Figure 3.2). The latter shows **3.5** as flexible helix with a bridged part connecting two helix segments. This connecting part is proximal to the cell membrane, as seen from the X-ray structure, and thus was selected as suitable substitution site for AMPP **1.22**. Switching the photoswitch between its linear *trans*- and crooked *cis*-form was predicted to shift both helix parts and alter receptor binding and membrane permeation of the LirAzo peptides.

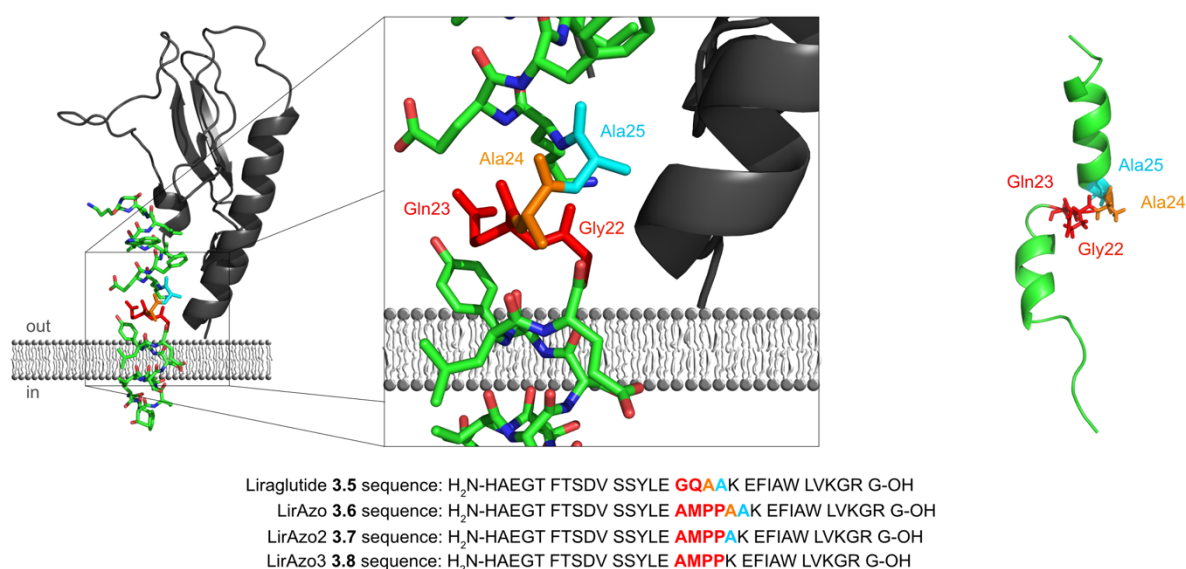


**Figure 3.2: Design approach for LirAzo 3.6, LirAzo2 3.7 and LirAzo3 3.8.** Left: X-ray crystal structure of GLP-1 (green) bound to the extracellular domain of GLP1-R (gray) (pdb: 3iol). Middle: zoom into substitution region, with marked amino acids Gly22 and Gln23 (both red), Ala24 (orange) and Ala25 (cyan). Primary sequences of liraglutide **3.5** and LirAzo versions **3.6**, **3.7** and **3.8**. Right: NMR structure of liraglutide **3.5** with marked substituted amino acids Gly22 and Gln23 (both red), Ala24 (orange) and Ala25 (cyan) (pdb: 4apd).

The three LirAzo versions **3.6**, **3.7** and **3.8** were initially evaluated with regard to their switching kinetics to check photoresponsivity and bistability. All three compounds exhibited high photoconversion rates and robust switching without photobleaching, as published for **3.6** and shown for **3.7** and **3.8** in Figure 3.3. Furthermore, all three peptides were bistable, abolishing the need for constant illumination, thus enabling the pre-illumination of the compound and direct application to the tissue.

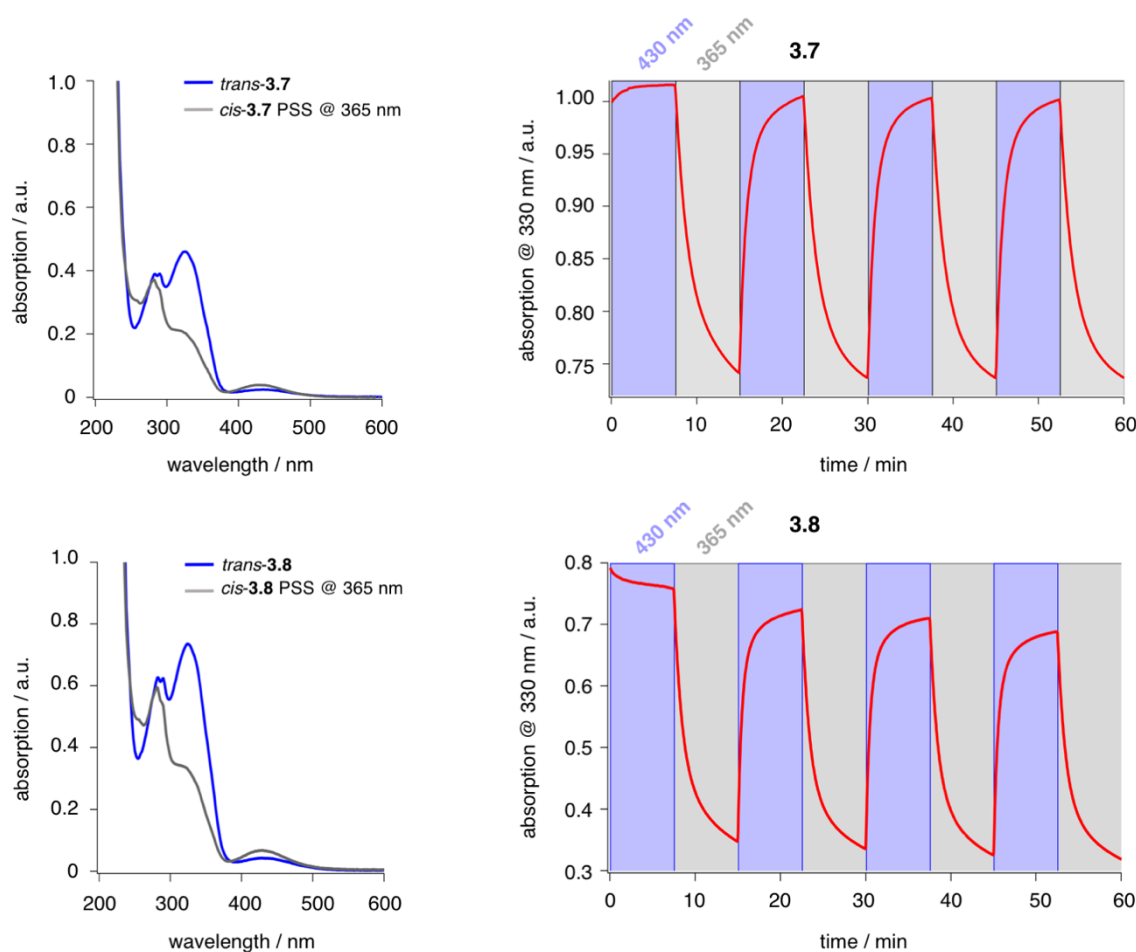


**Figure 3.3:** UV/Vis spectra and UV switching kinetics of LirAzo2 **3.7** and LirAzo3 **3.8**. Top left: UV/Vis spectra of *cis/trans*-3.7. Top right: UV switching kinetics of **3.7** measured through the absorption at 330 nm after photoswitching with 365 nm UV light (*trans* → *cis*) and 430 nm blue light (*cis* → *trans*). Bottom left: UV/Vis spectra of *cis/trans*-3.8. Bottom right: UV switching kinetics of **3.8** measured through the absorption at 330 nm after photoswitching with 365 nm UV light (*trans* → *cis*) and 430 nm blue light (*cis* → *trans*).

To determine the lead candidate, the three LirAzo peptides **3.6**, **3.7** and **3.8** were assessed through cAMP dose-response assays in CHO cells stably expressing the GLP-1R (CHO-GLP-1R) (Figure 3.4). While **3.7** and **3.8** showed  $EC_{50}$  values in the micromolar range without full receptor activation and any detectable isomer-bias, both isomers of LirAzo **3.6** showed only a slightly decreased potency, with isomer-dependent activation of the GLP-1R (see publication for details). For this reason, compounds **3.7** and **3.8** were dismissed and research was concentrated on LirAzo **3.6**.

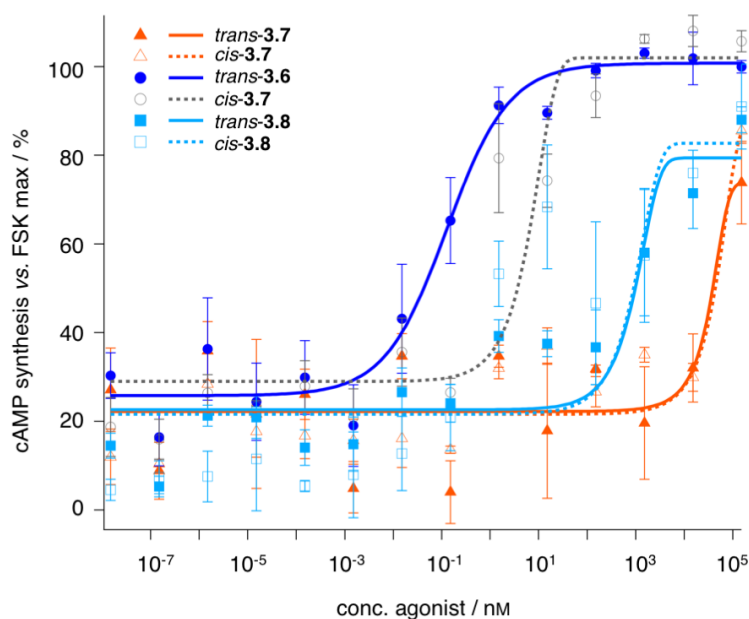


**Figure 3.4:** cAMP dose-response curves for peptides LirAzo 3.6, LirAzo2 3.7 and LirAzo3 3.8. Dose-responses were obtained in CHO-GLP-1R cells and plotted against a forskolin (FSK) maximum activation. Values represent mean  $\pm$  SEM ( $n = 3$  technical repeats).

### 3.4 SUMMARY AND OUTLOOK

Type 2 diabetes (T2D) is the major type of diabetes and nearly 10% of the global adult population will be affected by 2040 (ref. 174). It can best be described as combination of increasing cellular insulin resistance and failure of pancreatic beta cells to adequately compensate for the excess need. The final result is reduction of the beta cell mass, insufficient endogenous insulin production and the need for administering exogenous insulin. Since prevailing risk factors comprise excess body weight and an unhealthy lifestyle, T2D in an early stage can be controlled through sport and diet, accompanied by medication with metformin, sulfonylureas, dipeptidyl peptidase IV inhibitors or incretin mimetica<sup>178</sup>. The latter are long-acting variants of the glucagon-like peptide 1 (GLP-1) and exert the same effects, *i.e.* boost insulin secretion from pancreatic beta cells, inhibit gastric emptying, suppress hunger by acting on the brain and help to substantially reduce the body weight. Furthermore, they act only in presence of permissive glucose levels, impeding the risk of hyperglycemia after treatment. Based on these striking results and advantages, incretin mimetica such as exenatide **3.4** (Byetta<sup>®</sup>) and liraglutide **3.5** (Victoza<sup>®</sup>) are believed to become a mainstay in the treatment of T2D, despite rising concerns about adverse effects such as gastrointestinal disturbance, thyroid cancer and pancreatitis<sup>193,195,196</sup>. The causalities behind this and in general the mechanism and action of T2D drugs remain enigmatic, and research is vital in this field to understand and combat this global emergency.

Incretin mimetica are valuable photopharmacological targets, as tight spatiotemporal control of drug activity would not only enable the reduction of adverse effects, but also deliver photochemical tools for the dissection and comprehension of beta physiology and control of neuronal signaling. Moreover, it was already shown that the pancreas, a class 4 photodruggable target, is amenable to a photopharmacological approach involving light<sup>38,67</sup>. Therefore, liraglutide **3.5**, with 97% sequence homology being very similar

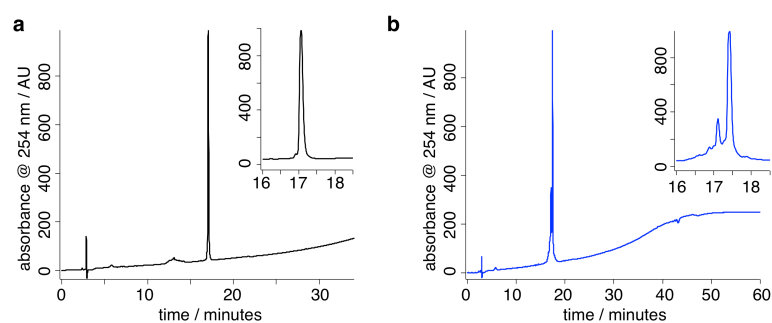
to native GLP-1, was selected for AMPP **1.22** photoswitch incorporation. The three peptides LirAzo **3.6**, LirAzo2 **3.7** and LirAzo3 **3.8** were synthesized in which **1.22** substitutes two, three or four amino acids in the central bridging part between the two helix segments of **3.5**. All three compounds exhibited good photophysical properties, *i.e.* showed robust switching kinetics for the 350 nm *trans* → *cis* and for the 430 nm *cis* → *trans* induced isomerization and were bistable in their *cis*-forms over days. After initial assessment of the potency of the LirAzo peptides towards the glucagon-like peptide 1 receptor (GLP-1R) through cAMP dose-response curves in CHO-GLP-1R cells, LirAzo **3.6** was selected as lead candidate. This was due to its slightly weaker potency than native GLP-1 towards GLP-1R and a nearly four-fold difference between its both isomers. The GLP-1R is known to boost insulin secretion through signaling *via* cAMP and Ca<sup>2+</sup>, and LirAzo **3.6** stimulation of GLP-1R was examined for both pathways in MIN6 cells endogeneously expressing the receptor. It was shown that **3.6** differently engages GLP-1R signaling, *i.e.* the *cis*-isomer provoked higher cAMP synthesis, while solely the *trans*-isomer engaged Ca<sup>2+</sup> influx into beta cells. This well-known signal bias of GPCR agonists is being intensively studied, as it is believed to be a possible actuator for drug side effects. Furthermore, insulin secretion was biased towards *cis*-**3.6**, while beta cell survival was prolonged after treatment with *trans*-**3.6**. Both the boosting of insulin secretion and protection of the beta cell mass are important effects of incretin mimetics and **3.6** can help to understand these processes.

To this end LirAzo **3.6** delivers a blue print not only for next generation of photoswitchable incretin mimetics, but for all compounds of this class. It also showcases the complexity and variety of GPCR signaling and the need for further remotely controllable compounds to dissect beta cell signaling in health and disease. The next step will be the implementation of atomic level molecular dynamic simulations to gain insight into *cis/trans*-**3.6**-GLP-1R binding interactions and possibly the crystallization of both receptor bound isomers. To enable *in vivo* application the complete analogue of liraglutide **3.5**, dubbed  $\gamma$ Ep-LirAzo **3.9**, which possesses the palmitoyl moiety at Lys25 has been synthesized. The fatty acid side chain promotes binding to serum albumin, enhances blood plasma distribution, prolongs the half-life and enables crossing of the blood brain barrier, facilitating drug action in the central nervous system. The next version  $\gamma$ Ep-LirAzo **3.9** will open the door to intensive *in vivo* testing and stressing of this photopharmacophore. Furthermore, as in case of the AMPP **1.22** modified AzoANP peptides, a red-shifted tetra-*ortho* chloro variant of this photoswitch will enable the *in vivo* application without the need of UV light.

## 3.5 EXPERIMENTAL

### 3.5.1 SPECTROSCOPIC AND SPECTROMETRIC DATA OF LIRAZO 3.6

#### 1.3. HPLC traces of Lira and LirAzo peptides



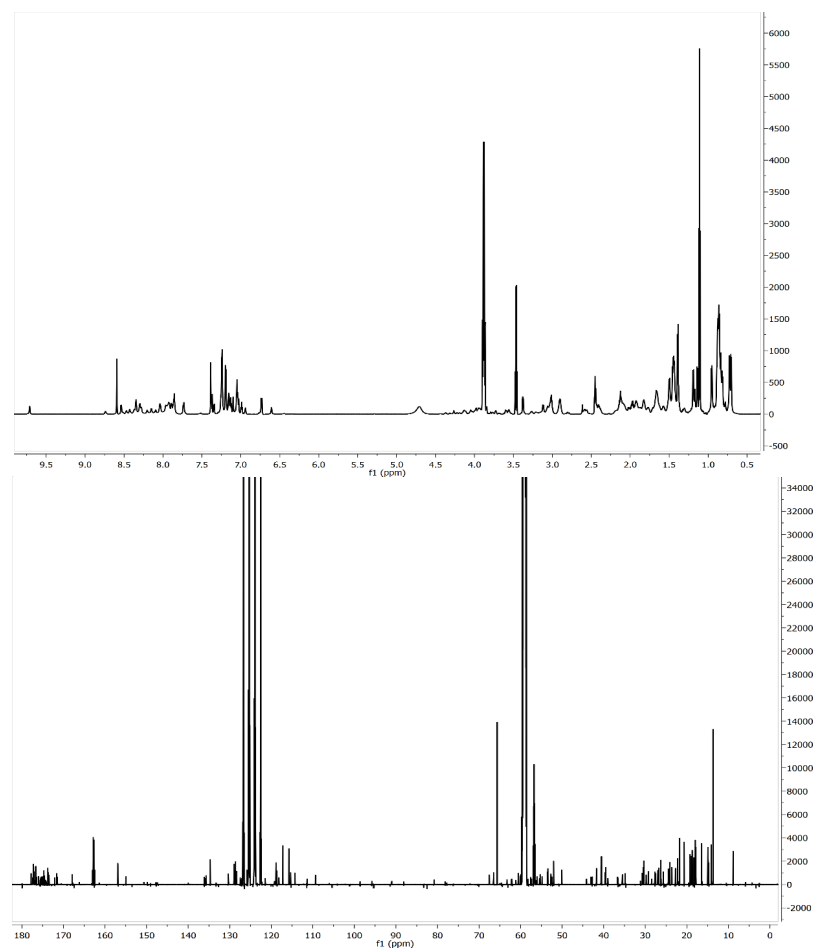
Above are analytical HPLC traces of a) Lira and b) **LirAzo** using a gradient MeCN/H<sub>2</sub>O = 10/90 → 100/0 within 40 min.

#### 1.4. Photoswitching of LirAzo peptide

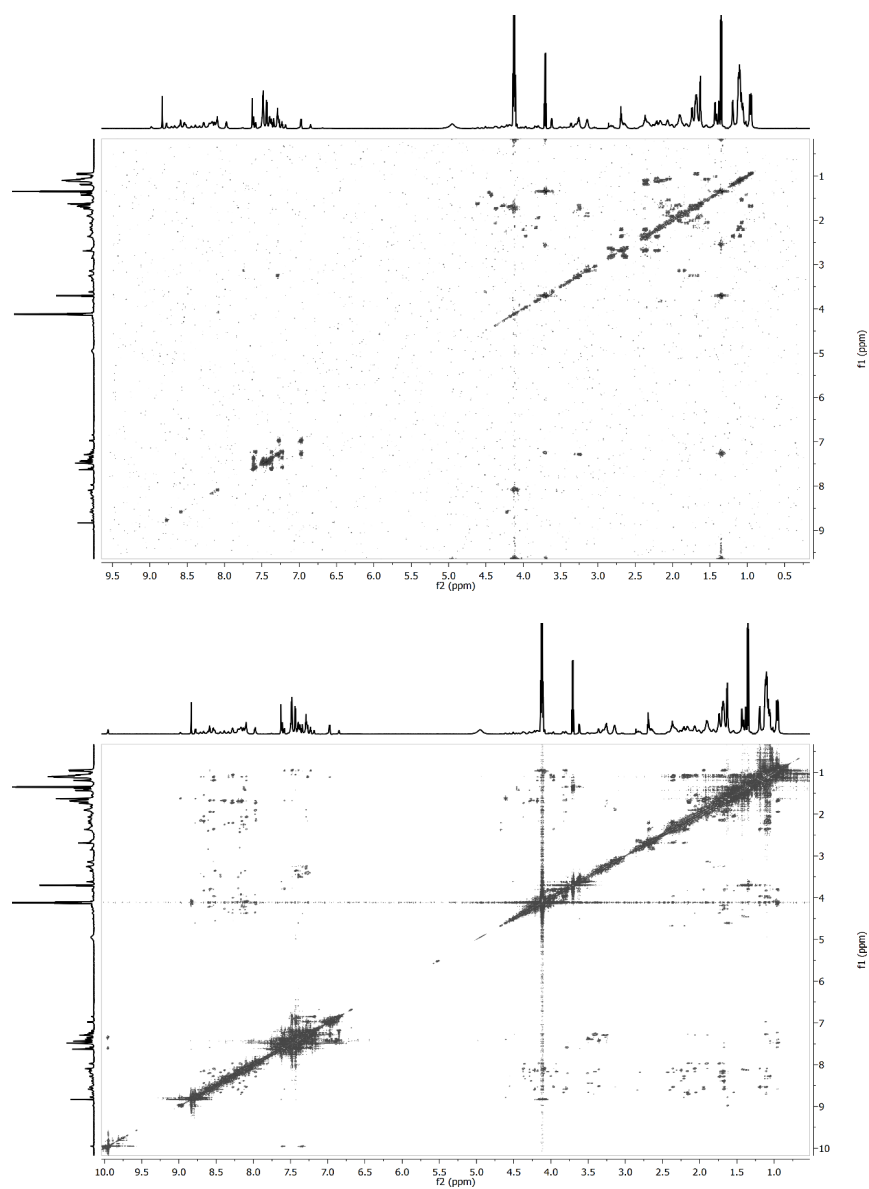
*cis/trans*-Isomerization was assessed by UV/Vis spectroscopy following the  $\pi$ - $\pi^*$ -band (330 nm) and double-exponential fitting of the slopes (Wavemetrics Igor v6.2).  $\tau$ -Values are given in Supplementary Table 1 and represented in Supplementary Figure 2.

## 1.5. NMR Spectra of Lira and *cis/trans*-LirAzo peptides

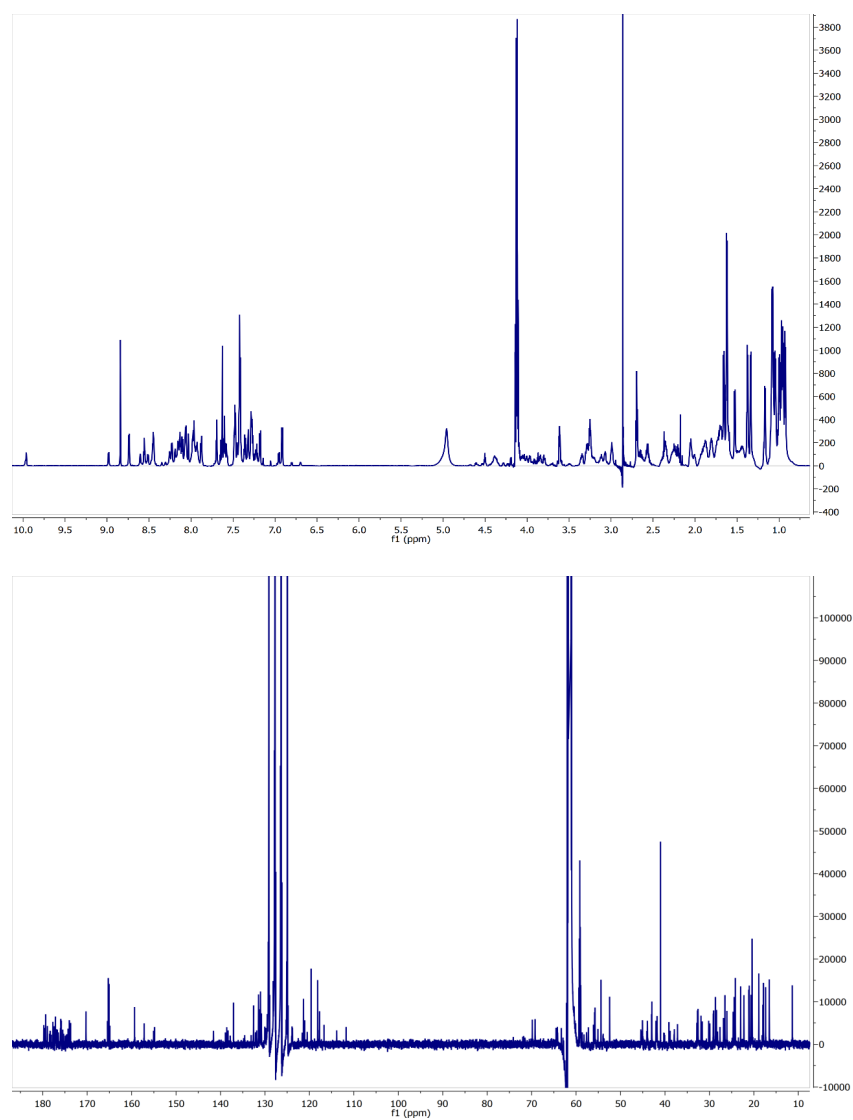
### 1.5.1. Lira



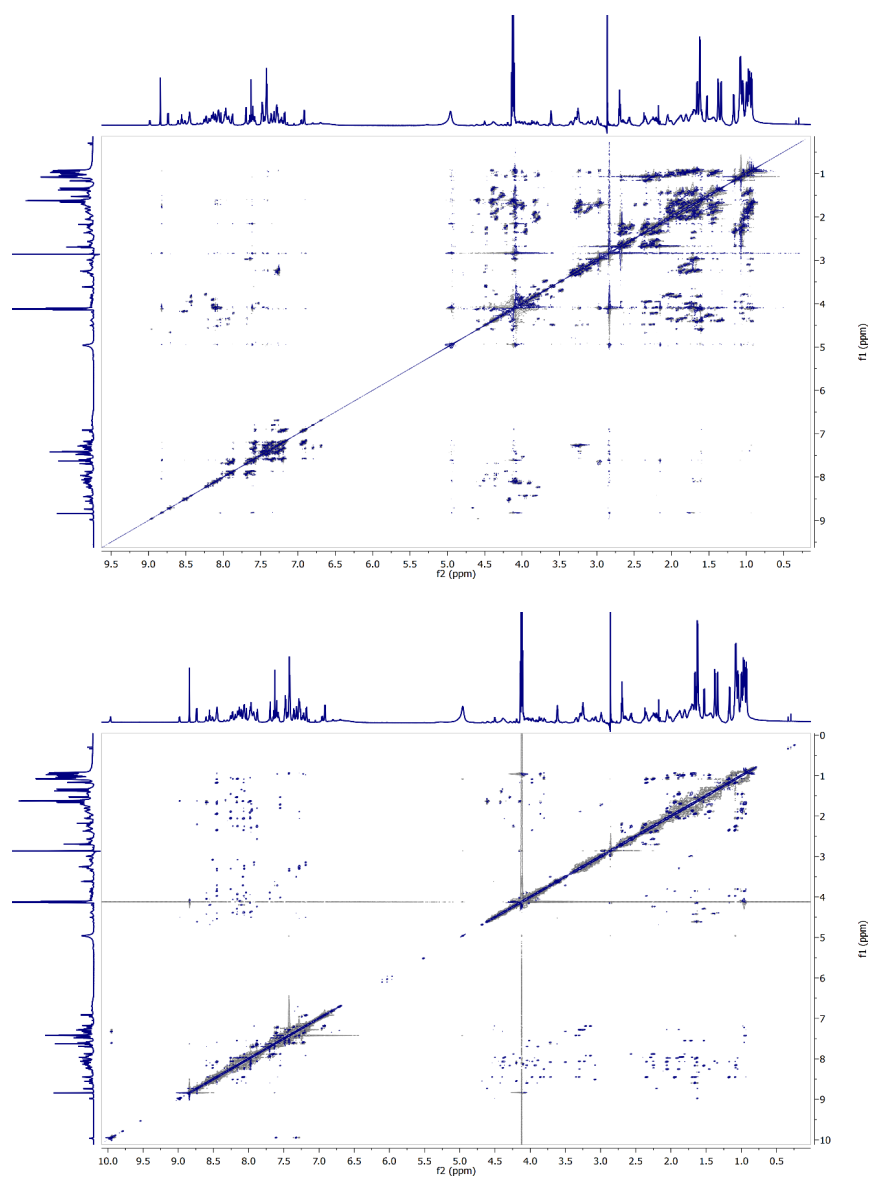
$^1\text{H}$ - (top) and  $^{13}\text{C}$ - (bottom) NMR spectra of Lira peptide.



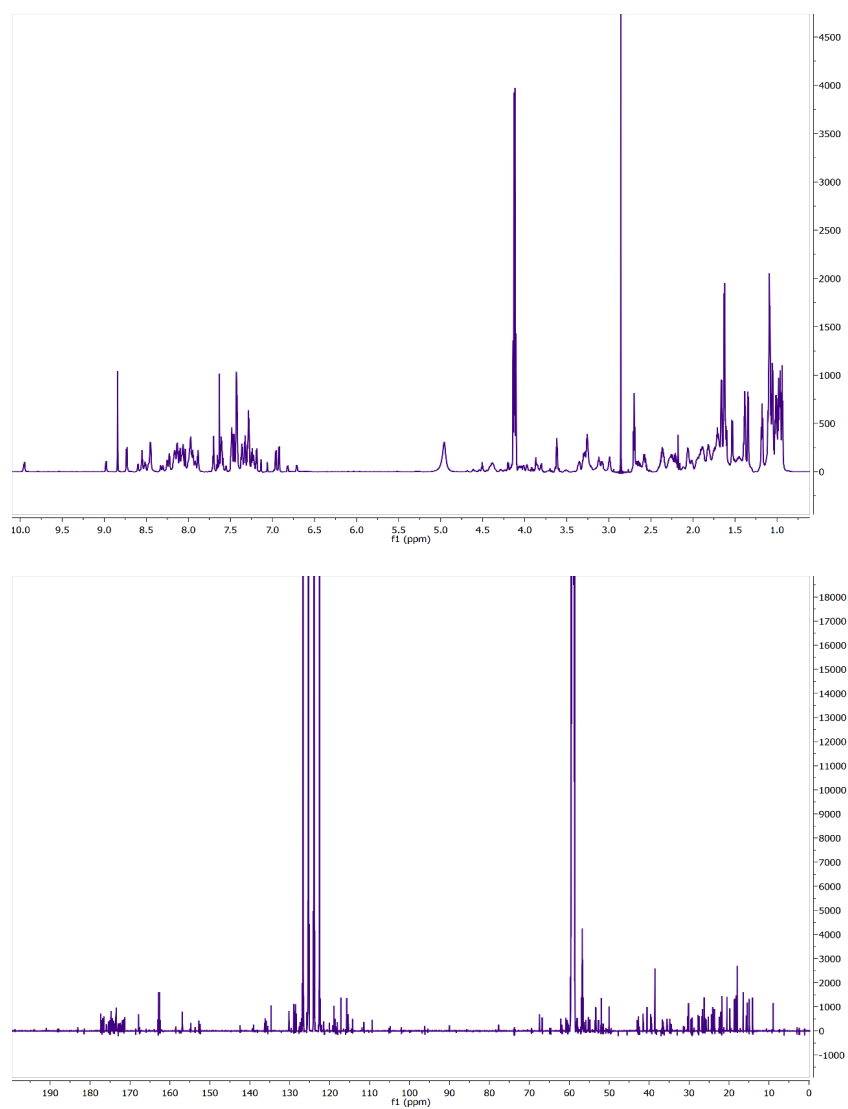
$^1\text{H}, ^1\text{H}$ -COSY (top) and  $^1\text{H}, ^1\text{H}$ -NOESY (bottom) NMR spectra of Lira peptide.

**1.5.2. *trans*-LirAzo**

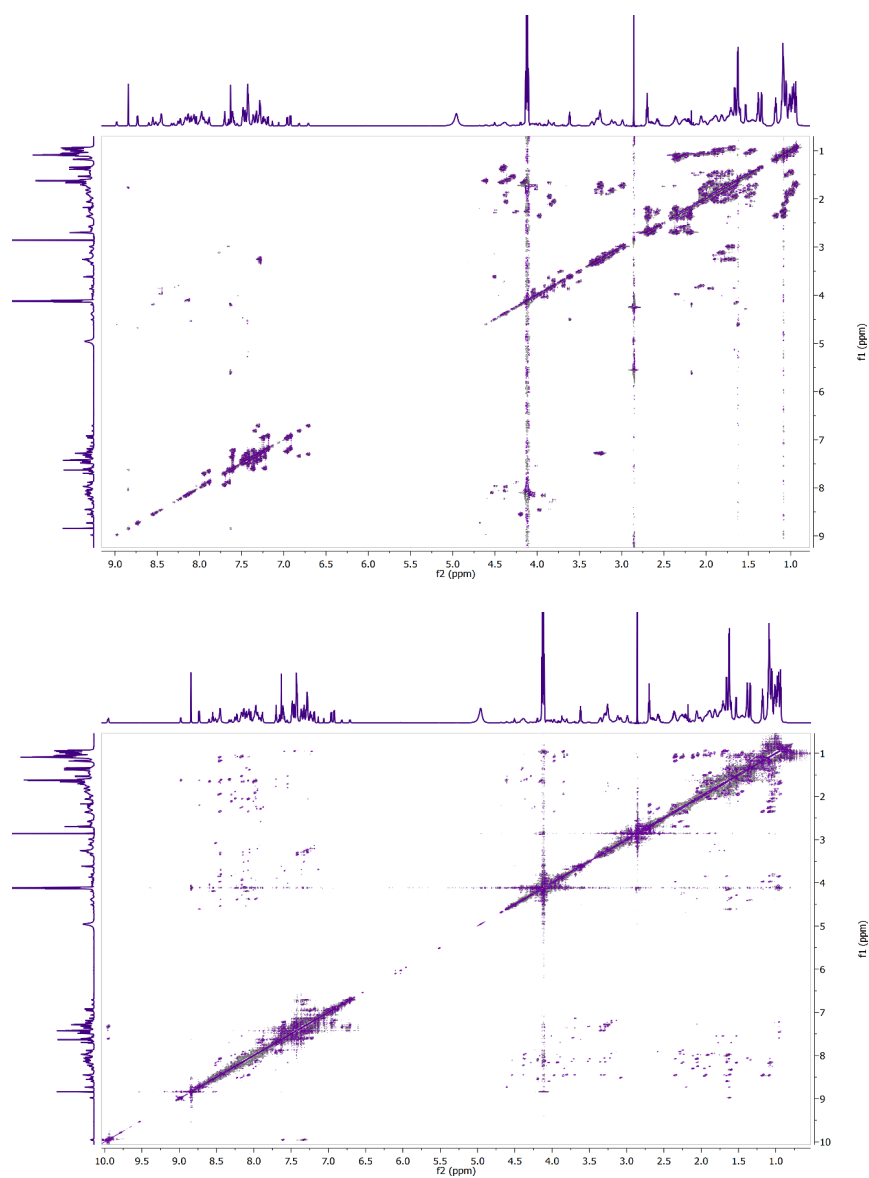
$^1\text{H}$ - (top) and  $^{13}\text{C}$ - (bottom) NMR spectra of *trans*-LirAzo peptide.



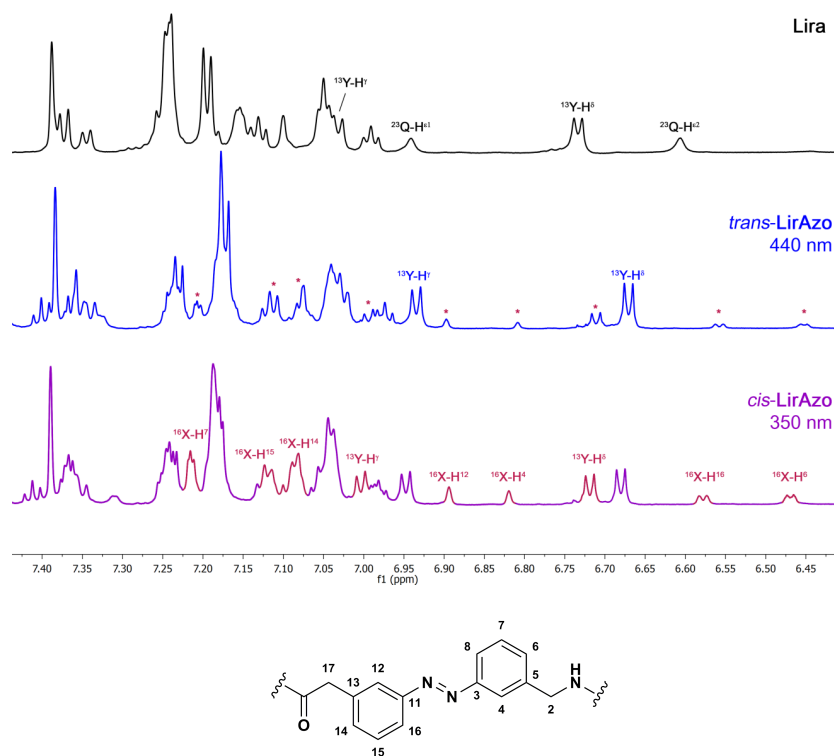
$^1\text{H}, ^1\text{H}$ -COSY (top) and  $^1\text{H}, ^1\text{H}$ -NOESY (bottom) NMR spectra of *trans*-LirAzo.

**1.5.3. *cis*-LirAzo**

$^1\text{H}$ - (top) and  $^{13}\text{C}$ - (bottom) NMR spectra of *cis*-LirAzo peptide.



$^1\text{H}, ^1\text{H}$ -COSY (top) and  $^1\text{H}, ^1\text{H}$ -NOESY (bottom) NMR spectra of *cis*-LirAzo.



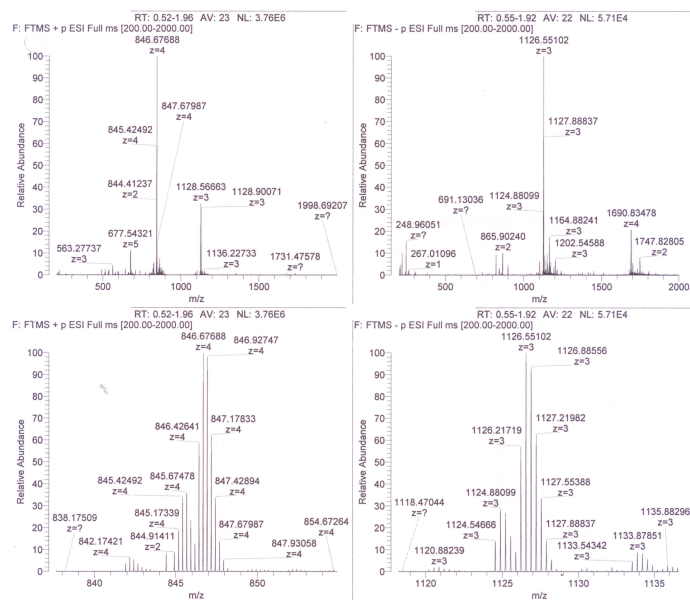
Selected aromatic signals of <sup>1</sup>H-NMR spectra of Lira (black) and *trans*-(blue)/*cis*-(purple)-**LirAzo** (top). Protons of the substituted glutamine residue (<sup>23</sup>Q, black) are undetectable in *cis/trans*-**LirAzo**. Signals emanating from AMPP (red asterisks) and tyrosine (<sup>19</sup>Y-H<sup>ε</sup> doublet) become more prominent for the *cis*-isomer, demonstrating changes in secondary and tertiary structure of **LirAzo** upon isomerization. Numeration of AMPP atoms (bottom). See also Supplementary Table 3.

**Supplementary Table 3:** H and C atom chemical shift data of *cis/trans*-AMPP in *trans*- and *cis*-LirAzo peptides.

AMPP	<i>trans</i> -LirAzo		<i>cis</i> -LirAzo	
	H [ppm]	C [ppm]	H [ppm]	C [ppm]
2	4.46, 4.38	45.2	4.26, 4.19	44.9
4	7.72	125.5	6.82	122.5
6	7.64	123.6	6.48	120.7
7	7.41	131.6	7.22	129.3
8	7.36	132.8	7.06	129.5
12	7.79	125.0	6.90	124.4
14	7.44	134.3	7.12	131.1
15	7.45	131.9	7.11	131.5
16	7.70	123.8	6.58	120.9
17	3.87	44.0	3.57, 3.45	43.8

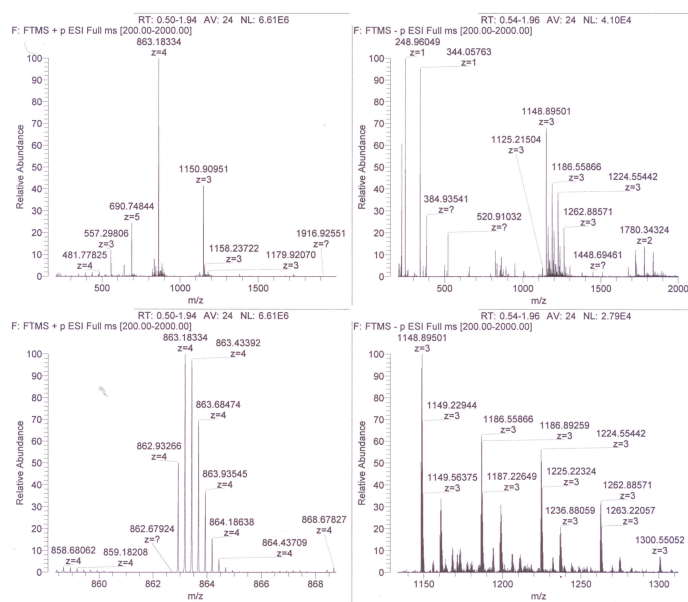
## 1.6. HRMS spectra of peptides

### 1.6.1. Lira



**HRMS (ESI):** calc. for  $C_{151}H_{232}N_{42}O_{47}^{4+}$  ( $M+4H$ ) $^{4+}$ : 846.6767 (monoisotopic), found: 846.6769.

## 1.6.2. LirAzo



**HRMS (ESI):** calc. for  $C_{159}H_{234}N_{42}O_{45}^{4+}$  ( $M+4H$ ) $^{4+}$ : 863.1831 (monoisotopic), found: 863.1833.

### 3.5.2 EXPERIMENTAL DATA OF ADDITIONAL COMPOUNDS LIRAZO2 3.8 AND LIRAZO3 3.6

#### 3.5.2.1 SYNTHESIS OF PEPTIDES LIRAZO2 3.7 AND LIRAZO3 3.8

The synthesis of peptides LirAzo2 **3.8** and LirAzo3 **3.6** followed the general peptide synthesis protocol stated in the APPENDIX. Table 3.1 depicts the coupling conditions of the different building blocks used for the automated peptide synthesis. As resin for peptides LirAzo2 **3.8** and LirAzo3 **3.6** a pre-loaded Wang LL *N*-(Fmoc)-Gly resin (NovaBiochem, Darmstadt/Germany) was used.

**Table 3.1: Coupling conditions for synthesis of peptides LirAzo2 3.8 and LirAzo3 3.6.**

Amino acid(s)	Coupling method	Steps	Time (s)	Temperature (°C)	Power (W)
Fmoc-Arg(Pbf)-OH	Arg double coupling	2	Step 1: 1500 Step 2: 300	Step 1: 25 Step 2: 75	Step 1: 0 Step 2: 23
Fmoc-His(Trt)-OH	Single amino acid 50 °C coupling	1	480	50	23
Fmoc-AMPP-OH <b>1.26</b>	Photoswitch coupling	1	1800	75	23
Fmoc-Ala-OH, Fmoc-Asp(Trt)-OH, Fmoc-Glu( <i>t</i> -Bu)-OH, Fmoc-Gly-OH, Fmoc-Ile-OH, Fmoc-Leu-OH, Fmoc-Lys(Boc)-OH, Fmoc-Phe-OH, Fmoc-Ser( <i>t</i> -Bu)-OH, Fmoc-Thr( <i>t</i> -Bu)-OH, Fmoc-Trp(Boc)-OH, Fmoc-Tyr( <i>t</i> -Bu)-OH, Fmoc-Val-OH	Standard single amino acid coupling	1	480	75	23

## 3.5.2.2 ANALYTICAL HPLC SPECTRUM AND MASS SPECTRUM OF LIRAZO2 3.8

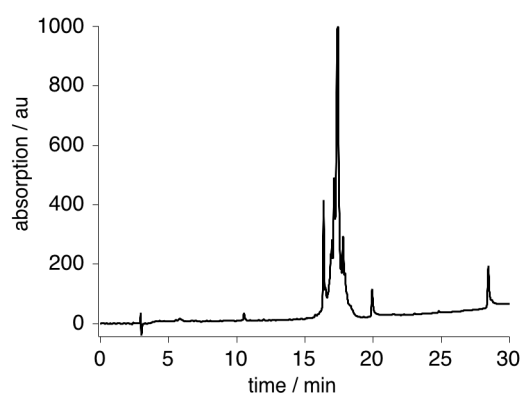


**Figure 3.5: HPLC spectrum of LirAzo2 3.8.** Analytical HPLC spectrum of **3.8** with a water/acetonitrile gradient 95:5 → 0:80 in 40 min.  $R_{t,cis}$  = 16.4 min,  $R_{t,trans}$  = 17.4 min.

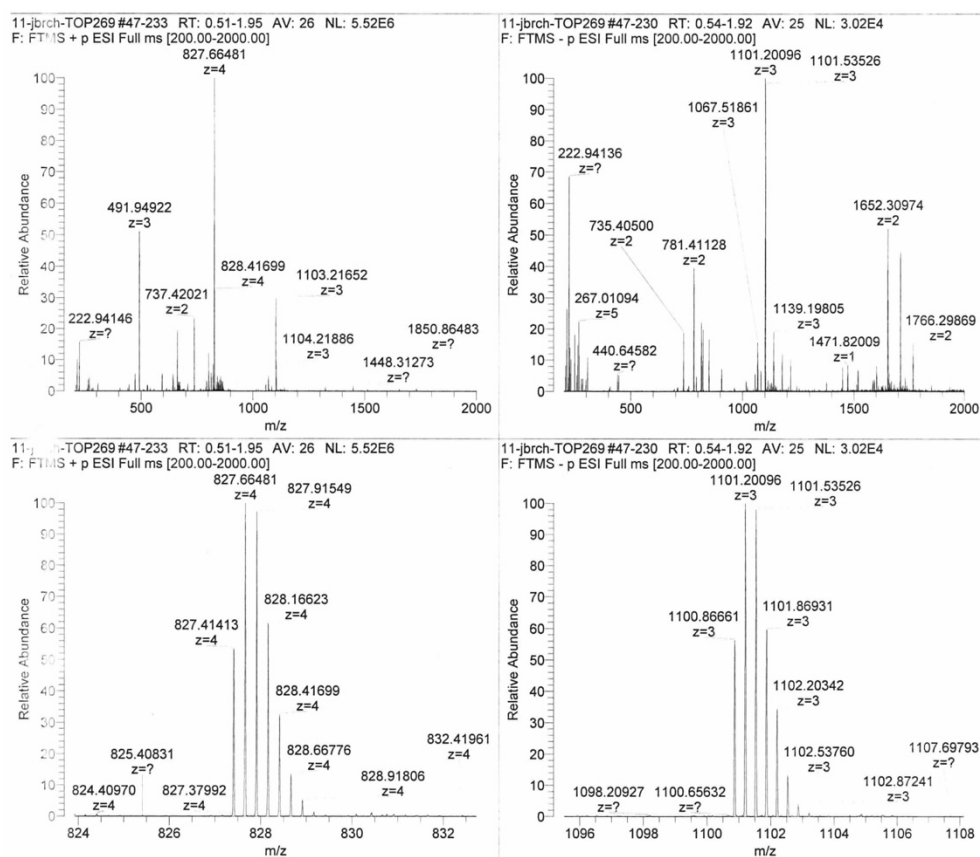


**Figure 3.6: HRMS ESI spectrum of LirAzo2 3.8.** HRMS (+ESI)  $m/z$ : calc. for  $C_{153}H_{223}O_{43}N_{40}^{3+}$  [ $M+3H$ ]: 1103.2170; found: 1103.2165. Calc. for  $C_{153}H_{224}O_{43}N_{40}^{4+}$  [ $M+4H$ ] $^{4+}$ : 827.6646; found: 827.6648.  $\Delta m$  = -0.45 ppm.

## 3.5.2.3 ANALYTICAL HPLC SPECTRUM AND MASS SPECTRUM OF LIRAZO3 3.6

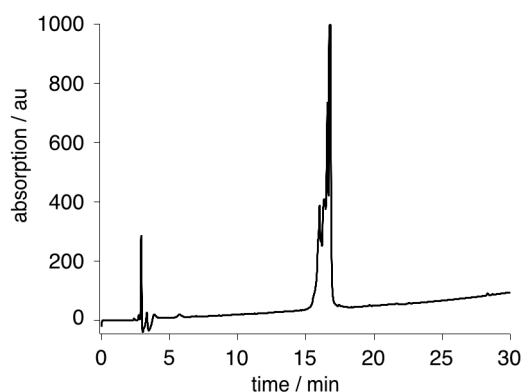


**Figure 3.7: HPLC spectrum of LirAzo3 3.6.** Analytical HPLC spectrum of **3.6** with a water/acetonitrile gradient 95:5 → 20:80 in 40 min.  $R_{t,cis}$  = 16.0 min,  $R_{t,trans}$  = 16.7 min.

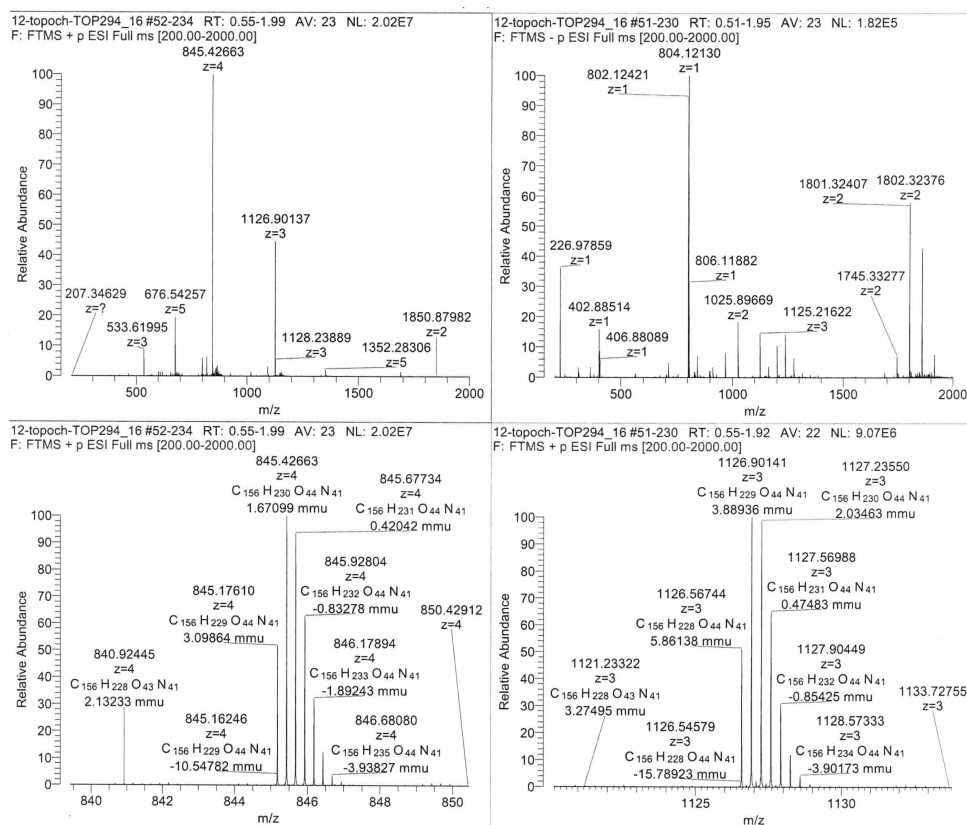


**Figure 3.8: HRMS ESI spectrum of LirAzo3 3.6.** HRMS (+ESI)  $m/z$ : calc. for  $C_{156}H_{229}O_{44}N_{41}^{3+}$   $[M+3H]^{3+}$ : 1126.8960; found: 1126.9014. Calc. for  $C_{156}H_{230}O_{44}N_{41}^{4+}$   $[M+4H]^{4+}$ : 845.4238; found: 845.4266.  $\Delta m$  = 2.83 ppm.

## 4 CONSTITUTIVE ACTIVATION OF A CLASS B G-PROTEIN COUPLED RECEPTOR USING TETHERED PHARMACOLOGY (EXONATIDE)

This work has been submitted to *Angewandte Chemie* on the 30<sup>th</sup> November 2016.

The previous two projects discussed in CHAPTER 2 and 3 utilized the PCLs TOP271 **2.1** and LirAzo **3.6** for controlling receptor activation and signaling. Especially the latter project not only demonstrated photocontrol of the GLP-1R through isomer-biased receptor activation, but also differential triggering of downstream signaling events, *i.e.* cAMP accumulation and intracellular Ca<sup>2+</sup> fluxes<sup>16</sup>. Although the PCL approach offers many advantages over PTLs, with the most concise being the evasion of genetic modification, tethered ligands in general have several benefits in an experimental environment. These comprise: i) a diffusion rate which is independent of the ligand-receptor binding and activation, ii) a defined ligand/receptor ratio of 1:1, iii) membrane-independent high local concentrations, iv) a negligible receptor pre-activation, v) eventual disturbances *in vivo* are only caused by the bioconjugation reaction and vi) fast and easy *in vitro* screening using a single transfected receptor construct. Given these aspects, we envisioned a benzyl guanine (BG) modified photoswitchable tethered incretin mimetic based on LirAzo **3.6** to be linked to a SNAP-tag fusion protein modified GLP-1R (SNAP-GLP-1R). This PTL BG-LirAzo **4.1** should allow constitutive activation and optical regulation of GLP-1R cAMP and Ca<sup>2+</sup> signaling, and should help to detect their regulation in post-endocytotic receptor trafficking. These processes remain elusive for GLP-1R and in general for class B GPCRs<sup>197</sup>, and their understanding them will mark a cornerstone in related drug development and future disease treatment.

The original approach involved the synthesis of the four BG-modified peptides BG-Ex4(1-39) **4.2** (exONatide), BG-Ex4(9-39) **4.3** (exOFFatide), BG-Lira **4.4** and BG-LirAzo **4.1**. While the latter two are based on liraglutide **3.5** and the photoswitchable LirAzo **3.6**, **4.2** and **4.3** are BG-modified versions of the blockbuster incretin mimetic exenatide **3.4** (Ex4(1-39)). Ex4(1-39) **4.2** thereby is a full length 1-39 amino acid agonist, while Ex4(9-39) **4.3** is the *N*-terminal truncated antagonist. All four peptides were designed based on the same concept, that is C-terminal substitution with a cysteine followed by disulfide bridge linkage with the reactive BG-pyridyldithiol derivative **4.5**. Although all four precursor peptides could be synthesized, only the agonist exONatide **4.2** and the antagonist exOFFatide **4.3** were successfully linked to the BG-compound. For this reason, and because **4.3** showed a lack in potency, only exONatide **4.2** was successfully used for the constitutive activation of SNAP-GLP-1R signaling.

## 4.1 MANUSCRIPT: CONSTITUTIVE ACTIVATION OF A CLASS B G-PROTEIN COUPLED RECEPTOR USING TETHERED PHARMACOLOGY

Manuscript



COMMUNICATION

WILEY-VCH

### Constitutive activation and reversible trafficking of a class B G protein-coupled receptor using tethered pharmacology

Tom Podewin,<sup>[a]</sup> Johannes Broichhagen,<sup>[a,d]</sup> Nicholas H. F. Fine,<sup>[b]</sup> Daniela Nasteska,<sup>[b]</sup> Philipp Leippe,<sup>[a]</sup> Manuel Gailer,<sup>[a]</sup> Teresa Buenaventura,<sup>[c]</sup> Nisha Kanda,<sup>[c]</sup> Sarah Janik,<sup>[a]</sup> Alejandra Tomas,<sup>[c]</sup> Dirk Trauner,<sup>[a]\*</sup> Anja Hoffmann-Röder<sup>[a]\*</sup> and David J. Hodson<sup>[b]\*</sup>

**Abstract:** Understanding the activation and trafficking of G protein-coupled receptors (GPCRs) using conditional approaches is paramount to developing new disease strategies. Here, we describe the design, synthesis and testing of **ExONatide**, a benzylguanine-linked agonist of the glucagon-like peptide-1 receptor (GLP-1R), a class B GPCR required for proper maintenance of glucose levels in humans. **ExONatide** covalently binds to cells expressing the SNAP-tagged GLP-1R, leading to long-lasting cAMP generation, Ca<sup>2+</sup> rises and intracellular trafficking. These effects can be readily switched OFF following cleavage of the introduced disulfide bridge using a cell-permeable reducing agent. Thus, **ExONatide** allows SNAP-tag-directed constitutive activation and trafficking of a class B GPCR in a reversible manner. This or similar compounds may be useful for understanding GLP-1R signaling both *in vitro* and *in vivo*, with broad applicability to other transmembrane proteins including GPCRs.

Selectively targeting and activating G protein-coupled receptors (GPCRs) is important for understanding their function/signaling. Self-labeling proteins such as SNAP-tag are ideal for these purposes, since they can be expressed conditionally both *in vitro*<sup>[1]</sup> and *in vivo*,<sup>[2]</sup> and covalently bind

molecules possessing a benzylguanine (BG) bioconjugation handle. Moreover, SNAP-tags can be fused onto a variety of proteins including GPCRs using recombinant engineering,<sup>[3]</sup> and CRISPR/Cas9 genome editing approaches have opened up the possibility to do the same *in vivo* in rodents.<sup>[4]</sup> The recently developed bio-orthogonal (iBOLT) and photoswitchable orthogonal remotely-tethered (PORTL) methods address 'tethered pharmacology', and form the basis of targeting receptors orthogonally.<sup>[5]</sup>

The glucagon-like peptide-1 receptor (GLP-1R) is an excellent candidate for such approaches. Following ligand binding, this class B G protein-coupled receptor (GPCR) primarily activates adenylyl cyclase through G<sub>s</sub>, leading to 3'-5'-cyclic adenosine monophosphate (cAMP) accumulation<sup>[6]</sup> and intracellular Ca<sup>2+</sup> fluxes.<sup>[7]</sup> These signaling processes are terminated by post-endocytotic receptor trafficking, where the GLP-1R is internalized into endosomes and lysosomes, before sorting and recycling to the membrane.<sup>[8]</sup> However, recent reports suggest that GPCR signaling continues even following receptor internalization into endosomes *via* cytosolic cAMP generation.<sup>[9]</sup>

- [a] Tom Podewin, Dr. Johannes Broichhagen, Philipp Leippe, Manuel Gailer, Sarah Janik, Prof. Dr. Dirk Trauner, Prof. Dr. Anja Hoffmann-Röder Ludwig-Maximilians-University Munich, Department of Chemistry and Centre for Integrated Protein Science (CIPSM) Butenandstr. 5-13, 81377 Munich, Germany
- [b] Nicholas H. F. Fine, Dr. Daniela Nasteska and Prof. Dr. David J. Hodson Institute of Metabolism and Systems Research (IMSR) and Centre of Membrane Proteins and Receptors (COMPARE), University of Birmingham, B15 2TT, United Kingdom and Centre for Endocrinology, Diabetes and Metabolism, Birmingham Health Partners, Birmingham, B15 2TH, U.K.
- [c] Teresa Buenaventura, Dr. Nisha Kanda, Dr. Alejandra Tomas Imperial College London, Section of Cell Biology and Functional Genomics, Department of Medicine, Imperial College London, W12 0NN, U.K.
- [d] Present Address: Dr. Johannes Broichhagen Max-Planck Institute of Medical Research, Jahnstr. 29, 69120 Heidelberg, Germany

\* Correspondence should be addressed to [d.hodson@bham.ac.uk](mailto:d.hodson@bham.ac.uk), [dirk.trauner@lmu.de](mailto:dirk.trauner@lmu.de) or [anja.hoffmann-roeder@lmu.de](mailto:anja.hoffmann-roeder@lmu.de). Supporting information for this article is given via a link at the end of the document.

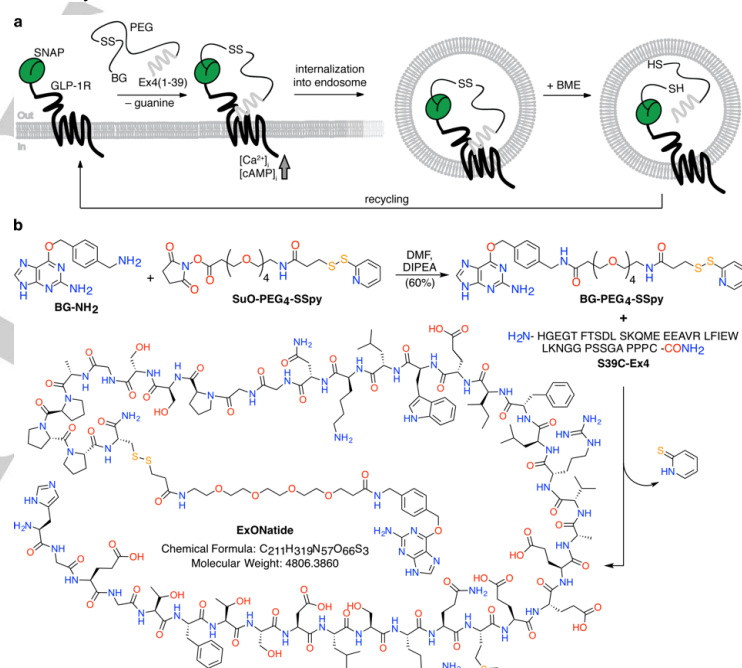


**Figure 1.** Logic and synthesis of **ExONatide**. a) After covalent labeling of a SNAP-tag with **ExONatide**, the GLP-1R can be activated, leading to Ca<sup>2+</sup> and cAMP rises together with internalization and trafficking, which can readily be terminated by reductive cleavage using  $\beta$ -mercaptoethanol (BME). b) Commencing with activated disulfide BG-PEG<sub>4</sub>-SSpy obtained by peptide coupling, a cysteine-containing peptide S39C-Ex4 obtained by solid-phase peptide synthesis (SPPS) can be installed by means of disulfide exchange.

## COMMUNICATION

WILEY-VCH

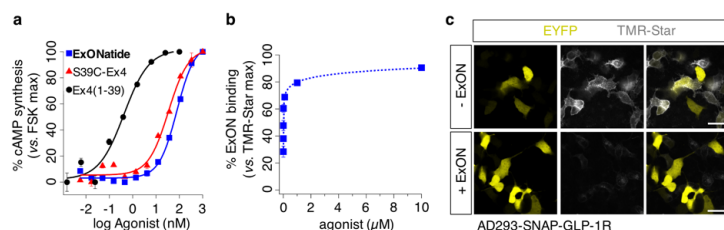


**Figure 2.** ExONatide signaling and binding. a) ExONatide, S39C-Ex4 and Ex4(1-39) all induce sigmoidal cAMP dose-response curves in AD293 cells transiently-transfected with SNAP-GLP-1R cells ( $n = 3$ ). b) Pre-incubation of the same cells with increasing concentrations of ExONatide exponentially decreases TMR-Star binding/fluorescence ( $n = 60$ -120 cells from 4 experiments). c) As for b), but representative images of cells pre-incubated with and without a high concentration (1  $\mu\text{M}$ ) of ExONatide (scale bar = 33  $\mu\text{m}$ ). Values are the mean  $\pm$  SEM.

How internalization and subsequent trafficking influence class B GPCR function is poorly understood.<sup>[10]</sup> Deciphering the mechanisms involved may be important for drug development and disease treatment, particularly regarding the GLP-1R, a blockbuster type 2 diabetes target,<sup>[11]</sup> which displays pleiotropic effects (e.g. on the brain, heart and immune system).<sup>[11-12]</sup> Key to this is the development of tools that allow constitutive activation and reversible trafficking of the GLP-1R in a highly conditional manner.

Herein, we describe the development and testing of ExONatide, a benzylguanidine-linked incretin-mimetic based upon Exenatide (Byetta®) that constitutively switches 'ON' the GLP-1R (Fig 1a). As shown by X-ray crystallography, peptides such as Liraglutide (Victoza®) and Exendin-4 (Ex4(1-39)) bind to the GLP-1R extracellular domain with their C-terminus solvent exposed.<sup>[13]</sup> We therefore set out to derivatize Ex4(1-39) by mutating and synthesizing the S39C-Ex4 variant by means of solid-phase peptide synthesis (SPPS) to install a free cysteine bioconjugation handle as the C-terminal amino acid. Linking BG-NH<sub>2</sub> to a PEG<sub>4</sub> spacer containing a pyridyl activated disulfide from commercially available substrates, ExONatide was obtained with high purity and efficiency on the milligram scale (see SI for details on synthesis, including RP-HPLC trace and HRMS for ExONatide) (Fig. 1b).

As reported, Ex4(1-39) was able to increase intracellular cAMP concentrations with an  $EC_{50} = 39.9 \pm 11.5 \mu\text{M}$ , as assessed using LANCE TR-FRET-based assays in transiently transfected SNAP-GLP-1R AD293 cells (Fig. 2a). By contrast, cAMP concentration-responses to ExONatide were slightly right-shifted ( $EC_{50} = 10.0 \pm 3.1 \text{ nM}$ ) (Fig. 2a). Suggesting that single amino acid substitutions can affect potency, the  $EC_{50}$  values for S39C-Ex4 and ExONatide were almost identical ( $EC_{50} = 4.9 \pm 0.8 \text{ nM}$ ) (Fig. 2a). Nonetheless, maximal cAMP responses were almost 100% (vs. 10  $\mu\text{M}$  FSK) for all compounds tested, implying full agonism (Fig. 2a).

SNAP-tag binding was determined by pre-incubating SNAP-GLP-1R transfected AD293 cells with ExONatide for 30 min

before washing the cells and adding TMR-Star ( $\lambda_{\text{Ex}} = 554 \text{ nm}$ ;  $\lambda_{\text{Em}} = 580 \text{ nm}$ ), a fast SNAP-labeling fluorophore. Increasing concentrations of ExONatide exponentially reduced TMR-Star intensity with a half-maximal binding concentration ( $BC_{50,30\text{min}} = 0.30 \pm 0.03 \mu\text{M}$ ) suggestive of near-quantitative SNAP-tag labeling (Fig. 2b) (Fig. S1).

We next sought to investigate whether ExONatide would allow constitutive activation of GLP-1R signaling in a physiologically more relevant system. This was done by following GLP-1-induced Ca<sup>2+</sup> fluxes using confocal microscopy. Both Ex4(1-39) and ExONatide induced large cytosolic Ca<sup>2+</sup> rises in Fluo8-loaded MIN6 beta cells stably expressing SNAP-GLP-1R (MIN6B1-SNAP-GLP-1R) (Fig. 3a). While resting baseline Ca<sup>2+</sup> levels could be completely restored following a washout period for Ex4(1-39), this was not the case for ExONatide ( $P < 0.01$  vs. Ex4(1-39)). However, addition of reducing agent allowed ExONatide effects to be subsequently reversed by washout (Fig. 3a) (non-significant vs. Ex4(1-39)).  $\beta$ -Mercaptoethanol (BME) was used for reductive cleavage, since it is cell permeable and the GLP-1R undergoes rapid internalization following activation.<sup>[14]</sup> Similar results were observed in MIN6 using the FRET-based cAMP biosensor Epac2-camps,<sup>[15]</sup> providing evidence for reversible signaling through the two main GLP-1R activation pathways (Fig. 3b). While MIN6 endogenously express GLP-1R that may give rise to background adenylyl cyclase activity, this did not appear to be a major issue here, since cAMP responses to ExONatide were reduced to almost control levels by BME. Moreover, an effect of reducing agent *per se* is unlikely, as Ca<sup>2+</sup> and FRET responses to Ex4(1-39) remained normal in the presence of BME (Fig. 3a and b). In line with the Ca<sup>2+</sup> and cAMP data, insulin secretory responses to ExONatide could only be washed out following reductive cleavage (Fig. 3c).

In response to binding, the GLP-1R undergoes

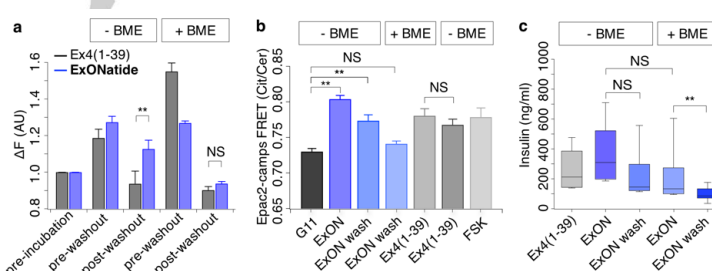
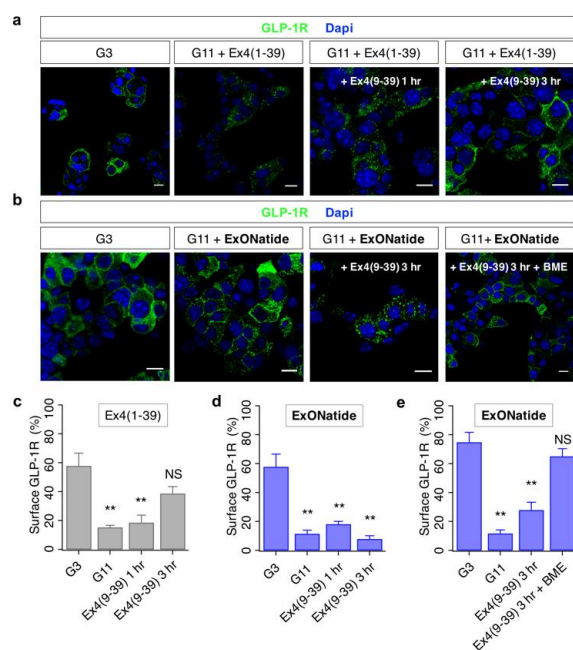


**Figure 3.** ExONatide leads to long-lasting Ca<sup>2+</sup> and cAMP signaling. a) ExONatide induces large Ca<sup>2+</sup> rises in MIN6B1-SNAP-GLP-1R beta cells similarly to Ex4(1-39), but this is only washed out following application of  $\beta$ -mercaptoethanol (BME) ( $n = 5$ -9 recordings). b) As for a), but FRET assays for intracellular cAMP synthesis ( $n = 40$ -71 cells from 3 experiments). c) As for a) but box and whiskers plot showing 5-95 percentile and median for insulin secretion ( $n = 8$  wells) (Ex4(1-39)-alone was used as a positive control). In all cases, BME-alone did not affect Ca<sup>2+</sup> or cAMP levels vs. control. \*\* $P < 0.01$  and NS, non-significant; one-way ANOVA (with Bonferroni's or Tukey's posthoc test) or Kruskal-Wallis test (with Dunn's multiple comparison test). Values are the mean  $\pm$  SEM unless otherwise stated.

## COMMUNICATION

WILEY-VCH

1 internalization before organellar (endosomal/lysosomal) sorting,  
 2 ligand removal and either recycling back to the membrane or  
 3 degradation.<sup>[9b, 10]</sup> To examine the effects of constitutive  
 4 activation on trafficking, MIN6B1-SNAP-GLP-1R cells were  
 5 treated with either Ex4(1-39) or **ExONatide** before  
 6 immunohistochemistry for GLP-1R localization using a  
 7 monoclonal antibody against the extracellular domain. Both  
 8 Ex4(1-39) and **ExONatide** induced internalization, as shown by  
 9 a decrease in cell surface GLP-1R expression and an increase  
 10 in punctate intracellular staining (Fig. 4a-d). However, this was  
 11 only reversed by the specific antagonist Ex4(9-39) for the native  
 12 agonist, with no significant membrane recycling detected for  
 13 **ExONatide** (Fig. 4a-d).<sup>[16]</sup> Supporting a role for SNAP-tag-  
 14 binding in irreversible internalization, almost complete recycling  
 15 of the GLP-1R to the plasmamembrane was seen following  
 16 addition of both BME and Ex4(9-39) (Fig. 4b and d). As for Ca<sup>2+</sup>  
 17 and cAMP signaling, BME-alone did not alter intracellular  
 18 trafficking (Fig. S2).



19  
 20  
 21  
 22  
 23  
 24  
 25  
 26  
 27  
 28  
 29  
 30  
 31  
 32  
 33  
 34  
 35  
 36  
 37  
 38  
 39  
 40  
 41  
 42  
 43  
 44  
 45  
 46  
 47  
 48  
 49  
 50  
 51  
 52  
 53  
 54  
 55  
 56  
 57  
 58  
 59  
 60  
 61  
 62  
 63  
 64  
 65

**Figure 4.** Constitutive trafficking by **ExONatide** in MIN6B1-SNAP-GLP-1R beta cells. a) Representative images showing that application of the agonist Ex4(1-39) at high glucose concentration (11 mM; G11) causes GLP-1R internalization, which can be reversed with the antagonist Ex4(9-39) (scale bar = 10  $\mu$ m). b) As for a), but following application of **ExONatide**. Note that GLP-1R internalization can only be reversed by Ex4(9-39) following application of BME. c) Surface GLP-1R expression is significantly reduced following application of Ex4(1-39), and this is reversed by application of Ex4(9-39). d) Surface GLP-1R expression is significantly reduced following application of **ExONatide**, but this is not reversed by application of Ex4(9-39). e) As for d), but showing plasmamembrane recycling of GLP-1R following treatment with BME. \*\* $P < 0.01$  and NS, non-significant *versus* G3 (one-way ANOVA with Tukey's posthoc test). In c) and d), samples were run in parallel, hence the same control value ( $n = 3-7$  experiments). Values are the mean  $\pm$  SEM.

In the present study, we describe an incretin-mimetic termed **ExONatide** that allows constitutive activation and internalization of the GLP-1R, a class B GPCR, when *N*-terminally fused to a SNAP-tag. Constitutive activation of class B

GPCRs has been described previously by means of cloning activating peptides onto the *N*-termini<sup>[17]</sup> and by co-expression of membrane-anchored peptides for probing ion channel or GPCR function.<sup>[18]</sup> However, using a SNAP-tagged receptor in conjunction with a BG-linked ligand bears several advantages: i) the ligand/receptor ratio is defined as 1:1 in terms of binding and potency; ii) local concentration can be considered high<sup>[19]</sup> and does not rely on membrane fluctuations; iii) pre-activation during expression and culture is absent; iv) disturbances *in vitro* and *in vivo* are limited by sole SNAP-tag fusion, *i.e.* it is highly conditional; and v) it is bidirectional and can be switched 'ON' and 'OFF' by virtue of the incorporated cleavage site.

Compared to native Ex4(1-39), the potency of **ExONatide** for cAMP generation was almost 250-fold lower, but still lying in the low nanomolar range. The reasons for this are unknown, but may reflect the single amino acid substitution rather than the presence of the PEG linker, since a similar right-shift of the concentration-response was detected for the S39C variant of Ex4(1-39). Indeed, single amino acid mutations on the extracellular face of the GLP-1R were reported to have a large effect on affinity and signaling bias,<sup>[20]</sup> and may similarly underlie diversity in peptide hormone binding. Importantly, the ligand concentration required for orthosteric activation was 10-fold less than that required for full SNAP-tag labeling, meaning that **ExONatide** bound to SNAP-GLP-1R fusion is always active.

Suggesting that activation of the GLP-1R may occur in a cooperative manner, the Hill coefficient was  $1.90 \pm 0.50$  and only minimal cAMP generation was observed at 10 nM **ExONatide**, despite ~50% SNAP-tag occupancy. Notably, **ExONatide** induced long-lasting GLP-1R re-distribution to the intracellular compartment that could only be reversed following addition of cell permeable reducing agent. Although SNAP-labeled fluorophores with cell surface-restricted disulfide cleavage sites have been reported,<sup>[21]</sup> they still rely on receptor activation by native ligand. By contrast, **ExONatide** provides a physiologically relevant tool for probing how class B GPCRs such as the GLP-1R signal within organelles (*e.g.* endosomes), as well as how alterations in kinetics may influence second messenger recruitment (*i.e.* signal bias), all based upon intracellular manipulation. Moreover, it is becoming increasingly apparent that the GLP-1R has broad-ranging physiological functions. While conditional knockout mouse models exist,<sup>[22]</sup> methods for constitutively activating the receptor are lacking. In combination with SNAP-GLP-1R animals, **ExONatide** may provide a powerful platform for dissecting out the role of GLP-1R signaling in a cell-specific manner *in vivo*.

In summary, **ExONatide** provides a template for the design and production of agonists, antagonists and modulators that allow constitutive yet reversible activation of cell surface receptor proteins, such as GPCRs, bearing a fused SNAP-tag. **ExONatide** and its congeners thus promise to open up new avenues of exploration for extracellular activation, including its kinetics and intracellular signaling.

## Experimental Section

Experimental details including solid-phase peptide synthesis, spectroscopic and spectrometric characterization and biological

## COMMUNICATION

WILEY-VCH

experiments can be found in the Supporting Information. ExONatide is available from the Trauner, Hoffmann-Röder and Hodson labs for academic use free of charge.

### Acknowledgements

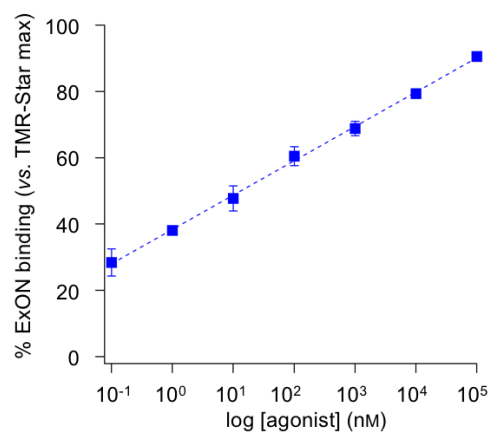
We are grateful to the SFB749 (T.P., M.G. and A.H.R.), the SFB TRR 152 (J.B. and D.T.), the SFB1032 (P.L. and D.T.) and the Center for Integrated Protein Science Munich (CIPSM) (T.P., J.B., P.L., M.G., D.T. and A.H.R.). T.P. was supported by an EASD Albert-Renold Young Scientist Fellowship (94571). A.T. was supported by an MRC Project Grant (MR/M012646/1) and a Diabetes UK Early-Career Small Grant (16/0005441). D.T. was supported by an Advanced Grant from the European Research Council (268795). D.J.H. was supported by Diabetes UK R.D. Lawrence (12/0004431), EFSD/Novo Nordisk Rising Star and Birmingham Fellowships, a Wellcome Trust Institutional Support Award, an MRC Project Grant (MR/N00275X/1) and an ERC Starting Grant (OptoBETA; 715884). MIN6B1 cells were provided by Prof. Philippe Halban (University of Geneva, Switzerland) with permission from Prof. Jun-ichi Miyazaki (University of Osaka) who produced the maternal MIN6 cell line.

**Keywords:** Tethered pharmacology • GPCR • GLP-1R • incretin • SNAP-tag • type 2 diabetes

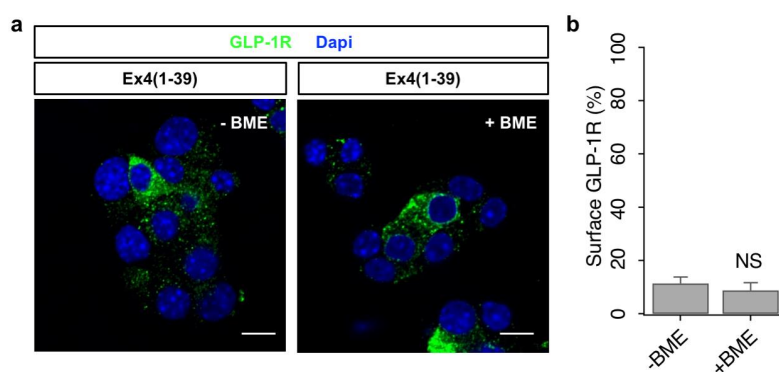
- [1] A. Keppler, S. Gendreizig, T. Gronemeyer, H. Pick, H. Vogel, K. Johnsson, *Nat. Biotechnol.* **2003**, *21*, 86-89.
- [2] G. Yang, F. de Castro Reis, M. Sundukova, S. Pimpinella, A. Asaro, L. Castaldi, L. Batti, D. Bilbao, L. Raymond, K. Johnsson, P. A. Heppenstall, *Nat. Methods* **2015**, *12*, 137-139.
- [3] D. Maurel, L. Comps-Agrar, C. Brock, M. L. Rives, E. Bourrier, M. A. Ayoub, H. Bazin, N. Tinel, T. Durroux, L. Prezeau, E. Trinquet, J. P. Pin, *Nat. Methods* **2008**, *5*, 561-567.
- [4] Randall J. Platt, S. Chen, Y. Zhou, Michael J. Yim, L. Swiech, Hannah R. Kempton, James E. Dahlman, O. Parnas, Thomas M. Eisenhaure, M. Jovanovic, Daniel B. Graham, S. Jhunjhunwala, M. Heidenreich, Ramnik J. Xavier, R. Langer, Daniel G. Anderson, N. Hacohen, A. Regev, G. Feng, Phillip A. Sharp, F. Zhang, *Cell* **2014**, *159*, 440-455.
- [5] a) Y. H. Tsai, S. Essig, J. R. James, K. Lang, J. W. Chin, *Nat. Chem.* **2015**, *7*, 554-561; b) J. Broichhagen, A. Damijonaitis, J. Levitz, K. R. Sokol, P. Leippe, D. Konrad, E. Y. Isacoff, D. Trauner, *ACS Central Science* **2015**, *1*, 383-393.
- [6] a) D. Gefel, G. K. Hendrick, S. Mojsov, J. Habener, G. C. Weir, *Endocrinology* **1990**, *126*, 2164-2168; b) B. Thorens, *Proc. Natl. Acad. Sci. U. S. A.* **1992**, *89*, 8641-8645; c) G. G. t. Holz, C. A. Leech, J. F. Habener, *J. Biol. Chem.* **1995**, *270*, 17749-17757.
- [7] a) J. Gromada, K. Bokvist, W. G. Ding, J. J. Holst, J. H. Nielsen, P. Rorsman, *Diabetes* **1998**, *47*, 57-65; b) G. G. Holz, C. A. Leech, R. S. Heller, M. Castonguay, J. F. Habener, *J. Biol. Chem.* **1999**, *274*, 14147-14156; c) G. G. Holz, *Diabetes* **2004**, *53*, 5-13.
- [8] S. N. Roed, A. C. Nohr, P. Wismann, H. Iversen, H. Brauner-Osborne, S. M. Knudsen, M. Waldhoer, *J. Biol. Chem.* **2015**, *290*, 1233-1243.
- [9] a) D. Calebiro, V. O. Nikolaev, M. C. Gagliani, T. de Filippis, C. Dees, C. Tacchetti, L. Persani, M. J. Lohse, *PLoS Biol.* **2009**, *7*, e1000172; b) R. S. Kuna, S. B. Girada, S. Asalla, J. Vallentyne, S. Maddika, J. T. Patterson, D. L. Smiley, R. D. DiMarchi, P. Mitra, *Am. J. Physiol. Endocrinol. Metab.* **2013**, *305*, E161-170; c) J. P. Vilardaga, F. G. Jean-Alphonse, T. J. Gardella, *Nat. Chem. Biol.* **2014**, *10*, 700-706.
- [10] S. N. Roed, P. Wismann, C. R. Underwood, N. Kulahin, H. Iversen, K. A. Cappelen, L. Schaffer, J. Lehtonen, J. Hecksher-Soerensen, A. Secher, J. M. Mathiesen, H. Brauner-Osborne, J. L. Whistler, S. M. Knudsen, M. Waldhoer, *Mol. Cell. Endocrinol.* **2014**, *382*, 938-949.
- [11] J. E. Campbell, D. J. Drucker, *Cell Metab.* **2013**, *17*, 819-837.
- [12] a) Daniel J. Drucker, *Cell Metab.* **2016**, *24*, 15-30; b) A. E. Hogan, G. Gaoatswe, L. Lynch, M. A. Corrigan, C. Woods, J. O'Connell, D. O'Shea, *Diabetologia* **2013**, *57*, 781-784.
- [13] a) C. R. Underwood, P. Garibay, L. B. Knudsen, S. Hastrup, G. H. Peters, R. Rudolph, S. Reedt-Runge, *J. Biol. Chem.* **2010**, *285*, 723-730; b) S. Runge, H. Thogersen, K. Madsen, J. Lau, R. Rudolph, *J. Biol. Chem.* **2008**, *283*, 11340-11347.
- [14] S. N. Roed, P. Wismann, C. R. Underwood, N. Kulahin, H. Iversen, K. A. Cappelen, L. Schaffer, J. Lehtonen, J. Hecksher-Soerensen, A. Secher, J. M. Mathiesen, H. Bräuner-Osborne, J. L. Whistler, S. M. Knudsen, M. Waldhoer, *Mol. Cell. Endocrinol.* **2014**, *382*, 938-949.
- [15] K. L. Everett, D. M. Cooper, *PLoS ONE* **2013**, *8*, e75942.
- [16] V. Serre, W. Dolci, E. Schaerer, L. Scrocchi, D. Drucker, S. Efrat, B. Thorens, *Endocrinology* **1998**, *139*, 4448-4454.
- [17] a) S. M. Nielsen, L. Z. Nielsen, S. A. Hjorth, M. H. Perrin, W. W. Vale, *Proc. Natl. Acad. Sci. U. S. A.* **2000**, *97*, 10277-10281; b) Y. Yin, X. E. Zhou, L. Hou, L.-H. Zhao, B. Liu, G. Wang, Y. Jiang, K. Melcher, H. E. Xu, *Cell Discovery* **2016**, *2*, 16042.
- [18] a) C. Choi, M. N. Nitabach, *Physiol. (Bethesda)* **2013**, *28*, 164-171; b) J. P. Fortin, Y. Zhu, C. Choi, M. Beinborn, M. N. Nitabach, A. S. Kopin, *Proc. Natl. Acad. Sci. U. S. A.* **2009**, *106*, 8049-8054.
- [19] V. M. Krishnamurthy, V. Semetey, P. J. Bracher, N. Shen, G. M. Whitesides, *J. Am. Chem. Soc.* **2007**, *129*, 1312-1320.
- [20] D. Wooten, C. A. Reynolds, K. J. Smith, J. C. Mobarec, C. Koole, E. E. Savage, K. Pabreja, J. Simms, R. Sridhar, S. G. Furness, H. Liu, P. E. Thompson, L. J. Miller, A. Christopoulos, P. M. Sexton, *Cell* **2016**, *165*, 1632-1643.
- [21] N. B. Cole, J. G. Donaldson, *ACS Chem. Biol.* **2012**, *7*, 464-469.
- [22] Eric P. Smith, Z. An, C. Wagner, Alfor G. Lewis, Eric B. Cohen, B. Li, P. Mahbod, D. Sandoval, D. Perez-Tilve, N. Tamarina, Louis H. Philipson, Doris A. Stoffers, Randy J. Seeley, David A. D'Alessio, *Cell Metab.* **2014**, *19*, 1050-1057.

## 4.2 SUPPLEMENTARY FIGURES

### 5 Supporting Figures and Tables



**Supporting Figure 1:** Logarithmic plot of concentration-dependent **ExONatide** binding to AD293-SNAP-GLP-1R cells.



**Supporting Figure 2:** Control of BME influence on trafficking in MIN6B1-SNAP-GLP-1R cells. a) Representative images showing that application of BME to native agonist Ex4(1-39) stimulated cells has no influence on trafficking (scale bar = 10  $\mu$ m). b) Plotted data from a), showing that there is no significant difference in BME- and non-BME-treated cells. NS, non-significant; Student's t-test. Values are the mean  $\pm$  SEM unless otherwise stated.

### 4.3 ADDITIONAL COMPOUNDS

In addition to the agonist exONatide **4.2**, the three additional peptides BG-Ex4(9-39) **4.3** (exOFFatide), BG-Lira **4.4** and BG-LirAzo **4.1** were synthesized following the original design approach, thus comprising preparation of the C-terminally cysteine-modified peptides S39C-Ex4(9-39) **4.7**, G36C-Lira **4.8** and G36C-LirAzo **4.9** (Figure 4.1). These peptides possess a reactive thiol group which enables the disulfide bond linking to the reactive BG- pyridyldithiol compound **4.5**. **4.5** itself contains a flexible polyethylene glycol linker with four units (PEG<sub>4</sub>), and allows the SNAP-tag bound ligand to reach the orthosteric site of the receptor. Although formation of the BG-PEG<sub>4</sub>-peptide disulfide bond seems trivial, besides exONatide **4.2** only the antagonist exOFFatide **4.3** was successfully synthesized *via* this route, whereas coupling of the peptides G36C-Lira **4.8** and G36C-LirAzo **4.9** with **4.5** proved to be difficult. The reason therefore is believed to be mainly due to the strong aggregation of the helical **4.8** and **4.9** peptides in concentrated solutions. Already at 0.5 mM concentrations the two peptides visibly aggregate, a known problem for the drug treatment with liraglutide **3.5**<sup>198</sup>. Even rising concentrations of trifluoro ethanol (TFE), which stabilizes secondary structures and helps to retain monomeric solutions<sup>199,200</sup>, failed to deliver the desired disulfide product after several days of reaction time. For this reason, and with positive results obtained for exONatide **4.2**, the synthesis of BG-Lira **4.8** and BG-LirAzo **4.9** was discarded at this point. ExOFFatide **4.3** could not meet expectations regarding potency and impaired GLP-1R inhibition, and thus further studies were likewise discarded.

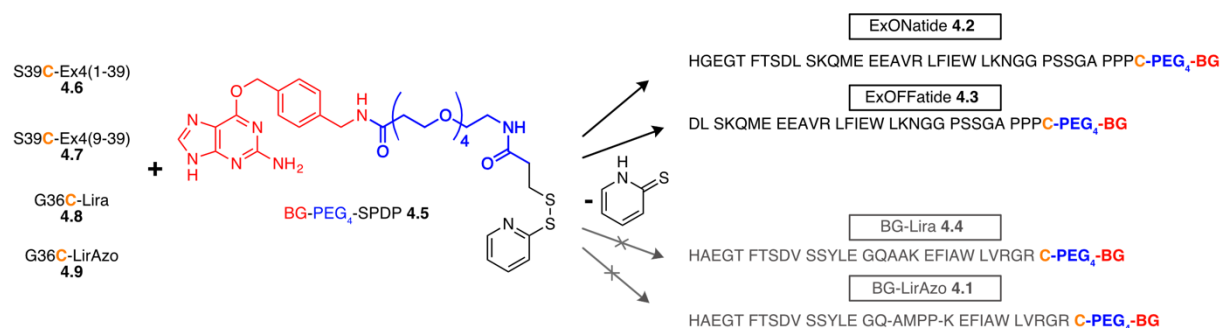


**Figure 4.1: Design scheme for BG-compounds exONatide 4.2, exOFFatide 4.3, BG-Lira 4.4 and BG-LirAzo 4.1.** Shown is the schematic reaction of precursor peptides S39C-Ex4(1-39) **4.6**, S39C-Ex4(9-39) **4.7**, G36C-Lira **4.8** and G36C-LirAzo **4.9** with reactive BG-PEG<sub>4</sub>-pyridyldithiol (SPDP) compound **4.5**, to form the desired BG-derivatives.

## 4.4 SUMMARY AND OUTLOOK

The incretin mimetic exenatide **3.4** (Byetta<sup>®</sup>) is a GLP-1R agonist and a blockbuster drug for the treatment of T2D. Like the native agonist GLP-1, it i) increases insulin secretion in a glucose-dependent manner, ii) decreases glucagon secretion and iii) suppresses hunger, *i.e.* reduces food intake<sup>201</sup>. The signaling of GLP-1R that leads to the boosting of insulin secretion has been intensively studied, but signal termination and receptor trafficking remain obscure<sup>202,203</sup>. The established paradigm for GPCR endocytic trafficking describes a rapid receptor desensitization after the ligand-bound receptors have signaled *via* heterotrimeric G-proteins<sup>204</sup>. This desensitization is mediated by GPCR kinases (GRKs), which selectively phosphorylate activated ligand-bound receptors. The phosphorylation triggers the recruitment of  $\beta$ -arrestin, which prevents G-protein interaction with the receptor thus terminating G-protein mediated signaling, and secondly it can bind the coat structure of clathrin coated pits, thus initiating the endocytosis of the  $\beta$ -arrestin-bound receptors. Subsequent post-endocytic fates after receptor internalization comprise the i) recycling of the receptor back to the plasma membrane, ii) lysosomal degradation or iii) a resting state in the endosomes<sup>204</sup>. The GLP-1R was shown to be rapidly internalized and recycled upon agonist stimulation, which contributes to receptor resensitization. Studies showed that prolonged treatment of GLP-1R with the agonists GLP-1, exenatide **3.4** and liraglutide **3.5** leads to a decline of the internalization maximum, which was suggested to correlate with the loss of a small pool of receptors due to degradation<sup>203</sup>. This can be interpreted as a receptor downregulation in a self-defense mode to prevent overstimulation through chronic treatment. This is an important finding, particularly in respect of the life-long treatment of T2D with incretin mimetics. Studies also showed that GLP-1Rs cycle for a prolonged period and exhibit prolonged cAMP signaling, which was linked to continuous signaling of internalized GPCRs<sup>205,206</sup>. In contrast, a recent study utilized new time-resolved fluorescence resonance energy transfer (TR-FRET) techniques to monitor real-time internalization of GLP-1R in HEK293t and connected the prolonged cAMP signaling to continuous cycling and resensitization of GLP-1Rs after agonist stimulation<sup>203</sup>. This controversial discussion shows the need for research tools to dissect the trafficking and post-endocytic fate of GLP-1Rs.

With exONatide **4.2** we hope to deliver such an instrument, extending the tethered ligand toolbox to the GLP-1R by applying the powerful SNAP-tag bioconjugation technology. **4.2** enables unprecedented activation of GLP-1R signaling and trafficking, and the constitutive receptor activation allows the monitoring of internalization and recycling of the continuously bound ligand-receptor complex. Thereby first trafficking studies showed that the covalently bound ligand prevents receptor recycling to the cell surface and resensitization, revealing a crucial role for the dissociation of the ligand-receptor complex in endosomal sorting. In depth analysis of internalized and constitutively activated GLP-1Rs will give information about whether endosomal cAMP signaling<sup>205,206</sup>, or fast receptor recycling are the reason for prolonged cAMP signaling of GLP-1R after stimulation<sup>203</sup>. Moreover, the fast progression in developing mice ubiquitously expressing the SNAP-tag on target proteins, will soon allow to test exONatide **4.2** *in vivo*, facilitating valuable insights into the treatment of T2D with incretin mimetics.

## 4.5 EXPERIMENTAL

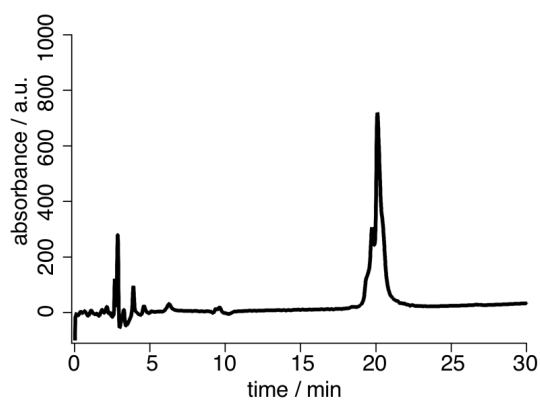
### 4.5.1 SPECTROSCOPIC AND SPECTROMETRIC DATA OF EXONATIDE 4.2

#### 2.2 S39C-Ex4 peptide

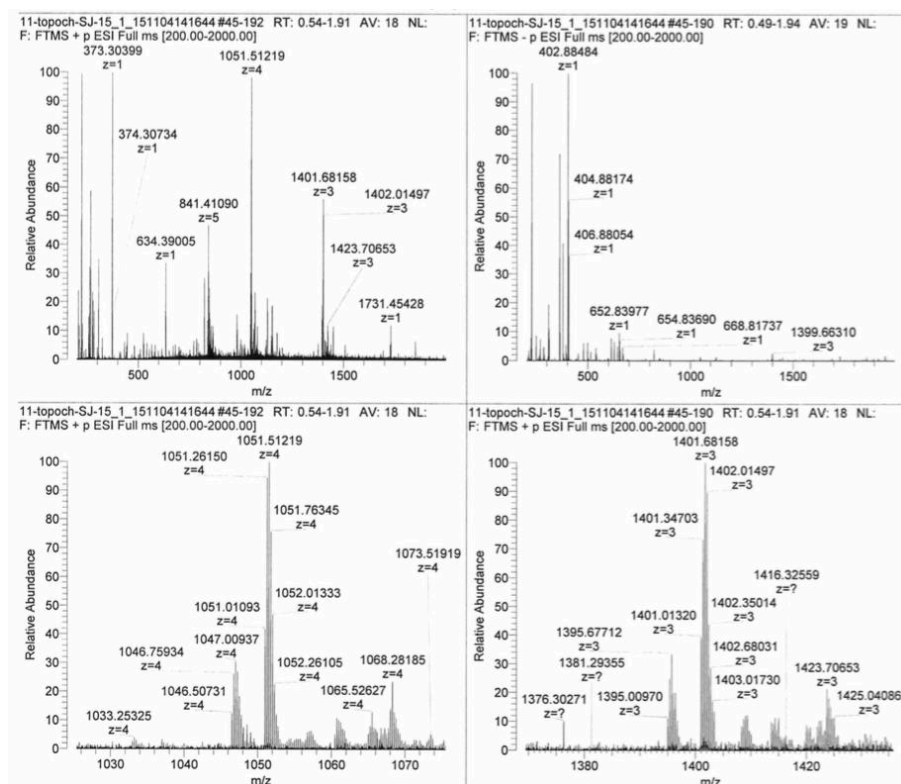
Peptide sequence:

H<sub>2</sub>N-HGEG TFTS DLSK QMEE EAVR LFIE WLKN GGPS SGAP PPC-CONH<sub>2</sub>

The peptide S39C-Ex4 was synthesized according to the generalized peptide synthesis protocol in chapter 1.2.



Analytical HPLC spectrum of peptide S39C-Ex4 with a water/acetonitrile (+0.1% TFA) gradient 90:10 → 20:80 in 40 min. Retention time of the peptide: 20.1 min.



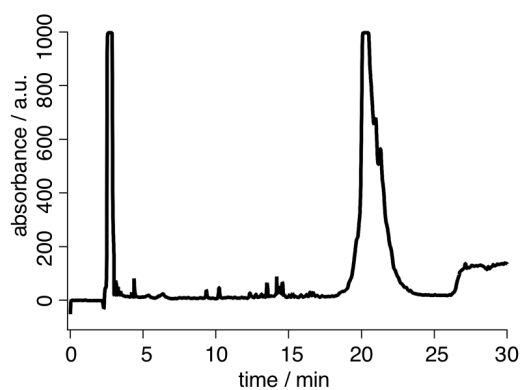
HR +ESI-mass spectrum of peptide S39C-Ex4.  $M(C_{184}H_{284}N_{50}O_{58}S_2) = 4201.0078$ ; calc. mass for  $C_{184}H_{288}N_{50}O_{58}S_2^{4+} [M+4H]$ :  $m/z = 1015.5101$ , found:  $m/z = 1051.5122$ ,  $\Delta m = 2.19$  ppm.

### 2.3 Synthesis of ExONatide

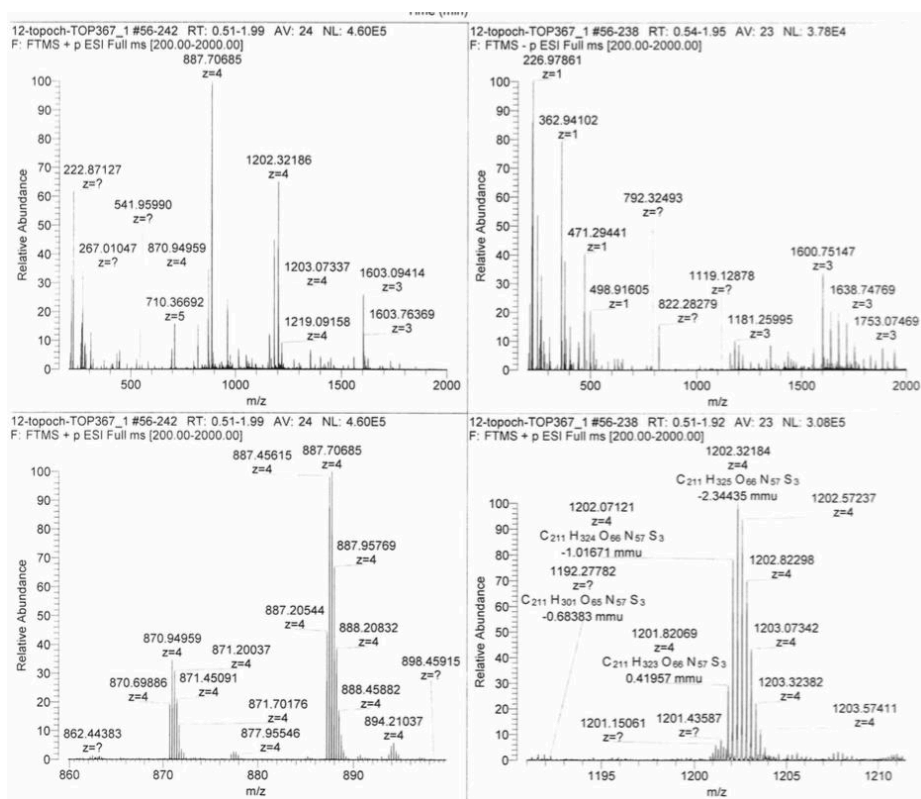
Peptide sequence:

H<sub>2</sub>N-HGEG TFTS DLSK QMEE EAVR LFIE WLKN GGPS SGAP PPC(PEG<sub>4</sub>\_BG)-CONH<sub>2</sub>

To a solution of 6.35 mg (1.50  $\mu$ mol, 1 equiv.) S39C-Ex4 in 595  $\mu$ L buffer (100  $\mu$ M Na<sub>2</sub>PO<sub>4</sub>, 150  $\mu$ M NaCl, 1 mM EDTA and 0.02% NaN<sub>3</sub>) was added 205  $\mu$ L (1.8  $\mu$ mol, 1.2 equiv.) of a 8.7 mM stock solution of BG-PEG<sub>4</sub>-SSpy in DMSO. The solution was mixed gently, sparged with argon and agitated in a thermocycler at 37 °C for 48 h. The mixture was filtered and directly injected on to a semi-preparative HPLC column. Lastly, the purified product was lyophilized from H<sub>2</sub>O/MeCN 60:40 with 0.1% TFA to afford 3.35 mg (693 nmol, 46%) of **ExONatide**.



Analytical HPLC spectrum of peptide **ExONatide** with water/acetonitrile gradient 90:10 → 20:80 in 40 min. Retention time of the peptide: 20.2 min.



HR +ESI-mass spectrum of peptide **ExONatide**.  $M(C_{211}H_{319}N_{57}O_{66}S_3) = 4805.2857$ ; calc. mass for  $C_{211}H_{323}N_{57}O_{66}S_3 [M+4H]^{4+}$ :  $m/z = 1202.3219$ , found:  $m/z = 1202.3218$ ,  $\Delta m = 0.05$  ppm.

## 4.5.2 EXPERIMENTAL DATA OF ADDITIONAL COMPOUNDS S39C-Ex4(9-39) 4.7, exOFFATIDE 4.3, G36C-LIRA 4.8 AND G36C-LIRAZO 4.9

### 4.5.2.1 SYNTHESIS OF PEPTIDES S39C-Ex4(9-39) 4.7, exOFFATIDE 4.3, G36C-LIRA 4.8 AND G36C-LIRAZO 4.9

The synthesis of peptides S39C-Ex4(9-39) 4.7, exOFFatide 4.3, G36C-Lira 4.8 and G36C-LirAzo 4.9 followed the general peptide synthesis protocol stated in the APPENDIX. Table 3.1 depicts the coupling conditions of the different building blocks used for the automated peptide synthesis. As resin for peptides S39C-Ex4(9-39) 4.7 and exOFFatide 4.3 a preloaded TentaGel® S-RAM *N*-(Fmoc)-Ser(*t*-Bu) resin (Rapp Polymere, Tübingen/Germany) was used. As resin for peptides G36C-Lira 4.8 and G36C-LirAzo 4.9 a preloaded Wang LL *N*-(Fmoc)-Gly resin (NovaBiochem, Darmstadt/Germany) was used.

**Table 4.1: Coupling conditions for synthesis of peptides S39C-Ex4(9-39) 4.7, exOFFatide 4.3, G36C-Lira 4.8 and G36C-LirAzo 4.9.**

Amino acid(s)	Coupling method	Steps	Time (s)	Temperature (°C)	Power (W)
Fmoc-Arg(Pbf)-OH	Arg double coupling	2	Step 1: 1500 Step 2: 300	Step 1: 25 Step 2: 75	Step 1: 0 Step 2: 23
Fmoc-His(Trt)-OH	Single amino acid 50 °C coupling	1	480	50	23
Fmoc-AMPP-OH 1.26	Photoswitch coupling	1	1800	75	23
Fmoc-Ala-OH, Fmoc-Asp( <i>t</i> -Bu)-OH, Fmoc-Gln(Trt)-OH, Fmoc-Glu( <i>t</i> -Bu)-OH, Fmoc-Gly-OH, Fmoc-Ile-OH, Fmoc-Leu-OH, Fmoc-Lys(Boc)-OH, Fmoc-Met-OH, Fmoc-Phe-OH, Fmoc-Ser( <i>t</i> -Bu)-OH, Fmoc-Thr( <i>t</i> -Bu)-OH, Fmoc-Trp(Boc)-OH,	Standard single amino acid coupling	1	480	75	23

## 4.5.2.2 ANALYTICAL HPLC SPECTRUM AND MASS SPECTRUM OF S39C-Ex4(9-39) 4.7

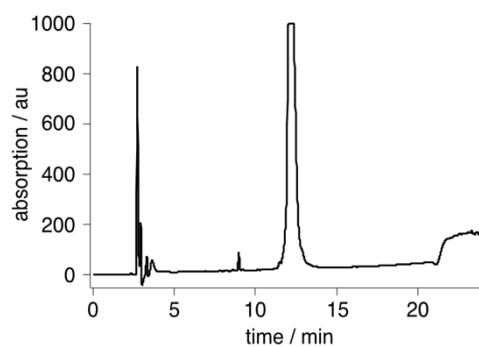


**Figure 4.2:** HPLC spectrum of S39C-Ex4(9-39) 4.7. Analytical HPLC spectrum of 4.7 with a water/acetonitrile gradient 95:5 → 20:80 in 40 min.  $R_t = 12.2$  min.

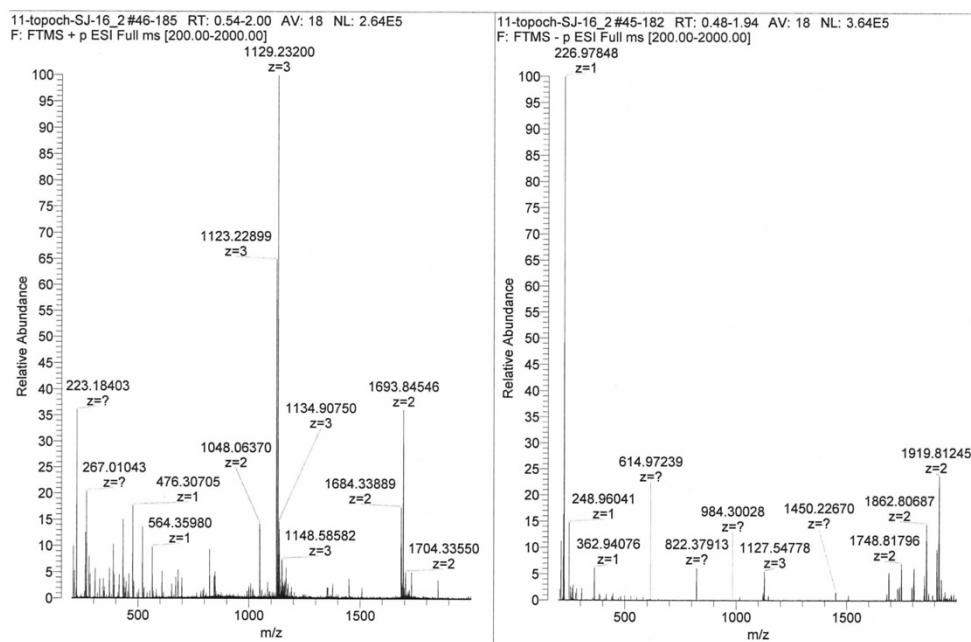


**Figure 4.3:** HRMS spectrum of S39C-Ex4(9-39) 4.7. HRMS (+ESI)  $m/z$ : calc. for  $C_{149}H_{237}O_{46}N_{40}S_2^{3+} [M+3H]^{3+}$ : 1129.2298; found: 1129.2320.  $\Delta m = 1.95$  ppm.

## 4.5.2.3 ANALYTICAL HPLC SPECTRUM AND MASS SPECTRUM OF EXOFFATIDE 4.3

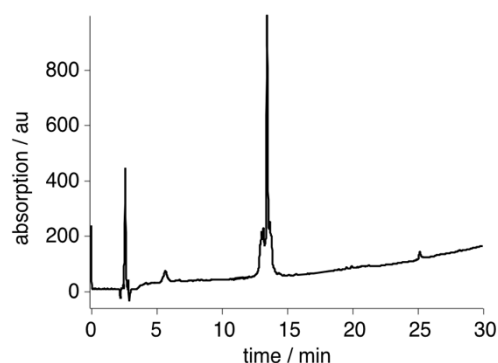


**Figure 4.4: HPLC spectrum of exOFFatide 4.3.** Analytical HPLC spectrum of 4.3 with a water/acetonitrile gradient 95:5 → 20:80 in 40 min.  $R_t = 14.0$  min.

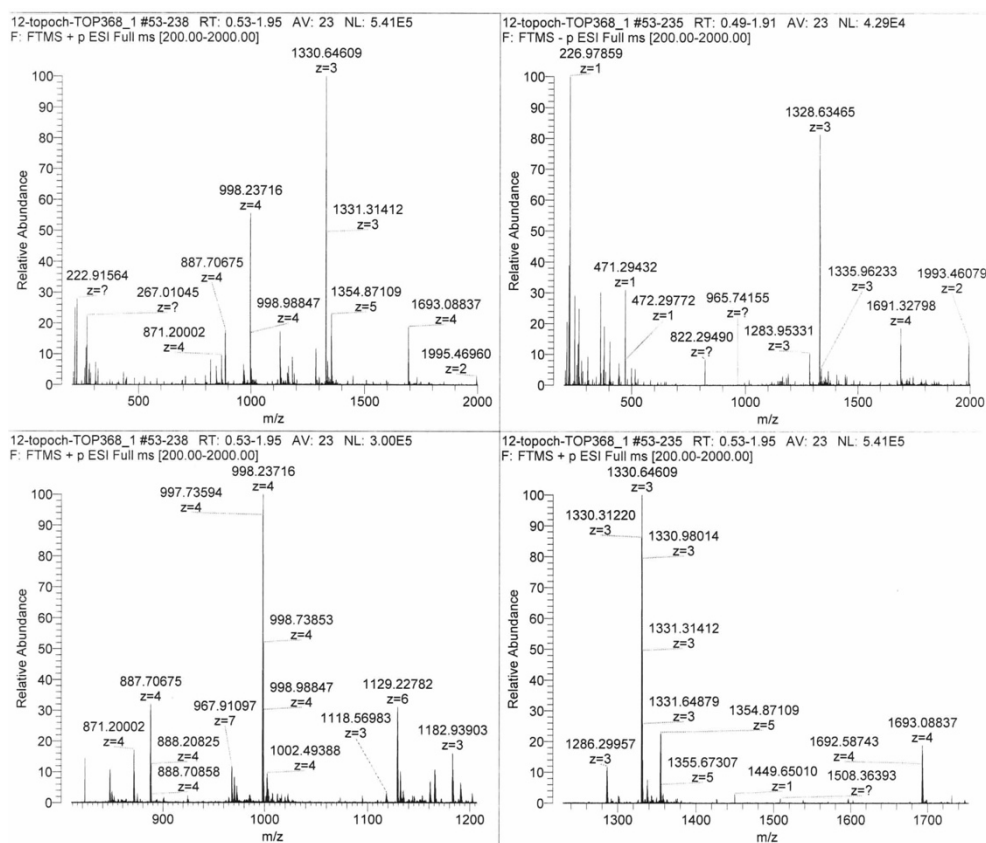


**Figure 4.5: HRMS spectrum of exOFFatide 4.3.** HRMS (+ESI)  $m/z$ : calc. for  $C_{176}H_{275}O_{53}N_{47}S_3$   $[M+3H]^+$ : 1330.6468; found: 1330.6461. Calc. for  $C_{176}H_{275}O_{53}N_{47}S_3$   $[M+4H]^{4+}$ : 998.2369; found: 998.2372.  $\Delta m = 0.30$  ppm.

## 4.5.2.4 ANALYTICAL HPLC SPECTRUM AND MASS SPECTRUM OF G36C-LIRA 4.8

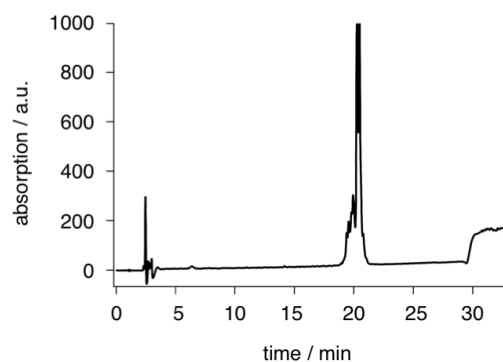


**Figure 4.6:** HPLC spectrum of G36C-Lira 4.8. Analytical HPLC spectrum of 4.8 with a water/acetonitrile gradient 95:5 → 20:80 in 40 min.  $R_t = 20.3$  min.

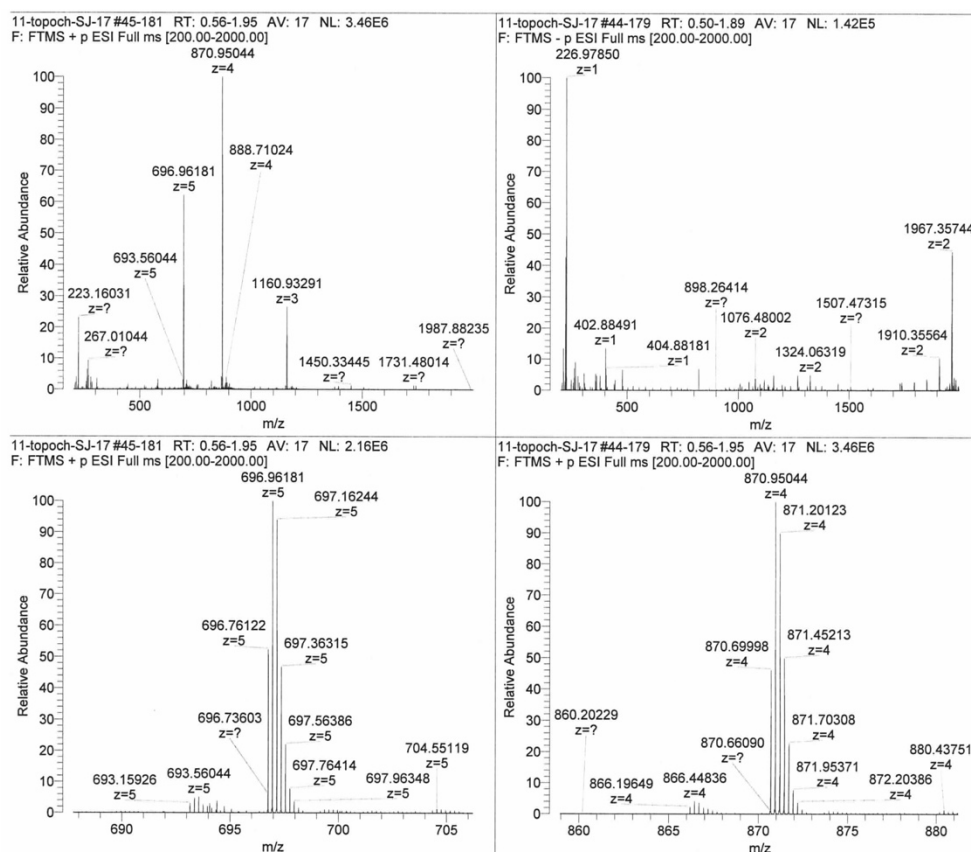


**Figure 4.7:** HRMS spectrum of G36C-Lira 4.8. HRMS (+ESI)  $m/z$ : calc. for  $C_{152}H_{243}O_{47}N_{47}S^{4+}$   $[M+3NH_4+H]^{4+}$ : 870.9435; found: 870.9504. Calc. for  $C_{152}H_{243}O_{47}N_{47}S^{4+}$   $[M+4NH_4+H]^{4+}$ : 696.9563; found: 696.9618.  $\Delta m = 7.9$  ppm.

## 4.5.2.5 ANALYTICAL HPLC SPECTRUM AND MASS SPECTRUM OF G36C-LIRAZO 4.9

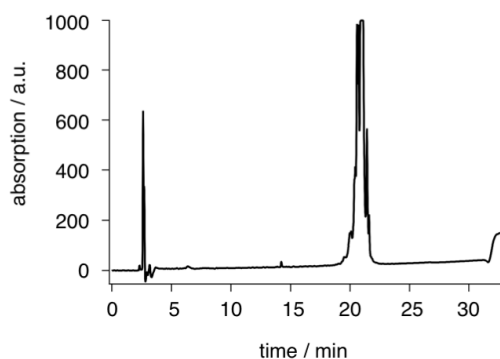


**Figure 4.8:** HPLC spectrum of G36C-LirAzo 4.9. Analytical HPLC spectrum of 4.9 with a water/acetonitrile gradient 95:5 → 20:80 in 40 min.  $R_t = 20.9$  min.

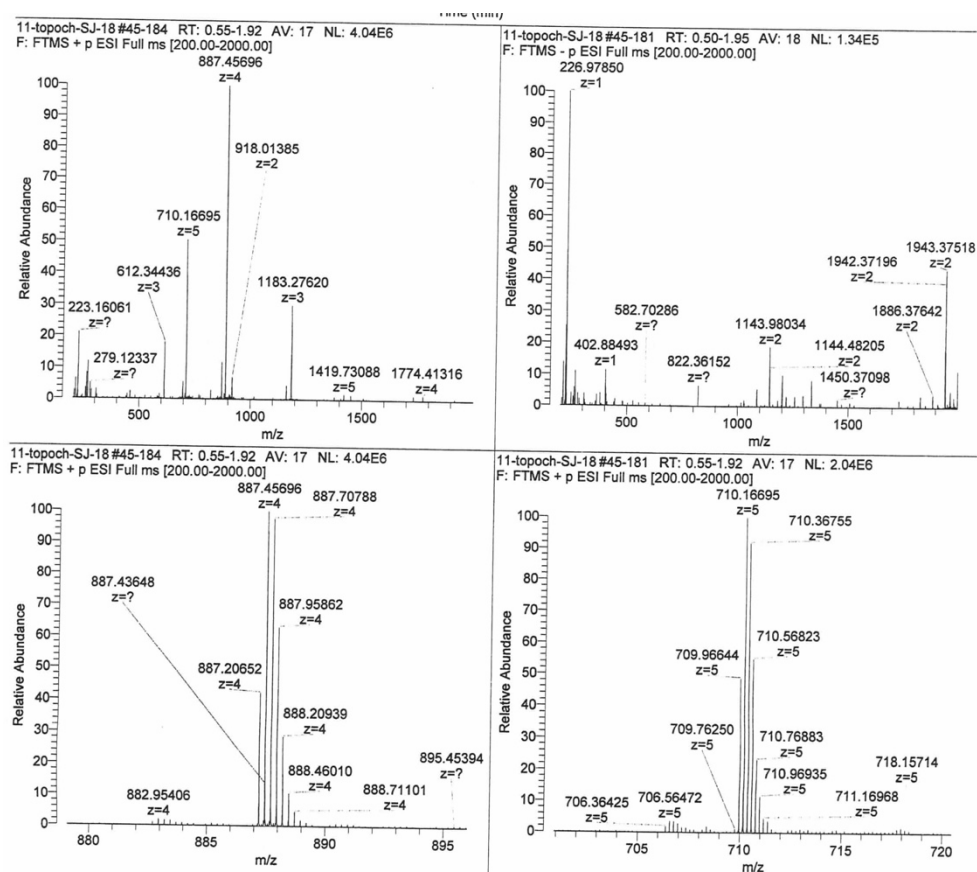


**Figure 4.9:** HRMS spectrum of G36C-LirAzo 4.9. HRMS (+ESI)  $m/z$ : calc. for  $C_{176}H_{274}O_{53}N_{47}S_3^{3+} [M+3H]^{3+}$ : 887.4500; found: 887.4570.  $\Delta m = 7.9$  ppm.

PART III

STRUCTURAL BIOLOGY OF AZOCHIG  
AND RELATED DERIVATIVES

## PART III: STRUCTURAL BIOLOGY OF AZOCHIGNOLIN AND RELATED DERIVATIVES

One of the most intriguing secrets of cellular biology and function is how proteins self-assemble into their designated native structures. Only correctly folded proteins are capable of evoking correct actions, such as biological activity, trafficking and regulation of cellular growth and differentiation<sup>27,207</sup>. The complexity and diversity in which various of these self-assembling molecular systems have evolved throughout many organisms is fascinating, as it demonstrates nature's elegant way in forming precise molecular systems for performing specific functions<sup>208</sup>. The correct molecular assembly not only brings functional groups in close structural proximity, for example to form active sites of receptors, but also is the key feature allowing high molecular concentrations in cells<sup>209</sup>. The ability to maintain this solubility was a critical key step in the formation of complex organisms, and loss of this ability can lead to molecular aggregation. Protein misfolding is the actuator for many age-related and degenerative diseases, including Alzheimer's and Creutzfeldt-Jakob's disease, as well as T2D and bovine spongiform encephalopathies (BSE)<sup>210,211</sup>. The fact that these amyloidoses or "protein misfolding diseases" are often age related, supports the association of protein aggregation with divergent protein behavior in biological systems under conditions, which alternate in a faster pace than set by evolution<sup>212</sup>. While the ageing human organism interferes with evolutionary tightly adapted cellular processes, overtaking and challenging the speed of evolutionary adaptation, humanity itself disrupts the global homeostasis of biochemical processes. This can best be exemplified with the recent disturbing uprise of multidrug resistant bacteria, which was and still is driven by over- and misuse of antibiotics over the last decades<sup>213,214</sup>. Science has already made great progress in unraveling such biochemical and biological nexuses, helping to expand health and wealth of the global population. However, due to the dazzling complexity and multiplicity of these biological patterns, a lion's share remains opaque. Most of the conducted studies are focused on understanding biological complexity of proteins, as they are the dominating class of molecules involved in literally all reactions taking place in living organisms<sup>208</sup>. Moreover, they are accessible for both theoretical and experimental investigations and descriptions, allowing the merging of this two often detached fields<sup>215,216</sup>. In respect of rising computational power and the development of super computers and artificial intelligence, the validation of growing sets of theoretical descriptions with experimental data will become an important task in the future.

But how can one study complex protein folding processes in experimental and theoretical detail? A feasible way to reduce complexity is to breakdown huge molecular systems into simplified and smaller units, which then can be studied separately in detail and at the end the obtained results and relationships can be transposed into a bigger picture. Thereby the smallest of these units in proteins is the amino acid sequence (primary structure), which is a combination of different lengths and sequences of the 20 proteinogenic amino acids. This is the principle protein code, and it contains the complete information on the folding process of the protein<sup>217</sup>. Divergences and mutations in the native sequence can cause inactivity, misfolding and altered trafficking. Climbing the ladder in biological complexity there are secondary

structures, for example  $\alpha$ -helices,  $\beta$ -sheets and  $\beta$ -loops, followed by the three-dimensional protein folding or tertiary structure, and the formation of subunits or quaternary protein structures (Figure III.1). Especially aberrations in the three-dimensional structure of proteins can lead to misfolding and aggregation, causing cellular toxicity and disease. By further increasing the biological complexity one passes the levels of macromolecular assemblies, cellular and tissue processes and in the end, comes to trying to understand whole organisms and the mystery of life itself<sup>208</sup>.

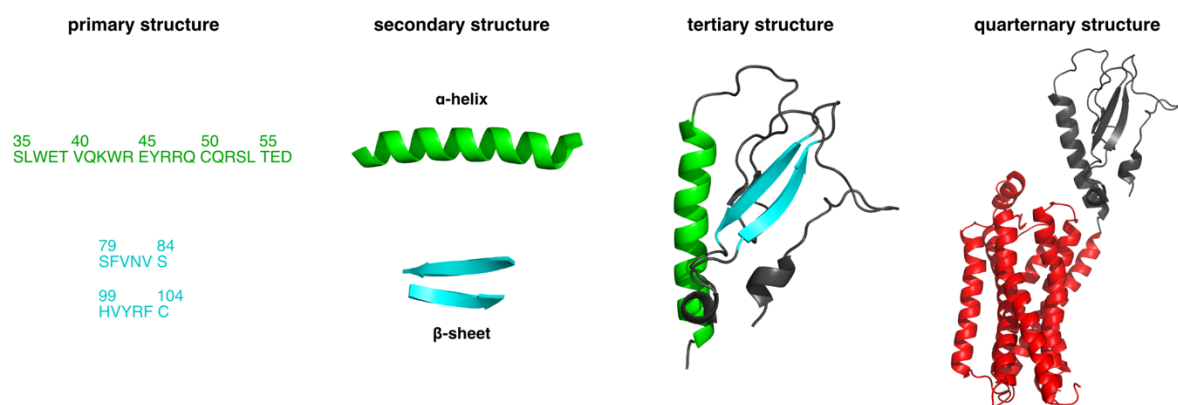


**Figure III.1: Breakdown of complex protein structures.** The full-scale protein folding is subdivided into four stages: primary structure (amino acid sequence), secondary structure (secondary structure motifs, *i.e.*  $\alpha$ -helix or  $\beta$ -sheet), tertiary structure (three-dimensional protein fold) and quaternary structure (global native structural protein formation with different subunits). Illustrated using the X-ray crystallographic structure of the extracellular domain of GLP-1R (pdb: 3iol) for the left, middle left and middle right figure. In the right figure the extracellular domain of GLP-1R (pdb: 3iol) was merged to the 7TM domain of the  $\beta_2$ AR receptor (pdb: 2RH1) to illustrate the arrangement of different subunits.

The pathway of protein folding follows similar steps, gradually increasing complexity through structural formation (Figure III.2). After the transcription of the genetic information stored in the DNA and protein synthesis on the ribosome, the resulting polypeptide chain can either be folded i) co-translational, ii) folded directly in the cytoplasm or iii) is transported for folding into specific compartments, *i.e.* mitochondria or the endoplasmic reticulum<sup>218–220</sup>. These folding steps are crucial for correct folding, as important protein regions that are buried in the native structure are inevitably solvent exposed, which could promote inappropriate reactions with other molecules in the crowded cellular environment<sup>27,209</sup>. For this reason, cells have developed quality control mechanisms that detect incorrectly folded proteins and trigger degradation in the ubiquitin-proteasome system<sup>221</sup>. The following steps of protein folding comprise the formation of intermediate states with secondary structures, which facilitate the formation of the native protein fold. In these intermediate states the formation of unstructured soluble oligomers, or pre-fibrillar aggregates, sparks the organization of larger aggregates, or protofilaments, which exhibit high kinetic stability and thus can exist for long periods. Interestingly, biological systems have avoided the use of alternating hydrophobic and polar residues that favor  $\beta$ -sheet formation as seen in amyloid fibrilles, to prevent the formation of such material<sup>222</sup>.

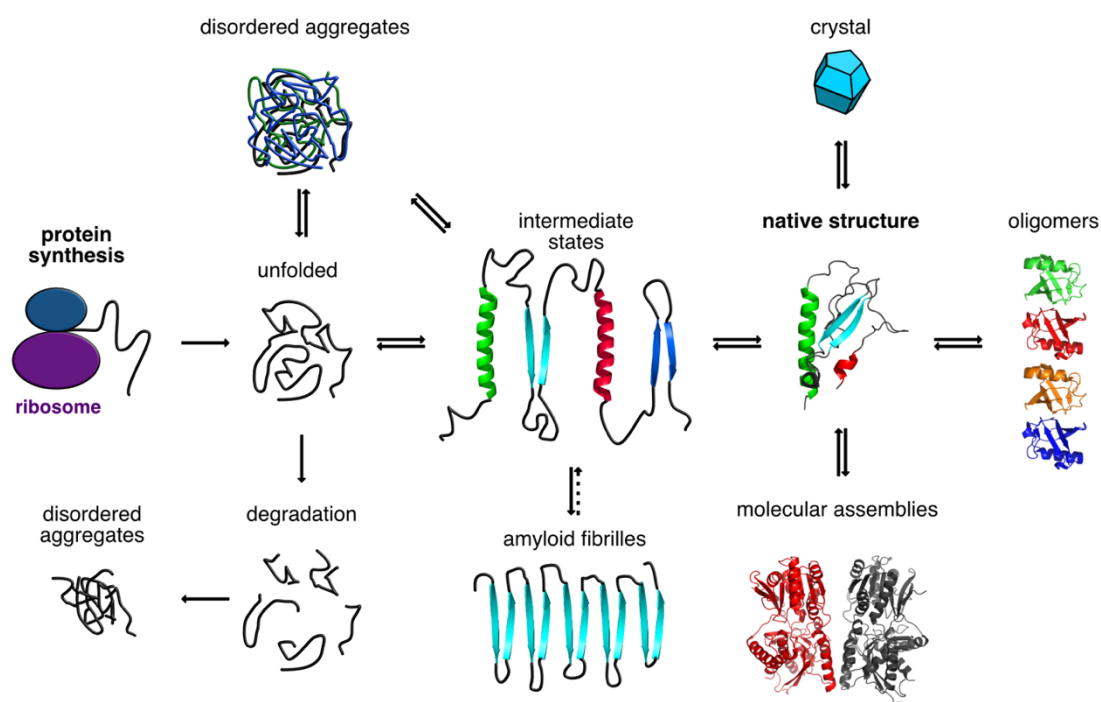


**Figure III.2: Schematic representation of possible protein structures.** After synthesis on the ribosome proteins are folded through intermediate states into their native protein structure. Following this way, they reversibly traverse *via* intermediate states and disordered aggregates, or are recognized by cellular quality control as misfolded proteins and are subsequently degraded in the ubiquitin-proteasome system. Formation of intermediate states can also lead to the formation of amyloid fibrilles, which can only slowly disaggregate and are the actuators of amyloidosis diseases. In the end, proteins in their native structure can form higher molecular systems, as exemplified through the molecular assembly of the homodimeric NPR-A receptor (pdb: 1yk0) and oligomeric ubiquitin structures (pdb: 5go8). The scheme was adapted and modified based on ref. 208.

For decades, it was assumed that protein folding follows the *Levinthal's paradox*, which states that a random search for the native protein structure upon the myriads of possible conformations would take an astronomical length of time<sup>223,224</sup>. This falsely led to the conclusion that folding events must occur through intermediate structures, like chemical reactions, which guide the folding to the native structure. Today we know that folding is a stochastic trial and error process comprising free energy minimization along a small explorational pathway<sup>216,225</sup>. Thereby the inherent movement of the flexible polypeptide chain allows even distal functional groups to get close to each other. This enables a small number of amino acids to form one or several critical cores, *i.e.* nucleation sites from which the folding is driven through the remaining protein structure<sup>215,226</sup>. These nucleation sites often form secondary structures, *i.e.* small  $\alpha$ -helical or  $\beta$ -sheet and  $\beta$ -turn motifs, as was shown through the study of a series of small proteins (60-100 residues) through different spectroscopic techniques<sup>227,228</sup>. Particularly  $\beta$ -hairpins, the basic elements of anti-parallel  $\beta$ -sheets, are believed to be initiators of protein folding and thus small model systems representing this secondary structure motif have become a mainstay in the experimental and computational research of protein structural folding and unfolding processes<sup>199,229-231</sup>. Thereby these self-contained model peptide systems offer enough detail while exhibiting a reasonable amount of complexity.

$\beta$ -turns are the most widely distributed type of turns and belong to the class of reversed turns, which also includes the lesser distributed  $\gamma$ - and  $\alpha$ -turns (and others)<sup>232</sup>. They usually contain three or four residues in

the turn segment, with the most common four-residue  $\beta$ -turns being classified as Types I and II<sup>233</sup>.  $\beta$ -Hairpins are  $\beta$ -turns flanked by two  $\beta$ -sheets and the structural dynamics and features have been extensively studied over the last decades. They are stabilized by effects of their turn propensities, as well as through cross-strand interactions between the two flanking sequences. These cross-strand interactions include aromatic-aromatic, aromatic-polar, hydrogen-bonding, hydrophobic and salt-bridge interactions<sup>26,232,234,235</sup>. Regarding these interactions three main models for the mechanism of hairpin folding have been developed: the zipper, the hydrophobic collapse and the broken-zipper model<sup>236</sup> (Figure III.3). The zipper mechanism is a statistical mechanic model based on observations of a single kinetic barrier separating folded and unfolded states<sup>237–240</sup>. It thus describes folding using minimal numbers of parameters: loss of conformational entropy, backbone stabilization through hydrogen bonding and formation of a stabilizing hydrophobic cluster. The mechanism comprises the following steps: formation of a bend structure with generation of initial hydrogen bonds in the turn region, which then progress towards the end of the two strands and, as the name implies, zip up the hairpin. After the establishment of the hydrogen bond network in the first step, the second step comprises formation of hydrophobic interactions, stabilizing the final hairpin structure<sup>241</sup>. Although this model seems reasonable and is the most prevailing one, there are arguments against turn nucleation through the strong contribution of hydrogen bonds<sup>236,242–244</sup>. In contrast, the hydrophobic collapse model predicts that folding is initiated by a chaotic formation of as many hydrophobic interactions as possible, which then rearrange to form a hydrophobic core. This core then serves as starting site for the formation of hydrogen bonds propagating in all directions<sup>245,246</sup>. This mechanism accounts for the importance of non-polar side chains in the structural formation of the hairpin, because they can stabilize hydrogen bonds by wrapping themselves around involved groups and thus shield off competing water molecules. However, this model omits the incipient formation of a turn nucleation site and hydrogen bonds possess a supreme proportion of structural stabilization. The broken-zipper model in principle is a combination of the two preceding models and involves the following steps: first the turn sequence initiates interactions between non-polar residues close to the turn region, which then invites distal hydrophobic interaction partners to join in and promote the growth of the hydrophobic core. An interesting feature of this model is that the unfolding process is not just a reversion of the folding, but it requires hydrophobic interactions proximal to the turn region to break first, followed by the rest of the hydrophobic core. All three models are still being critically discussed and it is not clear, whether there is a general folding mechanism applicable to all possible  $\beta$ -hairpin folding processes, or if every sequence folding mechanism is unique. This shows the need for further model systems, new techniques and more detailed experimental and theoretical data sets to eventually establish a universal folding mechanism.

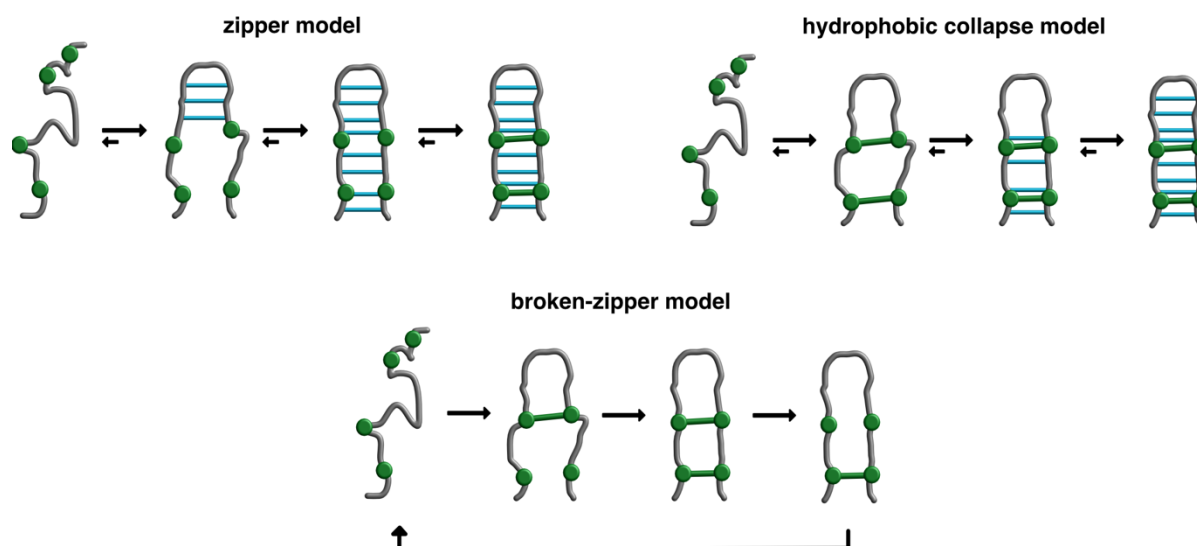


**Figure III.3: Different models for  $\beta$ -hairpin formation in peptides.** Shown are the zipper, hydrophobic collapse and broken-zipper models suggested for the folding mechanisms of  $\beta$ -hairpin secondary structure motifs. Figure elements are the peptide chain (gray), hydrogen bonds (cyan lines), non-polar residues (green balls) and hydrophobic interactions (green lines). The figure was adapted and modified based on ref. 241.

The monitoring of folding and unfolding events in small peptides can be done experimentally by several techniques, including circular dichroism (CD), NMR spectroscopy and differential scanning calorimetry (DSC)<sup>199,229,241,243,247</sup>. A drawback in all these experimental assessments of model systems is the need to chemically or mechanically induce the folding transitions, *i.e.* by regulating pH and salt conditions or with denaturing concentrations and reagents, which limits them to the supra microsecond timescale<sup>248</sup>. To reach the domain of nanoseconds additional time-resolved techniques have been developed, such as the temperature jump (T-jump) experiment and direct energy transfer through raman processes<sup>249</sup>. While the former uses the energy absorption of a dye by irradiation to induce a temperature rise of up to ten degrees and trigger peptide unfolding, the latter relies on energy excitation through raman scattering. However, the dyes used for the T-jump experiments tend to interact with the tested molecules causing artefacts, while raman excitation is often too slow for the monitoring of the ultra-fast protein folding processes. The bypass of these issues is the use of optical-pump probe spectroscopy, which harnesses the speed of light through modern laser techniques and allows to explore the limits of time-resolution on the sub-nanosecond timescale<sup>20</sup>. Using this method, the changes in peptide structure are induced using ultra-fast conformational switches, as this is the rate limiting step for detection. Azobenzene photoswitches are exquisitely suited for this task because, as described in PART I, their reversible photoconversion happens on the timescale of a few hundred femtoseconds. Furthermore, with the pump/excitation pulse for the photoswitch being in the near UV region, any feasible wavelengths in the visible or infrared spectrum can be used for detection. Intriguingly, photoconversion of azobenzene in the UV region is in this case an advantageous trait, and contrasts the general red-shifting efforts for chromophores used in photopharmacology. A prevailing method developed to detect  $\beta$ -hairpin folding events comprises the monitoring of changes in the absorption wavelengths of the amide-I bands in the IR region through infrared spectroscopy<sup>23,250,251</sup>. The amide-I bands correspond to carbonyl-stretching vibrations and are sensitive to changes in the backbone conformations

of peptides, *i.e.* they can be used to detect shifts in the hydrogen bonding pattern. Hydrogen bonded carbonyl groups have lower energy vibrational modes compared to higher energy bands in the solvated state, and thus show red-shifted absorption bands in the IR spectrum. Since the detectable changes are relatively small, differential IR spectra are used for visualization (Figure III.4).

A variety of photoswitchable  $\beta$ -hairpin peptide model systems has been developed in the last decade, and folding and unfolding events have been extensively studied using the above mentioned experimental and theoretical techniques<sup>251–253</sup>. A prominent example is the Azobenzene-Tryptophan-Zipper peptide (AzoTrpZip, ATZ, **III.1**), consisting of two strands with two aromatic tryptophan amino acids each (the zipper motif), which are connected through the AMPP **1.22** photoswitch<sup>23,80,253</sup>. This peptide adopts hairpin-like conformations when the photoswitch is in its *cis*-state, which are stabilized by cross-strand hydrogen bonds and by hydrophobic interactions between the two opposing tryptophan pairs. Unfolding into an ensemble of stabilized globular structures occurs upon irradiation and formation of the *trans*-peptide. The rigid *trans*-photoswitch prevents tight interactions between the *N*- and *C*-terminal tails as observed in the *cis*-peptide. Detailed mechanistic studies revealed the energetic landscape and structural intermediates of the folding and unfolding processes, and describe a high energetic barrier of 48 kJ mol<sup>-1</sup> between the two structures<sup>23,254</sup>. Moreover, they suggest a hydrophobic collapse model for the folding of this  $\beta$ -hairpin and indicate the formation of the hydrophobic core as rate limiting step. However, the obtained results can only be applied to this specific peptide and other model systems eventually provide different results. This shows the need to expand the existing model peptide systems library to understand the dynamics of protein folding and formulate universal mechanisms for future experimental and theoretical applications.

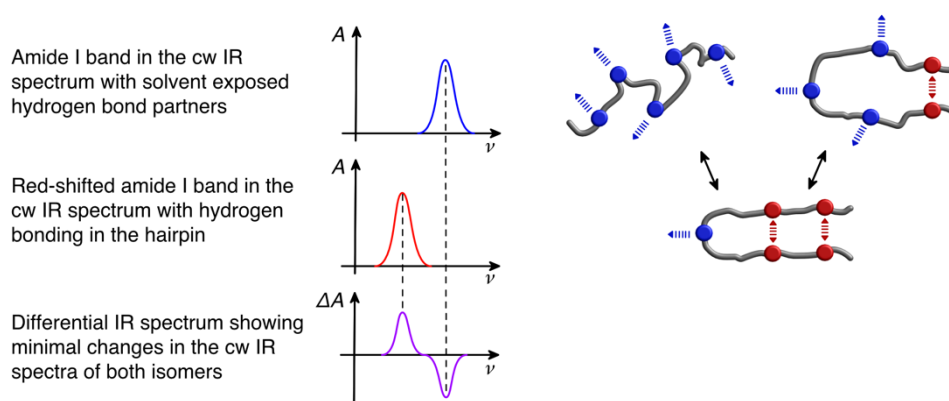


**Figure III.4: Different shifts of the peptide amide-I band in continuous wave IR spectra.** The absorption bands in the continuous wave (cw) IR spectra of peptide backbone carbonyls depend on whether they are hydrogen bonded or exposed to the solvent. They are red-shifted in case of hydrogen bonded carbonyls as they display lower energy vibrational modes compared to carbonyls interacting with the solvent.

## 5 PHOTOCONTROLLED CHIGNOLIN-DERIVED $\beta$ -HAIRPIN PEPTIDOMIMETICS

A part of this work was published in *Chem. Commun.* **51**, 4001-4004 (2015).

Most of what we know today about the structural formation of  $\beta$ -hairpins is based on studies about the GB1 and the Peptide 1 hairpin, with the former being a small 16-residue peptide derived from the C-terminal end of the B1 domain of protein G from *streptococcus* bacteria, and the latter being an artificial 15-residue peptide<sup>255-257</sup>. The GB1 peptide was the first natural sequence found to fold autonomously in aqueous solution, and together with the designed Peptide 1 it has granted deep insight into structural relations, diversity of the turn region and details on hairpin folding mechanics. A relatively new model system is the artificial decapeptide chignolin **5.1**, which is also based on the central part of the GB1 hairpin<sup>258</sup>. This peptide was designed during the search for autonomous elements (AEs) in proteins, which can be defined as small native protein segments with high foldability stabilized by local interactions with neighbouring amino acids. They have their origin in the fragment assembly method for protein structure analysis that implies that small AE segments in proteins function as folding nucleus and dictate the folding of the rest of the passive regions<sup>259,260</sup>. Furthermore, it is believed that AEs represent early ancestral proteins, which were much smaller than their present-day relatives, and that these have evolved from their early predecessors by assembly of small AE pieces or gradual elongation<sup>261,262</sup>.

The primary structure GYDPETGTWG of chignolin **5.1** has emerged from a statistical method, in which the eight central amino acids of the GB1 hairpin were selected based on comparison of over 100 non-homologous proteins for stable  $\beta$ -hairpin analogs<sup>258,263</sup>. Chignolin **5.1**, besides sharing a ~60% sequence homology with the blueprint GB1 hairpin, has also ~50% sequence homology with turn segments in other proteins, *e.i.* hyaluronate lyase, galactose oxidase and the retinoic acid receptor  $\gamma$ 1<sup>258</sup>. The two terminal Gly1 and Gly10 residues function as terminal spacers to prevent any accidental charges interfering with the folding of the remaining eight residues. The central four amino acids Pro4, Glu5, Thr6 and Gly7 form the turn region and thus **5.1** is classified as Type II 4:4  $\beta$ -hairpin, the same as the GB1 hairpin<sup>264,265</sup>.

Initially it was found that the native hairpin structure of **5.1** is stabilized through five hydrogen bonds between Asp3 and Glu5, Thr6, Gly7 and Thr8 proximal to the turn region, and through hydrophobic interactions between Tyr2 – Pro4 and Tyr2 – Trp9 (Figure 5.1). A large body of work has focused on dissecting the folding steps involved in the formation of the hairpin and to determine the driving and stabilizing forces. Recent simulations predict a turn-centric hydrophobic collapse model<sup>255</sup>; this means that the initial step of folding is the formation of the turn sequence through hydrogen bond formation between the central amino acids Glu5-Thr6, joined by the rearrangement of Pro4. Subsequent formation of two more hydrogen bonds is followed by the rearrangement of Gly7 into the turn region, which brings the C- and N-terminal strands closer together. This in turn enforces the hydrophobic interactions between Tyr2 and Trp9, followed by formation of the remaining hydrogen bonds. It should be noted that Pro4 is an

important contributor to the initial hairpin folding process, by forcing Asp3 into a conformation that supports the formation of the native hydrogen bond cluster<sup>255,266</sup>. Furthermore, weak intrastrand Tyr2 – Pro4 help to maintain the hairpin structure during the folding process. The proposed mechanism agrees with studies on the GB1 hairpin and Peptide 1, which also support a dominant role for turn formation in initiating the folding<sup>240,256,267</sup>. However, the role of hydrophobic interactions remains ambiguous, as the initial driving forces after turn formation in all models is the formation of native or supportive non-native hydrogen bonds, with loose hydrophobic contacts contributing marginally to the hairpin folding. Moreover, if native intrastrand Tyr2 – Pro4 hydrophobic contacts miss to form, non-native Pro4 – Trp9 interactions can occur that delay folding due to packing frustration for the correct Tyr2 – Trp9 cross-strand packing<sup>255</sup>.

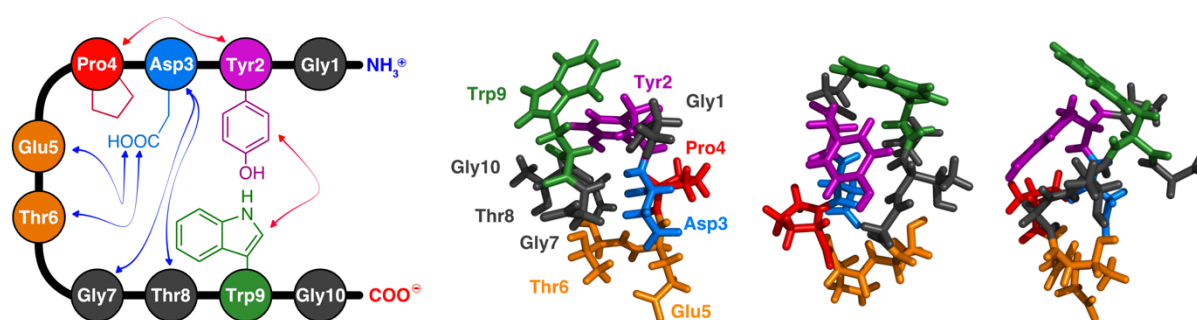


**Figure 5.1: Stabilizing interactions in the chignolin 5.1  $\beta$ -hairpin.** Left: schematic representation of 5.1 residues and interactions stabilizing the  $\beta$ -hairpin. The hydrophobic interactions between Tyr2 – Pro4 and Tyr2 – Trp9 are shown as red arrows. The hydrogen bonds between Asp3:N – Thr8:O, Glu5:N – Asp3:O $^{\delta}$ , Gly7:N – Asp3:O, Thr6 – Asp3:O $^{\delta}$  and Thr8:N – Asp3:O are presented as blue arrows. Right: three representative rotations of the crystal structure of chignolin 5.1 (pdb: 1UAO).

The remaining questions drive the search for answers in new experimental model systems that have altered turn regions, hydrogen bonding networks and hydrophobic interactions, and allow either the confirmation and extension of existing data and mechanisms, or challenge present ideas about protein folding. Peptides comprising azobenzene conformational switches as optical responsive turn elements, as for example in the ATZ peptide **III.1** or cyclic protein disulfide isomerase compounds, made it possible to control folding and unfolding events<sup>80,96,254,268,269</sup>. Moreover, they shifted the focus away from turn nucleation driven folding contemplation towards a more general view of hairpin formation, enforced by stabilizing hydrogen networks and hydrophobic interactions. Although one can argue that folding events in these unnatural systems are not representative for natural proteins, they do facilitate experimental monitoring of folding events with high spatio-temporal precision. As chignolin 5.1 represents one of the smallest proteins with  $\beta$ -hairpin structure available hitherto, we aimed to transform 5.1 into a photoswitchable model system by introducing AMPP **1.22** into the central turn sequence. The resulting AzoChignolin peptides AzoChig1 **5.2**, AzoChig2 **5.3** and AzoChig3 **5.4** and their folding dynamics are described in the following communication.

## 5.1 COMMUNICATION: PHOTOCONTROLLED CHIGNOLIN-DERIVED $\beta$ -HAIRPIN PEPTIDOMIMETICS

# ChemComm

## COMMUNICATION



View Article Online  
View Journal | View Issue



Cite this: *Chem. Commun.*, 2015, 51, 4001

Received 24th December 2014,  
Accepted 19th January 2015

DOI: 10.1039/c4cc10304a

www.rsc.org/chemcomm

### Photocontrolled chignolin-derived $\beta$ -hairpin peptidomimetics†

T. Podewin,<sup>a</sup> M. S. Rampp,<sup>b</sup> I. Turkanovic,<sup>b</sup> K. L. Karaghiosoff,<sup>a</sup> W. Zinth<sup>\*b</sup> and A. Hoffmann-Röder<sup>\*a</sup>

The synthesis of novel, chignolin-derived peptides comprising the azobenzene photoswitch [3-(3-aminomethyl)phenylazo]phenylacetic acid (AMPP) is reported. Reversible photoswitching behavior led to folding into  $\beta$ -hairpin-like structures, as unequivocally demonstrated by CD, FT-IR and NMR spectroscopy.

Understanding the mechanisms, by which particular sequences of amino acids are folded into well-defined three-dimensional protein structures, is a challenging problem in the field of molecular biology. The complexity of possible conformational transitions and different timescales of folding prevents accurate predictions and simulations for larger amino acid ensembles. Moreover, it is believed that certain key secondary motifs, e.g.  $\beta$ -hairpins and  $\beta$ -sheets, serve as nucleation sites for protein folding, providing insight into the early events of secondary structure formation. In particular  $\beta$ -hairpin-forming peptides have received much attention as model systems for both experimental and theoretical studies of the initial folding steps.<sup>1–4</sup> For instance, light-triggered folding of two amino acids strands into a  $\beta$ -hairpin peptide has been investigated by means of azobenzene photoswitches,<sup>5–10</sup> such as [3-(3-aminomethyl)phenylazo]phenylacetic acid<sup>11–13</sup> (AMPP). Upon incorporation into the peptide backbone, the latter offers the possibility to control the hairpin structure by initiating a reversible folding (*cis*-form) or unfolding (*trans*-form) transition.

Herein, we present a peptidomimetic model system for photocontrolled reversible  $\beta$ -hairpin formation based on chignolin<sup>14</sup> and AMPP. The decapeptide chignolin (GYDPETGIWG) was designed by Honda *et al.* on the basis of the central part of the GB1 hairpin<sup>14–17</sup> and is the smallest  $\beta$ -hairpin known to be stable in solution. As such

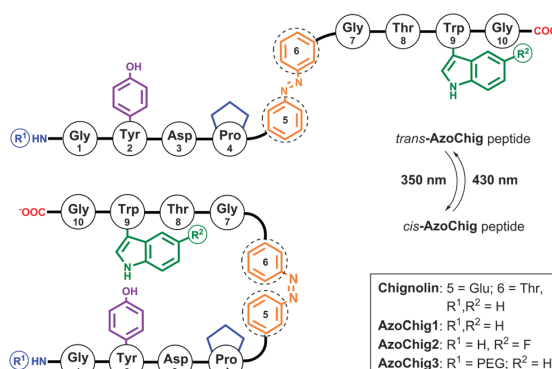


Fig. 1 Representative schematic illustration of reversible *cis*  $\rightleftharpoons$  *trans* isomerization of **AzoChig** peptides at 350 and 430 nm, respectively.

and in combination with ultrafast initiation of structural changes upon photoswitching, chignolin derivatives are particularly attractive targets for folding studies of protein nuclei. Therefore, the peptide **AzoChig1** (GYDP-AMPP-GTWG) was designed, in which the two central amino acids Glu5 and Thr6 of chignolin's four-residue turn sequence were substituted by AMPP (Fig. 1). Besides, peptidomimetic **AzoChig2** (GYDP-AMPP-GT(5FW)G) with a 5-fluoro-*L*-tryptophan (5FTp, 5FW) residue instead of Trp9 was synthesized to enhance key hydrophobic interactions between aromatic Tyr2 and Trp9. Fluorinated amino acid residues are known to be tolerated by a variety of proteins without introducing much steric perturbation and usually favor protein folding and stability due to their increased hydrophobicity.<sup>18,19</sup> For instance, the hydrophobicity of 5FTp, derived from 1-octanol-water partitioning experiments, is significantly higher than that of native Trp.<sup>20,21</sup> However, systematic studies towards structure-guiding effects of fluorinated amino acids have mostly focused on  $\alpha$ -helical systems<sup>19,22</sup> and only a limited number of approaches for fluorination of specific  $\beta$ -sheet positions have been reported, so far.<sup>23</sup> Finally, since both peptides **AzoChig1** and **AzoChig2** showed high solubility only in polar solvents like MeOH and MeCN, **AzoChig3** ((TEG)GYDP-AMPP-GTWG), equipped

<sup>a</sup> Department of Organic Chemistry, Faculty of Chemistry and Pharmacy, Ludwig-Maximilians-University LMU, 81377 Munich, Germany.  
E-mail: anja.hoffmann-roeder@cup.lmu.de

<sup>b</sup> Department for BioMolecular Optics, Faculty of Physics, Ludwig-Maximilians-University LMU, 80538 Munich, Germany.  
E-mail: wolfgang.zinth@physik.uni-muenchen.de

† Electronic supplementary information (ESI) available: Experimental procedures, analytical data and selected spectra of all new compounds. See DOI: 10.1039/c4cc10304a



## Communication

View Article Online

ChemComm

with an additional, N-terminal triethylene glycol residue, was prepared to furnish a photoswitchable and water-soluble chignolin derivative. Key amino acid building blocks for the solid-phase peptide synthesis (SPPS) of photocontrolled chignolin-derived  $\beta$ -hairpins were prepared, as follows (ESI<sup>†</sup>): Fmoc-protected AMPP derivative was synthesized in seven steps according to the known strategy of Renner *et al.*<sup>12</sup> Thus, (9*H*-fluoren-9-yl)methyl-(3-aminobenzyl)carbamate, derived from Fmoc-protection of 3-(aminomethyl)aniline, was reacted with 2-(3-nitrosophenyl)acetic acid under Mills conditions to afford the AMPP building block in 59% yield.

Fmoc-protection of commercially available 5FTrp yielded the requisite fluorinated building block, while the Fmoc-TEG derivative was synthesized in five steps starting from triethylene glycol.<sup>24</sup> The chignolin-derived peptides were assembled in an automated microwave-assisted CEM Liberty 1 peptide synthesizer on a pre-loaded Fmoc-Gly-Wang LL resin (Novabiochem).

After Fmoc-deprotection by piperidine in *N*-methylpyrrolidone (NMP), the standard amino acid couplings were performed using HBTU-HOBt and diisopropylethylamine in DMF for activation. In contrast, incorporation of the non-standard building blocks required modified coupling procedures and the use of the more

reactive HATU-HOAt-*N*-methylmorpholine cocktail. Release from the resin with simultaneous deprotection using TFA-H<sub>2</sub>O mixtures (95:5) followed by preparative RP-HPLC, finally provided the targeted chignolin-derived peptidomimetics with yields of 10–33%.

Photomodulation of  $\beta$ -hairpins with azobenzene derivatives as backbone elements mostly relies on an ultrafast *trans*  $\leftrightarrow$  *cis* isomerization, which can be induced by light of different wavelengths and involves large changes in geometry and dipole moments.<sup>25,26</sup> For instance, *cis*-AMPP-TrpZip peptides forming a  $\beta$ -hairpin-like structure can rapidly unfold within 1 ns by photoisomerization of AMPP to its *trans*-isomeric state.<sup>12,27,28</sup>

In chignolin, the  $\beta$ -hairpin conformation is stabilized by H bonds of Asp3:N-Thr8:O, Gly7:N-Asp3:O<sup>δ</sup>, Thr8:N-Asp3:O, Glu5:N-Asp3:O<sup>δ</sup> and Thr6:N-Asp3:O<sup>δ</sup>, as well as by hydrophobic interactions between Tyr2:Pro4 and Tyr2:Trp9.<sup>29</sup> The newly synthesized **AzoChig** derivatives should retain most of the aforementioned stabilizing interactions, and in particular **AzoChig2** comprising the 5FTrp residue should reveal enhanced hydrophobic interactions between Tyr2 and Trp9 (*vide supra*).

RP-HPLC analyses and NMR spectroscopy demonstrate the structural integrity and purity of the assembled **AzoChig1–3**

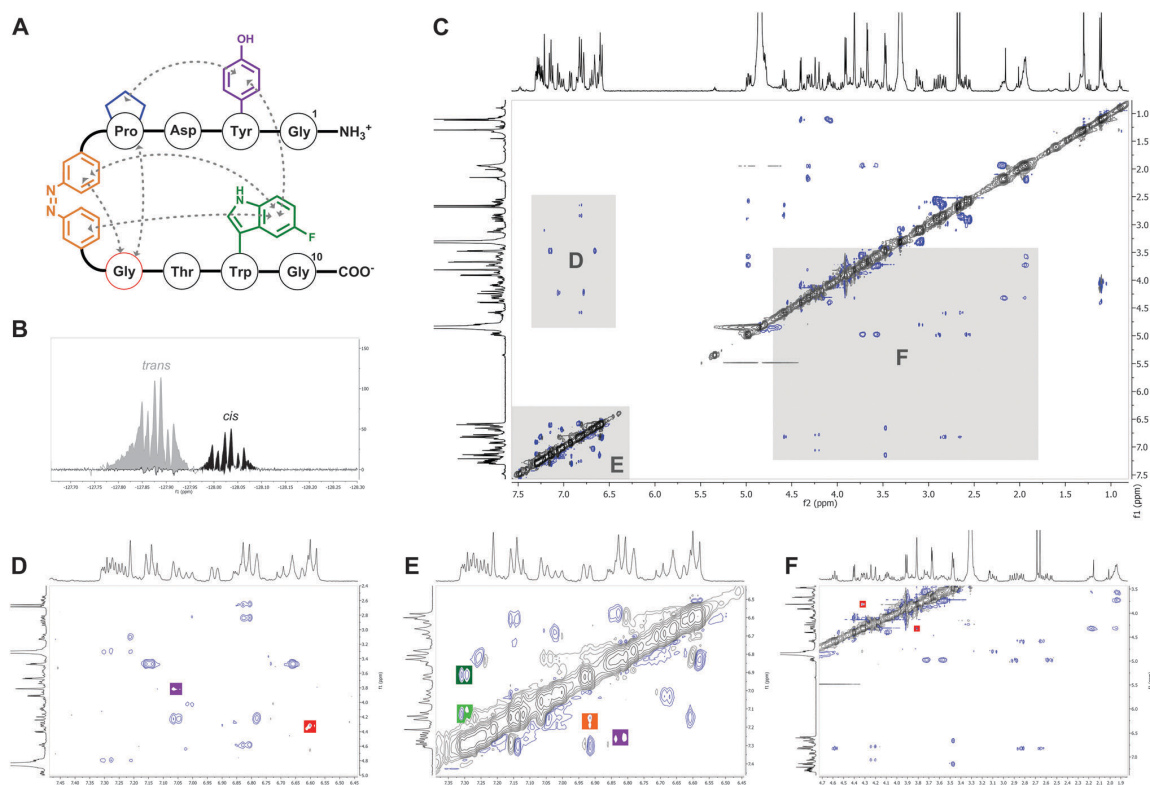


**Fig. 2** (A) Schematic structure of *cis*-**AzoChig2** with observed NOE cross peaks (gray) between Tyr2, Pro4, AMPP5,6 and Trp9; (B) <sup>19</sup>F-NMR spectra of *cis*- (black) and *trans*-**AzoChig2** (grey) peptides in MeOH-*d*<sub>4</sub> at 26 °C, *c* = 2 mM; (C) <sup>1</sup>H,<sup>1</sup>H-ROESY-NMR spectra of **AzoChig2** in MeOH-*d*<sub>4</sub> at 26 °C, *c* = 2 mM; (D) <sup>1</sup>H,<sup>1</sup>H-ROESY-NMR section from 7.5–6.5 and 5.0–2.4 ppm. Marked NOE cross peaks: Tyr2/H<sub>3</sub>,H<sub>5</sub> ↔ Pro4/H<sub>α</sub> (red) and AMPP5,6/H<sub>8</sub> ↔ Gly7/H<sub>α</sub>,H<sub>α</sub>' (purple); (E) <sup>1</sup>H,<sup>1</sup>H-ROESY-NMR section from 7.4–6.4 and 7.4–6.5 ppm. Marked NOE cross peaks: Tyr2/H<sub>2</sub>,H<sub>6</sub> ↔ Trp9/H<sub>6</sub> (purple), AMPP5,6/H<sub>7</sub> ↔ AMPP5,6/H<sub>16</sub> (orange), AMPP5,6/H<sub>7</sub> ↔ Trp9/H<sub>4</sub> (dark green) and AMPP5,6/H<sub>16</sub> ↔ Trp9/H<sub>4</sub> (green); (F) <sup>1</sup>H,<sup>1</sup>H-ROESY-NMR section from 4.7–1.9 and 7.5–3.5 ppm. Marked NOE cross peaks: Pro4/H<sub>α</sub> ↔ Gly7/H<sub>α</sub>,H<sub>α</sub>' (red).



mimetics (ESI†). To elucidate the three-dimensional solution structures of *cis*-/*trans*-**AzoChig1–3**,  $^1\text{H}$  and  $^{13}\text{C}$ , as well as correlation (COSY), hetero nuclear single quantum (HSQC) and hetero nuclear multiple bond (HMBC) NMR spectra were recorded in 10 mM MeOH- $d_4$  solutions at 400 and 600 MHz.<sup>30</sup> Unfortunately though, **AzoChig3** aggregates strongly in solution, which leads to heavy signal broadening and precludes any precise signal assignments. In contrast, sharp  $^1\text{H}$  NMR signals, unequivocally assignable were obtained for *cis*-/*trans*-**AzoChig1** and **2**, enabling their application to total correlation (TOCSY) and rotating-frame nuclear Overhauser enhancement (ROESY) spectroscopy at 400 MHz in MeOH- $d_4$  (Fig. 2C–F). All samples were kept in the dark for two days before measurement, yielding *trans*-configured peptides.

The  $^1\text{H}$  NMR spectra of **AzoChig1** and **AzoChig2** peptides show distinct peak offsets for the aromatic residues Tyr2, AMP5,6 and Trp9 (8.0–6.5 ppm) upon *cis*  $\leftrightarrow$  *trans* isomerizations. Moreover, NOE cross-peaks detected between Tyr2:Trp9, Pro4:Gly7, AMP5,6: Gly7 and AMP5,6:Trp9 in the ROESY spectra of *cis*-**AzoChig1** and *cis*-**AzoChig2**, depict the expected formation of folded structures for both derivatives (Fig. 2D–F), with NOE signals between aromatic Tyr2, AMP5,6 and Trp9 moiety, pinpointing the presence of turns stabilized by hydrophobic interactions. The  $^{19}\text{F}$  NMR spectra of *cis*- and *trans*-**AzoChig2** finally reveal distinct downfield shifts of the fluorine signals (Fig. 2B), indicating significant changes in the electronic structure and interactions upon isomerization.

To substantiate the presence of unfolded *trans*-conformations and their conversions into the desired  $\beta$ -hairpin structures upon azobenzene *trans*-to-*cis* isomerizations, UV/Vis, FT-IR, and CD spectroscopic measurements were performed. Therefore, 1 mM stock solutions of **AzoChig1–3** peptides in MeOH were prepared and stored in the dark at room temperature for two days,

furnishing *trans*-configured peptides. Using these stock solutions, peptide samples with concentrations of  $c = 76 \mu\text{M}$  (**AzoChig1**),  $77 \mu\text{M}$  (**AzoChig2**) and  $78 \mu\text{M}$  (**AzoChig3**) were prepared through dilution with MeOH to record stationary UV/Vis absorption spectra before and after illumination at appropriate wavelengths (Fig. 3A). Irradiation of the *trans*-peptides at  $\lambda = 350 \text{ nm}$  for 180 s led to reversible formation of photostationary states comprising in each case 84% of the *cis*-conformer. The UV spectra of *trans*-**AzoChig1** and *trans*-**AzoChig3** are very similar and show characteristic maxima at 322 nm and 291 nm due to the  $\pi \rightarrow \pi^*$  *trans*-azobenzene transition and the absorptions by Trp9 and Tyr2. The latter maximum is shifted towards 299 nm in the **AzoChig2** spectrum as a result of the presence of the 5FTrp moiety.

Stationary FT-IR spectra of the *trans*-**AzoChig** peptides were recorded using 5 mM solutions in MeOH- $d_4$ , which were kept again in the dark for two days. MeOH- $\text{H}_2\text{O}$  mixtures were spared to avoid the undesired aggregation of the peptidomimetics. The spectra of all peptides are similar featuring the characteristic bands of the azobenzene chromophore and the peptide backbones (amide I and II bands around  $1655 \text{ cm}^{-1}$  and  $1450 \text{ cm}^{-1}$ , respectively, Fig. 3B). The peak at  $1675 \text{ cm}^{-1}$  originates from traces of TFA used during preparation of the samples. The difference spectra were recorded for *trans*  $\rightarrow$  *cis* and *cis*  $\rightarrow$  *trans* isomerizations (Fig. 3C). Most prominent in the difference spectra is the dispersive line shape in the range of the amide I band, which points to a change in the H-bonding pattern upon isomerization of the azobenzene. In the *cis*-isoform there is an excess of strong H bonds, red-shifted relative to weaker H bonds, which were found preferentially in the *trans*-form of the peptides. This feature, similar to the one observed previously in ATZ,<sup>12,27,28</sup> points to a change of the peptide structure with an open *trans*-form to a compact *cis*-form. Latter thereby shows

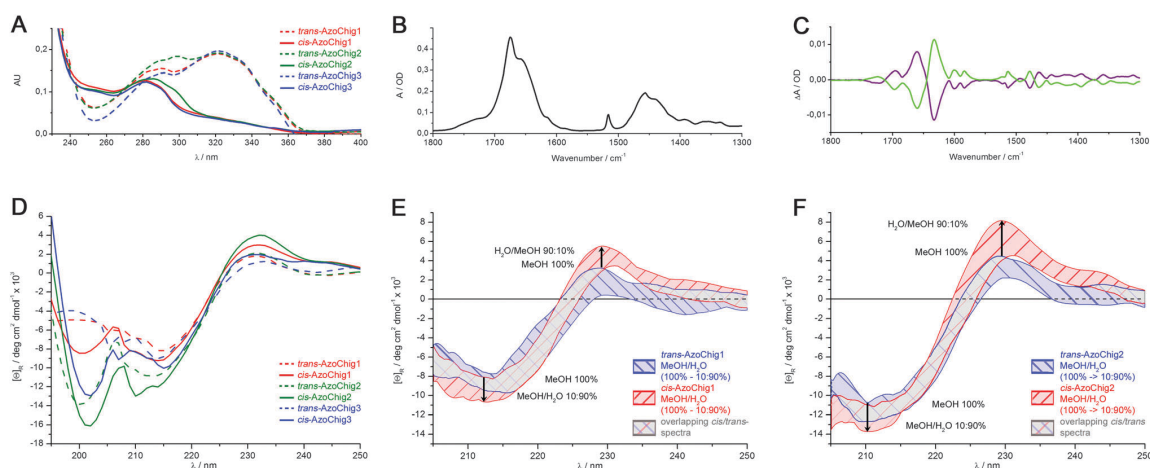


**Fig. 3** (A) UV/Vis spectra of *cis*-/*trans*-**AzoChig1–3** at 25 °C,  $c = 76–78 \mu\text{M}$ ; (B) representative FT-IR absorption spectrum of **AzoChig1** at 25 °C in MeOH- $d_4$ ,  $c = 5 \text{ mM}$ ; (C) absorption difference spectra of **AzoChig1** induced by irradiations at 350 nm (*trans*  $\rightarrow$  *cis*, green curve) and 430 nm (*cis*  $\rightarrow$  *trans*, purple curve) in MeOH- $d_4$ ,  $c = 5 \text{ mM}$ ; (D) CD spectra of *cis*-/*trans*-**AzoChig1–3** at 5 °C in MeOH,  $c = 76–78 \mu\text{M}$ ; (E) solvent-dependent CD spectra of *cis*-**AzoChig1** (red hatched band) and *trans*-**AzoChig1** (blue hatched band) at 5 °C in MeOH- $\text{H}_2\text{O}$  ratios reaching from 100% MeOH  $\rightarrow$  MeOH- $\text{H}_2\text{O}$  10/90 with  $c = 82–112 \mu\text{M}$ . The gray crossed band represents overlapping spectra; (F) solvent-dependent CD spectra of *cis*-**AzoChig2** (red hatched band) and *trans*-**AzoChig2** (blue hatched band) at 5 °C in MeOH- $\text{H}_2\text{O}$  ratios reaching from 100% MeOH  $\rightarrow$  MeOH- $\text{H}_2\text{O}$  10/90 with  $c = 84–102 \mu\text{M}$ . The gray crossed band represents overlapping spectra.



## Communication

View Article Online

ChemComm

additional stronger, presumably interstrand H bonds pointing to a  $\beta$ -hairpin-like structure.

CD spectra in the 195–250 nm range were determined for *trans*-**AzoChig1–3** peptides at concentrations of  $c = 76$ – $78 \mu\text{M}$  in MeOH at  $5^\circ\text{C}$  (*vide supra*). Solvent-dependent CD spectra of **AzoChig1** and **AzoChig2** were recorded at concentrations of  $c = 82$ – $112 \mu\text{M}$  in MeOH–H<sub>2</sub>O mixtures at  $5^\circ\text{C}$ . For the *cis*-azo isomers, CD spectra were recorded after irradiation at 350 nm for 180 s, *i.e.*, at the *cis*-photostationary state (Fig. 3D). All three *cis*-azo peptides feature distinct maxima at 231 nm – assigned to stacking of Trp9 to Tyr2 – as well as minima at 212 nm and 200 nm, and pronounced positive signals below 195 nm. Hence, they strongly resemble the spectra of native chignolin suggesting a folded, hairpin-like structure. The enhanced hydrophobic interactions between Tyr2 and 5FTrp9 in **AzoChig2** become visible by the increase of the CD signal in the 231 nm range. Temperature-dependent CD spectra of *cis*-**AzoChig1** and *cis*-**AzoChig2** in the  $5$ – $60^\circ\text{C}$  range (data not shown, see ESI<sup>†</sup>) reveal a thermal unfolding process to be working at higher temperatures, similar to native chignolin. The CD spectra of *trans*-**AzoChig1–3** display small maxima at 231 nm and minima at 213 nm but deviate in the 200 nm range. The deep minimum found for **AzoChig2** at 200 nm can be tentatively interpreted in terms of a better ordering of the peptide part due to the increased hydrophobic interaction of 5FTrp9 with Tyr2.

Moreover, solvent-dependent CD measurements were performed using mixtures of MeOH–H<sub>2</sub>O (Fig. 3E and F, see ESI<sup>†</sup>), with ratios from 10–100% MeOH. The MeOH–H<sub>2</sub>O spectra of the *cis*-/*trans*-**AzoChig1** and *cis*-/*trans*-**AzoChig2** peptidomimetics show increasing values for the maximum around 230 nm and deeper minima at 200 nm with increasing water amounts. Presumably, the hydrophobic turn region of the *cis*-peptides becomes more stabilized by hydrophobic interactions between Tyr2:Trp9 in aqueous surroundings, which leads to the observed increase in molar ellipticity at 230 nm. Furthermore, interstrand interactions are stabilized by water-mediated hydrogen bonding as reflected by the decreased ellipticity around 200 nm. Finally and at higher water ratios, the observed CD signals of **AzoChig1** and **AzoChig2** approximate nicely the reported molar ellipticity characteristics of the parent peptide chignolin.<sup>14</sup>

We have presented a novel class of photoswitchable  $\beta$ -hairpin model peptides derived from the designer mini protein chignolin by substitution of two central amino acids from the turn sequence by the known azobenzene chromophore AMPP. The resulting **AzoChig1–3** peptidomimetics were assembled by SPPS and carefully characterized at both photoisomeric states using UV/VIS, IR, CD, and NMR spectroscopy. In the *trans*-state of AMPP, the peptides mostly exhibit a disordered structure, while *trans*  $\rightarrow$  *cis* photoisomerization of the azobenzene chromophore induces folded  $\beta$ -hairpin-like structures.

Support from LMU Munich, the Deutsche Forschungsgemeinschaft (SFB 749, project A5) and the Excellence Cluster CIPSM – Center of Integrated Protein Science Munich – is gratefully acknowledged.

## Notes and references

- C. E. Stotz and E. M. Topp, *J. Pharm. Sci.*, 2004, **93**, 2881–2894.
- A. G. Cochran, N. J. Skelton and M. A. Starovasnik, *Proc. Natl. Acad. Sci. U. S. A.*, 2001, **98**, 5578–5583.
- A. Lewandowska, S. Oldziej, A. Liwo and H. A. Scheraga, *Biophys. Chem.*, 2010, **151**, 1–9.
- K. Lindorff-Larsen, S. Piana, R. O. Dror and D. E. Shaw, *Science*, 2011, **334**, 517–520.
- S. Samanta, A. A. Beharry, O. Sadovski, T. M. McCormick, A. Babalhavaej, V. Tropepe and G. A. Woolley, *J. Am. Chem. Soc.*, 2013, **135**, 9777–9784.
- A. M. Ali and G. A. Woolley, *Org. Biomol. Chem.*, 2013, **11**, 5325–5331.
- F. Zhang, K. M. Mueller, G. A. Wooley and K. M. Arndt, *Methods Mol. Biol.*, 2012, **813**, 195–210.
- M. Blanco-Lomas, S. Samanta, P. J. Campos, G. A. Woolley and D. Sampedro, *J. Am. Chem. Soc.*, 2012, **134**, 6960–6963.
- A. A. Beharry, T. Chen, M. S. Al-Abdul-Wahid, S. Samanta, K. Davidov, O. Sadovski, A. M. Ali, S. B. Chen, R. S. Prosser, H. S. Chan and G. A. Woolley, *Biochemistry*, 2012, **51**, 6421–6431.
- O. Sadovski, A. A. Beharry, F. Zhang and G. A. Woolley, *Angew. Chem., Int. Ed.*, 2009, **48**, 1484–1486.
- A. A. Beharry and G. A. Woolley, *Chem. Soc. Rev.*, 2011, **40**, 4422–4437.
- S.-L. Dong, M. Löweneck, T. E. Schrader, W. J. Schreier, W. Zinth, L. Moroder and C. Renner, *Chem. – Eur. J.*, 2006, **12**, 1114–1120.
- A. Aemissegger, V. Kräutler, W. F. van Gunsteren and D. Hilvert, *J. Am. Chem. Soc.*, 2005, **127**, 2929–2936.
- S. Honda, K. Yamasaki, Y. Sawada and H. Morii, *Structure*, 2004, **12**, 1507–1518.
- M. Bonomi, D. Branduardi, F. L. Gervasio and M. Parrinello, *J. Am. Chem. Soc.*, 2008, **130**, 13938–13944.
- B. Ma and R. Nussinov, *J. Mol. Biol.*, 2000, **296**, 1091–1104.
- S. Honda, T. Akiba, Y. S. Kato, Y. Sawada, M. Sekijima, M. Ishimura, A. Ooishi, H. Watanabe, T. Odahara and K. Harata, *J. Am. Chem. Soc.*, 2008, **130**, 15327–15331.
- B. C. Buer, J. L. Meagher, J. A. Stuckey and E. N. G. Marsh, *Proc. Natl. Acad. Sci. U. S. A.*, 2012, **109**, 4810–4815.
- M. Salwiczek, E. K. Nyakatura, U. I. M. Gerling, S. Ye and B. Koksche, *Chem. Soc. Rev.*, 2012, **41**, 2135–2171.
- Z. J. Xu, M. L. Love, L. Y. Ma, M. Blum, P. M. Bronskill, J. Bernstein, A. A. Grey, T. Hofmann, N. Camerman and J. T. Wong, *J. Biol. Chem.*, 1989, **264**, 4304–4311.
- C.-Y. Wong and M. R. Eftink, *Biochemistry*, 1998, **37**, 8947–8953.
- C. J. Pace and J. Gao, *Acc. Chem. Res.*, 2012, **46**, 907–915.
- G. A. Clark, J. D. Baleja and K. Kumar, *J. Am. Chem. Soc.*, 2012, **134**, 17912–17921.
- S. Keil, C. Claus, W. Dippold and H. Kunz, *Angew. Chem., Int. Ed.*, 2001, **40**, 366–369.
- H. Fliegl, A. Köhn, C. Hättig and R. Ahlrichs, *J. Am. Chem. Soc.*, 2003, **125**, 9821–9827.
- J. Dokić, M. Gothe, J. Wirth, M. V. Peters, J. Schwarz, S. Hecht and P. Saalfrank, *J. Phys. Chem.*, 2009, **113**, 6763–6773.
- A. A. Deeg, M. S. Rampp, A. Popp, B. M. Pilles, T. E. Schrader, L. Moroder, K. Hauser and W. Zinth, *Chem. – Eur. J.*, 2014, **20**, 694–703.
- T. E. Schrader, W. J. Schreier, T. Cordes, F. O. Koller, G. Babitzki, R. Denschlag, C. Renner, M. Löweneck, S.-L. Dong, L. Moroder, P. Tavan and W. Zinth, *Proc. Natl. Acad. Sci. U. S. A.*, 2007, **104**, 15729–15734.
- S. Enemark and R. Rajagopalan, *Phys. Chem. Chem. Phys.*, 2012, **14**, 12442–12450.
- In consequence of the limited solubility of peptidomimetics **AzoChig1** and **AzoChig2** in aqueous solutions and their intrinsic aggregation tendency at very high concentrations ( $> 5 \text{ mM}$ ), spectroscopic conformational analyses were performed in MeOH, similar to related model studies (see *e.g.* ref. 12 and 28 and following references: (a) M. Erdélyi, A. Karlén and A. Gogoll, *Chem. – Eur. J.*, 2006, **12**, 403–412; (b) M. Erdélyi, V. Langer, A. Karlén and A. Gogoll, *New J. Chem.*, 2002, **26**, 834–843; (c) Y. J. Chung, B. R. Huck, L. A. Christianson, H. E. Stanger, S. Kräuthauser, D. R. Powell and S. H. Gellman, *J. Am. Chem. Soc.*, 2000, **122**, 3995–4004). Finally, it must be emphasized that so far, the **AzoChig** peptides represent first model compounds and will be further optimized for folding studies under more physiological conditions. These optimizations require greater divergence from the original chignolin design and are subject to extended future studies.



## 5.2 SUPPLEMENTARY FIGURES

### 4 UV/Vis, CD and FT-IR spectra of AzoChig1-3 peptides

#### 4.1 UV/Vis spectra of AzoChig1-3 peptides

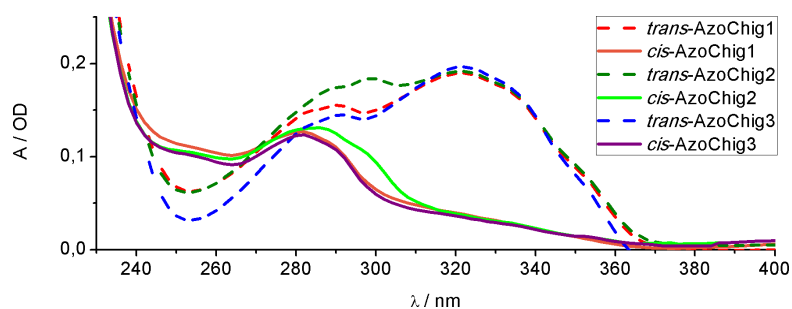


**Figure 17:** UV/Vis spectra of *cis/trans*-AzoChig1-3 peptides in methanol,  $c = 77 \mu\text{M}$  AzoChig1,  $c = 77 \mu\text{M}$  AzoChig2 and  $c = 78 \mu\text{M}$  AzoChig3.

#### 4.2 CD spectra of AzoChig1-3 peptides

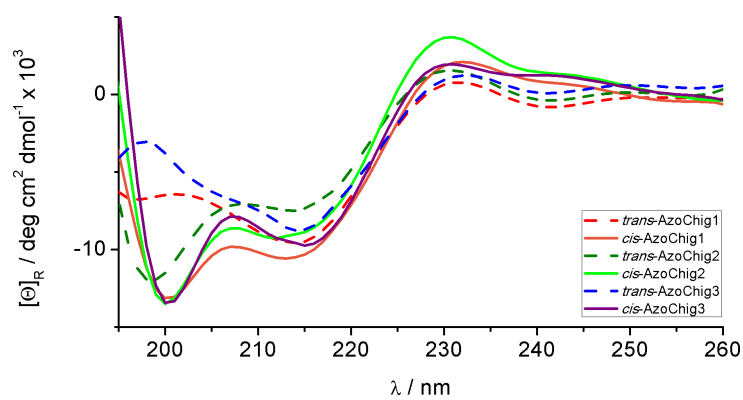


**Figure 18:** CD spectra of *cis/trans*-AzoChig1-3 peptides in methanol,  $c = 77 \mu\text{M}$  AzoChig1,  $c = 77 \mu\text{M}$  AzoChig2 and  $c = 78 \mu\text{M}$  AzoChig3.

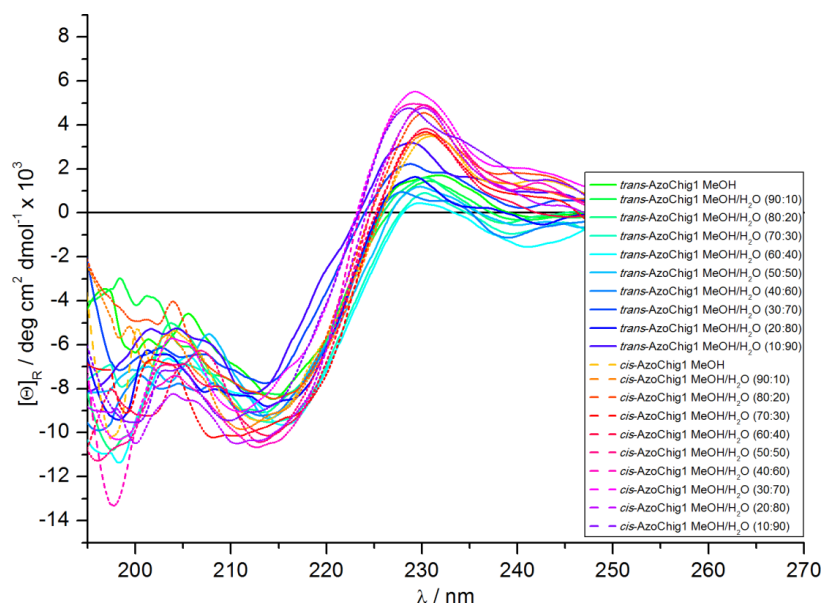


**Figure 12:** Solvent dependent CD spectra of *cis*-AzoChig1 (dashed lines, red to purple) and *trans*-AzoChig1 (solid lines, green to blue) peptides in methanol/water ratios from 100% methanol to 10:90% methanol/water. The CD spectra were measured at 5 °C with concentrations of  $c = 82\text{-}112 \mu\text{M}$ .

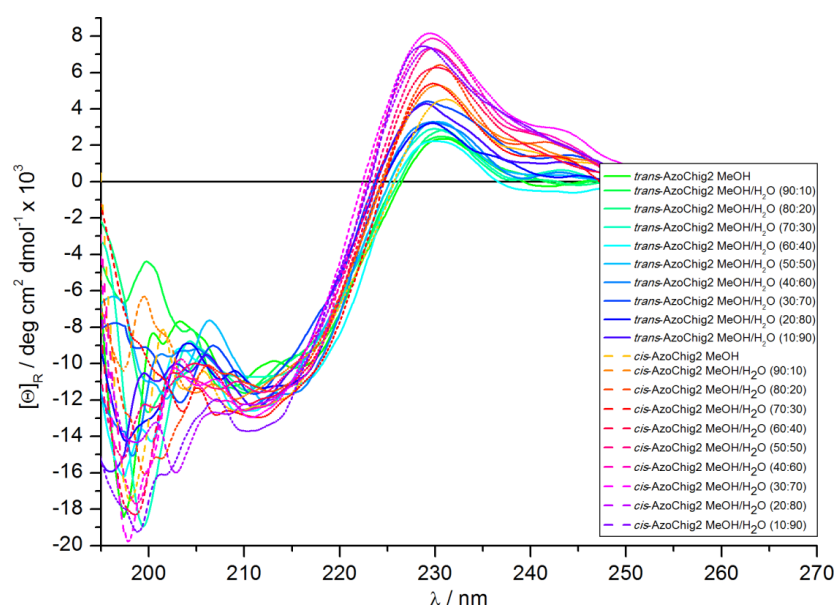


**Figure 13:** Solvent dependent CD spectra of *cis*-AzoChig2 (dashed lines, red to purple) and *trans*-AzoChig2 (solid lines, green to blue) peptides in methanol/water ratios from 100% methanol to 10:90% methanol/water. The CD spectra were measured at 5 °C with concentrations of  $c = 84\text{-}102 \mu\text{M}$ .

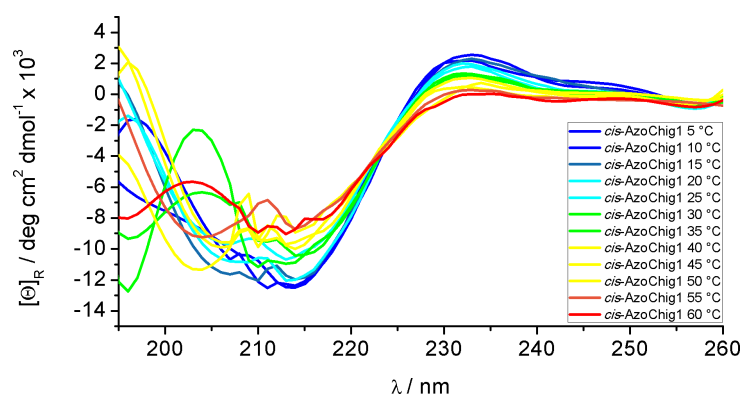


Figure 14: Temperature dependent CD spectra of the *cis*-AzoChig1 peptide in methanol,  $c = 76 \mu\text{M}$ .

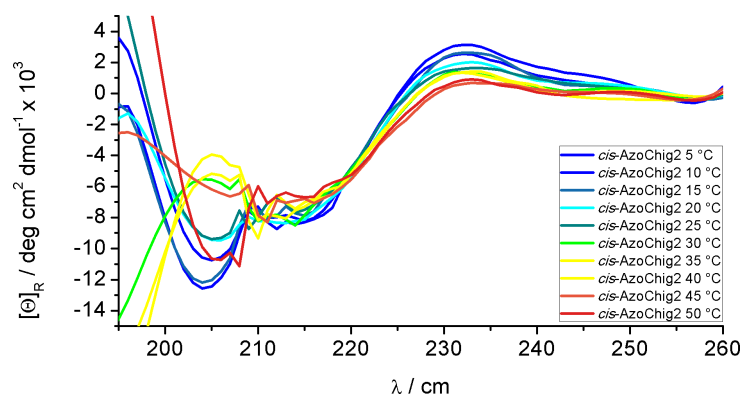
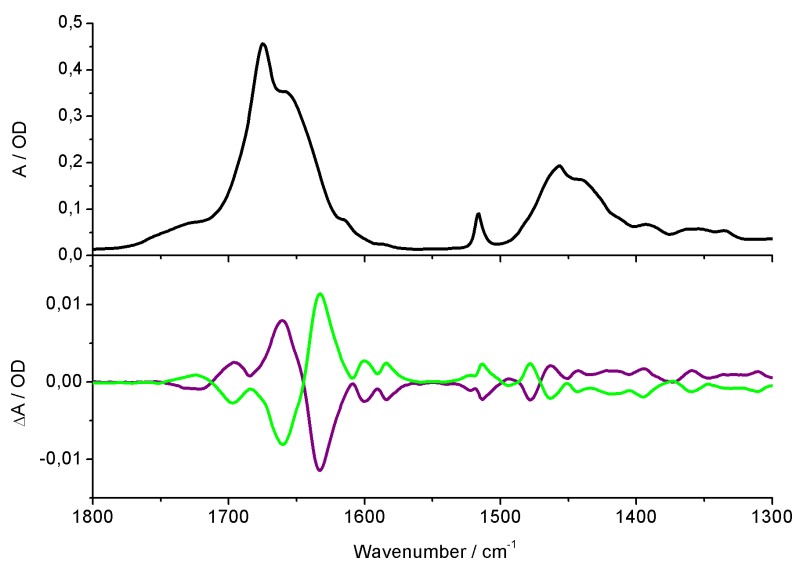
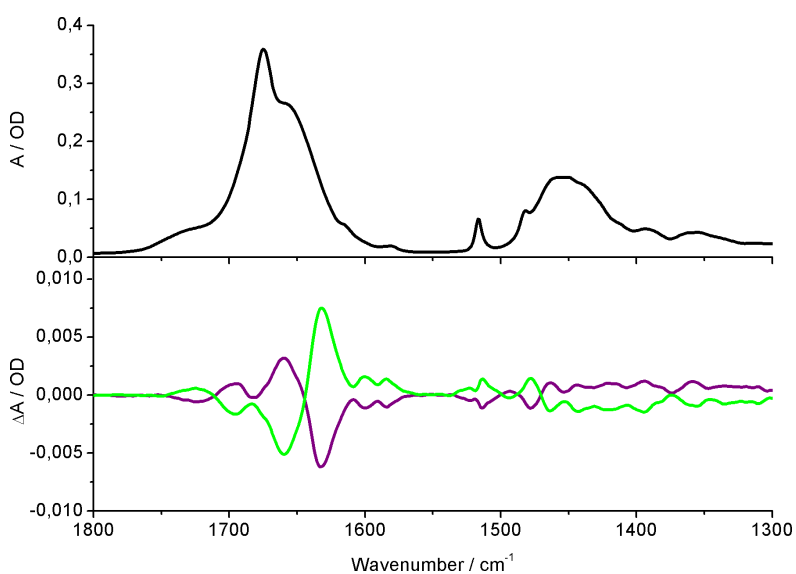


Figure 15: Temperature dependent CD spectra of *cis*-AzoChig2 peptide in methanol,  $c = 77 \mu\text{M}$ .

### 4.3 FT-IR spectra of AzoChig1-3 peptides



**Figure 16:** Top: FT-IR spectrum of **AzoChig1** peptide in methanol- $d_4$ ,  $c = 5.0$  mM; Bottom: IR differential spectra of the *cis*  $\rightarrow$  *trans* (purple) and *trans*  $\rightarrow$  *cis* (green) isomerization of **AzoChig1** peptide in methanol- $d_4$ ,  $c = 5.0$  mM.



**Figure 17:** Top: FT-IR spectrum of **AzoChig2** peptide in methanol- $d_4$ ,  $c = 5.0$  mM; Bottom: IR differential spectra of the *cis*  $\rightarrow$  *trans* (purple) and *trans*  $\rightarrow$  *cis* (green) isomerization of **AzoChig2** peptide in methanol- $d_4$ ,  $c = 5.0$  mM.

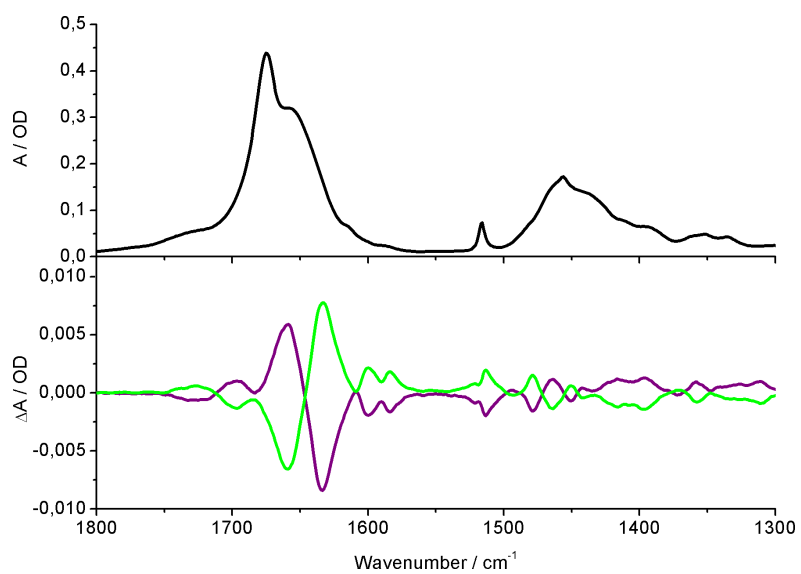


**Figure 18:** Top: FT-IR spectrum of **AzoChig3** peptide in methanol-d<sub>4</sub>, *c* = 5.0 mM; Bottom: IR differential spectra of the *cis* → *trans* (purple) and *trans* → *cis* (green) isomerization of **AzoChig3** peptide in methanol-d<sub>4</sub>, *c* = 5.0 mM.

## 5.3 ADDITIONAL COMPOUNDS

### 5.3.1 AZOCHIGNOLIN-RELATED MUTANTS

The native chignolin **5.1**  $\beta$ -hairpin structure is stabilized through a hydrogen bonding network and hydrophobic interactions between Tyr2, Pro4 and Trp9. Most of these interactions are presumably retained in the AzoChignolin peptides, as the photoswitch only substitutes the central Glu5 and Thr6 amino acids, not altering the important hydrogen contributor Asp3. To test the contribution of hydrophobic interactions to folding and stabilization of the hairpin, we initially synthesized AzoChig2 **5.3** with a more hydrophobic 5-fluoro-Trp9 residue. Indeed, **5.3** exhibited a higher exciton coupling of Tyr2 – Trp9 in the CD spectrum, indicating a stronger hydrophobic stacking of both aromatic residues. This exciton coupling is characteristic for cross-strand coupling between Trp – Trp, Tyr – Trp and Tyr – Tyr aromatic pairs and can be used to monitor cross-strand interactions and estimate folded hairpin content<sup>243,270,271</sup>. The Tyr2 – Trp9 pair in chignolin **5.1** generates a strong negative band at 200 nm and a prominent positive band at 230 nm, whereby the latter is more particular. While the AzoChig1 **5.2** and AzoChig2 **5.3** peptides both show the band at 230 nm, **5.2** lacks the negative band at 200 nm. This can be explained with the relative orientation of the Tyr2 to Trp9 in **5.2**, because intensity and exact wavelengths of the exciton coupling bands are strongly dependent on the two coupling partners and their relative orientation to each other<sup>272</sup>. As was shown for AzoChig1 **5.2** and AzoChig2 **5.3**, the exciton coupling bands at 230 nm (and 200 nm for **5.3**) of the Tyr2 – Trp9 pair are reduced upon isomerization of the folded *cis*- to the unfolded *trans*-form and vice versa. Furthermore, in **5.3** this band was more prominent than in **5.2**, showing the enhanced hydrophobic contact in the fluorinated compound. Although this finding is hard to directly translate into a quantitative assertion about hairpin content, it is a good indicator for interstrand interactions and folding.

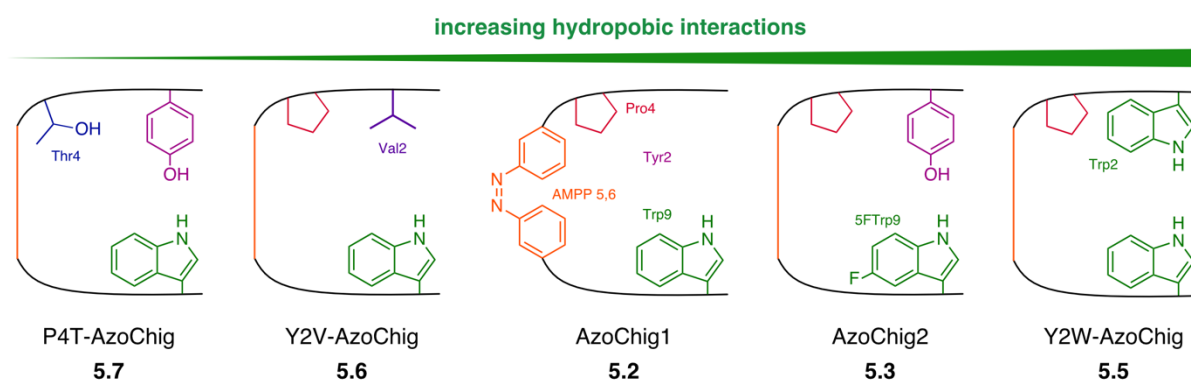


**Figure 5.2: Predicted influence of substituents on hydrophobic interactions in AzoChignolin peptides.** Introduction of hydrophobic 5-fluoro-L-tryptophan (5FTp) in **5.3** and Trp2 in **5.5** increase cross-strand hydrophobic interactions and stabilize the hairpin. Substitution of Tyr2 with Val2 in **5.6** and Pro4 with Thr4 in **5.7** reduce hydrophobic interactions leading to an impaired stabilization of the hairpin.

To assess the dominant sort of hydrophobic interactions in AzoChig1 **5.2**, *i.e.* whether hydrophobic contact and/or hydrophobic stacking are the major stabilizing forces, two mutant compounds were synthesized in which Tyr2 was replaced by tryptophan and valine (Figure 5.2). It was anticipated that these two peptides

Y2W-AzoChig **5.5** and Y2V-AzoChig **5.6** exhibit reinforced hydrophobic interactions, *i.e.* hydrophobic contact and stacking, between Trp2 – Trp9 in **5.5**, and solely hydrophobic contact without stacking between Val2 – Trp9 in **5.6**. The initial assessment *via* CD spectroscopy showed a weak positive band at 230 nm and two slight and equal minima at 202 and 214 nm for the exciton coupling between Trp2 – Trp9 in unfolded *trans*-**5.5** (Figure 5.3). In *cis*-**5.5** the extrema at 214 and 230 nm are amplified, while the minimum at 202 nm remains the same. This corresponds to the CD signals in the *cis*-/*trans*-AzoChig1 **5.2** peptide, which show small extrema at 216 and 230 nm in the *trans*-peptide and enhanced signals in the *cis*-form. Although the amplitude of the extrema in both isomers seems significantly stronger in **5.2** than in **5.5**, this does not necessarily indicate reduced hairpin stabilization of the latter. Since the intensity of the extrema is dependent on the electronic properties and relative orientation of the exciton coupling partners to each other, it rather allows a qualitative judgement over folded hairpin contents for the *cis*-/*trans*-isomers of **5.5**. In contrast, both *cis*-/*trans*-Y2V-AzoChig **5.6** peptides exhibit very similar spectra with a strong minimum at 200 nm and no maximum at 230 nm, as a result of the missing exciton coupling between Val2 – Trp9 (Figure 5.3). Here, the CD spectra resemble random-coiled structures, and the similarity between both spectra indicates a diminished hairpin stability and restricted folding events in the *cis*-/*trans*-peptides. This correlates with Tyr2 being the major contributor to hydrophobic interactions and consequently substitution with a hydrophobic, but non-aromatic valine residue abolishes the important hydrophobic stacking between Tyr2 – Trp9 as well as the minor intrastrand stabilization by Tyr2 – Pro4.

The folding and unfolding dynamics of the Y2W-AzoChig **5.5** and Y2V-AzoChig **5.6** peptides were primarily detected with differential IR spectroscopy (Figure 5.3). This method helps to detect minimal differences in the cw IR spectra for peptidic *cis*-/*trans*-isomers and has been also applied to the AzoChig1 **5.2** and AzoChig2 **5.3** peptides. The IR spectra of **5.5** and **5.6** both show a pronounced peak at 1674  $\text{cm}^{-1}$  and a broad shoulder at 1655  $\text{cm}^{-1}$ , with smaller additional signals at 1456  $\text{cm}^{-1}$  and lower wavenumbers, corresponding to the amide-II bands. Most prominent in the differential IR spectra of *cis*-/*trans*-**5.5** and -**5.6** is the dispersive line shape in the region of the amide-I band, with peak shifts from 1659 to 1634  $\text{cm}^{-1}$  for *trans*  $\rightarrow$  *cis* **5.5** and 1659 to 1631  $\text{cm}^{-1}$  for *trans*  $\rightarrow$  *cis* **5.6**. The weaker absorption changes at smaller wavenumbers correspond to changes in the amide-II band and of the AMPP **1.22** photoswitch. Similar to **5.2** the red-shifting of the amide-I band to lower wavenumbers in **5.5** and **5.6** shows a change in the hydrogen bonding pattern towards formation of stronger hydrogen bonds in the *cis*-form, whereas weaker hydrogen bonds are present in the *trans*-peptides. Since these changes occur in a spectral region characteristic for  $\beta$ -sheets and  $\beta$ -hairpins<sup>1,2</sup>, the results for **5.5** and **5.6** indicate increased hairpin contents of the *cis*-peptides. The direct comparison of the differential spectra of **5.5** with **5.6** shows higher signal differences between both isomers in the former peptide. This agrees with the expected enhanced hydrophobic interactions in **5.5** and supports their role in hairpin stabilization. However, substitution of Tyr2 with valine in **5.6** abolishes the intrastrand stabilization between Tyr2 – Pro4, which was identified crucial for the correct folding pathway in native chignolin **5.1**. To rule out this effect and assess the contribution of the Tyr2 – Trp9 interaction to hairpin stabilization, a W9V-AzoChig peptide should be synthesized, since this mutant would retain hydrophobic contact between the C- and N-terminal strand, but simultaneously abolish the hydrophobic clustering as in **5.1**. Meanwhile, time-resolved IR spectra of

**5.5** and **5.6** will be conducted and will allow to i) monitor the folding and unfolding events on a picosecond timescale, ii) dissect the contribution of hydrogen bonds and hydrophobic interactions to the hairpin formation process and iii) deliver an experimental control for the established folding mechanisms of **5.1** and related peptides.

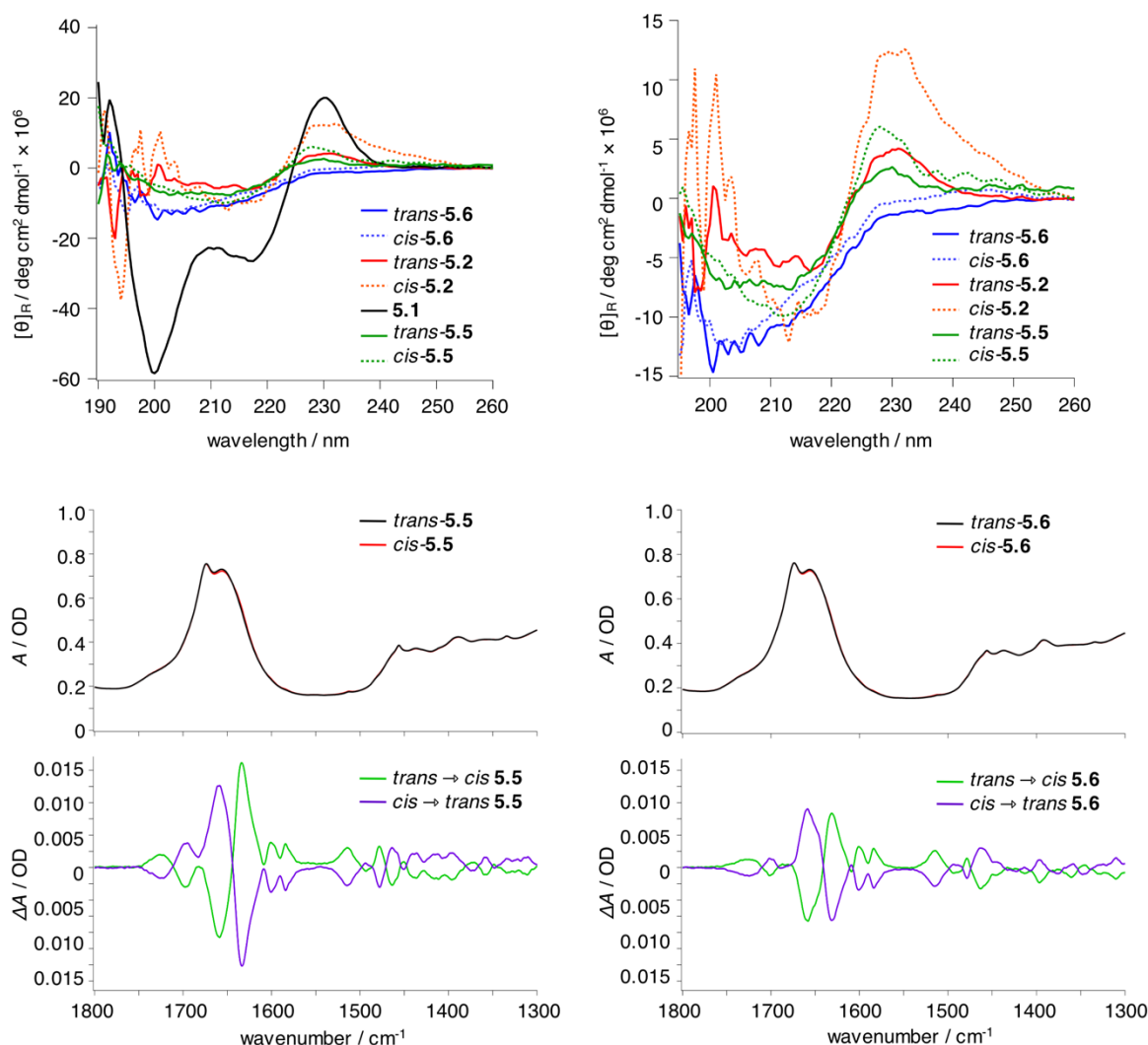


**Figure 5.3:** CD and IR spectra of Y2W-AzoChig 5.5 and Y2V-AzoChig 5.6. Top left: CD spectra of chignolin 5.1 and the *cis*-/*trans*-isomers of the AzoChignolin peptides 5.2, 5.5 and 5.6. Top right: zoom into CD spectra of *cis*-/*trans*-5.2, -5.5 and -5.6. CD spectra of 5.2, 5.5 and 5.6 were recorded in methanol at 5 °C. The CD spectrum of 5.1 was recorded at 5 °C in 20 mM PBS pH 5.5. Bottom left: on top are shown the FT IR spectra of *cis*-/*trans*-5.5 in deuterated methanol at 25 °C, on the bottom are shown the differential FT IR spectra of the folding (*trans* → *cis*) and unfolding (*cis* → *trans*) processes of 5.5. Bottom right: on top are shown the FT IR spectra of *cis*-/*trans*-5.6 in deuterated methanol at 25 °C, on the bottom are shown the differential FT IR spectra of the folding (*trans* → *cis*) and unfolding (*cis* → *trans*) processes of 5.6. The FT IR spectra shown here are not methanol and TFA corrected.

Moreover, we wanted to elucidate the role of Pro4 in the AzoChignolin peptides. In chignolin **5.1** the intra-strand Tyr2 – Pro4 interaction is crucial for locking the *N*-terminal strand in a native-like conformation and Pro4 bends the peptide backbone, directing Asp3 to the required position for the formation of a hydrogen bonding network. In the AzoChignolin peptides the AMPP **1.22** photoswitch generates a different turn, and thus we were curious about whether the Pro4 bend is still needed for hairpin formation. Therefore, the P4T-

AzoChig 5.7 peptide in which Pro4 is substituted by a threonine was synthesized. Threonine, offering an ideal *O*-glycosylation site, was chosen in respect of another project that focuses on the introduction of glycosylated amino acids into the AzoChignolin hairpin, to evaluate the effect of glycosylation patterns on hairpin folding. Alas, peptide 5.7 proved to be completely insoluble in water, acetonitrile and methanol, preventing any in-depth characterization by spectroscopic methods. Nevertheless, it is interesting that the bend and fixation of the N-terminal strand by Pro4 remains essential for the formation of the hairpin in AzoChignolin peptides, even though the central native turn sequence has been modified.

### 5.3.2 THE Y2AZOPHE-CHIG PEPTIDE

In the AzoChignolin peptides the photoswitch AMPP 1.22 substitutes the central amino acids Glu5 and Thr6. Although this was successfully used to photocontrol hairpin formation, the substitution of two amino acids and 20% sequence alteration still represents an invasive method. To maintain the original peptide sequence, we decided to develop a photochromic chignolin in which the photoswitch is located in the side-chain of the peptide. Therefore, the peptide Y2AzoPhe-Chig 5.8 comprising the photoswitchable amino acid AzoPhe 1.24 (AP2) as a substitute for Tyr2 was synthesized and evaluated (Fig. 5.4). In this compound the isomerization of the side-chain azobenzene moiety of AP2 was predicted to cause hairpin folding and unfolding through several possible factors, *i.e.* i) switching between a lengthy and rigid *trans*-form and a more compact *cis*-structure, ii) changes in the hydrophobic surface area between a weaker *cis*- and stronger *trans*-form and iii) alteration of the dipole moments.

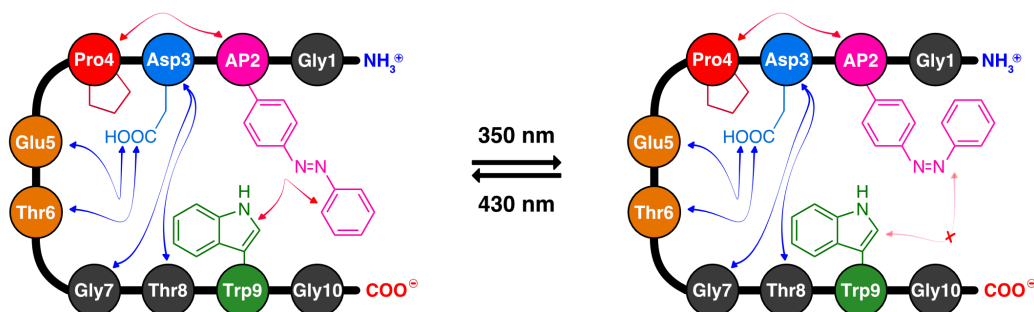


**Figure 5.4: Predicted interactions in Y2AzoPhe-Chig 5.8.** The different hydrophobic surface areas and structures of the *cis*-/*trans*-isomers of the AzoPhe2 (AP2) where predicted to induce structural rearrangements between the *cis*- and *trans*-5.8 peptide.

As consequence of retaining the native turn sequence with the polar residues Glu5 and Thr6 Y2AzoPhe-Chig 5.8 is soluble in aqueous media, a major prerequisite for folding experiments under physiological conditions. Although recent MD simulations of AzoChig1 5.2 show no severe differences between hairpin folding in aqueous or organic solvents, folding studies conducted in organic solvents are criticized for not being representative for folding processes in natural environments. Thus, the solubility in aqueous buffered solutions displays a great advantage of 5.8. The photophysical properties of 5.8 were as expected fast and robust, with switching kinetics of  $\tau_{trans \rightarrow cis} = 42.7 \pm 1.4$  s and  $\tau_{cis \rightarrow trans} = 52.7 \pm 2.0$  s (Figure 5.5). The AP2 photoswitch showed no signs of bleaching or degradation after several switching cycles and the *cis*-form

was bistable with an observed rate constant of the thermal *cis* → *trans* back-relaxation of  $k_{\text{obs}} = 2.99 \times 10^6$  au/min.

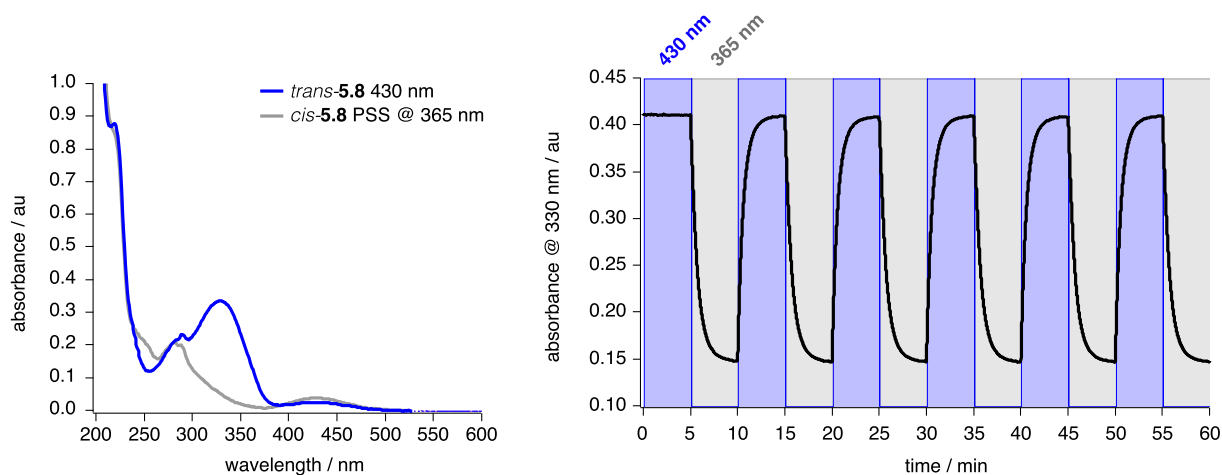


**Figure 5.5:** UV spectra and switching kinetics for *cis*-/*trans*-Y2AzoPhe-Chig **5.8**. Left: UV spectra of *cis*-/*trans*-**5.8** at 365 and 430 nm, respectively, 25 °C in PBS 20 mM pH 5.5. Right: switching kinetics of **5.8** for the *cis* → *trans* and *trans* → *cis* isomerization at 430 or 365 nm, respectively. Measured in PBS 20 mM pH 5.5 at 25 °C as absorbance change of the *trans*-**5.8** n- $\pi^*$  transition at 330 nm.

At first the *cis*-/*trans*-isomers of Y2AzoPhe-Chig **5.8** were structurally characterized by NMR spectroscopy, and the recorded  $^1\text{H}$ -NMR spectra of both isomers were compared to the spectrum of native chignolin **5.1** (Figure 5.6). Of special interest is the aromatic region, as it shows changes in the chemical induced shifts (CIS) of the backbone NHs that deliver informations of conformational alterations of the peptides (Table 5.1). Indeed, changes in the signals of the aromatic residues can be detected, e.g. of Tyr2 and Trp9 in **5.1** and AP2 and Trp9 in *cis*-/*trans*-**5.8**, respectively. Striking is the difference between the shifts of Trp9-NH $\epsilon$ 1 in **5.1** and *trans*-**5.8**, compared to the nearly 0.3 ppm upfield shifted signal in *cis*-**5.8**. This is probably due to a kinked conformation of the azobenzene that allows AP2 to envelope Trp9, which leads to an enforced shielding of Trp9 through AP2 in *cis*-**5.8** and the dehydration of the Trp9-NH $\epsilon$ 1 proton. Similar results were observed for temperature dependent structure relaxation experiments in hairpins with tryptophan and tyrosine zipper motifs<sup>272,273</sup>. The CIS values of the backbone NH proton signals between **5.1** and the *trans*-isomer of **5.8** vary for Asp3, Glu5, Thr6, Gly7 and Gly10, while they remain similar for *cis*-**5.8**. Particularly, the different CISs for the prevailing hydrogen bond hub Asp3 and the turn-related residues Glu5, Thr6 and Gly7 suggest structural changes upon *cis* ↔ *trans* isomerization of **5.8**. The latter three residues show prominent upfield shifted backbone NH signals, which presumably correlates to a higher solvent exposure and lower hairpin content in the *trans*-peptide<sup>274</sup>. The same trend can be observed for the CISs of H $\alpha$  protons of Pro4, Glu5, Thr6 and Gly7 in *trans*-**5.8**, which show upfield shifted signals compared to **5.1** and *cis*-**5.8** (Table 5.2). Again, this points to an unfolded structure or lower hairpin content in the *trans*-peptide, as residues involved in the turn formation usually exhibit downfield shifted H $\alpha$  proton signals in Type II turns<sup>275</sup>.

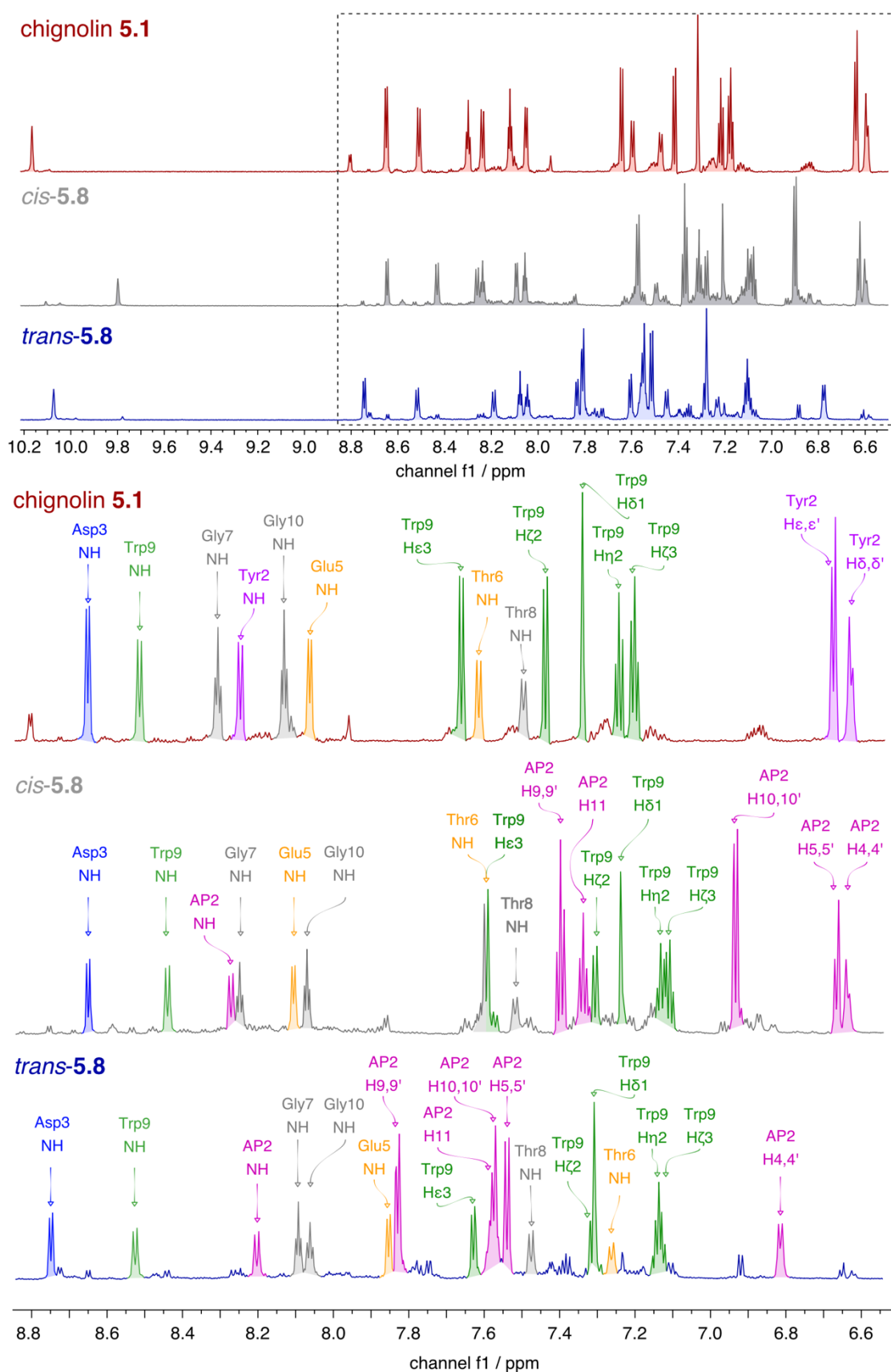


**Figure 5.6:** NMR spectra in the aromatic region of chignolin 5.1 and *cis*-/*trans*-Y2AzoPhe-Chig 5.8. Top: overview of the aromatic region in the <sup>1</sup>H-NMR spectra of peptides 5.1 and *cis*-/*trans*-5.8. Bottom: detailed view of the aromatic region between 8.8 – 6.6 ppm. NMR spectra were recorded at 25 °C with 3 mM concentrations in aqueous phosphate buffered solution (pH 5.5, 20 mM PBS) supplemented with 10% D<sub>2</sub>O and 4,4-dimethyl-4-silapentane-1-sulfonic acid (DSS) as internal standard.

**Table 5.1: <sup>1</sup>H NMR CIS values in the aromatic region of 5.1 and *cis/trans*-Y2AzoPhe-Chig 5.8.** Listing of CIS values for the <sup>1</sup>H NMR signals in the aromatic region of peptides 5.1 and *cis/trans*-5.8 with  $\Delta$ 5.1/*cis/trans*-5.8 for comparing the different signal shifts. ↑ Represents upfield and ↓ downfield shifts.

Residue	Proton	5.1 (ppm)	<i>cis</i> -5.8 (ppm)	$\Delta$ 5.1/ <i>cis</i> -5.8 (ppm)	<i>trans</i> -5.8 (ppm)	$\Delta$ 5.1/ <i>trans</i> -5.8 (ppm)
<b>Tyr2</b>	NH	8.24				
	H $\delta$ , $\delta'$	6.59				
	H $\epsilon$ , $\epsilon'$	6.64				
<b>AP2</b>	NH		8.26		8.19	
	H4,4'		6.60		6.78	
	H5,5'		6.63		7.51	
	H9,9'		7.37		7.81	
	H10,10'		6.90		7.55	
	H11		7.31		7.55	
<b>Asp3</b>	NH	8.65	8.64	↑ 0.01	8.74	↓ 0.09
<b>Glu5</b>	NH	8.05	8.09	↓ 0.04	7.83	<b>↑ 0.22</b>
<b>Thr6</b>	NH	7.59	7.57	↑ 0.02	7.23	<b>↑ 0.36</b>
<b>Gly7</b>	NH	8.30	8.24	↑ 0.06	8.08	<b>↑ 0.22</b>
<b>Thr8</b>	NH	7.47	7.50	↓ 0.03	7.45	↑ 0.02
<b>Trp9</b>	NH	8.51	8.43	↑ 0.08	8.52	↓ 0.01
	H $\delta$ 1	7.32	7.21	<b>↑ 0.11</b>	7.28	↑ 0.04
	H $\epsilon$ 3	7.64	7.57	↑ 0.07	7.60	↑ 0.04
	H $\zeta$ 2	7.41	7.28	<b>↑ 0.13</b>	7.28	<b>↑ 0.13</b>
	H $\zeta$ 3	7.17	7.08	↑ 0.09	7.10	↑ 0.07
	H $\eta$ 2	7.22	7.10	<b>↑ 0.12</b>	7.11	<b>↑ 0.11</b>
<b>Gly10</b>	NH	8.12	8.08	↑ 0.04	8.05	↑ 0.07

**Table 5.2: <sup>1</sup>H NMR CIS values of the H $\alpha$  protons of 5.1 and *cis/trans*-5.8.** Listing of CIS values for the <sup>1</sup>H NMR signals of the H $\alpha$  protons of peptides 5.1 and *cis/trans*-5.8 with  $\Delta$ 5.1/*cis/trans*-5.8 for comparing the different signal shifts. ↑ Represents upfield and ↓ downfield shifts, bold values mark changes  $\geq 0.10$  ppm.

H $\alpha$	5.1 (ppm)	<i>cis</i> -5.8 (ppm)	$\Delta$ 5.1/ <i>cis</i> -5.8 (ppm)	<i>trans</i> -5.8 (ppm)	$\Delta$ 5.1/ <i>trans</i> -5.8 (ppm)
<b>Gly1</b>	3.81	3.79	↑ 0.02	3.85	↓ 0.04
<b>Tyr2 / AP2</b>	4.93	4.90		4.90	
<b>Asp3</b>	4.26	4.31	↓ 0.05	4.37	<b>↓ 0.11</b>
<b>Pro4</b>	4.13	4.19	↓ 0.06	3.92	<b>↑ 0.21</b>
<b>Glu5</b>	4.24	4.25	↓ 0.01	4.13	<b>↑ 0.11</b>
<b>Thr6</b>	4.34	4.34	→ 0.00	4.26	↑ 0.03
<b>Gly7</b>	3.97, 3.84	3.96, 3.79	↑ 0.04	3.78, 3.57	<b>↑ 0.22</b>
<b>Thr8</b>	4.48	4.41	↑ 0.07	4.51	↓ 0.03
<b>Trp9</b>	4.76	4.74	↑ 0.02	4.80	↓ 0.04
<b>Gly10</b>	3.93, 3.88	3.89, 3.86	↑ 0.03	3.92, 3.88	↑ 0.01

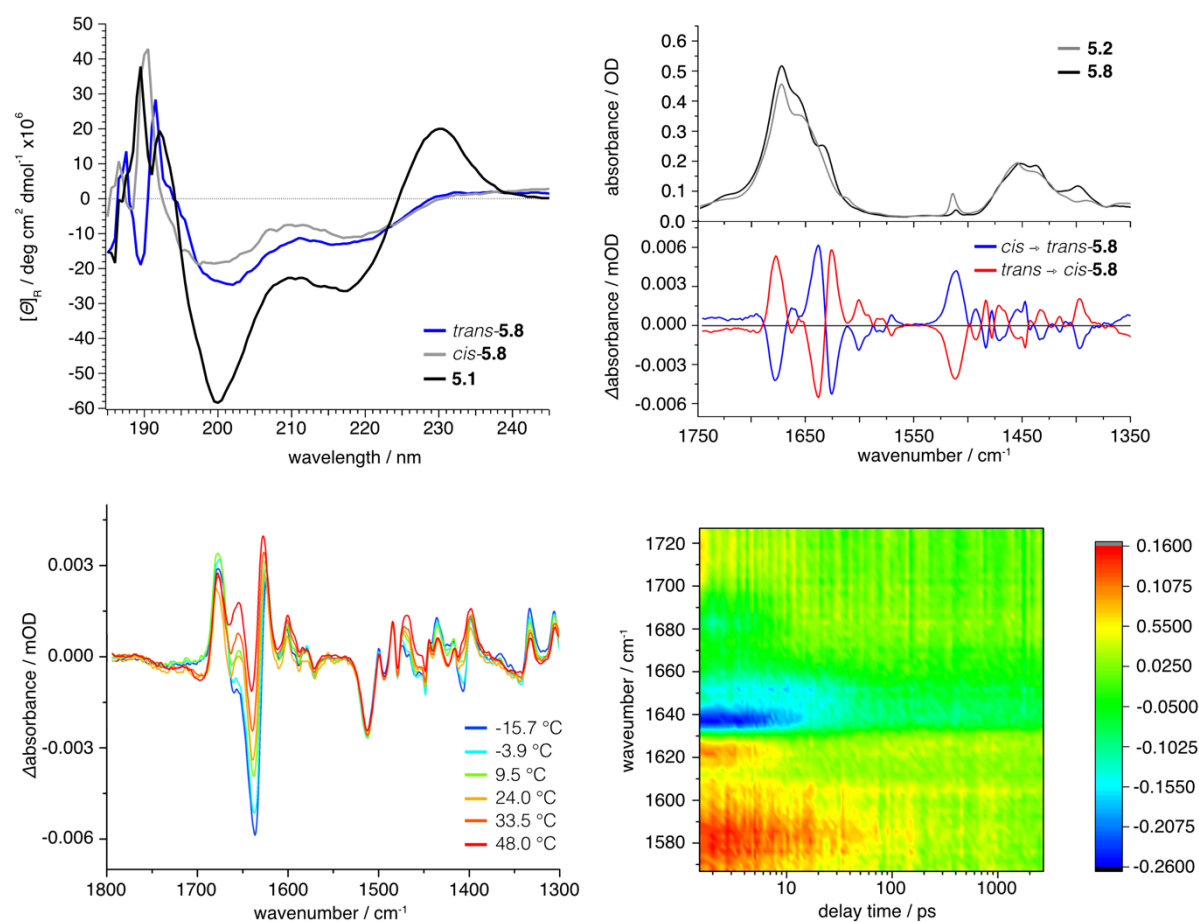


**Figure 5.7: CD and FT IR spectra of *cis*-/*trans*-Y2AzoPhe-Chig 5.8.** Top left: CD spectra of chignolin **5.1** and *cis*-/*trans*-**5.8** at 5 °C in 20 mM PBS pH 5.5. Top right: FT IR spectra of AzoChig1 **5.2** and **5.8** and differential FT IR spectra of the *trans* → *cis* and *cis* → *trans* isomerization of **5.8**. Bottom left: temperature dependent differential FT IR spectra of the *trans* → *cis* isomerization of **5.8**. Bottom right: ultra-fast FT IR spectrum of the *trans* → *cis* isomerization of **5.8**. All the FT IR spectra were recorded in deuterated methanol at 25 °C at approx. 5 mM concentrations.

Next, CD and FT IR spectroscopy were conducted to assess the secondary structure content of the *cis*-/*trans*-isomers of Y2AzoPhe-Chig **5.8** (Fig. 5.7). The CD spectra of both isomers show strong positive values below 200 nm, accompanied by two minima at 202 and 215 nm or 200 and 218 nm for the *trans*- and the *cis*-peptide, respectively. The positive band below 200 nm is more pronounced in the *cis*-isomer, which is very similar to chignolin **5.1**. Both minima in the CD spectrum of the *cis*-isomer are weaker, which would point to a diminished AP2 – Tyr2 interaction in this isomer. However, both CD spectra lack the prominent band at 230 nm, because the necessary stacking conformation between AP2 and Trp9 causing the prominent exciton coupling band is not possible. Due to the high similarity of the CD spectra between both isomers it is not possible to distinguish whether the desired peptide folding dynamics upon isomerization occur, or subsequent structural rearrangements of the AP2 moiety lead to the the observed changes. To detect alterations in the hydrogen bonding network upon formation of *cis*- or *trans*-**5.8**, differential spectra for the *trans* → *cis* and *cis* → *trans* isomerization were recorded, along with melting curves and ultra-fast time-resolved IR spectra of the former isomerization process (Fig. 5.7). Unfortunately, the differential spectra only show marginal shifts of the amide-I band, which are also close to the detection limit of 0.005 mOD. Furthermore, the melting curves for the *trans* → *cis* isomerization show bleaching of

bands in the amide-I region, rather than shifting what usually would be expected for a folding or unfolding process. Furthermore, the ultra-fast time-resolved IR spectra for the *trans* → *cis* isomerization show a very fast signal decay and rise in the amide-I band region at 1621 and 1639  $\text{cm}^{-1}$ , which is completed after 7 ps. Below 1600  $\text{cm}^{-1}$  the spectrum shows some slower processes, which are completed after 50 ps. Alas, the retrieved CD and FT IR data is not sufficient to enable a clear statement on the folding dynamics of the **5.8** peptide. However, the IR spectra suggest that sterical rearrangements of AP2 lead to small conformational shifts in the peptide structure, albeit insufficient to trigger further folding or unfolding processes.

## 5.4 SUMMARY AND OUTLOOK

In the recent decades, various small peptide model systems for the study of the structure and folding of protein secondary structure elements have been developed<sup>26,276</sup>. Chignolin **5.1**, an artificial decapeptide designed by statistical analysis of turn sequences in native proteins, was extensively studied as a model for the formation of  $\beta$ -hairpin segments<sup>258</sup>. Particularly, this structural element is believed to serve as a nucleation site for folding of proteins and thus a deeper understanding of the folding dynamics constitutes an important step in deciphering the mystery of protein folding and misfolding<sup>27,211</sup>. Although there is an abundant amount of experimental and theoretical data available, a general folding mechanism, if there is any, remains elusive. The three proposed mechanisms – the zipper, the hydrophobic collapse and the broken-zipper model – differ in the contribution of hydrogen bonds and hydrophobic interactions to the stabilization of the hairpin structure, and the succession of the single folding steps. Although the steadily rising computing power has enabled more sophisticated theoretical models, they still often lead to deviating observations when compared to experimental results. This shows the need for additional model peptide systems that act as experimental and theoretical playgrounds, and enable the convergence of both approaches.

To contribute to this task, we developed the AzoChignolin peptides AzoChig1 **5.2** and AzoChig2 **5.3**<sup>21</sup>. They are based on chignolin **5.1** and possess the photoswitch AMPP **1.22** as an optical responsive turn element, substituting the central turn residues Glu5 and Thr6 in the native chignolin **5.1**. The reversible *cis*  $\leftrightarrow$  *trans* isomerization of **1.22** enables the optical control over folding and unfolding of the  $\beta$ -hairpin structure of the AzoChignolin peptides, and thus represents a useful experimental tool to study folding dynamics with high temporal resolution. The desired folding and unfolding events upon azobenzene isomerization were initially demonstrated through NMR, CD and FT IR spectroscopy, and the focus now lies on in-depth studies of the intrinsic folding events. Therefore, ultra-fast FT IR spectroscopy and atomic resolution MD simulations are currently being conducted to provide a more precise picture of the contribution and succession of hydrophilic and hydrophobic interactions in the AzoChignolin peptides.

To further expand the AzoChignolin model system and to alter cross-strand hydrophobic interactions, the two variants Y2W-AzoChig **5.5** and Y2V-AzoChig **5.6** were synthesized in which the central hydrophobic interaction partner Tyr2 was substituted by tryptophan and valine. As expected, the CD spectra of **5.5** and **5.6** revealed hairpin folding and unfolding processes in the former peptide, which were abolished in the latter peptide. Likewise, the differential FT IR spectra monitored for both compounds show greater shifts in the amide-I band region for **5.5**, while **5.6** exhibited only minor changes. As with the original AzoChignolin peptides, ultra-fast FT IR spectroscopy and MD simulations are currently underway to elucidate the role of individual hydrophobic interactions in this hairpin system. However, it remains unclear whether the abolished hydrophobic stacking between Tyr2 and Trp9, or rather the lack of intrastrand hydrophobic contact between Tyr2 and Pro4 are responsible for the diminished hairpin contents in the valine modified peptide **5.6**. To clarify this, a new variant T9V-AzoChig will be synthesized and together with **5.5** and **5.6** it should deliver more insight into folding contributions of the hydrophobic interactions in this system.

A different approach was chosen for the Y2AzoPhe-Chig **5.8** peptide, where the photoswitch AzoPhe **1.24** was incorporated as a side-chain modification by substituting Tyr2. Thereby, the turn sequence remains unchanged, which facilitates native turn nucleation and folding instead of turn formation through azobenzene isomerization as in the former AzoChignolin peptides. Although **5.8** was envisioned to shift between a folded and unfolded state driven by structural changes in the side-chain azobenzene of the AP2 residue upon isomerization, no such transition was detected. The CD spectra of both *cis*-/*trans*-isomers are very similar, showing only slightly shifted and reduced extrema in the *cis*-form. The differential FT IR spectra show no significant changes in the amide-I band region, which would necessarily occur if there were noticeable changes in the hydrogen bond network upon AP2 isomerization, *i.e.* if folding or unfolding processes take place. Moreover, the ultra-fast FT IR spectra of the *trans* → *cis* isomerization of **5.8** show two time constants with 7 and 50 ps, respectively. These times are too fast for protein folding processes, which are typically on a timescale of several hundred nanoseconds or microseconds. On the contrary, the NMR spectra of *cis*-/*trans*-**5.8** show distinct chemical shift values for the H $\alpha$  and NH peptide backbone protons, with the signals of the *trans*-peptide exhibiting larger deviations to chignolin **5.1** than the those in the corresponding *cis*-isomer. Nevertheless, these results point to small sterical rearrangements of the peptide residues induced by the *cis* ↔ *trans* AP2 isomerization, rather than large conformational shifts of the whole hairpin. MD simulations that are currently being executed will hopefully help to shed light on the nature of these sterical effects.

## 5.5 EXPERIMENTAL

### 5.5.1 SPECTROSCOPIC AND SPECTROMETRIC DATA OF AZOCHIG1 5.1, AZOCHIG2 5.2 AND AZOCHIG3

#### 5.3

### 3 Analysis of peptides AzoChig1-3

#### 3.1 AzoChig1 peptide

The peptide **AzoChig1** was synthesized according to the previously stated peptide synthesis strategy. After global deprotection and cleavage from the resin and subsequent diethyl ether precipitation, the peptide was purified by RP-HPLC with a water/acetonitrile (80:10 → 40:60) gradient. The product was obtained upon lyophilisation with a water/acetonitrile (60:40) mixture. HR ESI-MS (positive), m/z: found 1103.4572  $[\text{C}_{54}\text{H}_{63}\text{O}_{14}\text{N}_{12}+\text{H}]^+$ , calc.: 1103.4508. HR ESI-MS (negative), m/z: found 1101.4420  $[\text{C}_{54}\text{H}_{61}\text{O}_{14}\text{N}_{12}-2\text{H}]^-$ , calc.: 1103.4508.

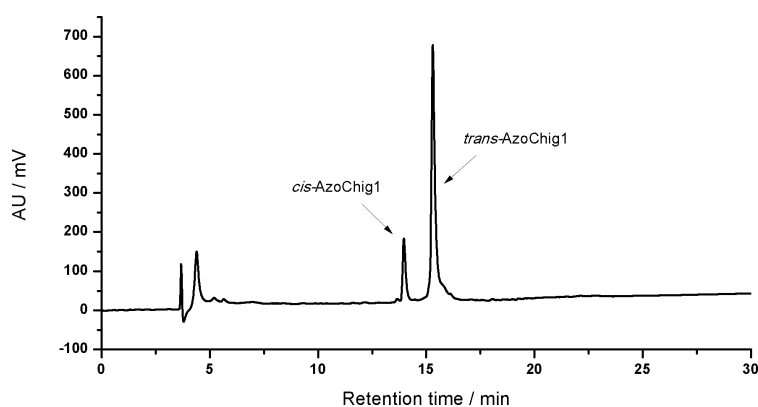


**Figure 1:** Analytical RP-HPLC spectrum of **AzoChig1** peptide. Retention time *cis* isomer = 13.9 min, *trans* isomer = 15.5 min.

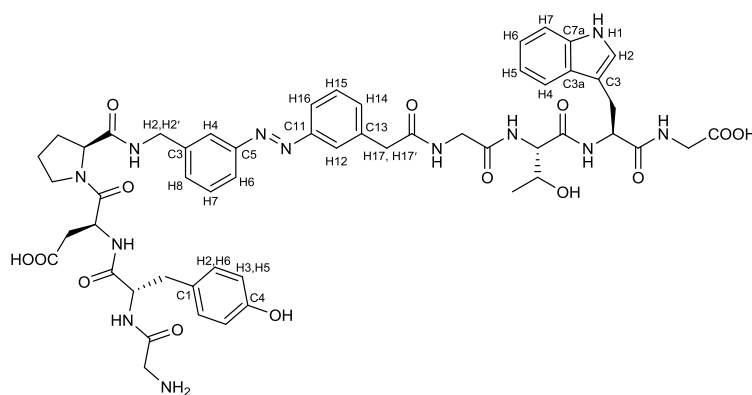


**Figure 2:** Numbering of certain H and C atoms in the **AzoChig1** peptide.

**Table 2:** <sup>1</sup>H- and <sup>13</sup>C-NMR chemical shifts of *trans*-AzoChig1 peptide. All NMR spectra were recorded in CD<sub>3</sub>OD, thus no NH and OH signals were recorded.

<i>trans</i> AzoChig1	H [ppm]	m	J [Hz]	C [ppm]	<i>trans</i> AzoChig1	H [ppm]	m	J [Hz]	C [ppm]
G01/NH2	-	-	-	-	AMPP56/C11	-	-	-	154.1
G01/H $\alpha$ ,H $\alpha'$	3.63	dd	16.0, 5.0	41.4	AMPP56/H12	7.96	s	-	125.1
G01/CO	-	-	-	167.7	AMPP56/C13	-	-	-	138.0
Y02/NH	-	-	-	-	AMPP56/H14	7.46	d	7.8	133.2
Y02/H $\alpha$	4.65	t	7.5	56.2	AMPP56/H15	7.47	t	7.8	133.4
Y02/H $\beta$ ,H $\beta'$	2.98, 2.83	dd	13.9, 7.9	38.3	AMPP56/H16	7.79	d	7.8	122.2
Y02/C1	-	-	-	128.3	AMPP56/H17,H17'	3.73	s	-	43.2
Y02/H2,H6	7.01	d	8.3	131.4	AMPP56/CO	-	-	-	174.4
Y02/H3,H5	6.68	d	8.3	116.2	G07/NH	-	-	-	-
Y02/C4	-	-	-	157.5	G07/H $\alpha$ ,H $\alpha'$	3.85	dd	16.5, 10.4	44.0
Y02/OH	-	-	-	-	G07/CO	-	-	-	172.1
Y02/CO	-	-	-	172.8	T08/NH	-	-	-	-
D03/NH	-	-	-	-	T08/H $\alpha$	4.29	d	4.1	60.2
D03/H $\alpha$	4.93	dd	8.7, 5.5	49.1	T08/H $\beta$	4.08	dq	6.2, 5.3	68.2
D03/H $\beta$ ,H $\beta'$	3.01, 2.61	dd	17.3, 4.7	37.0	T08/H $\gamma$	1.05	d	6.5	19.9
D03/COOH	-	-	-	174.9	T08/OH	-	-	-	-
D03/CO	-	-	-	171.6	T08/CO	-	-	-	172.3
P04/N	-	-	-	-	W09/NH	-	-	-	-
P04/H $\alpha$	4.46	dd	8.9, 3.5	62.2	W09/H $\alpha$	4.70	dd	8.0, 5.5	55.6
P04/H $\beta$ ,H $\beta'$	2.20, 2.07	d	8.3	30.8	W09/H $\beta$ ,H $\beta'$	3.32, 3.13	m	-	28.6
P04/H $\gamma$ ,H $\gamma'$	1.97	bs	-	25.4	W09/NH	-	-	-	-
P04/H $\delta$ ,H $\delta'$	3.75, 3.60	m	-	48.6	W09/H2	7.13	s	-	124.8
P04/CO	-	-	-	174.2	W09/C3	-	-	-	110.9
AMPP56/NH	8.31	t	6.1	-	W09/C3a	-	-	-	128.8
AMPP56/H2,H2'	4.52, 4.41	d	15.5	43.5	W09/H4	7.29	d	8.4	112.3
AMPP56/C3	-	-	-	141.3	W09/H5	7.00	t	7.9	119.8
AMPP56/H4	7.78	s	-	121.6	W09/H6	7.06	t	7.9	122.4
AMPP56/C5	-	-	-	154.2	W09/H7	7.56	d	7.9	119.3
AMPP56/H6	7.76	d	7.8	123.2	W09/C7a	-	-	-	137.9
AMPP56/H7	7.47	t	7.8	130.5	W09/CO	-	-	-	174.3
AMPP56/H8	7.40	d	7.4	131.0	G10/NH	-	-	-	-
AMPP56/N9	-	-	-	-	G10/H $\alpha$ ,H $\alpha'$	3.92	d	16.5	41.9
AMPP56/N10	-	-	-	-	G10/COOH	-	-	-	171.7

**Table 3:** <sup>1</sup>H- and <sup>13</sup>C-NMR chemical shifts of *cis*-AzoChig1 peptide. All NMR spectra were recorded in CD<sub>3</sub>OD, thus no NH and OH signals were recorded.

<i>cis</i> AzoChig1	H [ppm]	m	J [Hz]	C [ppm]	<i>cis</i> AzoChig1	H [ppm]	m	J [Hz]	C [ppm]
G01/NH2	-	-	-	-	AMPP56/C11	-	-	-	154.8
G01/H $\alpha$ ,H $\alpha'$	3.61	dd	16.0, 5.0	41.4	AMPP56/H12	6.69	s	-	121.6
G01/CO	-	-	-	167.0	AMPP56/C13	-	-	-	137.6
Y02/NH	-	-	-	-	AMPP56/H14	6.88	d	7.8	121.1
Y02/H $\alpha$	4.62	m	7.5	56.3	AMPP56/H15	7.27	t	7.8	130.2
Y02/H $\beta$ ,H $\beta'$	2.88, 2.74	dd	13.6, 8.1	38.3	AMPP56/H16	7.14	m	-	130.0
Y02/C1	-	-	-	128.2	AMPP56/H17,H17'	3.47	s	-	43.1
Y02/H2,H6	6.90	d	8.3	131.3	AMPP56/CO	-	-	-	174.3
Y02/H3,H5	6.62	d	8.3	116.1	G07/NH	-	-	-	-
Y02/C4	-	-	-	157.4	G07/H $\alpha$ ,H $\alpha'$	3.90	dd	16.5, 10.4	44.0
Y02/OH	-	-	-	-	G07/CO	-	-	-	172.1
Y02/CO	-	-	-	172.5	T08/NH	-	-	-	-
D03/NH	-	-	-	-	T08/H $\alpha$	4.39	d	4.4	60.0
D03/H $\alpha$	4.97	m	-	48.5	T08/H $\beta$	4.09	m	-	68.5
D03/H $\beta$ ,H $\beta'$	2.92, 2.60	dd	17.3, 4.7	37.1	T08/H $\gamma$	1.10	d	6.5	19.9
D03/COOH	-	-	-	174.6	T08/OH	-	-	-	-
D03/CO	-	-	-	171.3	T08/CO	-	-	-	172.1
P04/N	-	-	-	-	W09/NH	-	-	-	-
P04/H $\alpha$	4.33	dd	8.9, 3.5	62.0	W09/H $\alpha$	4.80	dd	8.0, 5.5	55.5
P04/H $\beta$ ,H $\beta'$	2.19, 2.07	m	-	30.8	W09/H $\beta$ ,H $\beta'$	3.35, 3.15	m	-	28.8
P04/H $\gamma$ ,H $\gamma'$	1.93	m	-	25.4	W09/NH	-	-	-	-
P04/H $\delta$ ,H $\delta'$	3.71, 3.54	m	-	48.6	W09/H2	7.13	m	-	124.8
P04/CO	-	-	-	174.1	W09/C3	-	-	-	111.0
AMPP56/NH	-	-	-	-	W09/C3a	-	-	-	128.8
AMPP56/H2,H2'	4.24, 4.20	d	15.5	43.5	W09/H4	7.27	d	8.4	112.3
AMPP56/C3	-	-	-	141.0	W09/H5	6.98	m	-	119.8
AMPP56/H4	6.80	s	-	120.7	W09/H6	7.06	m	-	122.3
AMPP56/C5	-	-	-	155.1	W09/H7	7.57	m	-	119.3
AMPP56/H6	6.59	d	7.8	119.6	W09/C7a	-	-	-	137.7
AMPP56/H7	7.13	m	-	124.7	W09/CO	-	-	-	174.3
AMPP56/H8	7.06	m	-	127.6	G10/NH	-	-	-	-
AMPP56/N9	-	-	-	-	G10/H $\alpha$ ,H $\alpha'$	3.94	d	16.5	42.0
AMPP56/N10	-	-	-	-	G10/COOH	-	-	-	172.9

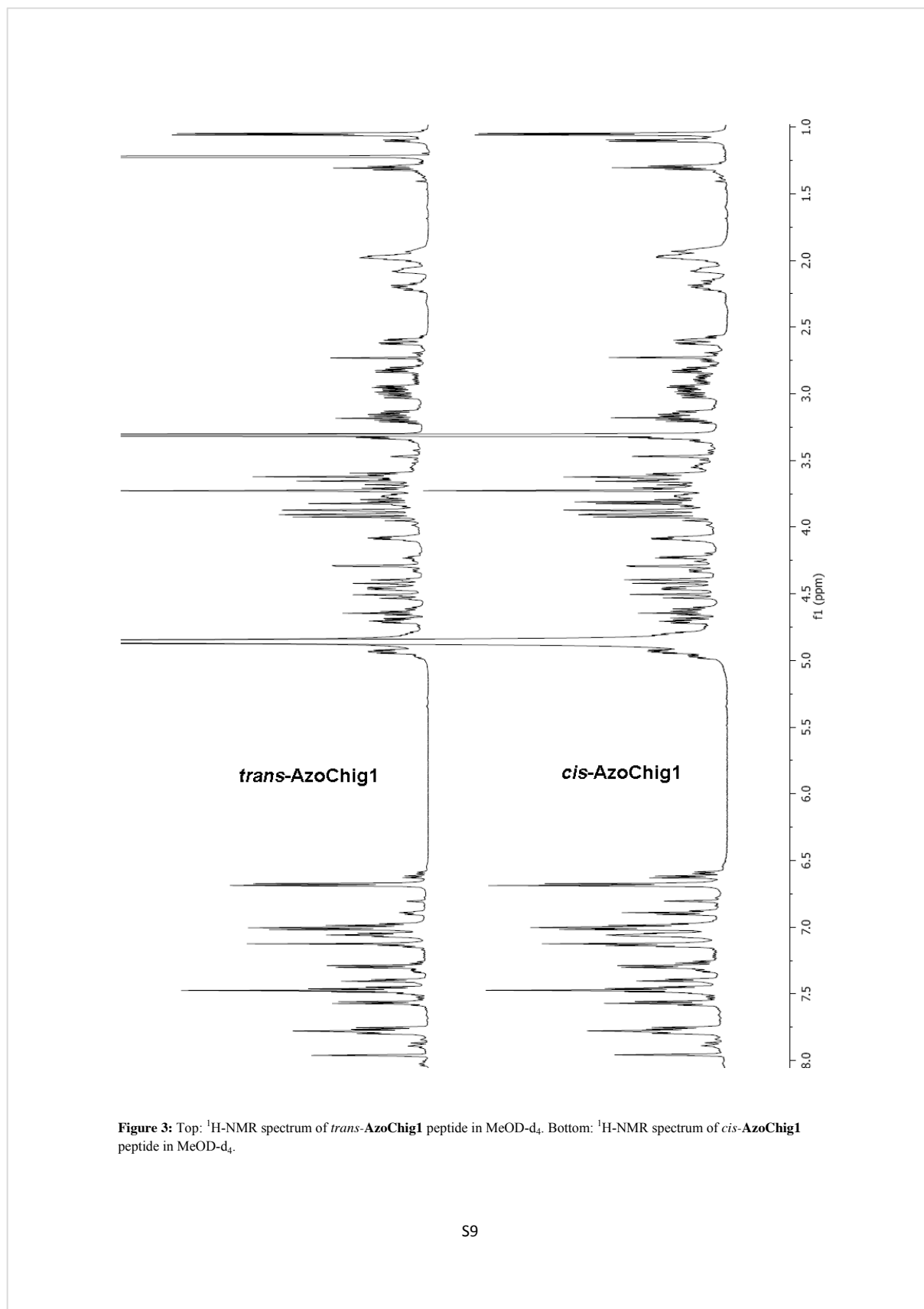


**Figure 3:** Top: <sup>1</sup>H-NMR spectrum of *trans*-AzoChig1 peptide in MeOD-d<sub>4</sub>. Bottom: <sup>1</sup>H-NMR spectrum of *cis*-AzoChig1 peptide in MeOD-d<sub>4</sub>.

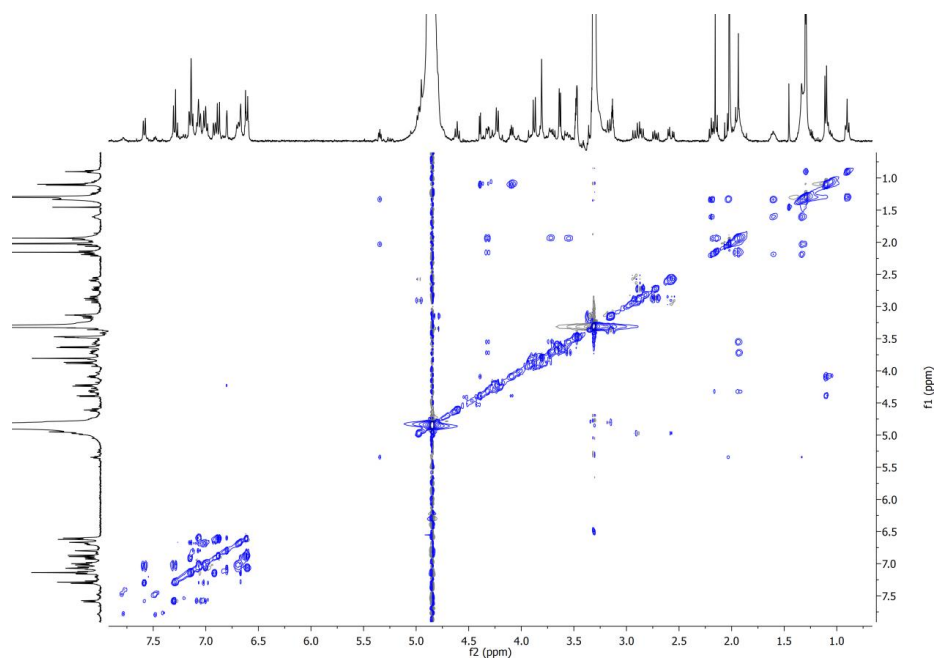


**Figure 4:**  $^1\text{H}$ ,  $^1\text{H}$ -TOCSY NMR spectrum of *cis*-AzoChig1 peptide in MeOD- $d_4$ ,  $c = 2$  mM.

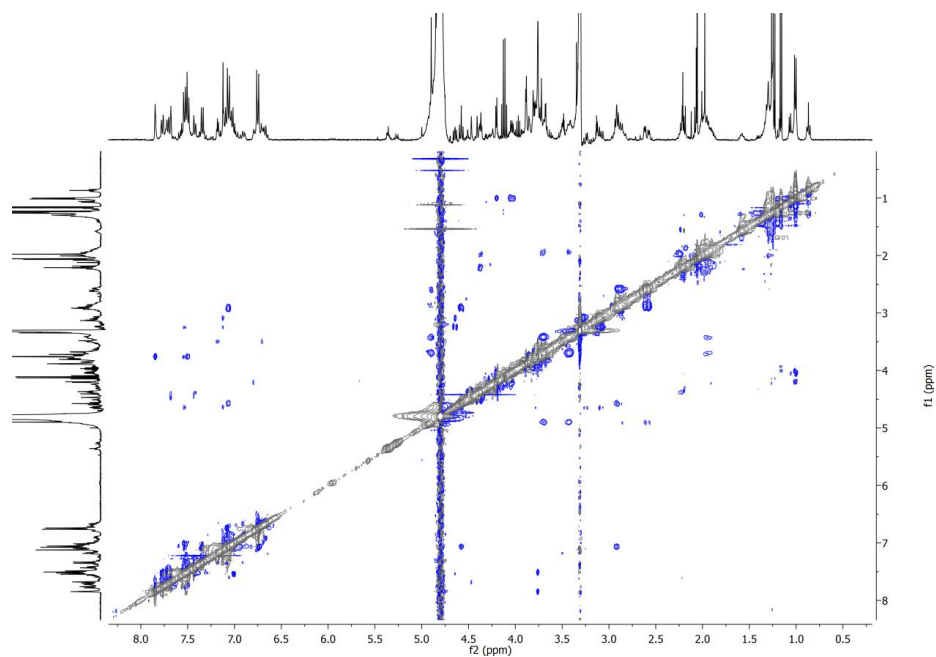


**Figure 5:**  $^1\text{H}$ ,  $^1\text{H}$ -ROESY NMR spectrum of *trans*-AzoChig1 peptide in MeOD- $d_4$ ,  $c = 2$  mM.

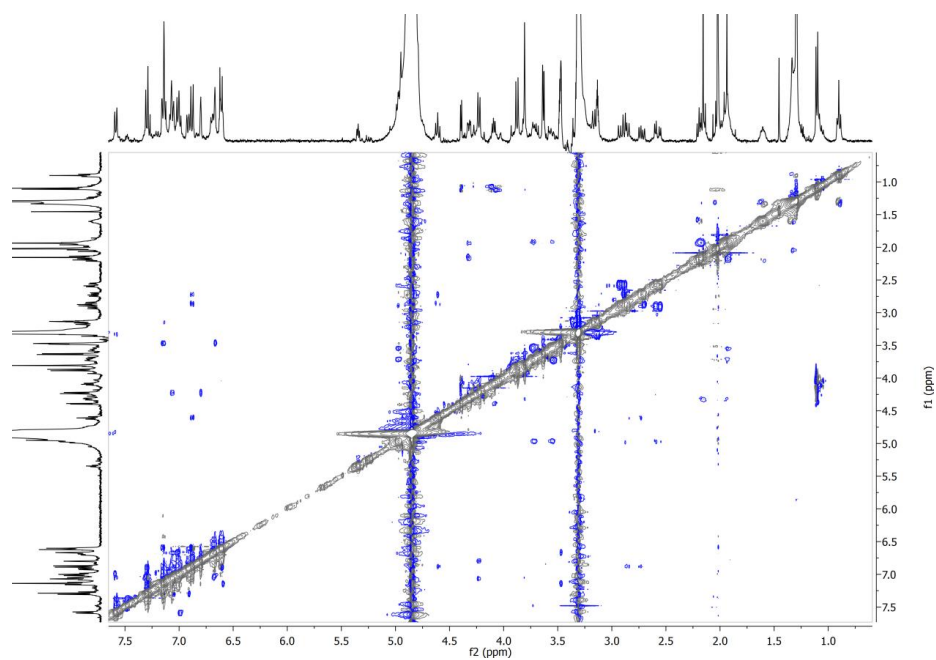


**Figure 6:**  $^1\text{H}$ ,  $^1\text{H}$ -ROESY NMR spectrum of *cis*-AzoChig1 peptide in MeOD- $d_4$ ,  $c = 2$  mM.

### 3.2 AzoChig2 peptide

The peptide **AzoChig2** was synthesized according to the previously stated peptide synthesis strategy. After global deprotection and cleavage from the resin and subsequent diethyl ether precipitation, the peptide was purified by RP-HPLC with a water/acetonitrile (80:10 → 40:60) gradient. The product was obtained upon lyophilisation with a water/acetonitrile (60:40) mixture. HR ESI-MS (positive),  $m/z$ : found 1227.4891  $[\text{C}_{54}\text{H}_{61}\text{FO}_{14}\text{N}_{12}+\text{iPrOH}+2\text{Na}+\text{H}]^{1+}$ , calc.: 1227.4858. HR ESI-MS (negative),  $m/z$ : found 1225.4738  $[\text{C}_{54}\text{H}_{60}\text{FO}_{14}\text{N}_{12}+\text{iPrOH}+2\text{Na}-\text{H}]^{1-}$ , calc.: 1225.4712.

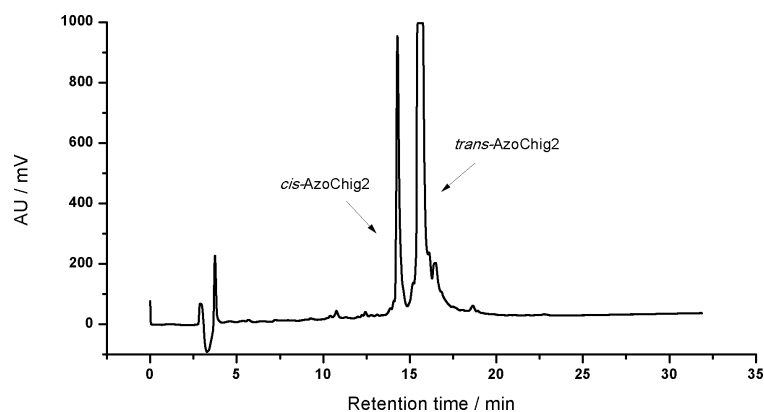


**Figure 7:** Analytical RP-HPLC spectrum of **AzoChig2** peptide. Retention time *cis* isomer = 14.3 min, *trans* isomer = 15.6 min.

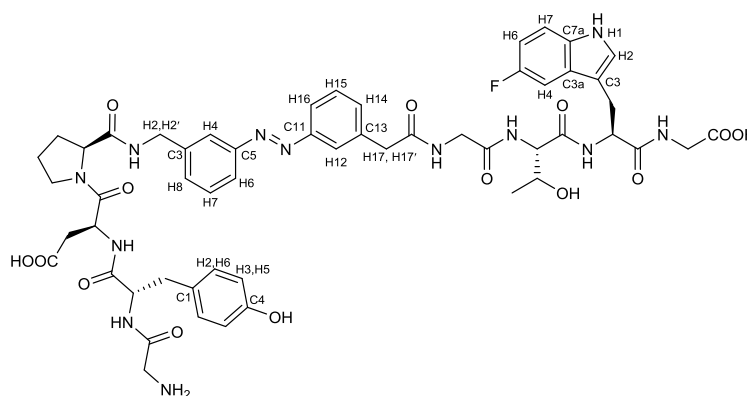


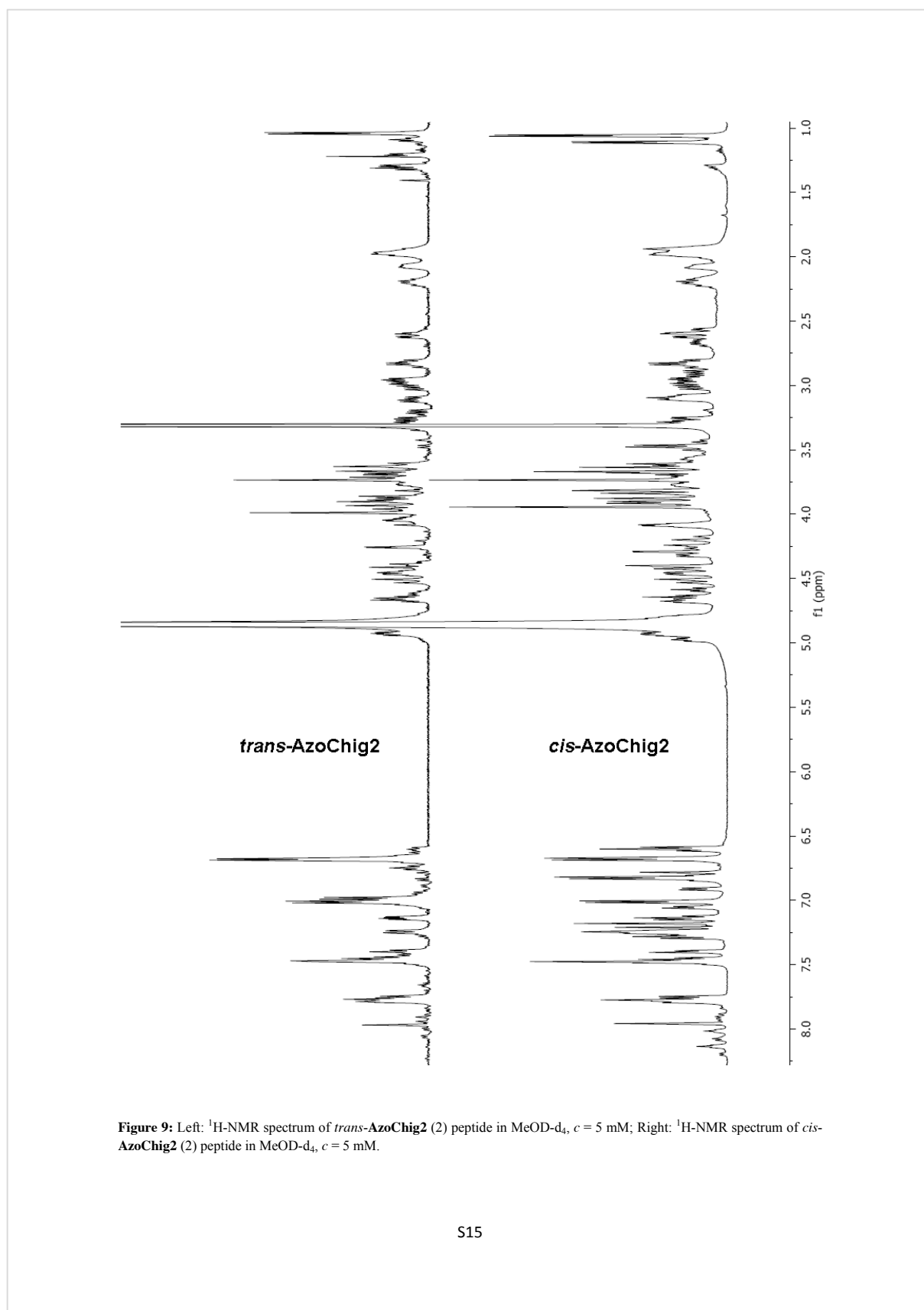
**Figure 8:** Numbering of certain H and C atoms in **AzoChig2** peptide.

**Table 4:** <sup>1</sup>H- and <sup>13</sup>C-NMR chemical shifts of *trans*-AzoChig2 peptide. All NMR spectra were recorded in CD<sub>3</sub>OD, thus no NH and OH signals were recorded.

<i>trans</i> AzoChig2	H [ppm]	m	J [Hz]	C [ppm]	<i>trans</i> AzoChig2	H [ppm]	m	J [Hz]	C [ppm]
G01/NH2	-	-	-	-	AMPP56/C11	-	-	-	154.1
G01/H $\alpha$ ,H $\alpha'$	3.65	dd	21.3, 16.5	41.4	AMPP56/H12	7.97	s	-	125.1
G01/CO	-	-	-	167.1	AMPP56/C13	-	-	-	138.0
Y02/NH	-	-	-	-	AMPP56/H14	7.46	d	7.8	131.0
Y02/H $\alpha$	4.63	t	7.5	56.2	AMPP56/H15	7.47	t	7.8	133.2
Y02/H $\beta$ ,H $\beta'$	2.97, 2.83	dd	13.5, 7.7	38.3	AMPP56/H16	7.77	d	8.0	122.3
Y02/C1	-	-	-	128.3	AMPP56/H17,H17'	3.74	s	-	43.2
Y02/H2,H6	7.01	d	8.3	131.4	AMPP56/CO	-	-	-	174.4
Y02/H3,H5	6.68	d	8.3	116.3	G07/NH	-	-	-	-
Y02/C4	-	-	-	157.5	G07/H $\alpha$ ,H $\alpha'$	3.89	dd	18.3, 16.0	44.1
Y02/OH	-	-	-	-	G07/CO	-	-	-	172.1
Y02/CO	-	-	-	172.8	T08/NH	-	-	-	-
D03/NH	-	-	-	-	T08/H $\alpha$	4.26	d	4.1	60.2
D03/H $\alpha$	4.93	dd	8.7, 5.5	48.7	T08/H $\beta$	4.04	m	-	68.2
D03/H $\beta$ ,H $\beta'$	3.01, 2.61	dd	17.3, 4.7	37.0	T08/H $\gamma$	1.04	d	6.3	19.9
D03/COOH	-	-	-	174.9	T08/OH	-	-	-	-
D03/CO	-	-	-	171.6	T08/CO	-	-	-	172.3
P04/N	-	-	-	-	W09/NH	-	-	-	-
P04/H $\alpha$	4.46	dd	8.9, 3.5	62.2	W09/H $\alpha$	4.65	t	7.3	56.2
P04/H $\beta$ ,H $\beta'$	2.20, 2.07	d	8.3	30.8	W09/H $\beta$ ,H $\beta'$	3.27, 3.11	dd	14.6, 7.7	28.0
P04/H $\gamma$ ,H $\gamma'$	1.97	bs	-	25.4	W09/NH	-	-	-	-
P04/H $\delta$ ,H $\delta'$	3.75, 3.60	m	-	48.6	W09/H2	7.18	s	-	125.0
P04/CO	-	-	-	174.2	W09/C3	-	-	-	107.7
AMPP56/NH	-	-	-	-	W09/C3a	-	-	-	130.3
AMPP56/H2,H2'	4.52, 4.41	d	15.5	43.5	W09/H4	7.24	dd	10.0, 2.1	103.7
AMPP56/C3	-	-	-	141.3	W09/C5	-	-	-	157.7
AMPP56/H4	7.75	s	-	121.6	W09/H6	6.75	dt	8.7, 1.8	109.5
AMPP56/C5	-	-	-	154.2	W09/H7	7.14	dd	8.5, 4.2	112.3
AMPP56/H6	7.73	d	8.0	123.2	W09/C7a	-	-	-	134.2
AMPP56/H7	7.47	t	7.8	133.2	W09/CO	-	-	-	174.2
AMPP56/H8	7.39	d	7.4	130.6	G10/NH	-	-	-	-
AMPP56/N9	-	-	-	-	G10/H $\alpha$ ,H $\alpha'$	3.92	dd	25.0, 18.0	41.9
AMPP56/N10	-	-	-	-	G10/COOH	-	-	-	172.1

**Table 5:** <sup>1</sup>H- and <sup>13</sup>C-NMR chemical shifts of *cis*-AzoChig2 peptide. All NMR spectra were recorded in CD<sub>3</sub>OD, thus no NH and OH signals were recorded.

<i>cis</i> AzoChig2	H [ppm]	m	J [Hz]	C [ppm]	<i>cis</i> -AzoChig2	H [ppm]	m	J [Hz]	C [ppm]
G01/NH2	-	-	-	-	AMPP56/C11	-	-	-	154.8
G01/H $\alpha$ ,H $\alpha'$	3.65	dd	21.3, 16.5	41.4	AMPP56/H12	6.69	s	-	121.4
G01/CO	-	-	-	167.1	AMPP56/C13	-	-	-	137.6
Y02/NH	-	-	-	-	AMPP56/H14	7.14	d	7.8	129.8
Y02/H $\alpha$	4.64	t	7.5	56.2	AMPP56/H15	7.28	t	8.1	130.3
Y02/H $\beta$ ,H $\beta'$	2.98, 2.83	m	-	38.3	AMPP56/H16	6.91	d	7.8	121.2
Y02/C1	-	-	-	128.3	AMPP56/H17,H17'	3.47	dd	15.2, 8.3	43.1
Y02/H2,H6	6.83	d	8.3	131.4	AMPP56/CO	-	-	-	173.9
Y02/H3,H5	6.59	d	8.3	116.1	G07/NH	-	-	-	-
Y02/C4	-	-	-	157.4	G07/H $\alpha$ ,H $\alpha'$	3.86	dd	18.3, 16.0	44.2
Y02/OH	-	-	-	-	G07/CO	-	-	-	172.1
Y02/CO	-	-	-	172.5	T08/NH	-	-	-	-
D03/NH	-	-	-	-	T08/H $\alpha$	4.41	d	4.1	59.9
D03/H $\alpha$	4.98	m	8.7, 5.5	48.5	T08/H $\beta$	4.09	m	-	68.5
D03/H $\beta$ ,H $\beta'$	2.91, 2.58	dd	17.3, 4.7	37.1	T08/H $\gamma$	1.11	d	6.3	19.8
D03/COOH	-	-	-	174.6	T08/OH	-	-	-	-
D03/CO	-	-	-	171.2	T08/CO	-	-	-	172.0
P04/N	-	-	-	-	W09/NH	-	-	-	-
P04/H $\alpha$	4.46	dd	8.9, 3.5	62.0	W09/H $\alpha$	4.59	t	7.5	56.2
P04/H $\beta$ ,H $\beta'$	2.20, 2.07	d	8.3	30.8	W09/H $\beta$ ,H $\beta'$	3.27, 3.11	dd	14.6, 7.7	28.1
P04/H $\gamma$ ,H $\gamma'$	1.97	bs	-	25.5	W09/NH	-	-	-	-
P04/H $\delta$ ,H $\delta'$	3.75, 3.60	m	-	48.6	W09/H2	7.21	s	-	125.0
P04/CO	-	-	-	174.2	W09/C3	-	-	-	111.3
AMPP56/NH	-	-	-	-	W09/C3a	-	-	-	129.1
AMPP56/H2,H2'	4.26, 4.19	d	15.5	43.5	W09/H4	7.27	m	-	104.1
AMPP56/C3	-	-	-	141.0	W09/C5	-	-	-	159.7
AMPP56/H4	6.78	s	7.8	120.7	W09/H6	6.83	m	-	110.5
AMPP56/C5	-	-	-	155.1	W09/H7	7.24	m	-	113.0
AMPP56/H6	6.61	d	8.0	119.8	W09/C7a	-	-	-	134.5
AMPP56/H7	7.13	t	8.5	129.8	W09/CO	-	-	-	172.5
AMPP56/H8	7.05	d	7.8	127.6	G10/NH	-	-	-	-
AMPP56/N9	-	-	-	-	G10/H $\alpha$ ,H $\alpha'$	3.92	dd	25.0, 18.0	41.9
AMPP56/N10	-	-	-	-	G10/COOH	-	-	-	172.1



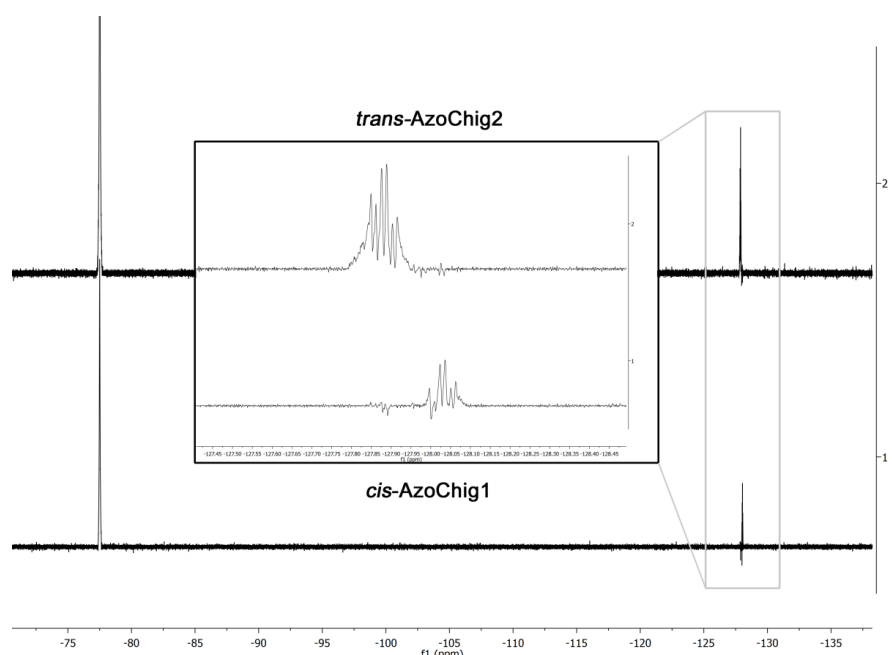


**Figure 10:** Top:  $^{19}\text{F}$ -NMR spectrum of *trans*-AzoChig2 (2) peptide in  $\text{MeOD-d}_4$ ,  $c = 2 \text{ mM}$ ; Bottom:  $^{19}\text{F}$ -NMR spectrum of *cis*-AzoChig2 (1) peptide in  $\text{MeOD-d}_4$ ,  $c = 5 \text{ mM}$ . Peak at -76 ppm originates from trifluoroacetic acid.

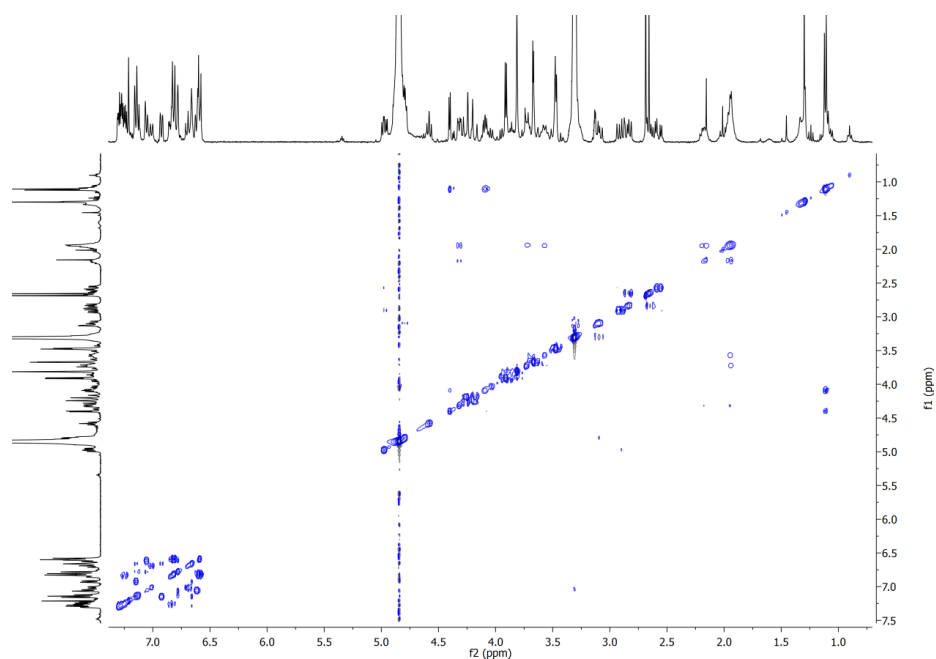


**Figure 11:**  $^1\text{H}$ ,  $^1\text{H}$ -TOCSY NMR spectrum of *cis*-AzoChig2 peptide in  $\text{MeOD-d}_4$ ,  $c = 2 \text{ mM}$ .

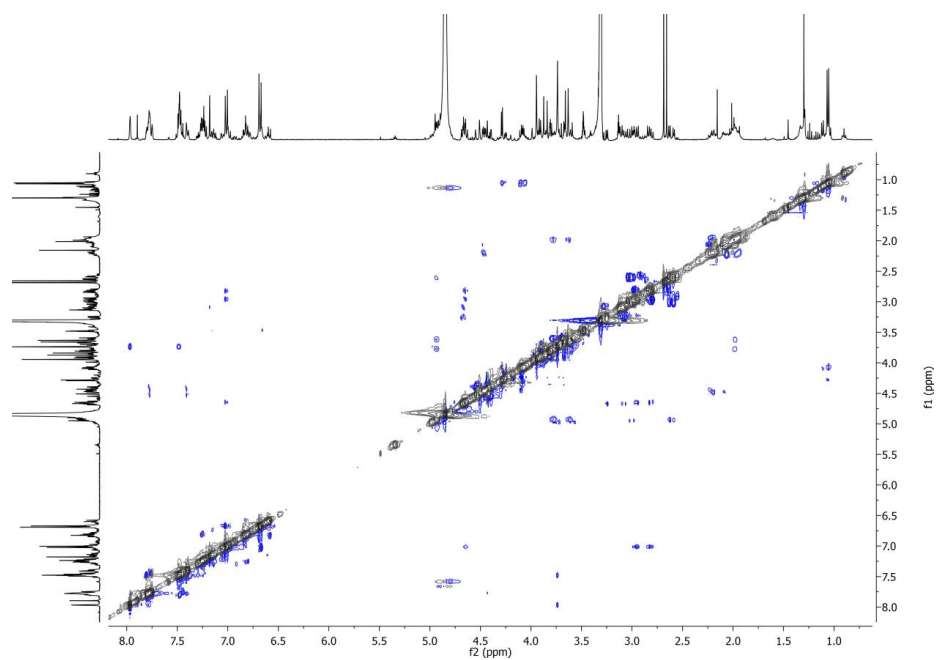


**Figure 12:**  $^1\text{H}$ ,  $^1\text{H}$ -ROESY NMR spectrum of *trans*-AzoChig2 peptide in MeOD- $d_4$ ,  $c = 2$  mM.

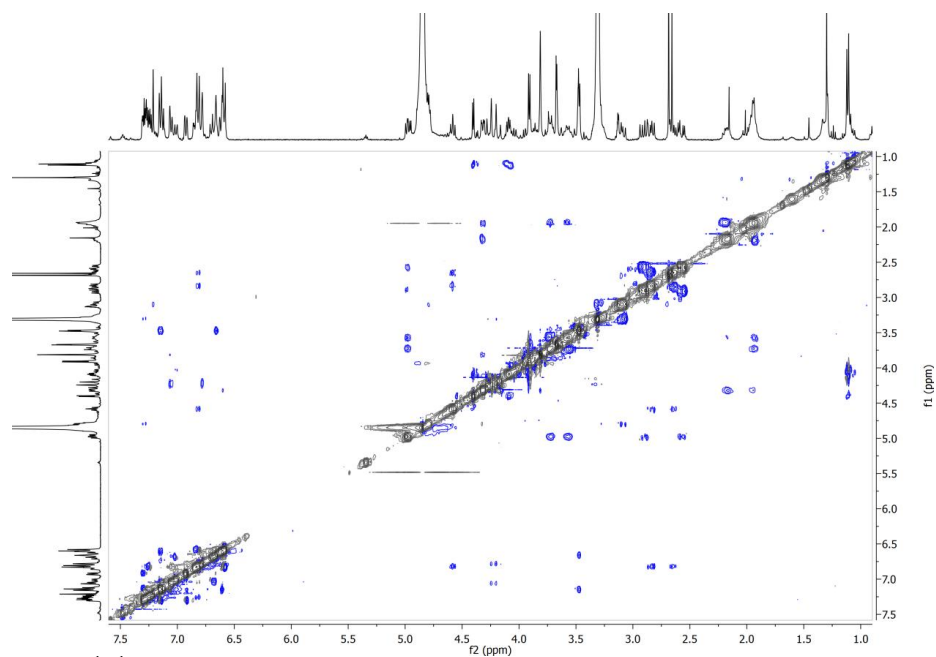


**Figure 13:**  $^1\text{H}$ ,  $^1\text{H}$ -ROESY NMR spectrum of *cis*-AzoChig2 peptide in MeOD- $d_4$ ,  $c = 2$  mM.

### 3.3 AzoChig3 peptide

The peptide **AzoChig3** was synthesized according to the previously stated peptide synthesis strategy. After global deprotection and cleavage from the resin and diethyl ether precipitation, the peptide was purified by RP-HPLC with a water/acetonitrile (80:10 → 40:60) gradient. The product was obtained upon lyophilisation with a water/acetonitrile (60:40) mixture. HR ESI-MS (positive), m/z: found 1306.5706 [ $C_{63}H_{80}O_{18}N_{13}+H$ ]<sup>+</sup>, calc.: 1306.5739. The signals of the recorded NMR spectra of the *cis/trans*-**AzoChig3** could not be assigned due to excessive signal broadening.

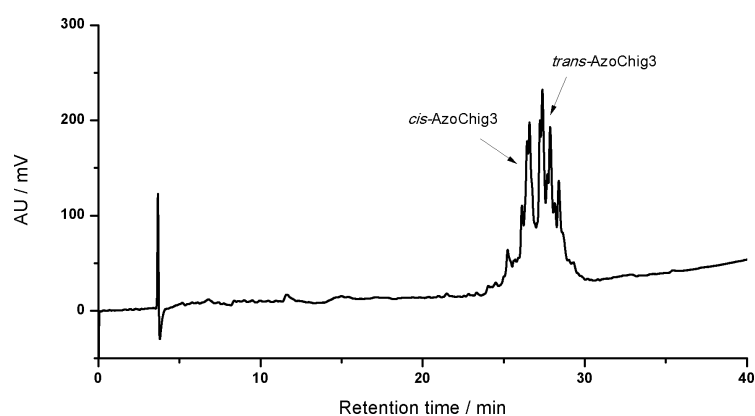


**Figure 14:** Analytical RP-HPLC spectrum of **AzoChig3** peptide. Retention time *cis* isomer = 27.4 min, *trans* isomer = 27.9 min.

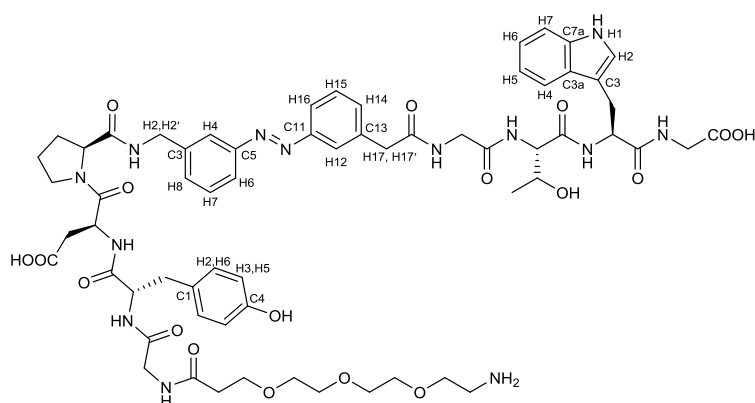


**Figure 15:** Numbering of certain H and C atoms in **AzoChig3** peptide.

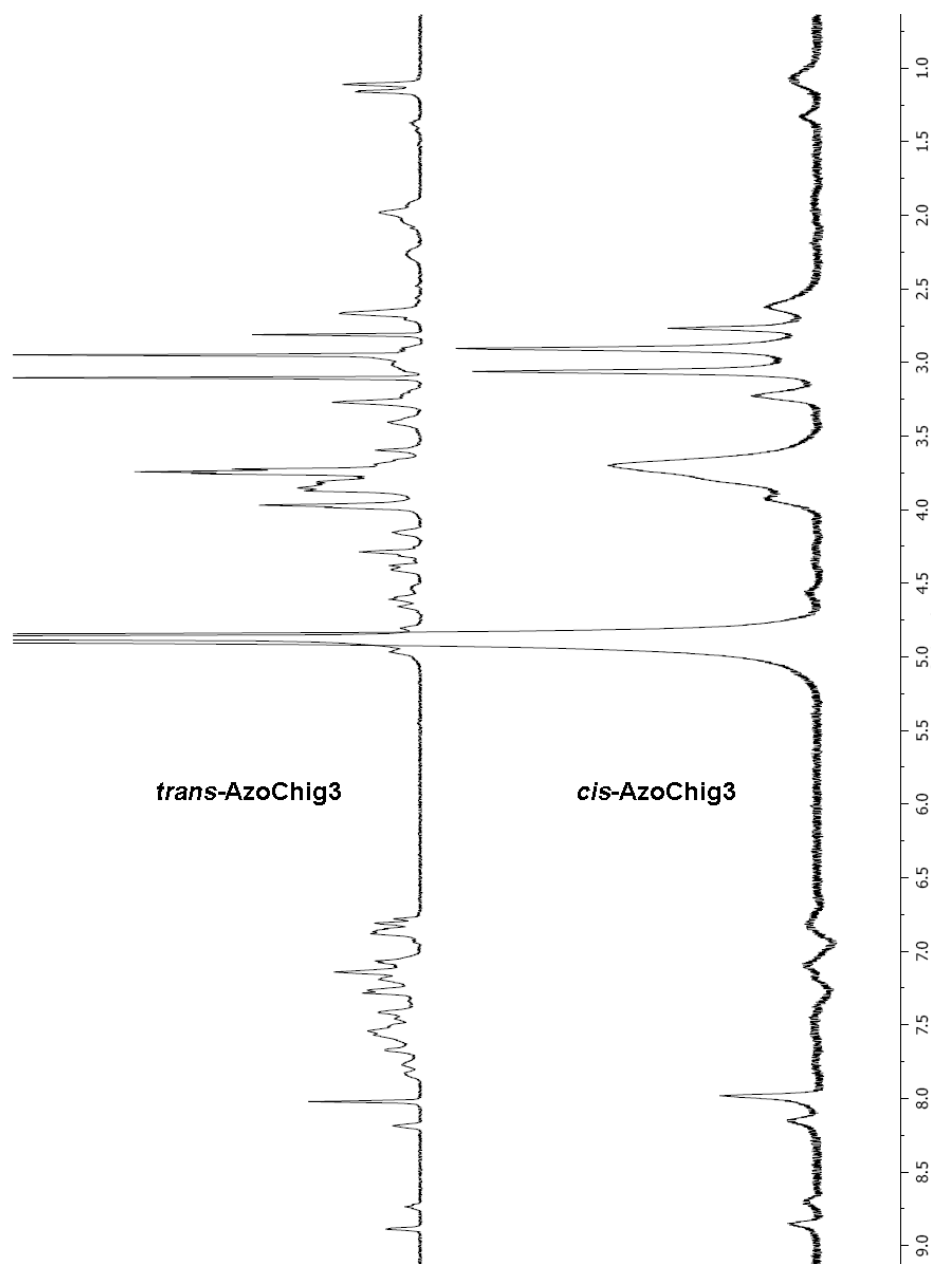


**Figure 16:** <sup>1</sup>H-NMR spectrum of *trans*-AzoChig3 (2) peptide in MeOD-d<sub>4</sub>. Bottom: <sup>1</sup>H-NMR spectrum of *cis*-AzoChig3 (2) peptide in MeOD-d<sub>4</sub>.

## 5.5.2 EXPERIMENTAL DATA OF ADDITIONAL COMPOUNDS CHIGNOLIN 5.1, Y2W-AZOCHIG 5.5, Y2V-AZOCHIG 5.6, P4T-AZOCHIG 5.7 AND Y2AZOPHE-CHIG 5.8

### 5.5.2.1 SYNTHESIS OF PEPTIDES CHIGNOLIN 5.1, Y2W-AZOCHIG 5.5, Y2V-AZOCHIG 5.5, P4T-AZOCHIG 5.7 AND Y2AZOPHE-CHIG 5.8

The synthesis of peptides chignolin 5.1, Y2W-AzoChig 5.5, Y2V-AzoChig 5.5, P4T-AzoChig 5.7 and Y2AzoPhe-Chig 5.8 followed the general peptide synthesis protocol stated in the APPENDIX. Table 5.3 depicts the coupling conditions of the different building blocks used for the automated peptide synthesis. As resin for all peptides a preloaded Wang LL *N*-(Fmoc)-Gly resin (NovaBiochem, Darmstadt/Germany) was used.

**Table 5.3: Coupling conditions for synthesis of peptides chignolin 5.1, Y2W-AzoChig 5.5, Y2V-AzoChig 5.5, P4T-AzoChig 5.7 and Y2AzoPhe-Chig 5.8.**

Amino acid(s)	Coupling method	Steps	Time (s)	Temperature (°C)	Power (W)
Fmoc-AMPP-OH 1.26, Fmoc-AzoPhe-OH 1.27	Photoswitch coupling	1	1800	75	23
Fmoc-Asp( <i>t</i> -Bu)-OH, Fmoc-Glu-OH, Fmoc-Gly-OH, Fmoc-Pro-OH, Fmoc-Thr( <i>t</i> -Bu)-OH, Fmoc-Trp(Boc)-OH, Fmoc-Tyr( <i>t</i> -Bu)-OH, Fmoc-Val-OH	Standard single amino acid coupling	1	480	75	23

## 5.5.2.2 ANALYTICAL HPLC SPECTRUM AND MASS SPECTRUM OF CHIGNOLIN 5.1

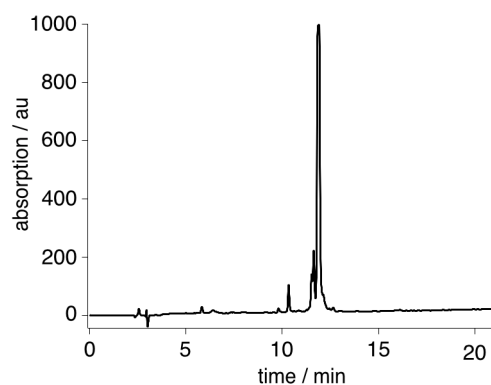


**Figure 5.8: HPLC spectrum of chignolin 5.1.** Analytical HPLC spectrum of 5.1 with a water/acetonitrile gradient 95:5 → 20:80 in 40 min.  $R_t = 11.9$  min.

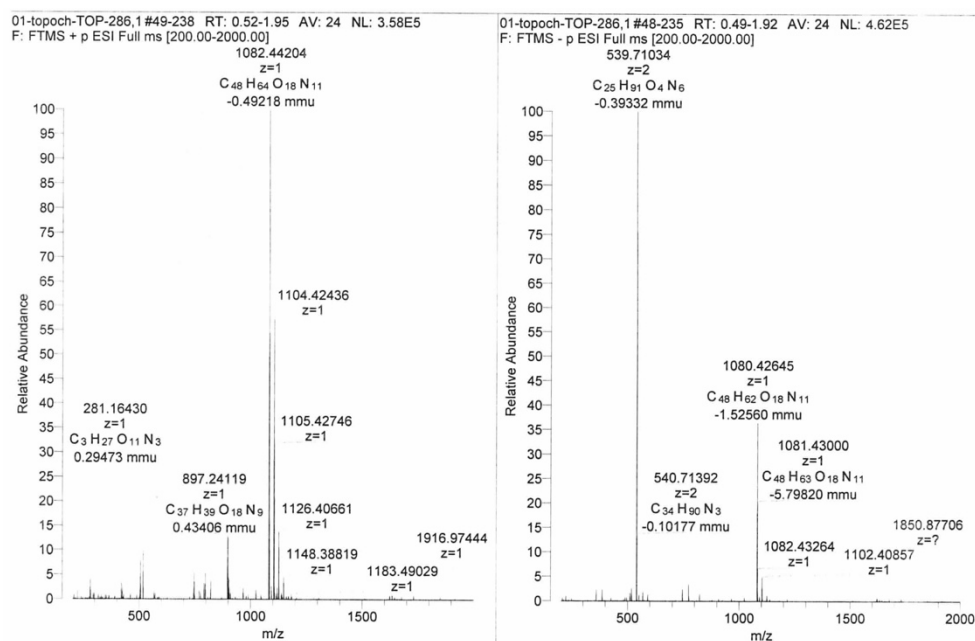


**Figure 5.9: HRMS spectrum of chignolin 5.1.** HRMS (+ESI) m/z: calc. for  $C_{48}H_{64}O_{18}N_{11}^+ [M+H]^+$ : 1082.4425; found: 1082.4420. Calc. for  $C_{48}H_{63}O_{18}N_{11}Na^+ [M+Na]^+$ : 1104.4250; found: 1104.4244.  $\Delta m = -0.54$  ppm.

## 5.5.2.3 ANALYTICAL HPLC SPECTRUM AND MASS SPECTRUM OF Y2W-AZOCHIG 5.5

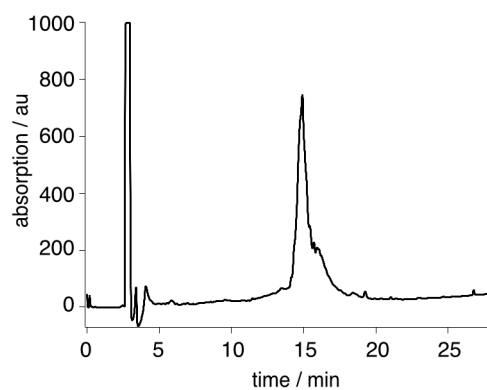


**Figure 5.10: HPLC spectrum of Y2W-AzoChig 5.5.** Analytical HPLC spectrum of 5.5 with a water/acetonitrile gradient 95:5 → 20:80 in 40 min.  $R_t = 14.9$  min.

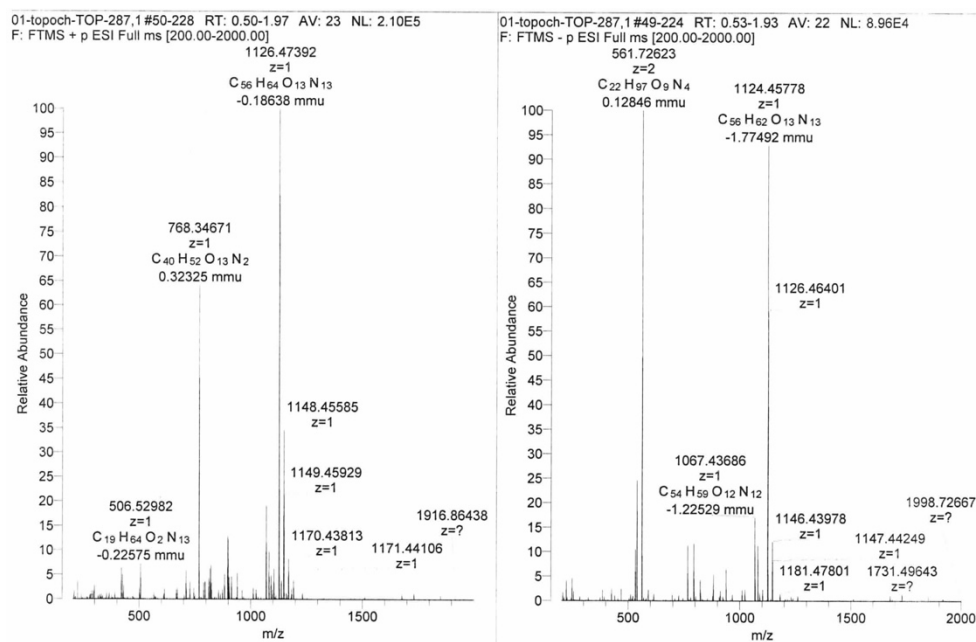


**Figure 5.11: HRMS spectrum of Y2W-AzoChig 5.5.** HRMS (+ESI)  $m/z$ : calc. for  $C_{56}H_{64}O_{13}N_{13}^+$   $[M+H]^+$ : 1126.4741; found: 1126.4739.  $\Delta m = -0.18$  ppm.

## 5.5.2.4 ANALYTICAL HPLC SPECTRUM AND MASS SPECTRUM OF Y2V-AZOCHIG 5.6

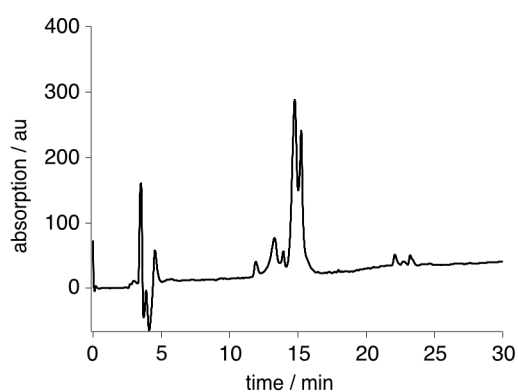


**Figure 5.12: HPLC spectrum of Y2V-AzoChig 5.6.** Analytical HPLC spectrum of 5.6 with a water/acetonitrile gradient 95:5 → 20:80 in 40 min.  $R_{t,cis}$  = 13.3 min,  $R_{t,trans}$  = 14.7 min.

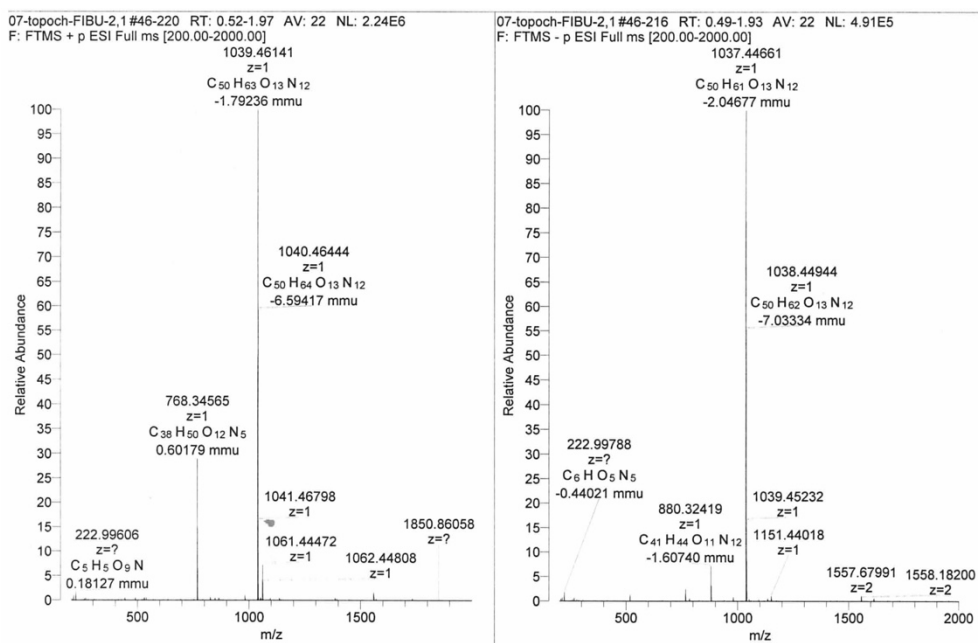


**Figure 5.13: HRMS spectrum of Y2V-AzoChig 5.6.** HRMS (+ESI) m/z: calc. for C<sub>50</sub>H<sub>63</sub>O<sub>13</sub>N<sub>12</sub><sup>+</sup> [M+H]<sup>+</sup>: 1039.4632; found: 1039.4614.  $\Delta m$  = -1.73 ppm.

## 5.5.2.5 ANALYTICAL HPLC SPECTRUM AND MASS SPECTRUM OF P4T-AZOCHIG 5.7

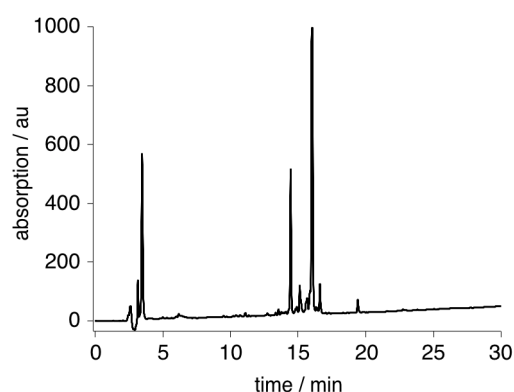


**Figure 5.14: HPLC spectrum of P4T-AzoChig 5.7.** Analytical HPLC spectrum of 5.7 with a water/acetonitrile gradient 95:5 → 20:80 in 40 min.  $R_{t,cis}$  = 14.4 min,  $R_{t,trans}$  = 16.0 min.

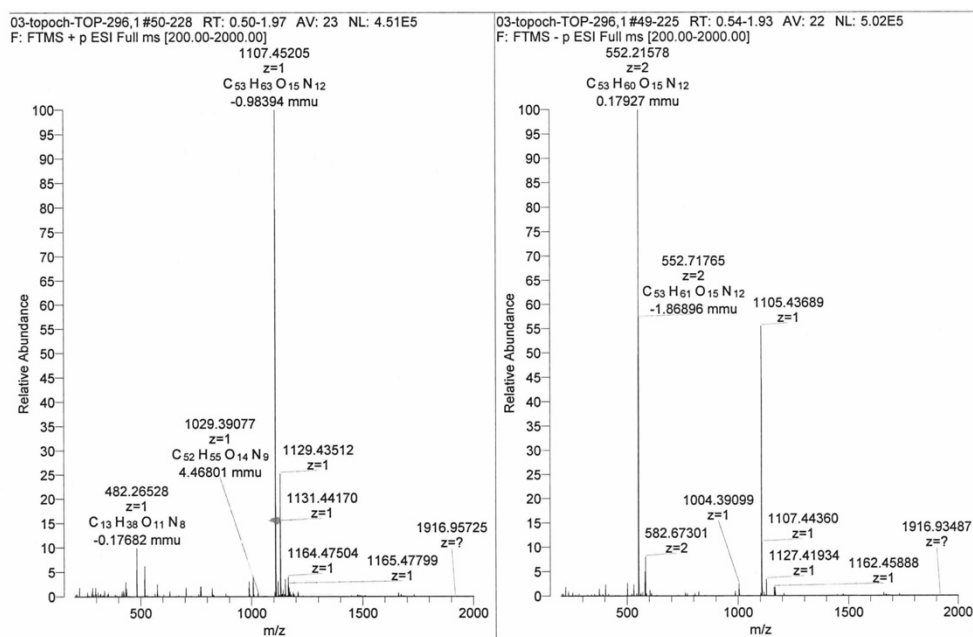


**Figure 5.15: HRMS spectrum of P4T-AzoChig 5.7.** HRMS (+ESI)  $m/z$ : calc. for  $C_{53}H_{63}O_{12}N_{15}^+ [M+H]^+$ : 1107.4521; found: 1107.4530. Calc. for  $C_{53}H_{62}O_{12}N_{15}Na^+ [M+Na]^+$ : 1129.4356; found: 1129.4351.  $\Delta m$  = -0.44 ppm.

## 5.5.2.6 ANALYTICAL HPLC SPECTRUM AND MASS SPECTRUM OF Y2AZOPHE-CHIG 5.8

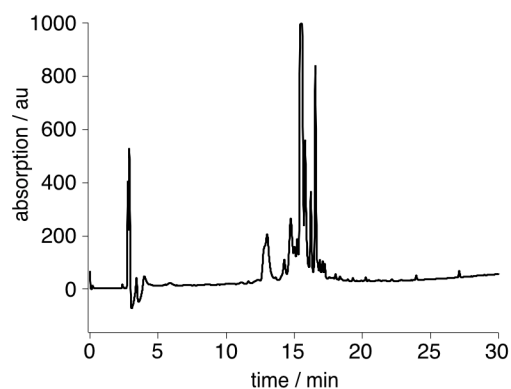


**Figure 5.16: HPLC spectrum of Y2AzoPhe-Chig 5.8.** Analytical HPLC spectrum of 5.8 with a water/acetonitrile gradient 95:5 → 20:80 in 40 min.  $R_{t,cis} = 13.4$  min,  $R_{t,trans} = 15.4$  min.

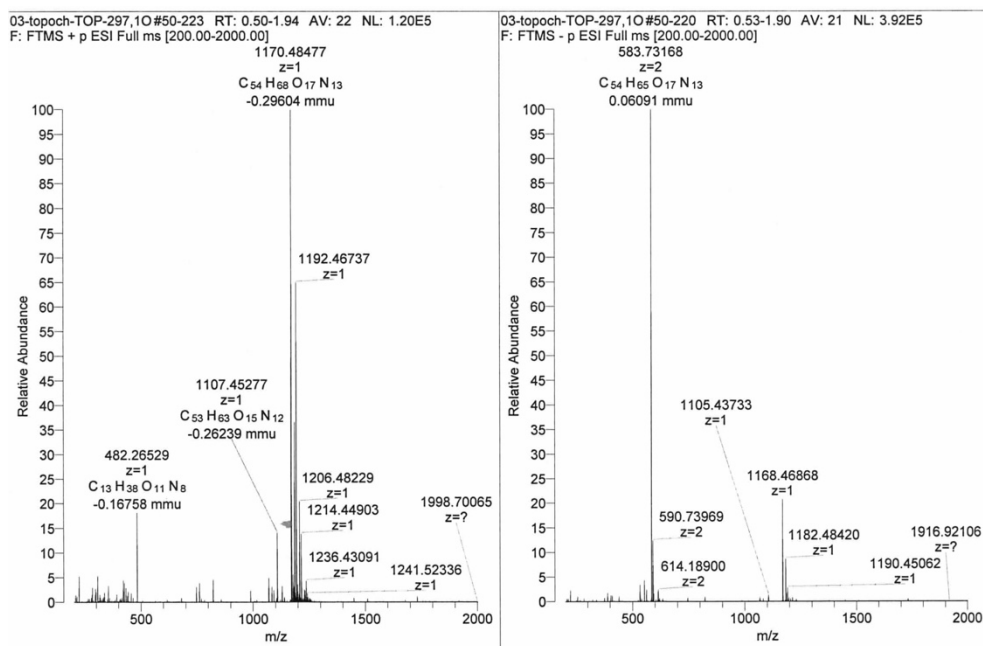


**Figure 5.17: HRMS spectrum of Y2AzoPhe-Chig 5.8.** HRMS (+ESI)  $m/z$ : calc. for C<sub>54</sub>H<sub>68</sub>O<sub>17</sub>N<sub>13</sub><sup>+</sup> [M+H]<sup>+</sup>: 1170.4851; found: 1170.4848. Calc. for C<sub>54</sub>H<sub>67</sub>O<sub>17</sub>N<sub>13</sub>Na<sup>+</sup> [M+Na]<sup>+</sup>: 1192.4674; found: 1192.4676.  $\Delta m = -0.26$  ppm.

# APPENDIX

## INDEX OF ABBREVIATIONS

<b>Abs.</b>	absolute
<b>AcOH</b>	Acetic acid
<b>AE</b>	Autonomous element
<b>AGT</b>	O <sup>6</sup> -alkylguanine DNA alkyltransferase
<b>An. RP-HPLC</b>	Analytical reversed-phase high pressure liquid chromatography
<b>au</b>	Arbitrary units
<b>BC</b>	Benzylcytosine
<b>BG</b>	Benzylguanine
<b>BPO</b>	Dibenzoylperoxid
<b>CD</b>	Circular dichroism
<b>CIS</b>	Chemical induced shift
<b>CNS</b>	Central nerve system
<b>DAE</b>	Diarylethenes
<b>DMAP</b>	4-Dimethylaminopyridine
<b>DMF</b>	<i>N,N'</i> -Dimethylformamide
<b>DMSO</b>	Dimethylsulfoxid
<b>DSS</b>	4,4-dimethyl-4-silapentane-1-sulfonic acid
<b>ED</b>	Electron donating
<b>EDG</b>	Electron donating group
<b>EW</b>	Electron withdrawing
<b>EWG</b>	Electron withdrawing group
<b>Fig.</b>	Figure
<b>FSK</b>	Forskolin
<b>FT IR</b>	Fourier-transformation infrared
<b>GPCR</b>	G-protein coupled receptor
<b>GRK</b>	GPCR kinase
<b>HKR</b>	HEPES-Krebs-Ringer
<b>HTI</b>	Hemithioindigo
<b>IR</b>	Infrared
<b>KHMDS</b>	Potassium bis(trimethylsilyl)amide
<b>LiHMDS</b>	Lithium bis(trimethylsilyl)amide
<b><i>m</i>-CPBA</b>	<i>meta</i> -Chloroperoxybenzoic acid
<b>MeCN</b>	Acetonitrile
<b>MeOH</b>	Methanol
<b>NBS</b>	<i>N</i> -Bromosuccinimid
<b>NMR</b>	Nuclear magnetic resonance

<b>OD</b>	Optical density
<b>PAM</b>	Photoswitchable allosteric modulator
<b>PBS</b>	Phosphate buffered saline
<b>PCL</b>	Photochromic ligand
<b>PEG</b>	Polyethylene glycol
<b>PhMe</b>	Toluene
<b>Pr. RP-HPLC</b>	Preparative reversed-phase high pressure liquid chromatography
<b>PSS</b>	Photostationary state
<b>PTL</b>	Photoswitchable tethered ligand
<b>Py</b>	Pyridine
<b>ROS</b>	Reactive oxygen species
<b>ROS</b>	Reactive oxygen species
<b>rt</b>	Room temperature
<b>SEM</b>	Standard error of the mean
<b>SPPS</b>	Solid-phase peptide synthesis
<b><i>t</i>-BuOH</b>	<i>tert</i> -Butanol
<b><i>t</i>-BuOI</b>	<i>tert</i> -Butylhypoiodite
<b>T2D</b>	Type 2 diabetes mellitus
<b>TFA</b>	Trifluoroacetic acid
<b>TFE</b>	Trifluoro ethanol
<b>THF</b>	Tetrahydrofuran
<b>UV</b>	Ultraviolet

## INDEX OF COMPOUNDS

## PART I

- 1.1 Retinal
- 1.2 Stilbene
- 1.3 Diarylethene
- 1.4 Hemithioindigo
- 1.5 Azobenzene
- 1.6 Bis(*para*-iodoacetamido)-azobenzene
- 1.7 DENAQ; (*E*)-2-((4-((4-(Diethylamino)phenyl)diazenyl)phenyl)amino)-*N,N,N*-triethyl-2-oxoethan-1-aminium
- 1.8 JB558; (*E*)-*N*-Cyclohexyl-5-((4-(diethylamino)phenyl)diazenyl)-1,3,4-thiadiazole-2-sulfonamide
- 1.9 Bis(*para*-chloroacetamido)-azobenzene
- 1.10 (*E*)-*N,N'*-(Diazene-1,2-diylbis(3-(piperidin-1-yl)-4,1-phenylene))bis(2-chloroacetamide)
- 1.11 (*E*)-*N,N'*-(Diazene-1,2-diylbis(3-(diethylamino)-4,1-phenylene))bis(2-chloroacetamide)
- 1.12 (*E*)-*N,N'*-(Diazene-1,2-diylbis(3-(pyrrolidin-1-yl)-4,1-phenylene))bis(2-chloroacetamide)
- 1.13 (*E*)-*N,N'*-(Diazene-1,2-diylbis(3-(4-methylpiperazin-1-yl)-4,1-phenylene))bis(2-chloroacetamide)
- 1.14 (*E*)-1-Methyl-4-(phenyldiazenyl)-1*H*-pyrazole
- 1.15 (*E*)-*N,N'*-(Diazene-1,2-diylbis(3,5-dimethoxy-4,1-phenylene))diacetamide
- 1.16 (*E*)-*N,N'*-(Diazene-1,2-diylbis(3,5-difluoro-4,1-phenylene))diacetamide
- 1.17 (*E*)-*N,N'*-(Diazene-1,2-diylbis(3,5-dichloro-4,1-phenylene))diacetamide
- 1.18 Diethyl 4,4'-(diazene-1,2-diyl)(*E*)-bis(3,5-difluorobenzoate)
- 1.19 (*Z*)-11,12-Dihydrodibenzo[*c,g*][1,2]diazocine
- 1.20 (*Z*)-*N,N'*-(11,12-Dihydrodibenzo[*c,g*][1,2]diazocine-2,9-diyl)diacetamide
- 1.21 (*Z*)-*N,N'*-(11,12-Dihydrodibenzo[*c,g*][1,2]diazocine-3,8-diyl)diacetamide
- 1.22 AMPP, 3-[3-(Aminomethyl)phenylazo]phenylacetic acid
- 1.23 APB, 4-[4-(Amino)phenylazo]benzoic acid
- 1.24 AzoPhe, (*S,E*)-2-Amino-3-(4-(phenyldiazenyl)phenyl)propanoic acid
- 1.25 *para*-BDCA, (*Z*)-*N,N'*-(11,12-Dihydrodibenzo[*c,g*][1,2]diazocine-2,9-diyl)bis(2-chloroacetamide)
- 1.26 Fmoc-AMPP, (*E*)-2-(3-(((9*H*-Fluoren-9-yl)methoxy)carbonyl)amino)methyl)phenyl)diazenyl)phenyl)acetic acid
- 1.27 Fmoc-AzoPhe, (*S,E*)-2-(((9*H*-Fluoren-9-yl)methoxy)carbonyl)amino)-3-(4-(phenyldiazenyl)phenyl)propanoic acid
- 1.28 AMBD, (*Z*)-2-(8-(((9*H*-Fluoren-9-yl)methoxy)carbonyl)amino)methyl)-11,12-dihydrodibenzo[*c,g*][1,2]diazocin-3-yl)acetic acid

- 1.29 *m*-BDCA, (*Z*)-*N,N'*-(11,12-Dihydrodibenzo[*c,g*][1,2]diazocine-3,8-diyl)bis(2-chloroacetamide)
- 1.30 DABT, (*E*)-*N,N'*-(Diazene-1,2-diylbis(benzo[*d*]thiazole-2,6-diyl))bis(2-chloroacetamide)
- 1.31 3-(Aminomethyl)anilin
- 1.32 (9*H*-Fluoren-9-yl)methyl (3-aminobenzyl)carbamate
- 1.33 2-(3-Nitrophenyl)acetic acid
- 1.34 2-(3-Nitrosophenyl)acetic acid
- 1.35 *L-N-tert*-Butoxycarbonyl-*para*-phenylalanine
- 1.36 *N*-(*tert*-Butoxycarbonyl)-*L*-phenylalanine-4'-azobenzene
- 1.37 *para*-Tolylacetic acid
- 1.38 *tert*-Butyl 2-(4-((bromotriphenylphosphaneyl)methyl)phenyl)acetate
- 1.39 *tert*-Butyl (*E*)-2-(4-(4-cyanostyryl)phenyl)acetate
- 1.40 2-(4-(4-((2,5-Dioxopyrrolidin-1-yl)methyl)phenethyl)phenyl)acetic acid
- 1.41 2-(4-(4-((2,5-Dioxopyrrolidin-1-yl)methyl)-2-nitrophenethyl)-3-nitrophenyl)acetic acid
- 1.42 (*Z*)-2-(8-((2,5-Dioxopyrrolidin-1-yl)methyl)-11,12-dihydrodibenzo[*c,g*][1,2]diazocin-3-yl)acetic acid
- 1.43 2-(3-Amino-4-(2-amino-4-((2,5-dioxopyrrolidin-1-yl)methyl)phenethyl)phenyl)acetic acid
- 1.44 (*Z*)-2-(8-((2,5-Dioxopyrrolidin-1-yl)methyl)-11,12-dihydrodibenzo[*c,g*][1,2]diazocin-3-yl)acetic acid
- 1.45 Methyl 2-(3-amino-4-(2-amino-4-((2,5-dioxopyrrolidin-1-yl)methyl)phenethyl)phenyl)acetate
- 1.46 Methyl (*Z*)-2-(8-((2,5-dioxopyrrolidin-1-yl)methyl)-11,12-dihydrodibenzo[*c,g*][1,2]diazocin-3-yl)acetate
- 1.47 (*Z*)-2,9-Dibromo-11,12-dihydrodibenzo[*c,g*][1,2]diazocine
- 1.48 (*Z*)-11,12-Dihydrodibenzo[*c,g*][1,2]diazocine-2,9-diamine
- 1.49 4,4'-(Ethane-1,2-diyl)dianiline
- 1.50 (*Z*)-11,12-Dihydrodibenzo[*c,g*][1,2]diazocine-3,8-diamine
- 1.51 2-Amino-6-nitrobenzothiazole
- 1.52 1,2-Bis(6-nitrobenzothiazol-2-yl)diazene
- 1.53 2-(4-(Bromomethyl)phenyl)acetic acid
- 1.54 *tert*-Butyl 2-(4-(bromomethyl)phenyl)acetate
- 1.55 *tert*-Butyl 2-(4-(4-(aminomethyl)phenethyl)phenyl)acetate
- 1.56 *Di-tert*-butyl (11,12-dihydrodibenzo[*c,g*][1,2]diazocine-2,9-diyl)(*Z*)-dicarbamate
- 1.57 4,4'-(Ethane-1,2-diyl)bis(3-nitroaniline)
- 1.58 (*E*)-2,2'-(Diazene-1,2-diyl)bis(benzo[*d*]thiazol-6-amine)

## PART II

- II.1 MAQ, (*E*)-2-((4-((4-(2-(2,5-Dioxo-2,5-dihydro-1*H*-pyrrol-1-yl)acetamido)phenyl)diazenyl)phenyl)amino)-*N,N,N*-triethyl-2-oxoethan-1-aminium

- II.2** 4-GluAzo, (2*S*,4*R*)-2-Amino-4-((*E*)-3-(4-((*E*)-phenyldiazenyl)phenyl)allyl)pentanedioic acid
- II.3** ATA-3, (*S,E*)-2-Amino-3-(5-(2-(3-((4-(dimethylamino)phenyl)diazenyl)benzyl)-2*H*-tetrazol-5-yl)-3-hydroxy-1*H*-pyrazol-4-yl)propanoic acid
- II.4** Metformin; *N,N*-Dimethylimidodicarbonimidic diamide
- 2.1** TOP271, SLRRS SCFGG RMDRI GAQ (AMPP, **1.22**) CNSFR Y
- 2.2** N24AzoPhe-ANP; SLRRS SCFGG RMDRI GAQSG LGC (AzoPhe, **1.24**) SFRY
- 2.3** S25AzoPhe-ANP; SLRRS SCFGG RMDRI GAQSG LGCN (AzoPhe, **1.24**) FRY
- 3.1** Metformin, *N,N'*-Dimethylimidodicarbonimidic diamide
- 3.2** Glimeperide, 3-Ethyl-4-methyl-*N*-(4-(*N*-(((1*r*,4*r*)-4-methylcyclohexyl)carbamoyl)sulfamoyl)phenethyl)-2-oxo-2,5-dihydro-1*H*-pyrrole-1-carboxamide
- 3.3** Sitagliptin, (*R*)-3-Amino-1-(3-(trifluoromethyl)-5,6-dihydro-[1,2,4]triazolo[4,3-*a*]pyrazin-7(8*H*)-yl)-4-(2,4,5-trifluorophenyl)butan-1-one
- 3.4** Exenatide, HEGGT FTSDL SKQME EEA VR LFIEW LKWGG PSSGA PPPS-NH<sub>2</sub>
- 3.5** Liraglutide, HAEGT FTSDV SSYLE GQAAK( $\gamma$ EP) EFAIW LVKGR G
- 3.6** LirAzo, HAEGT FTSDV SSYLE (AMPP, **1.22**) AAK EFAIW LVKGR G
- 3.7** LirAzo2, HAEGT FTSDV SSYLE (AMPP, **1.22**) AK EFAIW LVKGR G
- 3.8** LirAzo3, HAEGT FTSDV SSYLE (AMPP, **1.22**) K EFAIW LVKGR G
- 3.9**  $\gamma$ Ep-LirAzo, HAEGT FTSDV SSYLE (AMPP, **1.22**) AAK( $\gamma$ EP) EFAIW LVKGR G
- 4.1** BG-LirAzo, HAEGT FTSDV SSYLE (AMPP, **1.22**) AAK EFAIW LVKGR C(PEG<sub>4</sub>)-BG
- 4.2** ExONatide, HEGGT FTSDL SKQME EEA VR LFIEW LKWGG PSSGA PPPC(PEG<sub>4</sub>)-BG
- 4.3** ExOFFatide, DL SKQME EEA VR LFIEW LKWGG PSSGA PPPC(PEG<sub>4</sub>)-BG
- 4.4** BG-Lira, HAEGT FTSDV SSYLE GQAAK EFAIW LVKGR C(PEG<sub>4</sub>)-BG
- 4.5** BG-PEG<sub>4</sub>-SPDP, *N*-(4-(((2-amino-9*H*-purin-6-yl)oxy)methyl)benzyl)-1-(3-(pyridin-2-yl)disulfaneyl)propanamido)-3,6,9,12-tetraoxapentadecan-15-amide
- 4.6** S39C-Ex4(1-39), HEGGT FTSDL SKQME EEA VR LFIEW LKWGG PSSGA PPPC-NH<sub>2</sub>
- 4.7** S39C-Ex4(9-39), DL SKQME EEA VR LFIEW LKWGG PSSGA PPPC-NH<sub>2</sub>
- 4.8** G36C-Lira, HAEGT FTSDV SSYLE GQAAK EFAIW LVKGR C
- 4.9** G36C-LirAzo, HAEGT FTSDV SSYLE (AMPP, **1.22**) AAK EFAIW LVKGR C

### PART III

- III.1** AzoTrpZip2, ATZ, SWTWE (AMPP, **1.22**) KWTWK-NH<sub>2</sub>
- 5.1** Chignolin, GYDPE TGTWG
- 5.2** AzoChig1, GYDP (AMPP, **1.22**) GTWG
- 5.3** AzoChig2, GYDP (AMPP, **1.22**) GT (5-FW) G
- 5.4** AzoChig3, PEG<sub>3</sub>-GYDP (AMPP, **1.22**) GTWG
- 5.5** Y2W-AzoChig, GWDP (AMPP, **1.22**) GTWG
- 5.6** Y2V-AzoChig, GVDP (AMPP, **1.22**) GTWG
- 5.7** P4T-AzoChig, GYDT (AMPP, **1.22**) GTWG
- 5.8** Y2AzoPhe-Chig, G (AzoPhe, **1.24**) DPE TGTWG

# INDEX OF FIGURES

**Figure 1:** Giovanni Stradano – Il laboratorio dell'alchemista.

## PART I

**Figure 1.1:** Examples for molecular switches.

**Figure 1.2:** Azobenzene (**1.5**) isomerization.

**Figure 1.3:** Modified azobenzene derivatives and their photophysical properties

**Figure 1.4:** Shifting of maximale absorption in azobenzenes with *ortho*-substituents.

**Figure 1.5:** Peptide backbone photoswitches AMPP and APB.

**Figure 1.6:** Side chain amino acid and crosslinker photoswitches AzoPhe **1.24** and *p*-BDCA **1.25**.

**Figure 1.7:** Overview of the synthesized photoswitches.

**Figure 1.8:** Photophysical properties and photoswitching kinetics of *m*-BDCA **1.29**.

**Figure 1.9:** Photophysical properties and photoswitching kinetics of DABT **1.30**.

**Figure 1.10:** Overview of the synthesized photoswitches and the targeted peptides.

## PART II

**Figure II.1:** Principles of photocontrol.

**Figure II.2:** Photopharmaceutical administration scenarios.

**Figure II.3:** Principle of SNAP- and CLIP-tag bioconjugation for simultaneous labeling and imaging.

**Figure II.4:** Examples for PCLs and PTLs for photopharmacological applications

**Figure 2.1:** X-Ray crystal structure based design scheme for N24AzoPhe-ANP **2.2** and S25AzoPhe-ANP **2.3**

**Figure 2.2:** UV/Vis spectra and UV switching kinetics of **2.2** and **2.3**.

**Figure 2.3:** Overview of AzoANP peptides and cGMP dose-response curves for TOP271 **2.1**, N24AzoPhe-ANP **2.2** and S25AzoPhe-ANP **2.3**.

**Figure 2.4:** HPLC spectrum of N24-AzoPhe-ANP **2.2**.

**Figure 2.5:** HRMS spectrum of N24-AzoPhe-ANP **2.2**.

**Figure 2.6:** HPLC spectrum of S25-AzoPhe-ANP **2.3**.

**Figure 2.7:** HRMS spectrum of S25-AzoPhe-ANP **2.3**.

**Figure 3.1:** Different drugs for the treatment of T2D.

**Figure 3.2:** Design approach for LirAzo **3.6**, LirAzo2 **3.7** and LirAzo3 **3.8**.

**Figure 3.3:** UV/Vis spectra and UV switching kinetics of LirAzo2 **3.7** and LirAzo3 **3.8**.

**Figure 3.4:** cAMP dose-response curves for peptides LirAzo **3.6**, LirAzo2 **3.7** and LirAzo3 **3.8**.

**Figure 3.5** HPLC spectrum of LirAzo2 **3.8**.

**Figure 3.6:** HRMS spectrum of LirAzo2 **3.8**.

**Figure 3.7:** HPLC spectrum of LirAzo2 **3.6**.

- Figure 3.8:** HRMS spectrum of LirAzo2 **3.6**.
- Figure 4.1:** Design scheme for BG-compounds exONatide **4.2**, exOFFatide **4.3**, BG-Lira **4.4** and BG-LirAzo **4.1**.
- Figure 4.2:** HPLC spectrum of S39C-Ex4(9-39) **4.7**.
- Figure 4.3:** HRMS spectrum of S39C-Ex4(9-39) **4.7**.
- Figure 4.4:** HPLC spectrum of exOFFatide **4.3**.
- Figure 4.5:** HRMS spectrum of exOFFatide **4.3**.
- Figure 4.6:** HPLC spectrum of G36C-Lira **4.8**.
- Figure 4.7:** HRMS spectrum of G36C-Lira **4.8**.
- Figure 4.8:** HPLC spectrum of G36C-LirAzo **4.9**.
- Figure 4.9:** HRMS spectrum of G36C-LirAzo **4.9**.

### PART III

- Figure III.1:** Breakdown of complex protein structures.
- Figure III.2:** Schematic representation of possible protein structures.
- Figure III.3:** Different models for  $\beta$ -hairpin formation in peptides.
- Figure III.4:** Different shifts of the peptide amide-I band in continuous wave IR spectra.
- Figure 5.1:** Stabilizing interactions in the chignolin **5.1**  $\beta$ -hairpin.
- Figure 5.2:** Predicted influence of substituents on hydrophobic interactions in AzoChignolin peptides.
- Figure 5.3:** CD and IR spectra of Y2W-AzoChig **5.5** and Y2V-AzoChig **5.6**.
- Figure 5.4:** Predicted interactions in Y2AzoPhe-Chig **5.8**.
- Figure 5.5:** UV spectra and switching kinetics for *cis/trans*-Y2AzoPhe-Chig **5.8**.
- Figure 5.6:** NMR spectra in the aromatic region of chignolin **5.1** and *cis/trans*-Y2AzoPhe-Chig **5.8**.
- Figure 5.7:** CD and FT IR spectra of *cis/trans*-Y2AzoPhe-Chig **5.8**.
- Figure 5.8:** HPLC spectrum of chignolin **5.1**.
- Figure 5.9:** HRMS spectrum of chignolin **5.1**.
- Figure 5.10:** HPLC spectrum of Y2W-AzoChig **5.5**.
- Figure 5.11:** HRMS spectrum of Y2W-AzoChig **5.5**.
- Figure 5.12:** HPLC spectrum of Y2V-AzoChig **5.6**.
- Figure 5.13:** HRMS spectrum of Y2V-AzoChig **5.6**.
- Figure 5.14:** HPLC spectrum of P4T-AzoChig **5.7**.
- Figure 5.15:** HRMS spectrum of P4T-AzoChig **5.7**.
- Figure 5.16:** HPLC spectrum of Y2AzoPhe-Chig **5.8**.
- Figure 5.17:** HRMS spectrum of Y2AzoPhe-Chig **5.8**.

# INDEX OF SCHEMES

## PART I

- Scheme 1.1:** Tuning of the azobenzene electronic system.
- Scheme 1.2:** Azobenzene (**1.5**) isomerization.
- Scheme 1.3:** Synthesis of Fmoc-AMPP **1.26**.
- Scheme 1.4:** Synthesis of Fmoc-AzoPhe **1.27**.
- Scheme 1.5:** Synthesis route towards Fmoc-AMBD **1.28**.
- Scheme 1.6:** Oxidative coupling approach for Fmoc-AMBD **1.28**.
- Scheme 1.7:** Synthesis of *p*-BDCA **1.25**.
- Scheme 1.8:** Synthesis of *m*-BDCA **1.29**.
- Scheme 1.9:** Synthesis of DABT **1.30**.

## INDEX OF TABLES

### PART II

- Table II.1:** Different classes of photodruggable targets.
- Table 2.1:**  $EC_{50}$  values of peptides ANP, TOP271 **2.1**, N24AzoPhe-ANP **2.2** and S25AzoPhe-ANP **2.3**.
- Table 2.2:** Table 2.2: Coupling conditions for synthesis of peptides N24AzoPhe-ANP **2.2** and S25AzoPhe-ANP **2.3**.
- Table 3.1:** Coupling conditions for synthesis of peptides LirAzo2 **3.8** and LirAzo3 **3.6**.
- Table 4.1:** Coupling conditions for synthesis of peptides S39C-Ex4(9-39) **4.7**, exOFFatide **4.3**, G36C-Lira **4.8** and G36C-LirAzo **4.9**.

### PART III

- Table 5.1:**  $^1\text{H}$  NMR CIS values in the aromatic region of **5.1** and *cis-/trans*-Y2AzoPhe-Chig **5.8**.
- Table 5.2:**  $^1\text{H}$  NMR CIS values of the  $H_{\alpha}$  protons of **5.1** and *cis-/trans*-**5.8**.
- Table 5.3:** Coupling conditions for synthesis of peptides chignolin **5.1**, Y2W-AzoChig **5.5**, Y2V-AzoChig **5.5**, P4T-AzoChig **5.7** and Y2AzoPhe-Chig **5.8**.

## GENERAL REMARKS

### Chemicals, solutions and compounds

The chemicals and solutions used throughout this work were either purchased from Sigma-Aldrich (Munich/Germany), ABCR (Karlsruhe/Germany) or VWR (Ismaning/Germany). Compounds and resins for peptide synthesis were purchased from NovaBiohem (Merck Millipore, Darmstadt/Germany), Orpegen Peptide Chemicals (Heidelberg/Germany) or Rapp Polymere (Tübingen/Germany).

### Thin-layer chromatography and flash chromatography on silica gel

Thin-layer chromatography reaction control was undertaken on aluminium foils (silicagel 60 F254, Merck KGaA, Grafen/Germany). Compounds were detected utilizing either fluorescence quenching at  $\lambda = 254$  nm or by dyeing with ninhydrin solution (1.5 g ninhydrin, 15 mL glacial acetic acid and 500 mL methanol). Flash chromatography was done on silica gel (grain size 35-70  $\mu\text{m}$ , Acros Organics, Geel/Belgium) with nitrogen pressure (0.2-1.0 bar).

### Peptide Synthesizer

Peptides were synthesised on a CEM Liberty 1 Peptide Synthesizer with a CEM Discovery Microwave (CEM GmbH, Kamp-Lintfort/Germany) under standard Fmoc conditions (with or without microwave). Detailed information on peptide synthesis protocols, resins, coupling reagents and conditions can be found under GENERAL PEPTIDE SYNTHESIS.

### Reversed-phase HPLC

Analytical RP-HPLCs were performed on Jasco (Jasco Germany GmbH, Groß-Umstadt/Germany) devices (PU-2080 Plus, LG-2080-02-S, DG-2080-53 and MD-2010 Plus) with a Phenomenex (Aschaffenburg/Germany) Aeris column (C18, 5  $\mu\text{m}$ , 250 x 4.6 mm). A water/acetonitrile gradient with 0.1% TFA with a flow of 1 mL $\cdot\text{min}^{-1}$  was used as eluent. Purification through semi-preparative RP-HPLCs was performed on Jasco (Groß-Umstadt/Germany) devices (PU-2087 Plus, LG-2080-02-S and UV-2075 Plus) with a Phenomenex (Torrance/USA) Aeris column (XBC18, 5  $\mu\text{m}$ , 250 x 21.2 mm). As eluent, a water/acetonitrile gradient with 0.1% TFA and 20 mL/min flow was used.

### NMR spectroscopy

NMR spectra were recorded on Varian (Darmstadt/Germany) AC 300 (300 MHz), WH 400 (400 MHz) and AMX 600 (600 MHz), as well as on Bruker (Billerica/USA) AV-III (800 MHz) devices. All spectra were recorded at room temperature and chemical shifts  $\delta$  are denoted in ppm based on TMS as external, or DSS as internal standard, respectively. Deuterated solvents  $\text{CDCl}_3$ ,  $\text{CD}_3\text{OD}$ ,  $\text{CD}_3\text{OH}$  and  $\text{DMSO-d}_6$  were used for the experiments. The detected resonances of the remaining protons in these solvents was used as internal standard [ $\delta$  ( $\text{CDCl}_3$ ) = 7.26,  $\delta$  ( $\text{CD}_3\text{OD}$ ) = 3.31 and  $\delta$  ( $\text{DMSO-d}_6$ ) = 2.50 ppm]. *J*-coupling constants are given in Hz and the multiplicity is abbreviated as s = singlet, d = doublet, t = triplet, q = quartet and m

= multiplet. NMR spectra were analyzed with CCPN Analysis V2.4.2 and MestReC V8.1.4-12489 (Mestrelab Research, Santiago de Compostela/Spain) software.

### **Mass spectrometry**

Electron ionization (EI) measurements were recorded on a Thermo Finnigan MAT 95 (Thermo Fisher Scientific Inc., Waltham/USA) mass spectrometer. Denoted are the ionization method, the mass-to-charge ratio value ( $m/z$ ) and the related fragmentation. The resolution of EI-MS is 1000 u and of HR-EI-MS is 5000 u. Electron spray ionization (ESI) measurements were performed on a Thermo Finnigan LTQFT (Thermo Fisher Scientific Inc., Waltham/USA) mass spectrometer, with the same denotation.

### **CD spectroscopy**

CD measurements were done on a Jasco 810 CD spectrometer with a Jasco CDF-4265 Peltier-Element (Jasco Germany GmbH, Groß-Umstadt/Germany) and with Milli-Q water, phosphate buffer (20mM, pH 5.5) or methanol as solvent. Used cuvettes were of 1 mm thickness. Baseline correction was achieved by pure Milli-Q water, phosphate buffer or methanol spectra. Calculation of sample concentrations was done via the specific absorption at 323 nm, with  $\epsilon_{\text{azobenzene}} = 25000 \text{ L} \cdot \text{mol}^{-1} \cdot \text{cm}^{-1}$ . Recorded spectra were evaluated with the software Origin 8.0 (OriginLab Corporation, Northampton/USA) and were not smoothed.

### **IR spectroscopy**

IR spectroscopy was performed with a Bruker IFS 66 (Bruker Optik GmbH, Ettlingen/Germany). All spectra were recorded with  $c = 5.0 \text{ mM}$  solutions in  $\text{CD}_3\text{OD}$  at different temperatures.

### **UV/Vis spectroscopy**

UV spectra were recorded on a Cary50 UV/Vis spectrometer (Agilent, Santa Clara/CA/USA) or a Jasco V-650 UV/Vis spectrometer, with a Jasco PAC-743 Peltier-Element (Jasco Germany GmbH, Groß-Umstadt/Germany) and Milli-Q water, phosphate buffer (20 mM pH 5.5) or methanol as solvent. Spectra were recorded at 5 °C and cuvettes used were of 1 or 10 mm thickness.

## GENERAL PEPTIDE SYNTHESIS

As resin for the solid-phase peptide synthesis amino acid preloaded resins, which deliver free carboxylic acids or amides with different amino acid loadings were used. The synthesis of the peptides was performed on a 0.1 mmol scale and with standard coupling reagents HBTU/HOBt·H<sub>2</sub>O (0.5 M) in DMF, activated with DIEA (2 M) in DMF. The amino acid building blocks with standard residual protecting groups were coupled with a fivefold excess (2 M solutions). Special amino acid building blocks were coupled with a two-fold excess of HATU/HOAt·H<sub>2</sub>O (2.0 eq., 0.5 M) in DMF and NMM (4.0 eq.) in DMF. Consequent Fmoc deprotection was performed by treatment with piperidine in DMF (1:4). Final Fmoc-deprotection was followed by global deprotection of residual protecting groups and cleavage from the resin with a TFA/phenol/triisopropylsilane/H<sub>2</sub>O (88:5:5:2) cocktail within 2 hrs at room temperature under inert atmosphere. The resultant solution was filtered, concentrated under reduced pressure and precipitated in 40 mL chilled diethyl ether and stored overnight at -32 °C. After centrifugation and removal of the diethyl ether the resulting precipitated crude peptide was purified with RP-HPLC to yield the desired peptide products.

## REFERENCES

1. Christie, J. M., Salomon, M., Nozue, K., Wada, M. & Briggs, W. R. LOV (light, oxygen, or voltage) domains of the blue-light photoreceptor phototropin (nph1): binding sites for the chromophore flavin mononucleotide. *Proc. Natl. Acad. Sci. U.S.A.* **96**, 8779–8783 (1999).
2. Oesterhelt, D. & Stoerkenius, W. Rhodopsin-like protein from the purple membrane of Halobacterium halobium. *Nat. New Biol.* **233**, 149–152 (1971).
3. Deisseroth, K. Optogenetics. *Nat. Methods* **8**, 26–29 (2011).
4. Broichhagen, J., Frank, J. & Trauner, D. A roadmap to success in photopharmacology. *Acc. Chem. Res.* **48**, 1947–1960 (2015).
5. Velema, W. A., Szymanski, W. & Feringa, B. L. Photopharmacology: beyond proof of principle. *J. Am. Chem. Soc.* **136**, 2178–2191 (2014).
6. Fehrentz, T., Schönberger, M. & Trauner, D. Optochemical genetics. *Angew. Chem. Int. Ed. Engl.* **50**, 12156–12182 (2011).
7. Clementi, F. & Fumagalli, G. *General and molecular pharmacology - Principles of drug action*. (John Wiley & Sons, Inc., 2015).
8. Hopkins, A. L. Network pharmacology: the next paradigm in drug discovery. *Nat. Chem. Biol.* **4**, 682–690 (2008).
9. Konrad, D. B., Frank, J. A. & Trauner, D. Synthesis of Redshifted Azobenzene Photoswitches by Late-Stage Functionalization. *Chem. Eur. J.* **22**, 4364–4368 (2016).
10. Broichhagen, J., Frank, J. & Johnston, N. A red-shifted photochromic sulfonylurea for the remote control of pancreatic beta cell function. *Chem. Commun.* **51**, 6018–6021 (2015).
11. Dong, M., Babalhavaeji, A., Samanta, S., Beharry, A. A. & Woolley, A. G. Red-Shifting Azobenzene Photoswitches for in Vivo Use. *Acc. Chem. Res.* **48**, 2662–2670 (2015).
12. Bléger, D. & Hecht, S. Visible-Light-Activated Molecular Switches. *Angew. Chem. Int. Ed. Engl.* **54**, 11338–11349 (2015).
13. Szobota, S. *et al.* Remote control of neuronal activity with a light-gated glutamate receptor. *Neuron* **54**, 535–545 (2007).
14. Lemoine, D. *et al.* Optical control of an ion channel gate. *Proc. Natl. Acad. Sci. U.S.A.* **110**, 20813–20818 (2013).
15. Banghart, M., Borges, K., Isacoff, E., Trauner, D. & Kramer, R. H. Light-activated ion channels for remote control of neuronal firing. *Nat. Neurosci.* **7**, 1381–1386 (2004).
16. Broichhagen, J. *et al.* Optical control of insulin secretion using an incretin switch. *Angew. Chem. Int. Ed. Engl.* **54**, 15565–15569 (2015).
17. Lerch, M. M., Hansen, M. J., van Dam, G. M., Szymanski, W. & Feringa, B. L. Emerging Targets in Photopharmacology. *Angew. Chem. Int. Ed. Engl.* **55**, 2–24 (2016).
18. Wiki Commons, W. Il laboratorio dell'alchimista, Giovanni Stradano. (2006). Accessed 27/9/2016. [https://commons.wikimedia.org/wiki/File:Il\\_laboratorio\\_dell%27alchimista,\\_Giovanni\\_Stradano,\\_studiolo\\_di\\_Francesco\\_I.jpg](https://commons.wikimedia.org/wiki/File:Il_laboratorio_dell%27alchimista,_Giovanni_Stradano,_studiolo_di_Francesco_I.jpg)
19. Goodman, M. & Kossoy, A. Conformational aspects of polypeptide structure. XIX. Azoaromatic side-chain effects. *J. Am. Chem. Soc.* **88**, 5010–5011 (1966).
20. Renner, C. & Moroder, L. Azobenzene as conformational switch in model peptides. *Chem. Bio. Chem.* **7**, 868–878 (2006).
21. Podewin, T. *et al.* Photocontrolled chignolin-derived  $\beta$ -hairpin peptidomimetics. *Chem. Commun.* **51**, 4001–4004 (2015).
22. Hatfield, M. P., Murphy, R. F. & Lovas, S. The CLN025 decapeptide retains a  $\beta$ -hairpin conformation in urea and guanidinium chloride. *J. Phys. Chem. B* **115**, 4971–4981 (2011).
23. Schrader, T. E. *et al.* Light-triggered beta-hairpin folding and unfolding. *Proc. Natl. Acad. Sci. U.S.A.* **104**, 15729–15734 (2007).
24. Jurt, S., Aemissegger, A., Güntert, P., Zerbe, O. & Hilvert, D. A Photoswitchable Mini-protein Based on the Sequence of Avian Pancreatic Polypeptide. *Angew. Chem. Int. Ed. Engl.* **118**, 6445–6448 (2006).
25. Aemissegger, A., Krätzler, V., van Gunsteren, W. F. & Hilvert, D. A photoinducible beta-hairpin. *J. Am. Chem. Soc.* **127**, 2929–2936 (2006).
26. Hughes, R. M. & Waters, M. L. Model systems for  $\beta$ -hairpins and  $\beta$ -sheets. *Curr. Opin. Struct. Biol.* **16**, 514–524 (2006).

27. Dobson, C. Protein folding and misfolding. *Nature* **426**, 884–890 (2003).
28. Luo, D.-G., Xue, T. & Yau, K.-W. How vision begins: An odyssey. *Proc. Natl. Acad. Sci. U.S.A.* **105**, 9855–9862 (2008).
29. Pearing, J. N., Salinas, R. Y., Baker, S. A. & Arshavsky, V. Y. Protein sorting, targeting and trafficking in photoreceptor cells. *Prog. Retin. Eye Res.* **36**, 24–51 (2013).
30. Stolik, S., Delgado, J. A., Pérez, A. & Anasagasti, L. Measurement of the penetration depths of red and near infrared light in human 'ex vivo' tissues. *J. Photochem. Photobiol. B, Biol.* **57**, 90–93 (2000).
31. Wiedbrauk, S. & Dube, H. Hemithioindigo-an emerging photoswitch. *Tetrahedron Lett.* **56**, 4266–4274 (2015).
32. Kroon, R., Lenes, M., Hummelen, J. C., Blom, P. W. & de Boer, B. Small Bandgap Polymers for Organic Solar Cells (Polymer Material Development in the Last 5 Years). *Polym. Rev.* **48**, 531–582 (2008).
33. Schultz, D. M. & Yoon, T. P. Solar synthesis: prospects in visible light photocatalysis. *Science* **343**, 1239176 (2014).
34. Göstl, R., Senf, A. & Hecht, S. Remote-controlling chemical reactions by light: towards chemistry with high spatio-temporal resolution. *Chem. Soc. Rev.* **43**, 1982–1996 (2014).
35. Ernst, O. P. *et al.* Microbial and animal rhodopsins: structures, functions, and molecular mechanisms. *Chem. Rev.* **114**, 126–163 (2014).
36. Koch, K. & Dell'Orco, D. Protein and signaling networks in vertebrate photoreceptor cells. *Front. Mol. Neurosci.* **8**, 67–81 (2015).
37. Gao, S. *et al.* Optogenetic manipulation of cGMP in cells and animals by the tightly light-regulated guanylyl-cyclase opsin CyclOp. *Nat. Commun.* **6**, 8046–8058 (2015).
38. Broichhagen, J. *et al.* Optical control of insulin release using a photoswitchable sulfonylurea. *Nat. Commun.* **5**, 5116–5127 (2014).
39. Karlsson, C. *et al.* Phototriggerable peptidomimetics for the inhibition of Mycobacterium tuberculosis ribonucleotide reductase by targeting protein-protein binding. *Org. Biomol. Chem.* **13**, 2612–2621 (2015).
40. Waldeck, D. H. Photoisomerization dynamics of stilbenes. *Chem. Rev.* **91**, 415–436 (1991).
41. Irie, M., Fukaminato, T., Matsuda, K. & Kobatake, S. Photochromism of diarylethene molecules and crystals: memories, switches, and actuators. *Chem. Rev.* **114**, 12174–12277 (2014).
42. Fujimoto, K., Maruyama, T., Okada, Y., Itou, T. & Inouye, M. Development of a new class of photochromic peptides by using diarylethene-based non-natural amino acids. *Tetrahedron* **69**, 6170–6175 (2013).
43. Babii, O. *et al.* Controlling Biological Activity with Light: Diarylethene-Containing Cyclic Peptidomimetics. *Angew. Chem. Int. Ed. Engl.* **53**, 3392–3395 (2014).
44. Cordes, T. *et al.* Photochemical Z→E Isomerization of a Hemithioindigo/Hemistilbene  $\omega$ -Amino Acid. *Chem. Phys. Chem.* **8**, 1713–1721 (2007).
45. Herre, S. *et al.* Photoactivation of an Inhibitor of the 12/15-Lipoxygenase Pathway. *Chem. Bio Chem.* **7**, 1089–1095 (2006).
46. Herre, S., Steinle, W. & Rück-Braun, K. Synthesis of Photoswitchable Hemithioindigo-Based  $\omega$ -Amino Acids and Application in Boc-Based Peptide Assembly. *Synthesis* **19**, 3297–3300 (2005).
47. Bandara, H. M. & Burdette, S. C. Photoisomerization in different classes of azobenzene. *Chem. Soc. Rev.* **41**, 1809–1825 (2012).
48. Beharry, A. A., Sadovski, O. & Woolley, A. G. Azobenzene Photoswitching without Ultraviolet Light. *J. Am. Chem. Soc.* **133**, 19684–19687 (2011).
49. Samanta, S. *et al.* Photoswitching Azo Compounds in Vivo with Red Light. *J. Am. Chem. Soc.* **135**, 9777–9784 (2009).
50. Yang, Y., Hughes, R. P. & Aprahamian, I. Visible light switching of a BF<sub>2</sub>-coordinated azo compound. *J. Am. Chem. Soc.* **134**, 15221–15224 (2012).
51. Mart, R. J. & Allemann, R. K. Azobenzene photocontrol of peptides and proteins. *Chem. Commun.* **52**, 12262–12277 (2016).
52. Russow, M.-M. & Hecht, S. Photoswitches: From Molecules to Materials. *Adv. Mater.* **22**, 3348–3360 (2010).
53. Turanský, R., Konôpka, M., Doltsinis, N. L., Štich, I. & Marx, D. Switching of functionalized azobenzene suspended between gold tips by mechanochemical, photochemical, and opto-mechanical means. *Phys. Chem. Chem. Phys.* **12**, 13922–13932 (2010).
54. Tong, X., Pelletier, M., Lasia, A. & Zhao, Y. Fast Cis–Trans Isomerization of an Azobenzene Derivative in Liquids and Liquid Crystals under a Low Electric Field. *Angew. Chem. Int. Ed. Engl.* **47**, 3596–3599 (2008).
55. Henzl, J., Mehlhorn, M., Gawronski, H., Rieder, K. & Morgenstern, K. Reversible cis–trans Isomerization of a Single Azobenzene Molecule. *Angew. Chem. Int. Ed. Engl.* **45**, 603–606 (2006).

56. Beharry, A. A. & Woolley, G. A. Azobenzene photoswitches for biomolecules. *Chem. Soc. Rev.* **40**, 4422–4437 (2011).
57. Knoll, H. Photoisomerism in Azobenzenes, *CRC Handbook of Organic Photochemistry and Photobiology* 89–1 - 89–16 (CRC Press LLC, 2004).
58. Tsuji, T., Takeuchi, H., Egawa, T. & Konaka, S. Effects of molecular structure on the stability of a thermotropic liquid crystal. Gas electron diffraction study of the molecular structure of phenyl benzoate. *J. Am. Chem. Soc.* **123**, 6381–6387 (2001).
59. Fliegl, H., Köhn, A., Hättig, C. & Ahlrichs, R. Ab Initio Calculation of the Vibrational and Electronic Spectra of trans- and cis-Azobenzene. *J. Am. Chem. Soc.* **125**, 9821–9827 (2007).
60. Knie, C. *et al.* ortho-Fluoroazobenzenes: Visible Light Switches with Very Long-Lived Z Isomers. *Chem. Eur. J.* **20**, 16492–16501 (2014).
61. Merino, E. Synthesis of azobenzenes: the coloured pieces of molecular materials. *Chem. Soc. Rev.* **40**, 3835–3853 (2011).
62. Sadovski, O., Beharry, A. A., Zhang, F. & Woolley, A. G. Spectral Tuning of Azobenzene Photoswitches for Biological Applications. *Angew. Chem. Int. Ed. Engl.* **48**, 1484–1486 (2009).
63. Pozhidaeva, N., Cornier, M., Chaudhari, A. & Woolley, G. Reversible Photocontrol of Peptide Helix Content: Adjusting Thermal Stability of the Cis State. *Bioconjugate Chem.* **15**, 1297–1303 (2004).
64. Flint, D. G., Kumita, J. R., Smart, O. S. & Woolley, G. A. Using an Azobenzene Cross-Linker to Either Increase or Decrease Peptide Helix Content upon Trans-to-Cis Photoisomerization. *Chem. Biol.* **9**, 391–397 (2001).
65. Kumita, J. R., Flint, D. G., Smart, O. S. & Woolley, A. G. Photo-control of peptide helix content by an azobenzene cross-linker: steric interactions with underlying residues are not critical. *Protein Eng.* **15**, 561–569 (2002).
66. Tochitsky, I. *et al.* Restoring visual function to blind mice with a photoswitch that exploits electrophysiological remodeling of retinal ganglion cells. *Neuron* **81**, 800–813 (2014).
67. Broichhagen, J. *et al.* A red-shifted photochromic sulfonylurea for the remote control of pancreatic beta cell function. *Chem. Commun.* **51**, 6018–6021 (2015).
68. Weston, C. E., Richardson, R. D., Haycock, P. R., White, A. J. & Fuchter, M. J. Arylazopyrazoles: azoheteroarene photoswitches offering quantitative isomerization and long thermal half-lives. *J. Am. Chem. Soc.* **136**, 11878–11881 (2014).
69. Bléger, D., Schwarz, J., Brouwer, A. M. & Hecht, S. o-Fluoroazobenzenes as readily synthesized photoswitches offering nearly quantitative two-way isomerization with visible light. *J. Am. Chem. Soc.* **134**, 20597–20600 (2012).
70. Beharry, A. A., Sadovski, O. & Woolley, G. A. Photo-control of peptide conformation on a timescale of seconds with a conformationally constrained, blue-absorbing, photo-switchable linker. *Org. Biomol. Chem.* **6**, 4323–4332 (2008).
71. Duval, H. Benzidination. *Bull. Soc. Chim. Fr.* **7**, 529 (1910).
72. Böckmann, M., Doltsinis, N. L. & Marx, D. Unraveling a Chemically Enhanced Photoswitch: Bridged Azobenzene. *Angew. Chem. Int. Ed. Engl.* **49**, 3382–3384 (2010).
73. Samanta, S., Qin, C., Lough, A. J. & Woolley, G. A. Bidirectional Photocontrol of Peptide Conformation with a Bridged Azobenzene Derivative. *Angew. Chem. Int. Ed. Engl.* **51**, 6452–6455 (2012).
74. Siewertsen, R., Schönborn, J., Hartke, B. & Renth, F. Superior Z - E and E - Z photoswitching dynamics of dihydrodibenzodiazocine, a bridged azobenzene, by S1(np\*) excitation at  $\lambda = 387$  and 490 nm. *Phys. Chem. Chem. Phys.* **13**, 1054–1063 (2011).
75. Sell, H., Näther, C. & Herges, R. Amino-substituted diazocines as pincer-type photochromic switches. *Beilstein J. Org. Chem.* **9**, 1–7 (2013).
76. Liu, C. C. & Schultz, P. G. Adding new chemistries to the genetic code. *Annu. Rev. Biochem.* **79**, 413–444 (2010).
77. Wang, L., Brock, A., Herberich, B. & Schultz, P. Expanding the genetic code of Escherichia coli. *Science* **292**, 498–500 (2001).
78. Bose, M., Groff, D., Xie, J., Brustad, E. & Schultz, P. G. The incorporation of a photoisomerizable amino acid into proteins in E. coli. *J. Am. Chem. Soc.* **128**, 388–389 (2006).
79. Behrendt, R., Renner, C. & Schenk, M. Photomodulation of the conformation of cyclic peptides with azobenzene moieties in the peptide backbone. *Angew. Chem. Int. Ed. Engl.* **38**, 2171–2173 (1999).
80. Dong, S.-L. *et al.* A Photocontrolled  $\beta$ -Hairpin Peptide. *Chem. Eur. J.* **12**, 1114–1120 (2006).
81. Renner, C., Behrendt, R., Spörlein, S. & Wachtveitl, J. Photomodulation of conformational states. I. Mono- and bicyclic peptides with (4-amino) phenylazobenzoic acid as backbone constituent. *Biopolymers* **54**, 489–500 (2000).

82. Hoppmann, C., Lacey, V. & Louie, G. Genetically encoding photoswitchable click amino acids in *Escherichia coli* and mammalian cells. *Angew. Chem. Int. Ed.* **53**, 3932–3936 (2014).
83. Hoppmann, C., Maslennikov, I., Choe, S. & Wang, L. In Situ Formation of an Azo Bridge on Proteins Controllable by Visible Light. *Journal of the American Chemical Society* **137**, 11218–11221 (2015).
84. Paudler, W. W. & Zeiler, A. G. Diazocine chemistry. VI. Aromaticity of 5,6-dihydrodibenzo[b,f][1,2]diazocine. *J. Org. Chem.* **34**, 3237–3239 (1969).
85. Matej, S. *Rev. Roum. Chim.* **11**, 843 (1966).
86. Chun, Z. Copper-Catalyzed Aerobic Oxidative Dehydrogenative Coupling of Anilines Leading to Aromatic Azo Compounds using Dioxygen as an Oxidant. *Angew. Chem. Int. Ed. Engl.* **122**, 6174–6177 (2010).
87. Takeda, Y., Okumura, S. & Minakata, S. Oxidative Dimerization of Aromatic Amines using tBuOI: Entry to Unsymmetric Aromatic Azo Compounds. *Angew. Chem. int. Ed. Engl.* **51**, 7804–7808 (2012).
88. Takeda, Y., Okumura, S. & Minakata, S. practical synthetic procedures A Practical Synthesis of Azobenzenes through Oxidative Dimerization of Aromatic Amines Using tert-Butyl Hypoiodite. *Synthesis* **45**, 1029–1033 (2013).
89. Talaty, E. & Fargo, J. Thermal cis–trans-isomerization of substituted azobenzenes: a correction of the literature. *Chem. Commun.* **2**, 65–66 (1967). doi:10.1039/C19670000065
90. Johnson, K. W. The Oxidation of 2-Aminobenzothiazole. *J. Org. Chem.* **8**, 557–563 (1943).
91. Wang, M., Funabiki, K. & Matsui, M. Synthesis and properties of bis (hetaryl) azo dyes. *Dyes Pigm.* **57**, 77–86 (2003).
92. Iranpoor, N., Firouzabadi, H. & Khalili, D. Heteroaromatic azo compounds as efficient and recyclable reagents for direct conversion of aliphatic alcohols into symmetrical disulfides. *Tetrahedron Lett.* **53**, 6913–6915 (2012).
93. Dempster, D. N., Morrow, T. & Rankin, R. Photochemical characteristics of cyanine dyes. Part 1.—3, 3'-diethyloxadicarbocyanine iodide and 3, 3'-diethylthiadcarbocyanine iodide. *J. Chem. Soc., Faraday Trans. 2* **68**, 1479–1496 (1972).
94. Escobedo, J. O., Rusin, O., Lim, S. & Strongin, R. M. NIR dyes for bioimaging applications. *Curr. Opin. Chem. Biol.* **14**, 64–75 (2010).
95. Broichhagen, J. *et al.* Allosteric Optical Control of a Class B G-Protein-Coupled Receptor. *Angew. Chem. Int. Ed. Engl.* **55**, 5865–5868 (2016).
96. Schrader, T. *et al.* Folding and Unfolding of Light-Triggered beta-Hairpin Model Peptides. *J. Phys. Chem. B* **115**, 5219–5226 (2011).
97. Chisholm-Burns, M. A. *et al.* *Pharmacotherapy principles & practice*. 1968 (McGraw-Hill Medical Pub., New York, 2008).
98. Edwards, I. R. & Aronson, J. K. Adverse drug reactions: definitions, diagnosis, and management. *Lancet* **356**, 1255–1259 (2000).
99. Carlet, J. *et al.* Society's failure to protect a precious resource: antibiotics. *Lancet* **378**, 369–371 (2011).
100. Velema, W. A. *et al.* Optical control of antibacterial activity. *Nat. Chem.* **5**, 924–928 (2013).
101. Longley, D. B. & Johnston, P. G. Molecular mechanisms of drug resistance. *J. Pathol.* **205**, 275–292 (2005).
102. Martínez, J. L. L. Antibiotics and antibiotic resistance genes in natural environments. *Science* **321**, 365–367 (2008).
103. Lehár, J. *et al.* Synergistic drug combinations tend to improve therapeutically relevant selectivity. *Nat. Biotechnol.* **27**, 659–666 (2009).
104. DiMasi, J. A., Feldman, L., Seckler, A. & Wilson, A. Trends in risks associated with new drug development: success rates for investigational drugs. *Clin. Pharmacol. Ther.* **87**, 272–277 (2010).
105. Gaudana, R., Ananthula, H. K., Parenky, A. & Mitra, A. K. Ocular drug delivery. *AAPS J.* **12**, 348–360 (2010).
106. Hanahan, D. & Weinberg, R. A. Hallmarks of cancer: the next generation. *Cell* **144**, 646–674 (2011).
107. Nicolaides, N. C., Sass, P. M. & Grasso, L. Advances in targeted therapeutic agents. *Expert Opin. Drug Discovery* **5**, 1123–1140 (2010).
108. Sawyers, C. L. The cancer biomarker problem. *Nature* **452**, 548–552 (2008).
109. Malhotra, V. & Perry, M. C. Classical chemotherapy: mechanisms, toxicities and the therapeutic window. *Cancer Biol. Ther.* **2**, 2–4 (2003).
110. Berndt, A. & Deisseroth, K. Expanding the optogenetics toolkit. *Science* **349**, 590–591 (2015).
111. Steinbeck, J. A. *et al.* Optogenetics enables functional analysis of human embryonic stem cell-derived grafts in a Parkinson's disease model. *Nat. Biotechnol.* **33**, 204–209 (2015).
112. Fan, W., Huang, P. & Chen, X. Overcoming the Achilles' heel of photodynamic therapy. *Chem. Soc. Rev.* **45**, 6488–6519 (2016).

113. Szymanski, W. & Reeßing, F. Beyond Photodynamic Therapy: Light-Activated Cancer Chemotherapy. *Curr. Med. Chem.* (2016).
114. Zhang, F. *et al.* The microbial opsin family of optogenetic tools. *Cell* **147**, 1446–1457 (2011).
115. Gorostiza, P. & Isacoff, E. Y. Optical switches for remote and noninvasive control of cell signaling. *Science* **322**, 395–399 (2008).
116. Deisseroth, K. *et al.* Next-generation optical technologies for illuminating genetically targeted brain circuits. *J. Neurosci.* **26**, 10380–10386 (2006).
117. Adamantidis, A. R., Zhang, F., Aravanis, A. M., Deisseroth, K. & de Lecea, L. Neural substrates of awakening probed with optogenetic control of hypocretin neurons. *Nature* **450**, 420–424 (2007).
118. Sharman, W. M., Allen, C. M. & van Lier, J. E. Role of activated oxygen species in photodynamic therapy. *Meth. Enzymol.* **319**, 376–400 (2000).
119. Brieke, C., Rohrbach, F., Gottschalk, A., Mayer, G. & Heckel, A. Light-Controlled Tools. *Angew. Chem. Int. Ed. Engl.* **51**, 8446–8476 (2012).
120. Kalka, K., Merk, H. & Mukhtar, H. Photodynamic therapy in dermatology. *J. Am. Acad. Dermatol.* **42**, 389–413 (2000).
121. Weissleder, R. & Ntziachristos, V. Shedding light onto live molecular targets. *Nat. Med.* **9**, 123–8 (2003).
122. Yoon, I., Li, J. Z. & Shim, Y. K. Advance in photosensitizers and light delivery for photodynamic therapy. *Clin. Endosc.* **46**, 7–23 (2013).
123. Frazier, C. C. Photodynamic therapy in dermatology. *Int. J. Dermatol.* **35**, 312–316 (1996).
124. Agostinis, P. *et al.* Photodynamic therapy of cancer: an update. *CA Cancer J. Clin.* **61**, 250–281 (2011).
125. Cheng, A. C. *et al.* Structure-based maximal affinity model predicts small-molecule druggability. *Nat. Rev. Drug Discov.* **25**, 71–75 (2007).
126. Zhao, B. & He, Y.-Y. Y. Recent advances in the prevention and treatment of skin cancer using photodynamic therapy. *Expert Rev. Anticancer Ther.* **10**, 1797–1809 (2010).
127. Bessler, N. M. Verteporfin therapy in age-related macular degeneration (VAM): an open-label multicenter photodynamic therapy study of 4,435 patients. *Retina* **24**, 512–520 (2004).
128. Nanashima, A. & Nagayasu, T. Current Status of Photodynamic Therapy in Digestive Tract Carcinoma in Japan. *Int. J. Mol. Sci.* **16**, 3434–3440 (2015).
129. Sobaniec, S. *et al.* Clinical assessment of the efficacy of photodynamic therapy in the treatment of oral lichen planus. *Lasers Med. Sci.* **28**, 311–316 (2013).
130. Simone, C. B. & Cengel, K. A. Photodynamic therapy for lung cancer and malignant pleural mesothelioma. *Semin. Oncol.* **41**, 820–830 (2014).
131. Baron, T. H. Photodynamic therapy: standard of care for palliation of cholangiocarcinoma? *Clin. Gastroenterol. Hepatol.* **6**, 266–267 (2008).
132. Kubiak, M., Łysenko, L., Gerber, H. & Nowak, R. Cell reactions and immune responses to photodynamic therapy in oncology. *Postepy Hig. Med. Dosw.* **70**, 735–742 (2016).
133. Kammerer, R. *et al.* Induction of immune mediators in glioma and prostate cancer cells by non-lethal photodynamic therapy. *PLoS ONE* **6**, e21834 (2011).
134. Ziółkowski, P. & Milach, J. Photodynamic therapy of transplantable interstitioma testis in Wistar rats; histopathological examination after Evans blue injections. *Patol. Pol.* **44**, 79–83 (1993).
135. Al-Watban, F. A. & Zhang, X. Y. Photodynamic therapy of human undifferentiated thyroid carcinoma-bearing nude mice using topical 5-aminolevulinic acid. *Photomed. Laser Surg.* **23**, 206–211 (2005).
136. Bown, S. G. *et al.* Photodynamic therapy for cancer of the pancreas. *Gut* **50**, 549–557 (2002).
137. Nathan, T. R. *et al.* Photodynamic therapy for prostate cancer recurrence after radiotherapy: a phase I study. *J. Urol.* **168**, 1427–1432 (2002).
138. McCarthy, J. R., Korngold, E., Weissleder, R. & Jaffer, F. A. A light-activated theranostic nanoagent for targeted macrophage ablation in inflammatory atherosclerosis. *Small* **6**, 2041–2049 (2010).
139. Quirk, B. J. *et al.* Photodynamic therapy (PDT) for malignant brain tumors—where do we stand? *Photodiagn. Photodyn. Ther.* **12**, 530–544 (2015).
140. Podewin, T. *et al.* Optical control of a receptor-linked guanylyl cyclase using a photoswitchable peptidic hormone. *manuscript* (2016).
141. Broichhagen, J. *et al.* Orthogonal Optical Control of a G Protein-Coupled Receptor with a SNAP-Tethered Photochromic Ligand. *ACS Cent. Sci.* **1**, 383–393 (2015).
142. Hinner, M. J. & Johnsson, K. How to obtain labeled proteins and what to do with them. *Curr. Opin. Biotechnol.* **21**, 766–776 (2010).
143. Gautier, A. *et al.* An engineered protein tag for multiprotein labeling in living cells. *Chem. Biol.* **15**, 128–136 (2008).

144. Vafabakhsh, R., Levitz, J. & Isacoff, E. Y. Conformational dynamics of a class C G-protein-coupled receptor. *Nature* **524**, 497–501 (2015).
145. Cole, N. B. & Donaldson, J. G. Releasable SNAP-tag probes for studying endocytosis and recycling. *ACS Chem. Biol.* **7**, 464–469 (2012).
146. Keppler, A. *et al.* A general method for the covalent labeling of fusion proteins with small molecules in vivo. *Nat. Biotechnol.* **21**, 86–89 (2003).
147. Los, G. V. *et al.* HaloTag: a novel protein labeling technology for cell imaging and protein analysis. *ACS Chem. Biol.* **3**, 373–382 (2008).
148. Chen, I., Howarth, M., Lin, W. & Ting, A. Y. Site-specific labeling of cell surface proteins with biophysical probes using biotin ligase. *Nat. Methods* **2**, 99–104 (2005).
149. Alberts, B. *Molekularbiologie der Zelle.* (Wiley-VCH Verlag GmbH, 2004).
150. Levitan, I. B. & Kaczmarek, L. K. *The neuron: cell and molecular biology.* (Oxford University Press USA, 2015).
151. Blaustein, R. O., Cole, P. A., Williams, C. & Miller, C. Tethered blockers as molecular ‘tape measures’ for a voltage-gated K<sup>+</sup> channel. *Nat. Struct. Biol.* **7**, 309–311 (2000).
152. Volgraf, M. *et al.* Allosteric control of an ionotropic glutamate receptor with an optical switch. *Nat. Chem. Biol.* **2**, 47–52 (2006).
153. Stawski, P., Sumser, M. & Trauner, D. A photochromic agonist of AMPA receptors. *Angew. Chem. Int. Ed. Engl.* **51**, 5748–5751 (2012).
154. Potter, L. R., Abbey-Hosch, S. & Dickey, D. M. Natriuretic peptides, their receptors, and cyclic guanosine monophosphate-dependent signaling functions. *Endocr. Rev.* **27**, 47–72 (2005).
155. Schulz, S. C-type natriuretic peptide and guanylyl cyclase B receptor. *Peptides* **26**, 1024–1034 (2005).
156. Song, W., Wang, H. & Wu, Q. Atrial natriuretic peptide in cardiovascular biology and disease (NPPA). *Gene* **569**, 1–6 (2015).
157. Goetze, J. P. *et al.* Atrial natriuretic peptides in plasma. *Clin. Chim. Acta* **443**, 25–28 (1999).
158. Sergeeva, I. A. & Christoffels, V. M. Regulation of expression of atrial and brain natriuretic peptide, biomarkers for heart development and disease. *Biochim. Biophys. Acta BBA - Mol. Basis. Dis.* **1832**, 2403–2413 (2013).
159. Saito, Y. Roles of atrial natriuretic peptide and its therapeutic use. *J. Cardiol.* **56**, 262–270 (2010).
160. Theilig, F. & Wu, Q. ANP-induced signaling cascade and its implications in renal pathophysiology. *Am. J. Physiol. Renal Physiol.* **569**, 1047–1055 (2015).
161. Zhang, S. *et al.* Cardiovascular and renal effect of CNAAC: An innovatively designed natriuretic peptide. *Eur. J. Pharmacol.* **761**, 180–188 (2015).
162. Buglioni, A. & Jr, J. C. A gut-heart connection in cardiometabolic regulation. *Nat. Med.* **19**, 534–536 (2013).
163. Magnusson, M. *et al.* Low plasma level of atrial natriuretic peptide predicts development of diabetes: the prospective Malmo Diet and Cancer study. *J. Clin. Endocrinol. Metab.* **97**, 638–645 (2012).
164. Gruden, G., Landi, A. & Bruno, G. Natriuretic peptides, heart, and adipose tissue: New findings and future developments for diabetes research. *Diabetes Care* **37**, 2899–2908 (2014).
165. Jujic, A. *et al.* Atrial Natriuretic Peptide in the high normal range is associated with lower prevalence of insulin resistance. *J. Clin. Endocrinol. Metab.* **101**, jc20153518 (2016).
166. Bold, D. A., Borenstein, H., Veress, A. & Sonnenberg, H. A rapid and potent natriuretic response to intravenous injection of atrial myocardial extract in rats. *Life Sci.* **28**, 89–94 (1981).
167. You, H. & Laychock, S. G. Atrial natriuretic peptide promotes pancreatic islet beta-cell growth and Akt/Foxo1a/cyclin D2 signaling. *Endocrinol.* **150**, 5455–5465 (2009).
168. You, H. & Laychock, S. G. Long-term treatment with atrial natriuretic peptide inhibits ATP production and insulin secretion in rat pancreatic islets. *Am. J. Physiol. Endocrinol. Metab.* **300**, E435–444 (2011).
169. Lee, B. & Laychock, S. G. Atrial natriuretic peptide and cyclic nucleotides affect glucose-induced Ca<sup>2+</sup> responses in single pancreatic islet-cells correlation with (Ca<sup>2+</sup> + Mg<sup>2+</sup>)-ATPase activity. *Diabetes* **46**, 1312–1318 (1997).
170. Matsuura, N. *et al.* Nitric oxide-cyclic GMP system potentiates glucose-induced rise in cytosolic Ca<sup>2+</sup> concentration in rat pancreatic beta-cells. *Life Sci.* **65**, 1515–1522 (1999).
171. Ropero, A. *et al.* The atrial natriuretic peptide and guanylyl cyclase-A system modulates pancreatic beta-cell function. *Endocrinology* **151**, 3665–3674 (2010).
172. Kuhn, M. Cardiac Actions of Atrial Natriuretic Peptide: New Visions of an Old Friend. *Circ. Res.* **116**, 1278–1280 (2015).

173. Potter, L. R., Yoder, A. R., Flora, D. R., Antos, L. K. & Dickey, D. M. Natriuretic peptides: their structures, receptors, physiologic functions and therapeutic applications. *Handb. Exp. Pharmacol.* **191**, 341–366 (2009).
174. Foundation, I. D. IDF Diabetes Atlas. **7**, 1–141 (2015).
175. Evans, J. M., Newton, R. W., Ruta, D. A., MacDonald, T. M. & Morris, A. D. Socio-economic status, obesity and prevalence of Type 1 and Type 2 diabetes mellitus. *Diabet. Med.* **17**, 478–480 (2000).
176. Prentki, M., Matschinsky, F. M. & Madiraju, S. R. Metabolic signaling in fuel-induced insulin secretion. *Cell Metab.* **18**, 162–185 (2013).
177. Ashcroft, F. M. & Rorsman, P. Diabetes mellitus and the  $\beta$  cell: the last ten years. *Cell* **148**, 1160–1171 (2012).
178. Nolan, C. J., Damm, P. & Prentki, M. Type 2 diabetes across generations: from pathophysiology to prevention and management. *Lancet* **378**, 169–181 (2011).
179. Maruthur, N. M. *et al.* Diabetes Medications as Monotherapy or Metformin-Based Combination Therapy for Type 2 Diabetes: A Systematic Review and Meta-analysis. *Ann. Int. Med.* **164**, 740–751 (2016).
180. Turner, R. C., Cull, C. A., Frighi, V. & Holman, R. R. Glycemic control with diet, sulfonylurea, metformin, or insulin in patients with type 2 diabetes mellitus: progressive requirement for multiple therapies (UKPDS 49). UK Prospective Diabetes Study (UKPDS) Group. *JAMA* **281**, 2005–2012 (1999).
181. Fineman, M. S. *et al.* Effect on glycemic control of exenatide (synthetic exendin-4) additive to existing metformin and/or sulfonylurea treatment in patients with type 2 diabetes. *Diabetes care* **26**, 2370–2377 (2003).
182. Inzucchi, S. E. *et al.* Management of hyperglycemia in type 2 diabetes: a patient-centered approach: position statement of the American Diabetes Association (ADA) and the European Association for the Study of Diabetes (EASD). *Diabetes Care* **35**, 1364–1379 (2012).
183. Hundal, R. S. *et al.* Mechanism by which metformin reduces glucose production in type 2 diabetes. *Diabetes* **49**, 2063–2069 (2000).
184. Collier, C. A., Bruce, C. R., Smith, A. C., Lopaschuk, G. & Dyck, D. J. Metformin counters the insulin-induced suppression of fatty acid oxidation and stimulation of triacylglycerol storage in rodent skeletal muscle. *Am. J. Physiol. Endocrinol. Metab.* **291**, E182–189 (2006).
185. Ashcroft, F. M. & Gribble, F. M. ATP-sensitive K<sup>+</sup> channels and insulin secretion: their role in health and disease. *Diabetologia* **42**, 903–919 (1999).
186. Drucker, D. J. & Nauck, M. A. The incretin system: glucagon-like peptide-1 receptor agonists and dipeptidyl peptidase-4 inhibitors in type 2 diabetes. *Lancet* **368**, 1696–1620 (2006).
187. Drucker, D. J. The biology of incretin hormones. *Cell Metabolism* **3**, 152–165 (2005).
188. Baggio, L. & Drucker, D. Biology of incretins: GLP-1 and GIP. *Gastroenterol.* **132**, 2131–2157 (2007).
189. Campbell, J. E. & Drucker, D. J. Pharmacology, physiology, and mechanisms of incretin hormone action. *Cell Metab.* **17**, 819–37 (2013).
190. McCormack, P. L. Exenatide Twice Daily: A Review of Its Use in the Management of Patients with Type 2 Diabetes Mellitus. *Drugs* **74**, 325–351 (2014).
191. Lund, A., Knop, F. K. & Vilsbøll, T. Glucagon-like peptide-1 receptor agonists for the treatment of type 2 diabetes: differences and similarities. *Eur. J. Intern. Med.* **25**, 407–414 (2014).
192. Meier, J. J. GLP-1 receptor agonists for individualized treatment of type 2 diabetes mellitus. *Nat. Rev. Endocrinol.* **8**, 728–742 (2012).
193. Knudsen, L. B. *et al.* Potent derivatives of glucagon-like peptide-1 with pharmacokinetic properties suitable for once daily administration. *J. Med. Chem.* **43**, 1664–1669 (2000).
194. Egan, A. G. *et al.* Pancreatic safety of incretin-based drugs--FDA and EMA assessment. *N. Engl. J. Med.* **370**, 794–797 (2014).
195. Meier, J. J. & Nauck, M. A. Risk of pancreatitis in patients treated with incretin-based therapies. *Diabetologia* **57**, 1320–1324 (2014).
196. Nauck, M. A. & Friedrich, N. Do GLP-1-based therapies increase cancer risk? *Diabetes Care* **36**, S245–S252 (2013).
197. Roed, S. N., Nøhr, A. C., Wismann, P. & Iversen, H. Functional consequences of glucagon-like peptide-1 receptor cross-talk and trafficking. *J. Biol. Chem.* **290**, 1233–1243 (2015).
198. Russell-Jones, D. Molecular, pharmacological and clinical aspects of liraglutide, a once-daily human GLP-1 analogue. *Mol. Cell. Endocrinol.* **297**, 137–140 (2009).
199. Blanco, F. *et al.* NMR solution structure of the isolated N-terminal fragment of protein-G B1 domain. Evidence of trifluoroethanol induced native-like beta-hairpin formation. *Biochemistry* **33**, 6004–6014 (1994).

200. Nelson, J. W. & Kallenbach, N. R. Persistence of the alpha-helix stop signal in the S-peptide in trifluoroethanol solutions. *Biochemistry* **28**, 5256–5261 (1989).
201. Holst, J. J. The physiology of glucagon-like peptide 1. *Physiol. Rev.* **87**, 1409–1439 (2007).
202. Widmann, C., Dolci, W. & Thorens, B. Internalization and homologous desensitization of the GLP-1 receptor depend on phosphorylation of the receptor carboxyl tail at the same three sites. *Mol. Endocrinol.* **11**, 1094–1102 (1997).
203. Roed, S. N. *et al.* Real-time trafficking and signaling of the glucagon-like peptide-1 receptor. *Mol. Cell. Endocrinol.* **382**, 938–949 (2014).
204. Hanyaloglu, A. C. & von Zastrow, M. Regulation of GPCRs by endocytic membrane trafficking and its potential implications. *Annu. Rev. Pharmacol. Toxicol.* **48**, 537–568 (2008).
205. Kuna, R. S. *et al.* Glucagon-like peptide-1 receptor-mediated endosomal cAMP generation promotes glucose-stimulated insulin secretion in pancreatic  $\beta$ -cells. *Am. J. Physiol. Endocrinol. Metab.* **305**, E161–170 (2013).
206. Irannejad, R, Tomshine, JC, Tomshine, JR & Chevalier, M. Conformational biosensors reveal GPCR signalling from endosomes. *Nature* **495**, 534–538 (2013).
207. Radford, S. E. & Dobson, C. M. From computer simulations to human disease: emerging themes in protein folding. *Cell* **97**, 291–298 (1999).
208. Vendruscolo, M., Zurdo, J., MacPhee, C. E. & Dobson, C. M. Protein folding and misfolding: a paradigm of self-assembly and regulation in complex biological systems. *Philos. Trans. A Math. Phys. Eng. Sci.* **361**, 1205–1222 (2003).
209. Ellis, R. J. Macromolecular crowding: an important but neglected aspect of the intracellular environment. *Curr. Opin. Struct. Biol.* **11**, 114–119 (2001).
210. Dobson, C. M. The structural basis of protein folding and its links with human disease. *Philos. Trans. R. Soc. Lond., B, Biol. Sci.* **356**, 133–145 (2001).
211. Selkoe, D. J. Folding proteins in fatal ways. *Nature* **426**, 900–904 (2003).
212. Dobson, C. M. Getting out of shape. *Nature* **418**, 729–730 (2002).
213. Walsh, C. Molecular mechanisms that confer antibacterial drug resistance. *Nature* **406**, 775–781 (2000).
214. Culyba, M. J., Mo, C. Y. & Kohli, R. M. Targets for Combating the Evolution of Acquired Antibiotic Resistance. *Biochemistry* **54**, 3573–3582 (2015).
215. Fersht, A. R. & Daggett, V. Protein folding and unfolding at atomic resolution. *Cell* **108**, 573–582 (2002).
216. Dinner, A. R., Sali, A., Smith, L. J., Dobson, C. M. & Karplus, M. Understanding protein folding via free-energy surfaces from theory and experiment. *Trends Biochem. Sci.* **25**, 331–339 (2000).
217. Anfinsen, C. B. Principles that govern the folding of protein chains. *Science* **181**, 223–230 (1973).
218. Hardesty, B. & Kramer, G. Folding of a nascent peptide on the ribosome. *Prog. Nucleic Acid Res. Mol. Biol.* **66**, 41–66 (2001).
219. Bukau, B. & Horwich, A. L. The Hsp70 and Hsp60 chaperone machines. *Cell* **92**, 351–366 (1998).
220. Hartl, F. U. & Hayer-Hartl, M. Molecular chaperones in the cytosol: from nascent chain to folded protein. *Science* **295**, 1852–1858 (2002).
221. Kaufman, R. J. *et al.* The unfolded protein response in nutrient sensing and differentiation. *Nat. Rev. Mol. Cell Biol.* **3**, 411–421 (2002).
222. Broome, B. M. & Hecht, M. H. Nature disfavors sequences of alternating polar and non-polar amino acids: implications for amyloidogenesis. *J. Mol. Biol.* **296**, 961–968 (2000).
223. Fernández, A., Belinky, A. & Boland, M. de las M. de L. Protein folding: where is the paradox? *J. Biomol. Struct. Dyn.* **20**, 331–332 (2002).
224. Rooman, M., Dehouck, Y., Kwasigroch, J. M., Biot, C. & Gilis, D. What is paradoxical about Levinthal paradox? *J. Biomol. Struct. Dyn.* **20**, 327–329 (2002).
225. Liu, F. & Gruebele, M. Downhill dynamics and the molecular rate of protein folding. *Chem. Phys. Lett.* **461**, 1–8 (2008).
226. Shakhnovich, E., Abkevich, V. & Ptitsyn, O. Conserved residues and the mechanism of protein folding. *Nature* **379**, 96–98 (1996).
227. Dobson, C. M. & Karplus, M. The fundamentals of protein folding: bringing together theory and experiment. *Curr. Opin. Struct. Biol.* **9**, 92–101 (1999).
228. Schuler, B., Lipman, E. A. & Eaton, W. A. Probing the free-energy surface for protein folding with single-molecule fluorescence spectroscopy. *Nature* **419**, 743–747 (2002).
229. Searle, M. S., Williams, D. H. & Packman, L. C. A short linear peptide derived from the N-terminal sequence of ubiquitin folds into a water-stable non-native  $\beta$ -hairpin. *Nat. Struct. Biol.* **2**, 999–1006 (1995).

230. Kim, D. E., Fisher, C. & Baker, D. A breakdown of symmetry in the folding transition state of protein L. *J. Mol. Biol.* **298**, 971–984 (2000).
231. Zimmerman, S. S. & Scheraga, H. A. Local interactions in bends of proteins. *Proc. Natl. Acad. Sci. U.S.A.* **74**, 4126–4129 (1977).
232. Marcelino, A. C. & Gierasch, L. M. Roles of  $\beta$ -turns in protein folding: From peptide models to protein engineering. *Biopolymers* **89**, 380–391 (2008).
233. Rotondi, K. S. & Gierasch, L. M. Natural polypeptide scaffolds:  $\beta$ -sheets,  $\beta$ -turns, and  $\beta$ -hairpins. *Biopolymers* **84**, 13–22 (2006).
234. Ciani, B., Jourdan, M. & Searle, M. S. Stabilization of  $\beta$ -Hairpin Peptides by Salt Bridges: Role of Preorganization in the Energetic Contribution of Weak Interactions. *J. Am. Chem. Soc.* **125**, 9038–9047 (2003).
235. Dyer, R. B. *et al.* The mechanism of beta-hairpin formation. *Biochemistry* **43**, 11560–11566 (2004).
236. Lewandowska, A., Oldziej, S., Liwo, A. & Scheraga, H. A. Mechanism of formation of the C-terminal  $\beta$ -hairpin of the B3 domain of the immunoglobulin-binding protein G from Streptococcus. IV. Implication for the mechanism of folding of the parent protein. *Biopolymers* **93**, 469–480 (2010).
237. Munoz, V. *et al.* Folding and Aggregation Kinetics of a  $\beta$ -Hairpin. *Biochemistry* **45**, 7023–7035 (2006).
238. Munoz, V., Thompson, P. A., Hofrichter, J. & Eaton, W. A. Folding dynamics and mechanism of  $\beta$ -hairpin formation. *Nature* **390**, 196–199 (1999).
239. Munoz, V., Henry, E. R., Hofrichter, J. & Eaton, W. A. A statistical mechanical model for  $\beta$ -hairpin kinetics. *Proc. Natl. Acad. Sci. U. S. A.* **95**, 5872–5879 (1998).
240. Bonomi, M., Branduardi, D. R., Gervasio, F. L. & Parrinello, M. The Unfolded Ensemble and Folding Mechanism of the C-Terminal GB1  $\beta$ -Hairpin. *J. Am. Chem. Soc.* **130**, 13938–13944 (2008).
241. Lewandowska, A., Oldziej, S., Liwo, A. & Scheraga, H.  $\beta$ -hairpin-forming peptides; models of early stages of protein folding. *Biophys. Chem.* **151**, 1–9 (2010).
242. Espinosa, J. F., Syud, F. A. & Gellman, S. H. Analysis of the factors that stabilize a designed two-stranded antiparallel beta-sheet. *Protein Sci.* **11**, 1492–1505 (2002).
243. Cochran, A. G., Skelton, N. J. & Starovasnik, M. A. Tryptophan zippers: stable, monomeric beta -hairpins. *Proc. Natl. Acad. Sci. U.S.A.* **98**, 5578–83 (2001).
244. Kobayashi, N., Honda, S., Yoshii, H. & MuneKata, E. Role of Side-chains in the Cooperative  $\beta$ -Hairpin Folding of the Short C-Terminal Fragment Derived from Streptococcal Protein G. *Biochemistry* **39**, 6564–6571 (2000).
245. Dinner, A. R., Lazaridis, T. & Karplus, M. Understanding  $\beta$ -hairpin formation. *Proc. Natl. Acad. Sci. U. S. A.* **96**, 9068–9073 (1999).
246. Fernández, A. & Scheraga, H. Insufficiently dehydrated hydrogen bonds as determinants of protein interactions. *Proc. Natl. Acad. Sci. U.S.A.* **100**, 113–118 (2003).
247. Cox, J., Evans, PA, Packman, LC & Williams, DH. Dissecting the structure of a partially folded protein: circular dichroism and nuclear magnetic resonance studies of peptides from ubiquitin. *J. Mol. Biol.* **234**, 483-492 (1993).
248. Volk, M. Fast initiation of peptide and protein folding processes. *Eur. J. Org. Chem.* **2001**, 2605–2621 (2001).
249. Leitner, D. M. & Straub, J. E. *Proteins: Energy, Heat and Signal Flow.* (Taylor & Francis, 2010).
250. Wachtveitl, J. *et al.* Ultrafast conformational dynamics in cyclic azobenzene peptides of increased flexibility. *Biophys. J.* **86**, 2350–2362 (2004).
251. Bredenbeck, J. *et al.* Picosecond conformational transition and equilibration of a cyclic peptide. *Proc. Natl. Acad. Sci. U.S.A.* **100**, 6452–6457 (2003).
252. Erdélyi, M., Karlén, A. & Gogoll, A. A New Tool in Peptide Engineering: A Photoswitchable Stilbene-type  $\beta$ -Hairpin Mimetic. *Chem. Eur. J.* **12**, 403–412 (2005).
253. Kräutler, V. *et al.* Use of molecular dynamics in the design and structure determination of a photoinducible beta-hairpin. *J. Am. Chem. Soc.* **127**, 4935–4942 (2005).
254. Deeg, A. A. *et al.* Isomerization- and temperature-jump-induced dynamics of a photoswitchable  $\beta$ -hairpin. *Chemistry* **20**, 694–703 (2014).
255. Enemark, S. & Rajagopalan, R. Turn-directed folding dynamics of  $\beta$ -hairpin-forming de novo decapeptide Chignolin. *Phys. Chem. Chem. Phys.* **14**, 12442–12450 (2012).
256. Thukral, L., Smith, J. C. & Daidone, I. Common Folding Mechanism of a  $\beta$ -Hairpin Peptide via Non-native Turn Formation Revealed by Unbiased Molecular Dynamics Simulations. *J. Am. Chem. Soc.* **131**, 18147–18152 (2009).

257. Santiveri, C. M., Rico, M. & Jiménez, M. A.  $^{13}\text{C}(\alpha)$  and  $^{13}\text{C}(\beta)$  chemical shifts as a tool to delineate beta-hairpin structures in peptides. *J. Biomol. NMR* **19**, 331–345 (2001).
258. Honda, S., Yamasaki, K., Sawada, Y. & Morii, H. 10 residue folded peptide designed by segment statistics. *Structure* **12**, 1507–1517 (2004).
259. Kinch, L., Wrabl, J. & Krishna, S. CASP5 assessment of fold recognition target predictions. *Proteins Struct. Funct. Bioinf.* **53**, 395–409 (2003).
260. Simons, K., Kooperberg, C., Huang, E. & Baker, D. Assembly of protein tertiary structures from fragments with similar local sequences using simulated annealing and Bayesian scoring functions. *J. Mol. Biol.* **268**, 209–225 (1997).
261. Gilbert, W. Genes-in-pieces revisited. *Science* **228**, 823–824 (1985).
262. Seidel, H. & Pompliano, D. Exons as microgenes? *Science* **257**, 1489–1490 (1992).
263. Honda, S., Kobayashi, N. & Munekata, E. Thermodynamics of a  $\beta$ -Hairpin Structure: Evidence for Cooperative Formation of Folding Nucleus. *J. Mol. Biol.* **295**, 269–278 (1999).
264. Sibanda, B., Blundell, T. L. & Thornton, J. M. Conformation of  $\beta$ -hairpins in protein structures: A systematic classification with applications to modelling by homology, electron density fitting and protein engineering. *J. Mol. Biol.* **206**, 759–777 (1989).
265. Sibanda, B. L. & Thornton, J. M. Beta-hairpin families in globular proteins. *Nature* **316**, 170–174 (1985).
266. Terada, T. & Shimizu, K. A comparison of generalized Born methods in folding simulations. *Chem. Phys. Lett.* **460**, 295–299 (2008).
267. Best, R. B. & Mittal, J. Microscopic events in  $\beta$ -hairpin folding from alternative unfolded ensembles. *Proc. Natl. Acad. Soc. U.S.A.* **108**, 11087–11092 (2011).
268. Renner, C., Cramer, J., Behrendt, R. & Moroder, L. Photomodulation of conformational states. II. Mono- and bicyclic peptides with (4-aminomethyl)phenylazobenzoic acid as backbone constituent. *Biopolymers* **54**, 501–514 (2000).
269. Löweneck, M. *et al.* A conformational two-state peptide model system containing an ultrafast but soft light switch. *Biophys. J.* **90**, 2099–2108 (2006).
270. Wu, L., McElheny, D., Setnicka, V., Hilario, J. & Keiderling, T. A. Role of different  $\beta$ -turns in  $\beta$ -hairpin conformation and stability studied by optical spectroscopy. *Proteins: Struct. Funct. Bioinf.* **80**, 44–60 (2012).
271. Roy, A., Bour, P. & Keiderling, T. A. TD-DFT modeling of the circular dichroism for a tryptophan zipper peptide with coupled aromatic residues. *Chirality* **21**, E163–71 (2009).
272. Wu, L., McElheny, D., Takekiyo, T. & Keiderling, T. Geometry and efficacy of cross-strand Trp/Trp, Trp/Tyr, and Tyr/Tyr aromatic interaction in a  $\beta$ -hairpin peptide. *Biochemistry* **49**, 4705–4714 (2010).
273. Mahalakshmi, R., Raghobama, S. & Balaram, P. NMR analysis of aromatic interactions in designed peptide beta-hairpins. *J. Am. Chem. Soc.* **128**, 1125–1138 (2006).
274. Vranken, W. F. & Rieping, W. Relationship between chemical shift value and accessible surface area for all amino acid atoms. *BMC Struct. Biol.* **9**, 20 (2009).
275. Ösapay, K. & Case, D. Analysis of proton chemical shifts in regular secondary structure of proteins. *J. Biomol. NMR* **4**, 215–230 (1994).
276. Lindorff-Larsen, K., Piana, S., Dror, R. O. & Shaw, D. E. How fast-folding proteins fold. *Science* **334**, 517–520 (2011).